



HAL
open science

Suivi et modélisation à haute résolution des flux hydriques d'une toiture végétalisée

Filip Stanic

► **To cite this version:**

Filip Stanic. Suivi et modélisation à haute résolution des flux hydriques d'une toiture végétalisée. Hydrologie. Université Paris-Est, 2020. Français. NNT : 2020PESC1012 . tel-03238705

HAL Id: tel-03238705

<https://pastel.hal.science/tel-03238705>

Submitted on 27 May 2021

HAL is a multi-disciplinary open access archive for the deposit and dissemination of scientific research documents, whether they are published or not. The documents may come from teaching and research institutions in France or abroad, or from public or private research centers.

L'archive ouverte pluridisciplinaire **HAL**, est destinée au dépôt et à la diffusion de documents scientifiques de niveau recherche, publiés ou non, émanant des établissements d'enseignement et de recherche français ou étrangers, des laboratoires publics ou privés.



École des Ponts
ParisTech

UNIVERSITÉ —
— PARIS-EST

Dissertation presented for the degree of

Doctor of Université Paris-Est

Specialty: Environmental Physics

Doctoral school: Sciences, Ingénierie et Environnement (SIE)

High resolution monitoring and modeling of hydrological fluxes in a green roof

by

Filip STANIĆ

Examination committee:

Ms. MASROURI Farimah

Mr. MAKSIMOVIĆ Čedo

Ms. PERRIER Edith

Mr. LU Ning

Mr. VERSINI Pierre-Antoine

Mr. CUI Yu-Jun

Mr. DELAGE Pierre

Mr. SCHERTZER Daniel

ENSG Nancy

Imperial College London

IRD France

Colorado School of Mines

École des Ponts ParisTech

École des Ponts ParisTech

École des Ponts ParisTech

École des Ponts ParisTech

Referee

Referee

Examiner

Examiner

PhD Supervisor

PhD Supervisor

PhD Co-director

PhD Director



Abstract

Green roofs are multifunctional type of Nature-Based Solutions that provide different ecosystem services among which the reduction and detention of the urban drainage outflow are the most important from the aspects of hydrology and stormwater management. As for various scientific fields, the issue of scales also appears as rather important scientific question in case of hydrology, and thus in case of green roofs. The idea behind it is to find a proper way of treating spatio-temporal variabilities of different processes involved in green roofs at larger scales, without masking heterogeneity characteristic for smaller scales. This is rather important for green roof designers, since the homogenization (averaging) in both space and time domain can impact the results of modeling significantly, providing unreliable insight into the hydrological performances of green roofs. This way, predictions of hydrological responses at larger urban (sub)catchment scales are also affected, which prevents from meeting regulation rules adopted by local authorities in charge of stormwater management.

In order to improve reliability of hydrological predictions, various thorough investigations were performed on Green Wave, a green roof of the Bienvenue building located close to Ecole des Ponts ParisTech, in suburban area of Paris. Firstly, different physical properties of the Green Wave substrate were measured in laboratory (specimen scale). The laboratory investigation of the hydraulic properties of the unsaturated / saturated Green Wave substrate, were carried out by means of the newly developed apparatus and the innovative methodology for determination of the hydraulic conductivity function.

Furthermore, on the specimen scale, spatial variability of the soil density field obtained using X-ray CT scanner is analyzed using Universal Multifractals, a theoretical framework convenient for characterizing both spatial and temporal variabilities of different geophysical fields. As a result of the investigation, new methodology and analytical functions for describing different soil properties such as the grain / pore size distribution, water retention curve and the hydraulic conductivity function, are derived. The obtained analytical functions proved to be able to interpret rather well the experimentally determined properties of the Green Wave substrate, and other soil types taken from the literature.

On the green roof scale, in-situ conditions were investigated using detailed monitoring system installed on Green Wave, where three main water balance components are measured: rainfall rate, water content indicator and drained discharge. Results showed that based on the multifractal analysis of temporal variabilities of three mentioned components, where the indicator of water content is measured by means of the network of TDR sensors distributed along the roof slope, it is possible to go beyond the standard investigation of the rainfall-runoff ratio and to analyze the impact of roof inclination on the lateral water movement within the substrate. The mentioned analysis showed that the roof inclination does not affect the peak outflow, allowing development of a new one-dimensional analytical hydrological model.

The proposed model is based on a cascade of non-linear reservoirs, where the leakage from each reservoir is described by means of the analytical function of hydraulic conductivity, also developed in this work. The model was proved as an adequate alternative for numerical

solving of Richards equation in terms of accuracy and reliability, but also as a significant improvement from the aspect of computational efficiency. As such, it can be further used to efficiently treat spatial heterogeneity of green roofs at the scale of a single roof and larger, allowing reliable investigation of hydrological impacts of this type of Nature-Based Solutions on the urban catchment scale.

Keywords: green roof; unsaturated medium; (multi)fractal soils; urban hydrology; modeling; monitoring

Résumé

Les toitures végétalisées représentent un type de solutions fondées sur la nature. Considérées comme multi-fonctionnelle, elles prodiguent de nombreux services éco-systémiques, parmi lesquels la réduction et le ralentissement des débits sont particulièrement utiles en gestion des eaux pluviales urbaines. Comme dans d'autres domaines scientifiques, la question des échelles relève d'une importance significative en hydrologie et a fortiori quand on s'intéresse au comportement hydrologique des toitures végétalisées.

Dans ce contexte, l'objectif de ces travaux de thèse est de trouver un moyen approprié de traiter les variabilités spatio-temporelles des différents processus hydrologiques mis en jeu à travers les échelles, sans masquer l'hétérogénéité caractérisant les échelles les plus fines. Ceci est important pour les concepteurs, car l'homogénéisation (dans l'espace et le temps) de ces processus dans un modèle peut avoir un impact significatif sur ses simulations, et produire des résultats peu fiables concernant les performances hydrologiques des toitures végétalisées. Agrégés à l'échelle du bassin versant urbain, ces estimations qui peuvent s'avérer erronées ne permettent pas de répondre au respect éventuel des règles de régulation adoptées par les autorités locales en charge de la gestion des eaux pluviales.

Afin d'améliorer la fiabilité des estimations réalisées à l'aide d'une modélisation hydrologique, diverses investigations ont été réalisées sur la Vague Verte de Champs-sur-Marne, une toiture végétalisée d'un hectare située à proximité de l'École des Ponts ParisTech, en banlieue parisienne. Tout d'abord, différentes caractéristiques physiques du substrat ont été mesurées en laboratoire à l'échelle d'échantillons. La quantification des propriétés hydrauliques du substrat insaturé / saturé - et plus particulièrement la détermination de la fonction de conductivité hydraulique - a été réalisée au moyen d'une méthodologie et d'un appareil nouvellement développés à cette occasion.

À l'échelle de l'échantillon, la variabilité spatiale du champ constitué par la densité du sol a été appréhendée à l'aide d'un microtomographe à rayons X. Les résultats ont ensuite été analysés dans le cadre des multifractals universels, particulièrement adapté pour caractériser les variabilités spatiales et temporelles de champs géophysiques complexes. Ces travaux ont permis de faire émerger de nouvelles méthodes et fonctions analytiques pour décrire les différentes propriétés du sol telles que la distribution granulométrique (ainsi que celle des pores), la courbe de rétention d'eau et la fonction de conductivité hydraulique. Ces nouvelles fonctions se sont avérées assez proches de celles issues des travaux effectués en laboratoire que ce soit pour le substrat de la vague verte, comme pour d'autres types de sols issus de la littérature.

Enfin, à l'échelle de la vague verte, le comportement hydrologique de la structure a été étudié à l'aide du suivi expérimental continu des trois principales composantes du bilan hydrique : la précipitation, la teneur en eau (à l'aide d'un réseau de sondes TDR répartis le long de la pente) et le débit en sortie d'ouvrage. Ces mesures analysées à l'aide d'une nouvelle analyse multifractale conduite sur la variabilité temporelle de trois composantes, ont montré qu'il est possible d'aller au-delà d'une simple quantification du coefficient de ruissellement et d'analyser l'impact de l'inclinaison du toit sur le mouvement latéral de l'eau à l'intérieur du substrat. Il en ressort que l'inclinaison du toit n'affecte pas le transfert de l'eau dans le substrat, permettant ainsi le développement d'un nouveau modèle hydrologique analytique unidimensionnel.

Le modèle proposé repose sur une cascade de réservoirs non linéaires, où la sortie de chaque réservoir est décrite au moyen d'une fonction analytique de la conductivité hydraulique

(également développée lors de ces travaux). Le modèle s'avère représenter une alternative intéressante pour la résolution numérique de l'équation de Richards en termes de précision et de fiabilité. Cette méthode entraîne également une amélioration significative du temps de calcul. Tel quel, ce modèle peut être utilisé pour tenir compte efficacement de l'hétérogénéité spatiale des toitures végétalisées à l'échelle du toit. Il doit aussi permettre de tenir compte de cette variabilité dans un bassin versant urbain où un certain nombre de toitures végétalisées seraient implémentées, et d'évaluer ainsi leur impact hydrologique à cette échelle.

Mots clés: toiture végétalisée; milieu insaturé; sols (multi)fractals; hydrologie urbaine; modélisation; instrumentation

List of Notations

| <i>Symbol</i> | <i>Meaning</i> |
|----------------------|---|
| z | Vertical distance [L] |
| t | Time [T] |
| A | Cross-sectional area [L ²] |
| V | Volume [L ³] |
| Q | (Out)flow [L ³ /T] |
| q | Water flux [L/T] |
| Π | Water head [L] |
| H_s | Thickness of the soil (substrate) [L] |
| Δz_d | Thickness of the ceramic disk [L] |
| ρ_{bulk} | Bulk (dry) density [M/L ³] |
| ρ_s | Density of the grain [M/L ³] |
| $\rho_{s,min}$ | Minimal grain density [M/L ³] |
| d_g | Diameter of grain [L] |
| $d_{g,max}$ | Maximal grain diameter [L] |
| $d_{g,min}$ | Minimal grain diameter [L] |
| C_c | Curvature coefficient [-] |
| C_u | Uniformity coefficient [-] |
| C_{MOC} | Percentage of organic matter [%] |
| d_p | Diameter of pore [L] |
| $d_{p,max}$ | Maximal pore diameter [L] |
| $d_{p,min}$ | Minimal pore diameter [L] |
| h_k | Suction expressed in water height [L] |
| Δh_k | Change of suction expressed in water height [L] |
| Δh_i | Imposed suction increment expressed in water height [L] |
| $h_{k,a}$ | Air entry value of suction expressed in water height [L] |
| s | Suction in pressure units [M/(LT ²)] |
| s_{ae} | Air entry value of suction in pressure units [M/(LT ²)] |
| φ | Porosity [-] |
| θ | Volumetric water content [-] |
| θ_s | Saturated volumetric water content [-] |
| θ_r | Residual volumetric water content [-] |

| | |
|-------------|--|
| S_e | Effective saturation degree [-] |
| D | Diffusivity coefficient [L^2/T] |
| C | Slope of the WRC (Water Retention Curve) [L^{-1}] |
| K_s | Saturated soil hydraulic conductivity [L/T] |
| K | Unsaturated soil hydraulic conductivity [L/T] |
| K_r | Relative hydraulic conductivity [-] |
| K_d | Saturated hydraulic conductivity of the ceramic disk [L/T] |
| k_a | Bulk soil dielectric permittivity [-] |
| U | Voltage [V] |
| R | Hydraulic radius [L] |
| A_w | Wet surface [L^2] |
| κ | Friction coefficient [$L^{1/3}/T$] |
| δ | Central angle for partially water filled pipe [rad] |
| r | Radius of the conduit [L] |
| λ | Resolution [-] |
| E | Euclidean dimension [-] |
| D_f | Fractal dimension [-] |
| γ | Singularity [-] |
| $c(\gamma)$ | Co-dimension function |
| p | Order of statistical moment [-] |
| $K(p)$ | Moment scaling function |
| α | Multifractality index [-] |
| C_1 | Mean intermittency [-] |

Table of Contents

| | |
|---|-----------|
| 1. INTRODUCTION..... | 1 |
| 1.1. GENERAL CONTEXT | 1 |
| 1.2. MAIN ISSUES (SCIENTIFIC QUESTIONS)..... | 1 |
| 1.3. PHD THESIS OBJECTIVES..... | 2 |
| 1.4. THESIS STRUCTURE..... | 4 |
| 1.5. PUBLICATIONS..... | 6 |
| 1.5.1. <i>Journal Papers</i> | 6 |
| 1.5.2. <i>Conference abstracts</i> | 7 |
| 1.5.3. <i>Conference papers</i> | 7 |
| 2. EXPERIMENTAL INVESTIGATION OF GREEN WAVE SUBSTRATE PROPERTIES | 9 |
| 2.1. A DEVICE FOR THE SIMULTANEOUS DETERMINATION OF THE WATER RETENTION PROPERTIES AND THE HYDRAULIC CONDUCTIVITY FUNCTION OF AN UNSATURATED COARSE MATERIAL; APPLICATION TO A GREEN-ROOF VOLCANIC SUBSTRATE | 10 |
| 2.1.1. <i>Introduction</i> | 10 |
| 2.1.2. <i>Material and methods</i> | 10 |
| 2.1.3. <i>Experimental results</i> | 21 |
| 2.1.4. <i>Conclusion</i> | 29 |
| 2.1.5. <i>References:</i> | 30 |
| 2.2. TWO IMPROVEMENTS TO GARDNER’S METHOD OF MEASURING THE HYDRAULIC CONDUCTIVITY OF NON-SATURATED MEDIA: ACCOUNTING FOR IMPEDANCE EFFECTS AND NON-CONSTANT IMPOSED SUCTION INCREMENT..... | 33 |
| 2.2.1. <i>Introduction</i> | 33 |
| 2.2.2. <i>Methods</i> | 34 |
| 2.2.3. <i>Experimental investigations</i> | 40 |
| 2.2.4. <i>Determination of hydraulic conductivity values</i> | 41 |
| 2.2.5. <i>Conclusion</i> | 47 |
| 2.2.6. <i>References:</i> | 47 |
| 3. SOIL PROPERTIES MODELS | 51 |

| | | |
|-----------|---|-----------|
| 3.1. | A NEW PHYSICALLY-BASED GRAIN SIZE DISTRIBUTION MODEL BASED ON THE APPLICATION OF THE UNIVERSAL MULTIFRACTALS ON THE RESULTS PROVIDED BY THE X-RAY COMPUTED TOMOGRAPHY | 52 |
| 3.1.1. | <i>Introduction</i> | 52 |
| 3.1.2. | <i>Universal Multifractal (UM) framework (Schertzer & Lovejoy, 1987)</i> | 53 |
| 3.1.3. | <i>Methodology</i> | 54 |
| 3.1.4. | <i>Results and Discussion</i> | 62 |
| 3.1.5. | <i>Conclusion</i> | 67 |
| 3.1.6. | <i>References:</i> | 68 |
| 3.2. | A NEW (MULTI)FRACTAL APPROACH TO ACCOUNT FOR CAPILLARY AND ADSORPTION PHENOMENA IN THE WATER RETENTION AND TRANSFER PROPERTIES OF UNSATURATED SOILS | 70 |
| 3.2.1. | <i>Introduction</i> | 70 |
| 3.2.2. | <i>Methodology</i> | 71 |
| 3.2.3. | <i>Results</i> | 77 |
| 3.2.4. | <i>Discussion</i> | 81 |
| 3.2.4. | <i>Conclusion</i> | 83 |
| 3.2.5. | <i>References:</i> | 84 |
| 4. | IN SITU INVESTIGATION CARRIED OUT ON GREEN WAVE | 89 |
| 4.1. | MEASUREMENT OF THE WATER BALANCE COMPONENTS OF A LARGE GREEN ROOF IN GREATER PARIS AREA..... | 90 |
| 4.1.1. | <i>Introduction</i> | 90 |
| 4.1.2. | <i>Materials and method</i> | 91 |
| 4.1.3. | <i>Data availability</i> | 99 |
| 4.1.4. | <i>Conclusion</i> | 102 |
| 4.1.5. | <i>References:</i> | 103 |
| 4.2. | APPLICATION OF UNIVERSAL MULTIFRACTALS (UM) ON MONITORED DATA OF WATER BALANCE COMPONENTS OF GREEN WAVE FOR ASSESSING ITS HYDROLOGICAL PERFORMANCES | 106 |
| 4.2.1. | <i>Introduction</i> | 106 |
| 4.2.2. | <i>Pilot Site</i> | 107 |
| 4.2.3. | <i>Universal Multifractal (UM) framework</i> | 107 |
| 4.2.4. | <i>Results</i> | 115 |
| 4.2.5. | <i>Conclusion</i> | 130 |
| 4.2.6. | <i>References:</i> | 131 |

| | |
|---|------------|
| 5. HYDROLOGICAL MODELING | 135 |
| 5.1. A CASCADE OF NON-LINEAR RESERVOIRS CONCEPT AND PROOF OF ITS PHYSICAL BASIS THROUGH COMPARISON WITH RICHARDS EQUATION; APPLICATION ON GREEN ROOFS | 136 |
| 5.1.1. <i>Introduction</i> | 136 |
| 5.1.2. <i>Methodology</i> | 137 |
| 5.1.3. <i>Results</i> | 142 |
| 5.1.4. <i>Conclusion & Perspectives</i> | 146 |
| 5.1.5. <i>References:</i> | 147 |
| 6. CONCLUSIONS & FUTURE WORK..... | 151 |
| 6.1. CONCLUSIONS..... | 151 |
| 6.2. FUTURE WORK..... | 152 |
| ACKNOWLEDGMENT..... | 155 |
| REFERENCES (CHAPTERS 1 & 6):..... | 157 |
| APPENDIX | 160 |
| A1: DERIVATION OF GARDNER’S METHOD | 160 |
| A2: KUNZE & KIRKHAM’S GRAPHICAL METHOD..... | 162 |
| A3: ANALOGY WITH THE DRY SIEVING METHOD..... | 164 |
| A4: SIMPLIFICATION OF HYDRAULIC CONDUCTIVITY FUNCTION | 166 |
| A5: NUMERICAL SCHEME FOR SOLVING RICHARDS EQUATION – FINITE DIFFERENCES METHOD | 169 |
| LIST OF FIGURES | 172 |
| LIST OF TABLES | 178 |

1. Introduction

1.1. General Context

Green roofs are the most widespread type of Nature-Based Solutions (NBS) that are using natural ecosystems in urban areas to provide biodiversity benefits (Kabisch et al., 2016). Green roofs provide different ecosystem services (Oberndorfer et al., 2007; Francis & Jensen, 2017) that help facing the unsustainable urbanization consequences by (i) reducing the urban heat island effects and (ii) mitigating and delaying the urban runoff peak (Stovin et al., 2012; Versini et al., 2016). The last benefit is of particular interest from the hydrological point of view, more precisely from the aspect of storm water management, since green roofs are designed to respect regulation rules adopted by local authorities based on minimizing the water quantities in sewer systems in terms of flow and volume rates (Petrucci et al., 2013).

In terms of hydrology, during the past two decades green roofs have been investigated from different aspects in various research studies. Part of the studies was focused on quantifying the hydrological performances of existing green roofs at building (roof) scale, based on the monitored rainfall-runoff data. This has been done by comparing retention and detention performances of green roofs (Johannessen et al., 2018) with different configuration parameters including type and thickness of the substrate, surface area, slope, presence and type of vegetation, etc. (Berndtsson, 2010; Li & Babcock, 2014). Other studies were oriented towards hydrological modeling at roof scale, where different kinds of models (Li & Babcock, 2014) use rainfall data as an input to compute runoff that was compared with monitored data afterwards. Based on matching quality between simulation and measurements, the ability of models to predict green roofs hydrological impacts under different critical conditions was estimated.

1.2. Main Issues (Scientific Questions)

Scale issues, common in hydrology, are also important in the case of green roofs. Clearly, each scale (*Figure 1.2-1*) has different dominant processes that need to be linked by preserving the main physically-based core that adapts to different scales while changing the level of details.

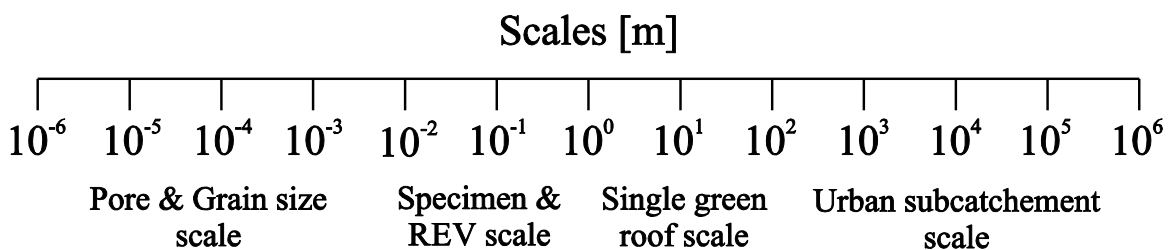


Figure 1.2-1. Illustration of different scales

In most studies on green roofs, the focus only concerns a single roof scale, while the link with larger and smaller ones is often not thoroughly explained. As previously mentioned, detailed investigations concerning both monitoring (Fassman-Beck et al., 2013; Hakimdavar et al., 2014; Stovin et al., 2015; etc.) and modeling (Hilten et al., 2008 – 1D; Palla et al., 2009 – 2D among others) are usually carried out at roof scale, while the urban catchment scale is investigated only in terms of predictions of hydrological responses by means of less physically-based hydrological models (Carter & Jackson, 2007; Versini et al., 2015; Versini et al., 2016; Ichiba et al., 2018) compared to those used at roof scale (to improve efficiency). Furthermore, scales smaller than that of a roof are usually not considered in hydrological practice. These gaps between scales cause different problems for green roof designers, that are reflected on hydrological modeling and thus impact the reliability of the predictions of hydrological responses at roof scale, and hence on urban catchment scale.

At roof scale, the investigated domain is usually considered as homogeneous structure, where the infiltration process is described by means of Richards law (Hilten et al., 2008; Hakimdavar et al., 2014), while the hydraulic properties of unsaturated porous medium (substrate) are described using different functions that depend on several (semi)-empirical parameters (Brooks & Corey, 1964; van Genuchten, 1980; etc.). As a result, by fitting these parameters good agreement between simulated and measured outflows is obtained for particular initial conditions and certain rainfall events, while in other cases, including change of scale, results might be less reliable.

One of the reasons for unreliable prediction is the use of the mentioned conventional functions for describing hydraulic properties of a green roof substrate. Besides not being fully physically-based, these functions are inappropriate for such unconventional granular materials of low grain densities (not to load roof significantly), that are adequate for plant growth (Stanić et al., 2019). Due to that, using these functions one can have realistic interpretation of soil hydraulic properties, and thus drained outflows, for certain range of soil water contents, while out of this range (wetter or dryer conditions) interpretation can be wrong.

The other important reason is the spatial heterogeneity of the substrate, which is usually neglected regardless of the scale investigated. In order to properly account for the spatial heterogeneity it is necessary to make a link with smaller scales, at which the hydraulic properties of a green roof substrate are experimentally determined, through development of new hydraulic properties functions. Also, in situ behavior of green roofs, beyond the standard rainfall-runoff measurements, is not thoroughly investigated up to date. Finally, the issue of efficient treatment of spatial heterogeneity, especially at larger scales, in physically-based hydrological models, remains to be solved.

1.3. PhD Thesis Objectives

Following the scientific questions raised in Chapter 1.2, the objectives of this work are:

- to develop the methodology for efficient and simple experimental determination of the soil hydraulic characteristics of green roof substrate. Those properties are crucial for any kind of physically-based simulations of water flow in unsaturated medium, and

thus they need to be reliably determined through experiments and not by fitting some of the mentioned functions. Efficiency and robustness are quite important aspects in this case, due to the fact that experimental investigation is not common in hydrological practice.

- to provide physical basis on the link between different scales, by analyzing the scaling behavior of various measured properties of a green roof substrate. The Universal Multifractal (UM) theoretical framework (Schertzer & Lovejoy, 1987) appears to be a convenient tool for performing such analysis, due to its ability to deal with both temporal and spatial variabilities of different geophysical fields.
- to propose physically-based alternative to tedious numerical models based on Richards equation. This is particularly important in terms of efficiency, since standard numerical models can be rather time consuming when the domain investigated is rasterized (usually the case at larger scales).

The research carried out in this thesis starts from the scale of the representative specimen used for the experimental determination of various soil properties, also known as representative elementary volume (REV) for modeling purposes. A REV is considered as large enough to keep a reasonably constant porosity when slightly changing its location inside a larger soil mass, but small enough not to mask any smaller scale spatial variability (Pinder & Celia, 2006; Pokrajac & Howard, 2010). After having conducted an experimental determination, new analytical models describing different soil properties have been developed by analyzing the soil density field, obtained by performing X-ray CT (computational tomography) on the REV, by means of UM framework. The largest scale considered in this thesis is that of a single green roof, used for installing a detailed monitoring system for different water balance components. Measurements carried out in situ are used for verifying the ratio between rainfall and runoff, for analyzing the impact of slope on green roof, and for analyzing the temporal variabilities of different water balance components. Finally, this work has been completed by developing a new physically-based model that can be effectively applied even at larger (catchment) scales.

All monitoring campaigns obtained during this thesis have been performed on the “Green Wave” of the Bienvenue building located close to Ecole des Ponts ParisTech, in the Descartes campus of Marne la Vallée, 18 km east of Paris (*Figure 1.3-1*). For now this large (1 ha) wavy-form vegetated roof, consisting of three waves, represents the largest green roof of the Greater Paris area. From its implementation in 2013, Green Wave has been considered as a demonstrative site oriented to Blue Green Solutions research (Versini et al., 2018). Implementation of the experimental set-up started during the European Blue Green Dream (BGD) project (<http://bgd.org.uk/>, funded by Climate-KIC) that aimed to promote a change of paradigm for efficient planning and management of new or retrofitted urban developments by promoting the implementation of BGS (Maksimović et al., 2013). The monitoring was anticipated and the building could be adapted to experimental purpose during its construction. It has also been supported by RadX@IdF, a regional project that notably aimed at analyzing the benefits of high-resolution rainfall measurement for urban storm water management. Today Green Wave is also part of the Fresnel multi-scale observation and modeling platform created in the Co-Innovation Lab at École des Ponts ParisTech. Fresnel aims to facilitate

synergies between research and innovation, as well as the pursuit of theoretical research, the development of a network of international collaborations, and various aspects of data science (<https://hmco.enpc.fr/portfolio-archive/fresnel-platform/>).



Figure 1.3-1. The “Green Wave” of the Bienvenue building located close to Ecole des Ponts ParisTech, Marne la Vallée

1.4. Thesis Structure

Having on mind rather wide range of topics considered in this thesis, including laboratory experiments at small scale, monitoring campaigns at the roof scale, and different kinds of modeling, it was realized that the classical form of the manuscript is inappropriate in this case, and hard for readers to follow. Thus, the main body of the thesis, excluding introduction and conclusion, is organized in four main Chapters following the previously described order of scales. These four Chapters consist of in total seven journal papers (published or submitted), arranged so that each Chapter contains one or two papers representing subchapters. Starting from the specimen scale (Chapter 1) and finalizing with the hydrological modeling (Chapter 5), a physically-based link between scales is obtained to help solving the scientific questions raised in Chapter 1.2.

For using any kind of deterministic physically-based hydrological model, it is necessary to know two main hydraulic properties of unsaturated porous medium: the water retention curve (WRC) and the hydraulic conductivity function (HCF). These properties need to be determined experimentally at specimen (REV) scale (see *Figure 1.2-1*) which is rarely considered in hydrology. Chapter 2 is focused on the innovative procedure for simultaneous and efficient experimental determination of the soil hydraulic properties. Based on the detailed outflow measurements collected while performing a multistep outflow test, both WRC and HCF have been experimentally determined. In Chapter 2.1 is presented a new

apparatus that can be easily adapted to two different techniques of controlling suction (i.e. hanging column and axis translation technique), which enables imposing accurate values of suctions by means of a specially designed mobile device. Furthermore, in Chapter 2.1 is also presented a new inverse analytical method for the experimental determination of the hydraulic conductivity function, which accounts for two boundary conditions met in step suction tests: the impedance of the high air entry value (HAEV) porous ceramic disk and a non-constant imposed suction increment.

In Chapter 3 are presented new physically-based functions that describe physical and hydraulic properties of porous medium, accounting for its heterogeneity and enabling hydrological models to treat the spatial heterogeneity in a proper manner. Based on the scaling behavior of the gray-scale images describing the (micro-)structure of the Green Wave substrate (Pore & Grain size scale in *Figure 1.2-1*), scanned using X-ray CT, analytical functions for pore and grain size distributions are derived. In case of grains, the scaling properties are described by means of the multifractal theory (UM framework) due to their non-constant densities, as explained in Chapter 3.1. On the contrary, the fractal-based approach is applied for describing the pore size distribution by using only one out of multiple fractal dimensions that describe the grain size distribution. This way, direct link between pores and grains is provided. Since the pore size distribution is strongly related to the retention and transport properties of capillary water, new water retention and hydraulic conductivity functions have been proposed in Chapter 3.2. Newly developed functions were validated through the comparison with experimentally determined hydraulic properties of the Green Wave substrate (Chapter 3.2) and with data published for other materials.

For analyzing performances of the green roof in terms of the rainfall – runoff ratio, temporal variabilities of different water balance components (the precipitation rate, the water content and the drained discharge) and water movement at inclination, detailed monitoring system described in Chapter 4 is installed on Green Wave. Different techniques for measuring these water balance components at roof scale are presented Chapter 4.1, together with almost three months of continuous time series for each of the components. In Chapter 4.2 are analyzed and compared temporal variabilities of monitored water balance components for three intensive rainfall events of short duration, by means of the Universal Multifractal Framework. This approach is convenient for analyzing the ability of green roofs to mitigate the rainfall and to provide attenuated fluctuations of drained discharge. Furthermore, by comparing the temporal variability of rainfall rate with that of water content at different locations along the slope, it is possible to make some conclusions about the dominant direction of water flow within the substrate.

Based on the work done in the three previous Chapters, a new physically-based hydrological model is proposed in Chapter 5. The measurements obtained on Green Wave (Chapter 4) confirm the conclusions made in previous studies that the water movement through the green roof substrate is dominantly vertical, with negligible lateral flow, even at slopes acceptable for green roofs. Thus, a one-dimensional model based on Richards equation appears to be sufficient for simulating the outflow drained from green roofs. The newly developed analytical model presented in Chapter 5.1 is based on the concept of cascade of non-linear reservoirs that are distributed one below another along the substrate thickness. The leakage

from each reservoir is described through a new hydraulic conductivity function presented in Chapter 3.2. A cascade containing the adequate number of non-linear reservoirs improves the standard non-linear reservoir approach by compensating some of the water retention properties ignored in the standard approach. The biggest advantage of this approach is its ability to provide in a much faster way the same results as those obtained by numerically solving Richards equation, confirming its accuracy and providing an important perspective in hydrological modeling - to efficiently and reliably account for the spatial heterogeneity at different scales.

1.5. Publications

1.5.1. Journal Papers

As previously mentioned, the thesis consists of 7 journal papers, among which 3 are published, 1 is under review, and 3 are ready for submission:

1. Stanić, F., Cui, Y.-J., Delage, P., De Laure, E., Versini, P.-A., Schertzer, D., Tchiguirinskaia, I. (2019), A device for the simultaneous determination of the water retention properties and the hydraulic conductivity function of an unsaturated coarse material; application to a green-roof volcanic substrate, *Geotechnical Testing Journal*, DOI: 10.1520/GTJ20170443.
2. Stanić, F., Cui, Y.-J., Delage, P., De Laure, E., Versini, P.-A., Schertzer, D., Tchiguirinskaia, I. (2019), Two improvements to Gardner's method of measuring the hydraulic conductivity of non-saturated media: accounting for impedance effects and non-constant imposed suction increment, *Water Resources Research*, DOI: 10.1029/2019WR026098.
3. Stanić, F., Tchiguirinskaia, I., Versini, P.-A., Cui, Y.-J., Delage, P., Scherzer, D., A new physically-based Grain Size Distribution model based on the application of the Universal Multifractals on the results provided by the X-ray Computed Tomography, *Ready for submission*
4. Stanić, F., Delage, P., Tchiguirinskaia, I., Versini, P.-A., Cui, Y.-J., , Schertzer, D., A new (multi)fractal approach to account for capillary and adsorption phenomena in the water retention and transfer properties of unsaturated soils, *Under revision in Water Resources Research*
5. Versini, P.-A., Stanić, F., Gires, A., Scherzer, D., Tchiguirinskaia, I. (2020), Measurement of the water balance components of a large green roof in Greater Paris Area, *Earth System Science Data*, DOI: 10.5194/essd-12-1025-2020.

-
6. Stanić, F., Versini, P.-A., Tchiguirinskaia, I., Delage, P., Cui, Y.-J., Scherzer, D., Application of Universal Multifractals (UM) on monitored data of water balance components of Green Wave for assessing its hydrological performances, *Ready for submission*
 7. Stanić, F., Versini, P.-A., Cui, Y.-J., Schertzer, D., Delage, P., Tchiguirinskaia, I., A cascade of non-linear reservoirs concept and proof of its physical basis through comparison with Richards equation; application on green roofs, *Ready for submission*

1.5.2. Conference abstracts

The following work has been presented at European Geoscience Union (EGU) conferences held between 2017 and 2019 in Vienna (Austria):

1. Stanić, F., Versini, P.-A., Schertzer, D., Delage, P., Tchiguirinskaia, I., Cui, Y.-J., Baudoin, G., *Large scale monitoring of a remarkable green roof: the Green Wave of Champs-sur-Marne through scales*, Presented at EGU Conference, Vienna (Austria), April 2017.
2. Stanić, F., Delage, P., Cui, Y.-J., Versini, P.-A., Tchiguirinskaia, I., Schertzer D., *Investigation of retention and transfer properties of green roofs: the Green Wave of Champs-sur-Marne (France)*, Presented at EGU Conference, Vienna (Austria), April 2018.
3. Stanić, F., Versini, P.-A., Schertzer, D., Delage, P., Cui, Y.-J., Tchiguirinskaia, I., *Analysis of different soil properties using Universal Multifractals Framework – application on green roof substrate*, Presented at EGU Conference, Vienna (Austria), April 2019.

1.5.3. Conference papers

Two conference papers have been recently accepted, and will be presented at E-UNSAT 2020 conference in Lisbon (Portugal):

1. Stanić, F., Delage, P., Cui, Y.-J., De Laure, E., Versini, P.-A., Schertzer D., Tchiguirinskaia, I., *Water retention and transfer properties of a green roof volcanic substrate*, Accepted for publication at E-UNSAT Conference Proceedings, Lisbon (Portugal), October 2020.
2. Stanić, F., Delage, P., Cui, Y.-J., De Laure, E., Versini, P.-A., Schertzer D., Tchiguirinskaia, I., *A new approach of accounting for impedance effects in Gardner's method of determining the hydraulic conductivity of unsaturated soils*, Accepted for publication at E-UNSAT Conference Proceedings, Lisbon (Portugal), October 2020.

2. Experimental investigation of Green Wave substrate properties

This Chapter is mainly focused on the experimental investigation of the hydraulic properties of a volcanic granular material used as a substrate for Green Wave. The experimental determination of the WRC the HCF, necessary for physically-based simulation of the water movement through Green Wave substrate, was carried out on a newly developed device presented in Chapter 2.1. It is a specially designed pressure plate apparatus adapted for accurate control of low suction values typical of coarse granular materials by means of two different techniques. Smaller suctions (up to 32 *kPa*) were imposed by using a hanging column system whereas larger suctions (between 32 and 50 *kPa*) were imposed by using the axis translation technique, in the same cell. The changes in suction during the tests were monitored by using a high accuracy differential pressure transducer. Transient suction changes were also used to determine the hydraulic conductivity function by means of both Gardner and Kunze and Kirkham's methods. The former technique was used at low suctions (< 4 *kPa*) to account for the impedance effects due to the low permeability of the high air entry value ceramic porous disk whereas the latter was used between 4 and 50 *kPa*. Good comparability was observed in the data from both methods, demonstrating the good performance of the device for accurate and efficient determination of the hydraulic properties of granular materials.

Based on tests carried out on this specific device, it was found necessary to account for i) impedance effects caused by the ceramic disk, and ii) the effects of non-constant imposed suction increments, the two boundary conditions dictated by the apparatus. Two analytical methods to solve the problem resulting from these two boundary conditions are presented in Chapter 2.2. The new method accounting for impedance effects is based on an analytical solution of the equations governing water transfers. Its validity is tested by considering experimental data from three distinct materials: the coarse Green Wave volcanic substrate considered in this work, together with literature data on a poorly graded sand and an undisturbed silty clay. Compared to the graphical Kunze and Kikham's method, our new method is less operator-dependent and hence more objective. It is also simpler than numerical back analysis methods, since it does not require any use of numerical code or parameter optimisation algorithm, providing a more direct and reliable determination of the HCF. An analytical solution is also proposed to account for a non-constant suction increment, and its validity is tested based on the comparison with the experimental data obtained on the Green Wave substrate.

2.1. A device for the simultaneous determination of the water retention properties and the hydraulic conductivity function of an unsaturated coarse material; application to a green-roof volcanic substrate

(Published in *Geotechnical Testing Journal*, DOI: 10.1520/GTJ20170443)

2.1.1. Introduction

Within the context of global warming, green roofs are considered as an efficient option to reduce the urban heat island (UHI) effect that characterizes large contemporary urban concentrations, thanks to the evapotranspiration of the vegetal (lawn or trees) grown on them. Green roofs are also interesting to reduce urban run-off. The substrates used in green roofs have to be light enough and to present satisfactory water retention and transfer properties. Coarse volcanic granular substrates appear to be relevant in this context, and they are frequently used in green roofs, like for instance in the case of Green Wave (Versini et al., 2018) – *Figure 1.3-1*.

The use of substrates in urban green roofs appears to be rather empirical to date, and very little data on their water retention and transfer properties are available. Also, whereas many investigations have been devoted to the determination of the water retention properties of unsaturated soils, much less data address their transfer properties, because of the technical difficulties met in their experimental determination. This is even truer in the case of coarse materials like the volcanic substrate considered here.

To cope with these limitations, the paper describes the development of a specific controlled suction device for coarse granular materials, based on both a tensiometry principle (through the hanging column technique) and the axis translation method. The device is used to determine the water retention properties of the volcanic substrate used in the Green Wave. The device is also used for a simultaneous determination of the change in hydraulic conductivity of the unsaturated substrate along a drying path, by means of Gardner (1956)'s and Kunze & Kirkham (1962)'s methods, with special care devoted to impedance effects. The experimental data obtained are compared to those derived from the water retention curves through Mualem (1976)'s approach, so as to check the validity, for the coarse material investigated in this work, of some models that are often used in the literature.

2.1.2. Material and methods

Material

The “Green wave” roof of the Bienvenüe building is presented in *Figure 1.3-1*. The VulkaTec volcanic material (VulkaTec Riebensahm GmbH, 2016) is presented in the photo of *Figure 2.1-1* and its main characteristics are presented in *Table 2.1-1*. The grain density was

determined by using water pycnometer, providing an average value of 2.35 Mg/m^3 , a small value compatible with the volcanic origin of the material. The dry density of the specimen tested was determined by calculating its volume (from its dimensions) and measuring its weight, providing a value of 1.42 Mg/m^3 , light enough not to load the roof significantly. The resulting porosity was found equal to 0.395. A percentage of 4 % of organic matter was determined by using the French standard AFNOR (1998), which consists in comparing the specimen weight before and after heating during at least 3 hours at temperature between 450 and 500 °C. The grain size distribution curve of the substrate, determined by sieving following the French standard AFNOR (1996) is presented in *Figure 2.1-2* (solid line).

The distribution of fine particles ($< 80 \mu\text{m}$) was obtained by sedimentation according to French standard AFNOR (1992). It can be noticed that 50% of the grains are larger than 1.6 mm with 10 % particles between 10 and 20 mm, in the coarse range and 13 % fine particles smaller than 80 μm .



Figure 2.1-1. Photo of the volcanic substrate used for the “Green Wave”

Also represented in *Figure 2.1-2* (dashed curve) is the grain size distribution curve of the material used for the test, with all particles smaller than 6 mm. Particles larger than 6 mm were discarded because we used a 70 mm diameter cell. For the same volume, a specimen with large particles discarded will contain more small particles, resulting in a larger porosity, in more water retained at a given suction, and in a larger hydraulic conductivity. Given that the proportion of the coarse particles discarded is 20%, a rough estimation of the over-estimation could be between 10 and 20 %.

Table 2.1-1. Basic characteristics of “Green Wave” substrate

| Density of the grains | Bulk (dry) density | Porosity | Curvature coefficient | Uniformity coefficient | Percentage of organic matter |
|-------------------------------|------------------------------------|---------------|-----------------------|------------------------|------------------------------|
| ρ_s [Mg/m ³] | ρ_{bulk} [Mg/m ³] | φ [-] | C_c [-] | C_u [-] | C_{MOC} [%] |
| 2.35 | 1.42 | 0.395 | 1.95 | 55 | 4 |

In Table 2.1-1 are also presented the curvature coefficient C_c ($C_c = (d_{g,30})^2 / (d_{g,60} \times d_{g,10}) = 1.95$) and the uniformity coefficient C_u ($C_u = d_{g,60} / d_{g,10} = 55$). According to ASTM D2487-06 (2006), the material can be regarded as well graded.

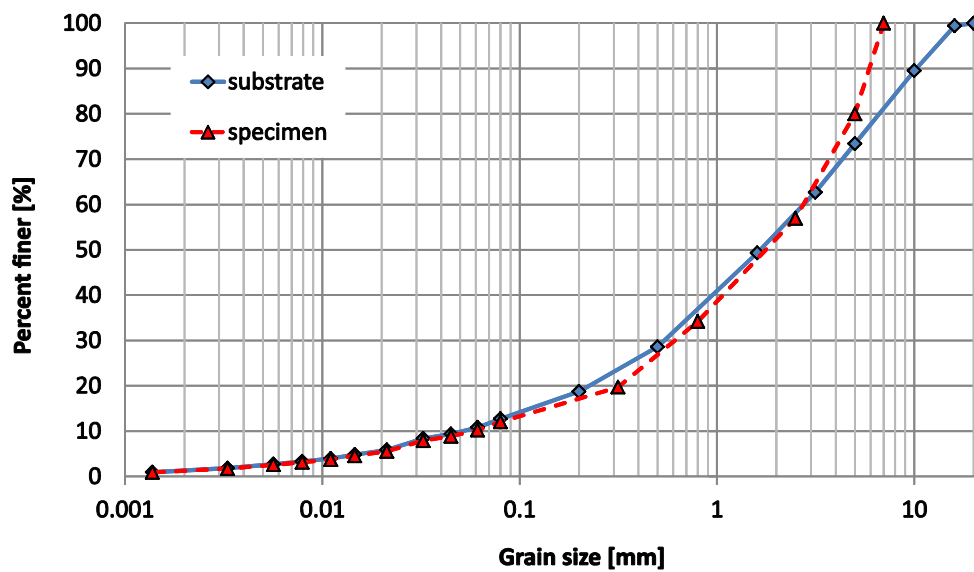


Figure 2.1-2. Grain size distribution curve of the volcanic substrate

Methods of controlling suction

The various methods of controlling suction in soils include the hanging column technique (Buckingham, 1907), the axis translation technique (Richards, 1941; Richards, 1947), the osmotic technique (Zur, 1966) and the vapour equilibrium technique (Peters et al., 2011; Esteban, 1990). A detailed description of these techniques and of their adaptation in geotechnical testing can be found in Delage (2002), Vanapalli et al. (2008), Blatz et al. (2008), Delage & Cui (2008) and Fredlund et al. (2012).

Given that the volcanic substrate investigated here is granular with rather large grain sizes (see Figure 2.1-1), it was initially decided to use the hanging column technique, because of its simplicity to use and of its good accuracy in both the control of low suctions and the measurement of water exchanges. However, one realized during the preliminary tests that, at the largest height imposed in the hanging column technique ($h_k = 3.2$ m, corresponding to a suction of $s = 32$ kPa), a significant amount of water still remained in the substrate. It was then decided to impose larger suctions by using the axis translation technique. Note that the

hanging column technique was kept at very low suctions because of its robustness and high accuracy in this range, in which a high precision air pressure regulator would have been required if using the axis-translation method.

In both cases, tests were conducted on a 24 mm high specimen placed into a metal 70 mm diameter cylindrical cell, in contact at its bottom with a 50 kPa air entry value ceramic porous disk. A thin metal disk (5 mm thick) was placed on top of the specimen, so as to monitor changes in height by means of a displacement sensor (Mitutoyo Brand).

The Hanging column technique

The implementation of the hanging column technique is presented in *Figure 2.1-3*. The cell is connected at its base through valve V2 to an outlet controlled by valve V3 and to a water reservoir through valve V1. The cell is also connected through a central tube to a mobile device that allows the imposition of water levels lower than that of the specimen, so as to apply suctions defined by the difference in water level between the specimen and the mobile part (up to 32 kPa at the maximum height of 3.2 m).

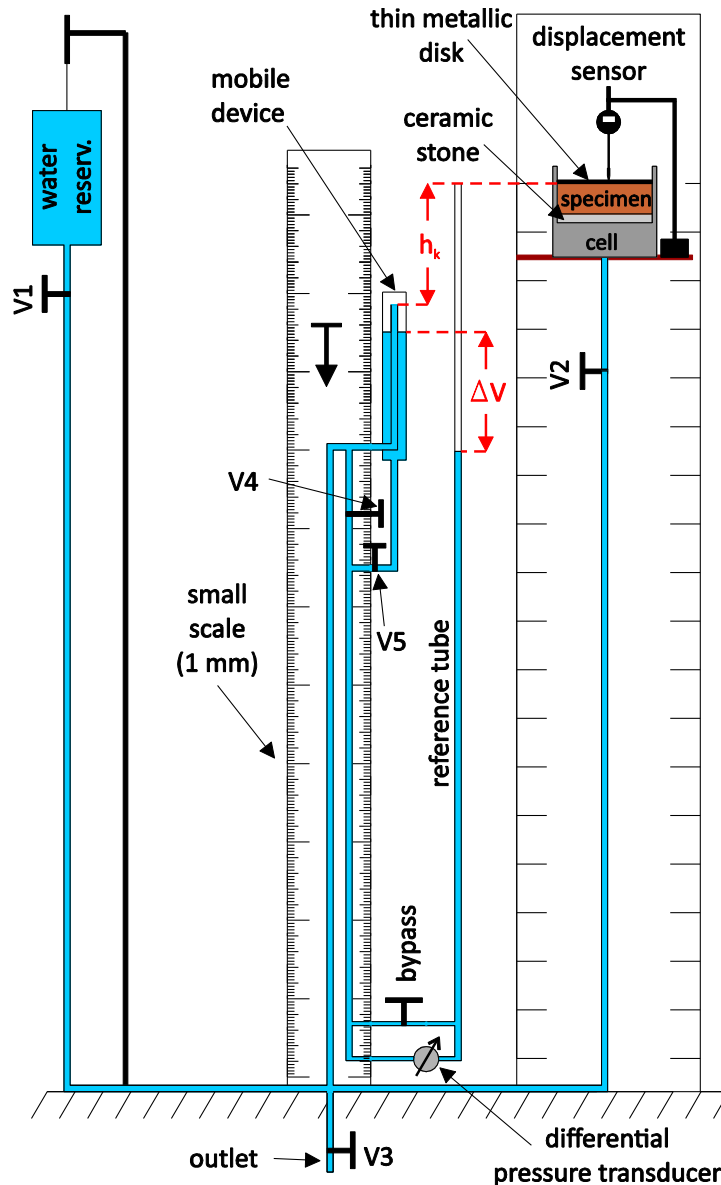


Figure 2.1-3. General lay-out of the hanging column system

The mobile device contains a smaller inner glass tube of $d_{inn} = 0.5 \text{ cm}$ and larger outer glass tube of diameter $d_{out} = 1.5 \text{ cm}$. The inner tube is connected to the specimen while the differential pressure transducer is connecting the outer tube with the reference glass tube (Figure 2.1-3). This pressure transducer (0.1 mm accuracy in water height) is able to provide high frequency measurements that are necessary for the determination of the hydraulic conductivity function. A monitoring rate of 10 s was adopted, chosen small enough to capture the change in the capillary potential at small times through the change of the water level in the mobile device. This change is detected as the height difference between the water levels either in the inner (valve V4 opened) or the outer tube (valve V5 opened), and the water level in the reference tube used to indicate constant reference water level. Most tubes used in the set-up are semi-rigid tubes made up of polyamide, except that used in the mobile device (inner and outer tubes) and the reference tube that are made up of glass.

The determination of the WRC along the drying path was carried out as follows:

Saturating the whole system

Before starting, all of the system has to be saturated, particularly the tubes connected to the differential pressure transducer, because air bubbles in the tubes can result in misleading data. Saturation was done by placing the reservoir filled with demineralized de-aired water above the specimen (*Figure 2.1-3*) and by opening valves V1 and V2 to let water infiltrate the specimen from the bottom to the top. Circulation of water within the specimen was let during one night, resulting in having a water layer laying above the specimen.

To determine the degree of saturation after infiltration and water circulation, a specific test was carried out on a specimen of same density, with the top face coinciding with the top of the cell, allowing for water overflowing. Eight pore volumes of water were circulated through the specimen by means of a graduated water column that was connected at the specimen bottom. The specimen was weighed after water circulation, and the volume of water could be calculated, knowing also the dry weight of the specimen that was measured before the test. The test provided a degree of saturation of 98%, which was found reasonably close to saturation. The 2% remaining were probably due to difficulty of fully saturating the small pores existing within the fine fraction ($13\% < 80 \mu\text{m}$). As in standard triaxial testing, full saturation could ideally be obtained by imposing a water back-pressure, which was not feasible in the present device.

Once saturation was completed, the water layer above the specimen was removed, valves V1 and V2 were closed. Prior to running the test, the mobile device was placed in such a position that the top of the inner tube full of water was at the same level as the top of the specimen, resulting in $h_k = 0$ (*Figure 2.1-3*). In order to check whether equilibrium was ensured, valve V2 (*Figure 2.1-3*) was opened. If there was no water movement in the inner tube, the experiment could start. Otherwise, the saturation procedure was repeated.

Imposing suction

Two methods were used, according to the value of suction imposed.

i) At smaller suctions, starting from saturation, it was observed that suction increases mobilized a significant volume of extracted water. Suction was then imposed by closing valves V2 and V5, by filling the inner tube up to the top and by moving down the mobile device at a position corresponding to the required suction. The water levels in the reference and outer tubes were carefully adjusted at the starting level in both tubes (*Figure 2.1-4a*).

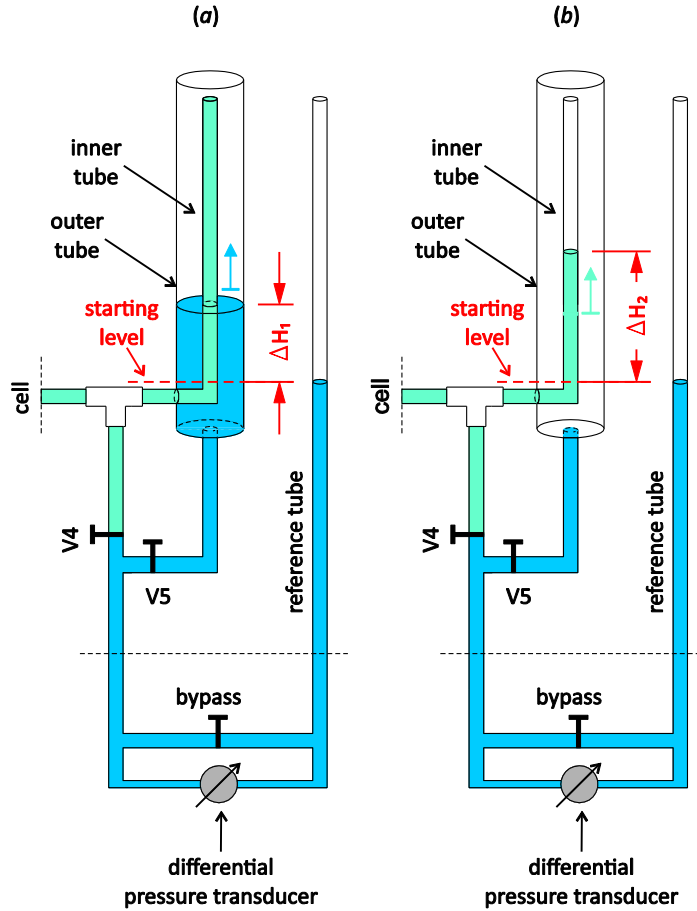


Figure 2.1-4. Description of the two procedures used: a) change in water level observed in the outer tube (ΔH_1) with valve V4 closed and valve V5 opened; b) change in water level observed in the inner tube (ΔH_2) with valve V4 opened and valve V5 closed.

The imposed suction was defined by the difference in height between the top of the specimen and the water level at the top of the inner tube (h_k in Figure 2.1-3). Valves V2 and V5 were then opened, resulting in water being extracted from the specimen under the effect of increased suction. The extracted volume of water (ΔV in Figure 2.1-3) flows from the top of the inner tube into the outer tube. It is monitored by the differential pressure transducer that measures the height difference between the water levels in the outer and reference tubes (ΔH_1 - Figure 2.1-4a). Once equilibrium is reached (after 6 – 24 hours), a point on the WRC is obtained from the pair of values $(\theta_i, h_{k,i})$ from the following equation:

$$\theta_i = \theta_{i-1} - \Delta V_i / V_{s,(i-\frac{1}{2})} \quad (2.1-1)$$

where ΔV_i is the volume of water [L^3] extracted from the specimen, $V_{s,(i-\frac{1}{2})}$ the average specimen volume [L^3] between the end and the start of the test, determined from the monitored changes in height of the specimen and $(\theta_i - \theta_{i-1})$ the difference in volumetric water content [-] between the end and the start of the test. Note however that the monitoring of the changes in specimen height during the tests indicated very small changes smaller than 0.5 mm (2%) along the whole test made up of 13 step increases in suction. The changes in height during each step were hence neglected.

ii) At larger suctions, the quantity of extracted water appeared to be much smaller and the procedure was changed to improve accuracy. The initial water level in the inner tube was no longer imposed at its top, but adjusted (by means of valve V3) at a lower level, in such a way that overflow was avoided during water extraction from the specimen. The changes in height in the inner tube were then directly measured by the differential pressure transducer by closing valve V5 and opening valve V4. The imposed suction was calculated at the end of the measurement from the difference in height between the final water level in the inner tube and the top of the specimen (ΔH_2 - *Figure 2.1-4b*).

Before each new suction step, water levels in the outer (i) / inner (ii) and reference tubes were adjusted to the same level by opening the bypass valve (*Figure 2.1-3*), in order to reset the differential pressure transducer. Water levels in the outer (i) / inner (ii) and reference tubes were then set to the required initial levels by carefully using valve V3, in order to eliminate extra water through the outlet.

In this study, only the drying path was considered. But the apparatus can also be used along wetting paths, along the following steps:

W1. Setting the initial position: the initial position of the mobile part is at the lowest vertical level, i.e. the final position at highest suction reached during the drying path. The specimen is hence capable to store more water, thus a higher change in water level is expected. The water level change is recorded in the outer tube while the inner tube is filled up with water to the top, and no longer used during the test. Initial water levels in the outer and reference tubes should be set at the top of the inner tube by opening valves V1, V4 and bypass and letting water flow over the top of the inner tube. After reaching the required position, all valves and bypass should be closed.

W2. Imposing suction: by opening valves V5 and V2, water from the outer tube enters the specimen. The resulting decrease in water level in the outer tube is captured by the differential pressure transducer.

W3. Reaching equilibrium: once equilibrium is reached, suction is calculated as the height difference between the water level in the outer tube and the top of the specimen. The corresponding water content is calculated like during the drying path, but with an opposite sign because water content is now increasing after each measurement ($\theta_i = \theta_{i-1} + \Delta V_i / V_{s,(i-\frac{1}{2})}$).

W4. Decreasing suction: to impose a lower suction, the mobile device is elevated, the outer and reference tubes are filled again, as described in step W1, and the W2 procedure is repeated. When a smaller change in water level in the outer tube is expected (lower suctions, higher water content), the inner tube should be used, by closing valve V5 and using valve V4, unlike in step W2.

W5. Final state of the wetting path: in order to bring back the specimen to zero suction, the mobile device should be located at the initial position of the drying path with the water levels in the inner and reference tubes corresponding to the specimen top. In case of a difference in height between the level in the inner tube and the top of the specimen (if h_k marked in *Figure 2.1-3* is higher than zero) after reaching equilibrium, the tubes should be refilled with water by opening valves V1, V4 and the bypass. After closing valve V1 and the bypass and opening

valve V2, without changing the vertical position of mobile device, no water movement in the inner tube should occur. If this is not the case, it means that zero suction is not obtained and the refilling procedure should be repeated.

As commented above, for determining the drying path the hanging column technique was used for heights up to 3.2 m corresponding to a maximum suction of 32 kPa. For higher suctions, the axis translation technique was applied.

The axis translation technique

The axis translation technique was carried out by applying increasing air pressure on the top specimen surface. To do so, a cap connected to the air pressure supply source was placed on the top of the cell. Tests were carried out while keeping the specimen and the mobile device at the same level, above the differential manometer in order to monitor the changes in height difference. The imposed suction was calculated as the difference between the air pressure applied on the specimen's upper surface and the change of water level inside the inner tube.

Before each test, the water level in the inner tube should be put at the same level as the top of the specimen, and some space should be left above the water level to allow for some level increase with no overflow during the measurement. Once the air pressure is imposed, valves V2 and V6 are simultaneously opened, resulting in an increase of the water level in the inner tube, until stabilization at equilibrium. The final suction is calculated as the difference between the applied air pressure and the pressure corresponding to the water level increment in the inner tube, captured by the pressure transducer. The corresponding water content is calculated by using Equation (2.1-1). This methodology was applied for suctions up to 50 kPa, the air entry value of the ceramic disk used. Higher suctions could be obtained with higher pressure and a ceramic disk of higher air entry value.

Determination of the HCF

Saturated state

The investigation on the HCF of the material started with the determination of the saturated one. To do so, the cell containing the specimen was disconnected from the device and connected to a Mariotte's bottle filled with demineralized, de-aired water, so as to run a constant head permeability test. Once the specimen was saturated, the position of the thin tube that goes through the Mariotte's bottle was set in such a way that the difference in height between its bottom and the top surface of the specimen represented the imposed water head ΔH [L]. The water level in the Mariotte's bottle had always to be above the bottom of the thin tube, in order to ensure a constant imposed water head. By measuring the water level change in the Mariotte's bottle ΔH [L] and the time necessary for obtaining this change Δt [T], the flux q [L/T] can be calculated.

$$q_j = \frac{\Delta H_j A_{mariotte}}{\Delta t_j A} \quad j = 1, 2, 3 \quad (2.1-2)$$

where $A_{mariotte}$ is the cross-section area [L²] of the Mariotte's bottle, decreased by the area of the thin tube. The saturated hydraulic conductivity K_s [L/T] is then calculated using Darcy's law.

$$K_{s,j} = \frac{q_j}{\Delta\Pi_j} H_s \quad j = 1, 2, 3 \quad (2.1-3)$$

The procedure was repeated for three different imposed water heads ($j = 1, 2, 3$), that were adjusted by changing the altitude of the bottom of the thin tube.

Unsaturated states

The various existing methods of measuring the hydraulic conductivity functions in unsaturated medium have been described in various papers or textbooks including Masrouri et al. (2008) and Fredlund et al. (2012). In steady state methods (Corey, 1957; Klute, 1972; Olsen et al., 1985, among others), a constant flow is imposed in a specimen put under given values of controlled suction. These methods are known to be rather long and tedious, due in particular to the need of very precisely measuring tiny transient flows along rather long periods of time. Alternatively, transient methods, in which the water outflow from the specimen submitted to suction steps is monitored (Gardner, 1956; Miller & Elrick, 1958; Kunze & Kirkham, 1962), are known to be easier to perform, with simpler equipment (Masrouri et al., 2008). For these reasons, transient methods were used in this work.

The HCF was hence determined by applying suction steps and monitoring the resulting changes in water content with time until equilibration, by means of the differential pressure transducer. It was planned to calculate the hydraulic conductivity of the specimen by using Gardner's method (Gardner, 1956). This method assumes that the change in suction for each step is small, in such a way that the diffusion coefficient $D(h_k)$ can reasonably be considered constant during the test:

$$D(h_k) = D = \frac{K(h_k)}{C(h_k)} = \frac{K(h_k)\Delta h_k}{\Delta\theta} \quad (2.1-4)$$

where $C(h_k)$ is the average slope of the WRC [L⁻¹] along the suction step corresponding to Δh_k [L] and $K(h_k)$ is the hydraulic conductivity [L/T]. Based on the analytical solution of the diffusion equation expressed in terms of a Fourier series, Gardner proposed an estimation of the water conductivity using the monitored volume $V(t)$ [L³] of water extracted from the specimen:

$$V(t) = V_\infty \left(1 - \frac{8}{\pi^2} \sum_{i=1,3,5,\dots}^{\infty} \frac{1}{i^2} e^{-\left(\frac{i}{2}\right)^2 \pi^2 \frac{t}{T}} \right) \quad (2.1-5)$$

$$T = \frac{H_s^2 C(h_k)}{K(h_k)} = \frac{H_s^2}{D} \quad (2.1-6)$$

where V_∞ is the total amount of water extracted during the suction step [L³]. As commented above, we observed in this work that the specimen height H_s remained reasonably constant, we hence adopted $H_s = 2.4$ cm.

Gardner's method is based on the fact that only the first member ($i = 1$) of the Fourier series in Equation (2.1-5) can be taken into account as a reasonable approximate solution, acceptable after $t > t_{bound} = \frac{4H_s^2}{3\pi^2 D}$. In such conditions, the equation corresponding to the first member of Equation (2.1-5) can be written as:

$$\ln[V_\infty - V(t)] = \ln \frac{8V_\infty}{\pi^2} - \pi^2 \frac{Dt}{4H_s^2} \quad (2.1-7)$$

showing that the term $\ln[V_\infty - V(t)]$ becomes a linear function of time t , with a slope depending on the diffusion coefficient D .

The hydraulic conductivity $K(h_k)$ can then be calculated using the following equation:

$$K(h_k) = \frac{D\Delta\theta}{\Delta h_k} \quad (2.1-8)$$

The experimental data obtained in this work indicated that Gardner's method is more relevant at higher suctions, in which i) less water exchanges occurred, ii) the condition of constant suction is ensured and iii) the assumption about a constant diffusion coefficient D is more satisfactorily fulfilled.

However, Gardner's method cannot be directly used when the saturated hydraulic conductivity of the ceramic disk is smaller than that of the specimen. Experimental data showed that this occurred during the first steps at low suction from the saturated state, during which higher hydraulic conductivity values are obtained. To cope with the cases in which impedance effects due to the ceramic disk occur, the method proposed by Kunze & Kirkham (1962) was adopted.

Kunze and Kirkham's method

Kunze & Kirkham (1962) considered the solution of the consolidation equation applied for various layers of soil with different hydraulic conductivities. Their solution is graphically presented through various curves showing the changes in $V(t)/V_\infty$ with respect to the variable $A_1^2 Dt/H_s^2$, in which the parameter A_1 is the first solution of equation $aA_n = \cot A_n$ and a is the ratio between the impedance of the ceramic disk and that of the specimen.

In order to determine the hydraulic conductivity $K(h_k)$ of the specimen, it is required to estimate parameters a and A_1 , by fitting the experimental data (presented in the form $V(t)/V_\infty$ versus t) with one of the theoretical curves. Kunze & Kirkham (1962) remarked that only a portion of the experimental data corresponded to the theoretical curves, so they recommended to rather fit the curves at small times, for which more accurate values of A_1^2 are obtained. The choice of the adequate theoretical curve provides the value of parameter a . It is then possible to determine the corresponding parameter A_1 from the *Table* presented in the paper of Kunze & Kirkham (1962). It is also necessary to graphically determine the reference time t_{RP} that corresponds to $A_1^2 Dt/H_s^2 = 1$. Finally, the diffusion coefficient is calculated as $D = H_s^2 / A_1^2 t_{RP}$ and the hydraulic conductivity by using Equation (2.1-8).

Another way to explore a possible impedance effect due to the ceramic porous disk is to apply Darcy’s law to the flux going through the saturated ceramic disk, as follows:

$$h_{k,top} = h_k - \Delta z_d \frac{\Delta V}{\Delta t} \frac{1}{AK_d} \tag{2.1-9}$$

where $h_{k,top}$ is the suction [L] at the top of the ceramic disk, Δz_s its thickness [L], and ΔV is the volume [L³] extracted from the specimen during the time interval Δt [T].

The change in suction at the top of the ceramic disk can hence be derived from the monitoring of the extracted water volume ΔV with respect to time. In the lack of any impedance effect, both suction values at top and bottom should be equal.

2.1.3. Experimental results

WRC

Figure 2.1-5 shows the continuous monitoring of the changes in suction with both the hanging column technique (steps 1 to 10) and the axis translation technique (steps 11 to 13).

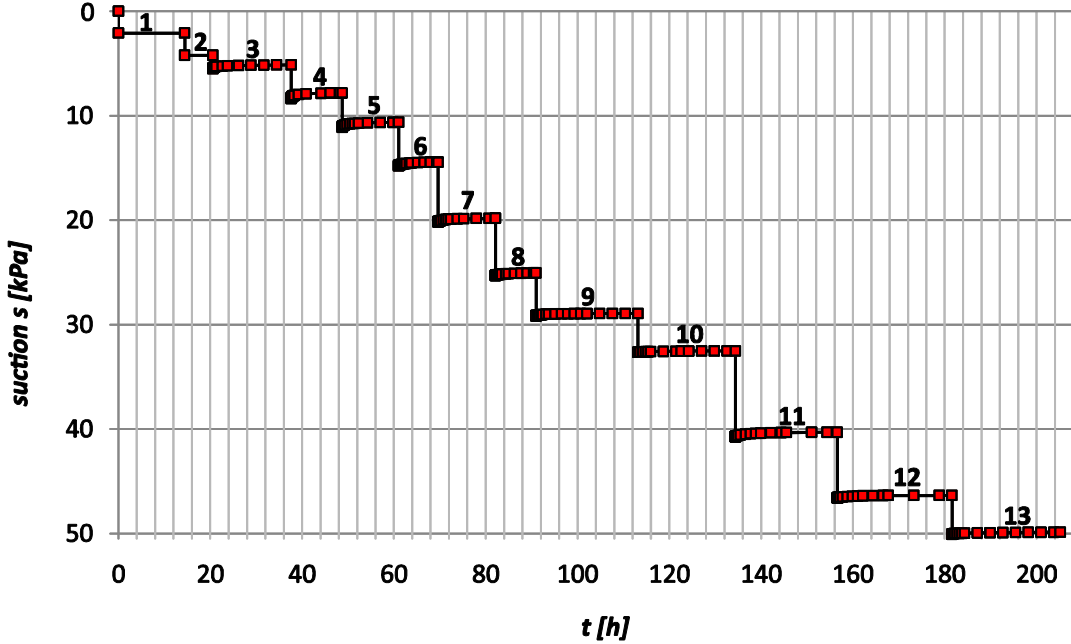


Figure 2.1-5. Continuous monitoring of the imposed suctions during the 13 steps, provided by the differential pressure transducer.

The outer tube was used for steps 1 and 2 that mobilized larger water volumes (valve V4 closed, valve V5 opened, see Figure 2.1-4a), while the subsequent 11 steps (3 – 13) were made by using the inner tube (valve V4 opened, valve V5 closed, see Figure 2.1-4b). In the former case, the imposed suction remains constant (Figure 2.1-6a, solid line with squares – the dashed line with triangles will be commented later on), while in the latter case (3 - 13), the initial instantaneous drop in height Δh_k (increase in suction) is followed by a slight progressive

increase in height, corresponding to a slight decrease in suction (see for example steps 11 - 12 in Figure 2.1-6b).

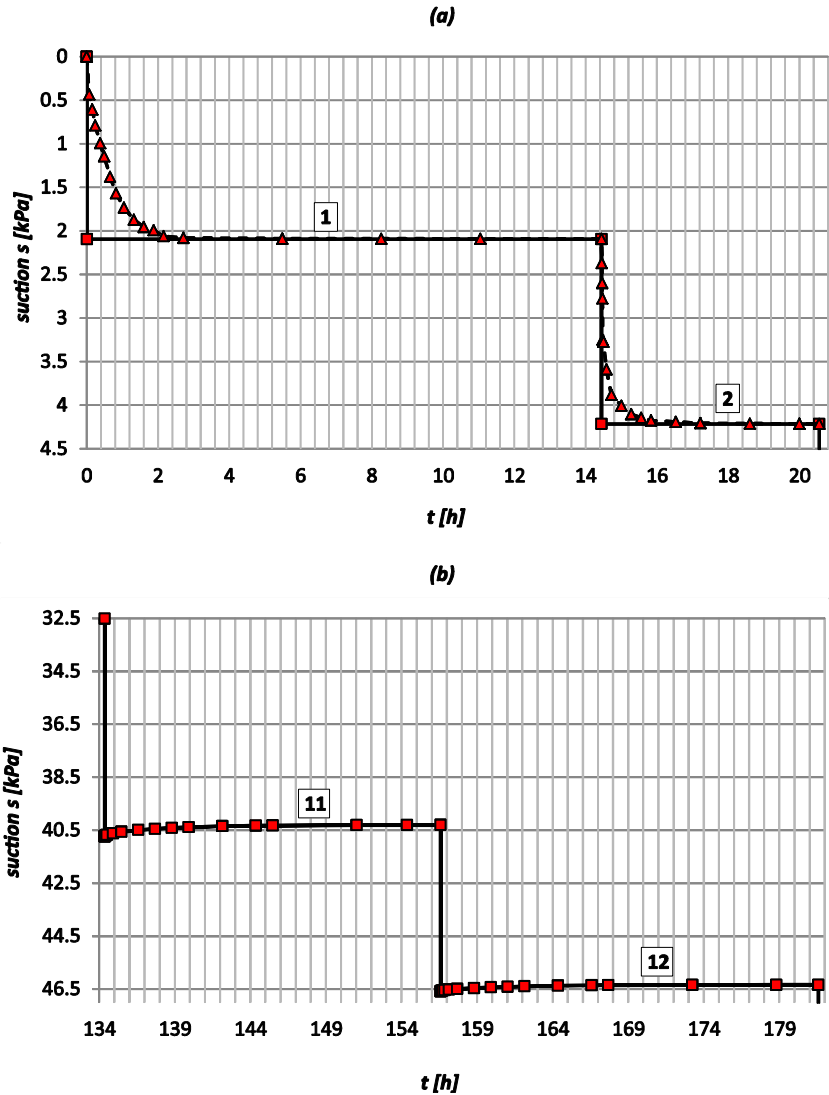


Figure 2.1-6. Zoom of the suction changes (solid line with rectangles – imposed suction; dashed line with triangles – calculated suction at the top of the ceramic disk): a) steps 1 and 2; b) steps 11 and 12

The corresponding drying path of the WRC is presented in Figure 2.1-7, in which the changes in volumetric water content θ are plotted with respect to changes in suction expressed in [kPa]. The curve evidences a significant decrease in water content for the initial steps at low suctions, with θ decreasing from the initial value of 0.395 down to 0.23 upon application of the first suction step of 2.1 kPa. The increment in volumetric water content progressively decreases afterwards, with a decrease in θ to 0.20 at a suction of 4.2 kPa. The curve finally becomes almost linear at suction larger than 14.2 kPa, indicating that the further suction increments extract small quantities of water. A final value of 0.11 is reached at 49.6 kPa.

Good compatibility is observed between the section obtained with the hanging column technique (1 – 10) and that with the axis translation method (11 – 13).

Figure 2.1-7 also shows that a good fitting is obtained by using the WRC expressions of Brooks & Corey (1964) and van Genuchten (1980), as follows:

$$- \text{ van Genuchten (vG): } \theta = \theta_r + \frac{\theta_s - \theta_r}{\left(1 + \left(\frac{s}{s_{ae}}\right)^{n_{vG}}\right)^{m_{vG}}}; \text{ with } m_{vG} = 1 - \frac{1}{n_{vG}} \quad (2.1-10)$$

where θ_s is the saturated volumetric water content ($\theta_s = 0.395$, see Figure 2.1-7), θ_r [-] the residual one, s_{ae} is the air entry value of suction [M/(LT²)], and n [-] an empirical parameter;

$$- \text{ Brooks \& Corey (BC): } \theta = \theta_r + (\theta_s - \theta_r) \left(\frac{s}{s_{ae}}\right)^{-\Lambda_{BC}} \quad (2.1-11)$$

where Λ_{BC} [-] is an empirical parameter, related to n_{vG} by the relation $\Lambda_{BC} = n_{vG} - 1$.

The fitting of the parameters of both vG and BC curves were made by first adopting values of s_{ae} and θ_r , taken equal to 0.32 kPa and 0.057, respectively. The best fitting was obtained with $n_{vG} = 1.35$ (vG expression) and $\Lambda_{BC} = 0.35$ (BC expression).

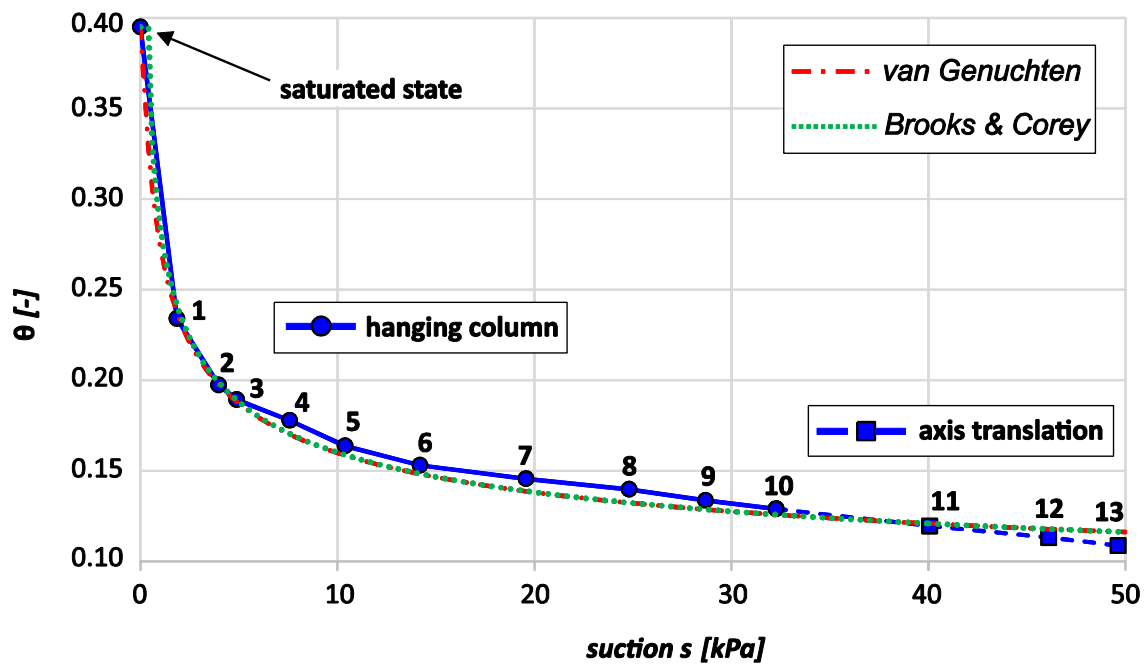


Figure 2.1-7. Water retention curve obtained using both techniques of controlling suction (hanging column and axis translation)

HCF

Saturated state

Figure 2.1-8 shows the data obtained from the steady-state permeability test, expressed in terms of changes in fluxes q_j with respect to the hydraulic gradient ($\Delta H_j / H_s$ - see Equation 2.1-3). The slope of the linear regression corresponding to the three measured points ($j = 1, 2, 3$) and to point (0, 0) provides a value $K_s = 8.11 \times 10^{-6} \text{ m/s}$.

The same approach carried out on the ceramic porous stone provided a value $K_d = 4.02 \times 10^{-8} \text{ m/s}$, confirming that the hydraulic conductivity of the saturated ceramic porous stone is significantly smaller than that of the saturated material. As a consequence, Kunze and Kirkham's method was used to interpret the data of the first suction steps (1 and 2) applied from the saturated state.

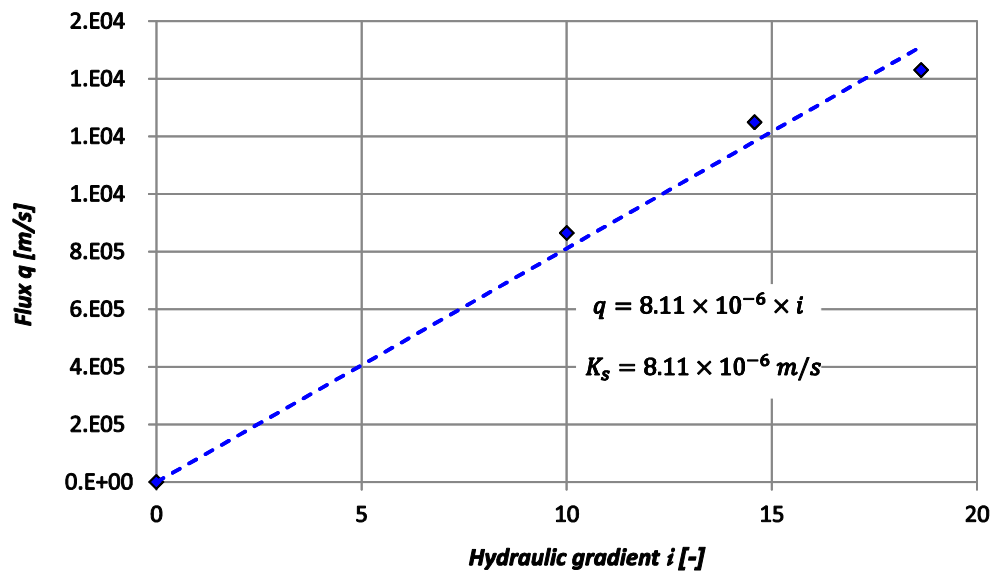


Figure 2.1-8. Data of the constant water head hydraulic conductivity measurement of the saturated material.

Unsaturated states

Figure 2.1-9 presents the experimental data of steps 1 and 2 presented in terms of changes in $V(t)/V_\infty$ with respect to a log scale of $A_1^2 D t_{RP} / H_s$, as proposed by Kunze and Kirkham. For step 1, Figure 2.1-9 shows excellent agreement of the data with the theoretical curve of parameter $a = 1$. The corresponding value of parameter A_1^2 is 0.74, according to Kunze and Kirkham (1962)'s graph, while the reference time t_{RP} is 47 min (2800 s - vertical arrow in Figure 2.1-9).

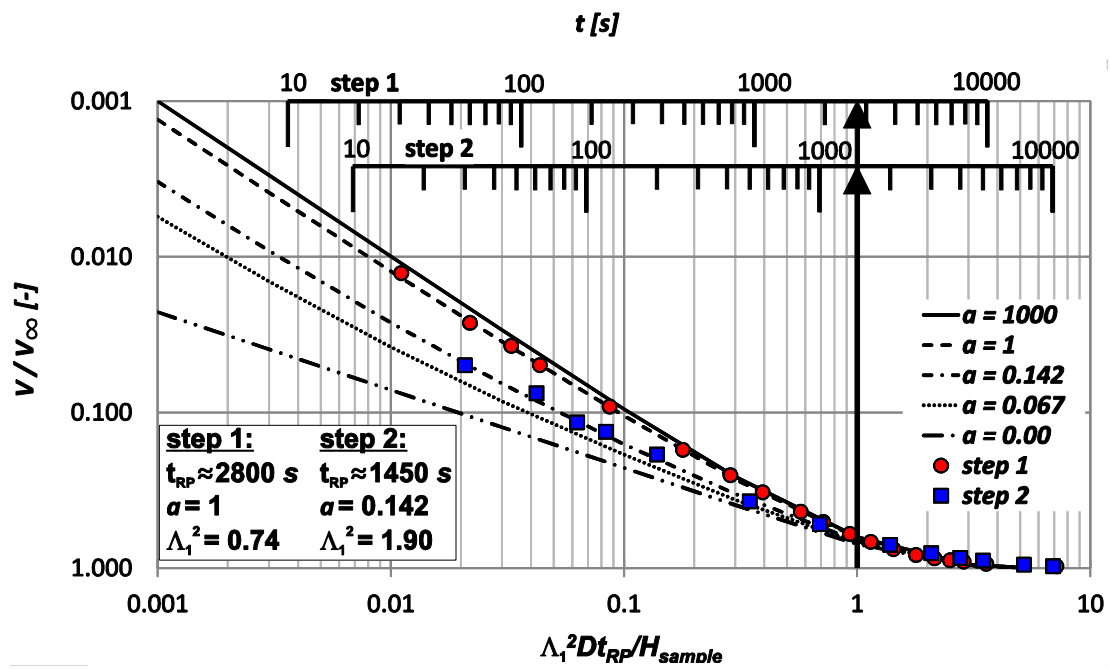


Figure 2.1-9. Kunze and Kirkham's method applied to steps 1 and 2 (arrow indicates t_{RP})

Finally, a hydraulic conductivity $K(s) = 2.14 \times 10^{-7}$ m/s is obtained for a suction of 2.1 kPa. This value is larger than that of the ceramic disk ($K_d = 4.02 \times 10^{-8}$ m/s), confirming the necessity of accounting for the impedance effect of the porous stone. Similarly, a value $a = 0.142$ is obtained for step 2, with $\Lambda_1^2 = 1.90$ with $t_{RP} = 24$ min (1440 s), resulting in a hydraulic conductivity value of 3.64×10^{-8} m/s, slightly smaller than that of the ceramic porous stone.

The calculations of the changes with time of the suction imposed on the top of the ceramic disk according to Equation (2.1-9) are presented in Figure 2.1-6a for steps 1 and 2 (dashed line with triangles). As expected, they confirm the perturbation due to the low permeability of the ceramic disk. This perturbation is stronger during step 1, in which almost 3 hours are necessary to reach the desired 2.1 kPa suction at the top, compared to step 2 in which the 4.2 kPa imposed suction is reached at the top after less than 2 hours.

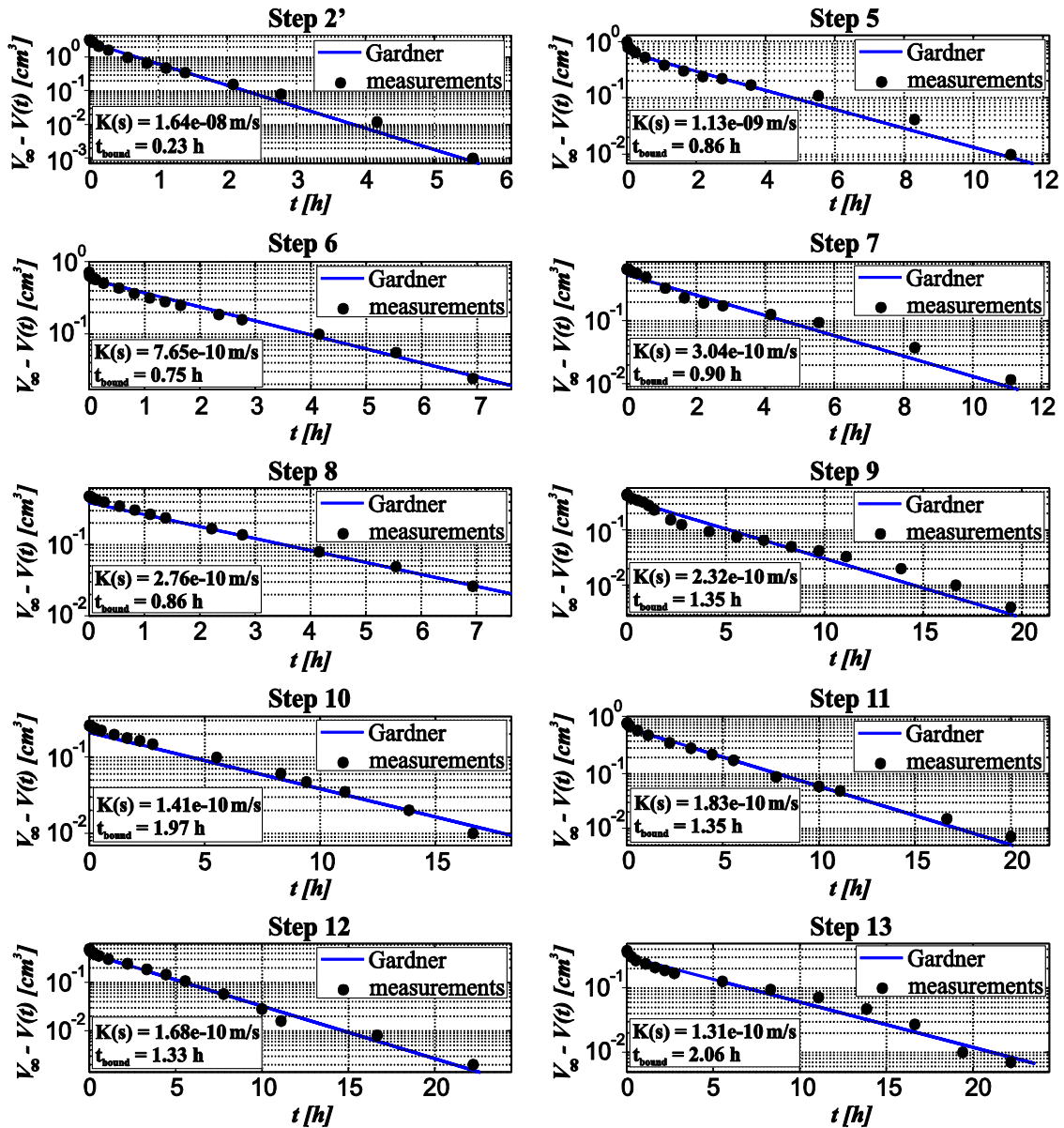


Figure 2.1-10. Data from Gardner's method, suction steps 2' and 5 – 13

Prior to use Gardner's method, the assumption of constant suction during each suction step has to be checked. Inspection of the suction steps applied for suctions higher than 4.1 kPa (steps 3 – 13, Figure 2.1-5) showed that the water level in the inner tube was slightly rising at the start of the step, hence decreasing the suction. The level changes in the inner tube during steps 3 and 4 are around 7.5 % of the imposed suction and 30 % of the imposed suction increment. These two steps do not reasonably ensure the constant suction condition, they will not be considered for the determination of the HCF. For suctions higher than 10 kPa (measurements 5 – 13, Figure 2.1-5), the level increase in the tube is smaller (less than 4 % of the imposed suction and less than 12 % of the imposed suction increment), and suction changes are considered to be reasonably compatible with the use of Gardner's method (see for example steps 11 and 12 in Figure 2.1-6b).

The application of Gardner's method is presented in *Figure 2.1-10*, that shows the changes in $\ln[V_\infty - V(t)]$ with respect to time for the measurements made during steps 2 and 5 – 13 (see Equation 2.1-7). In all cases, the linearity of the $\ln[V_\infty - V(t)]$ function is satisfactory. As recommended by Gardner, the fitting is only based on the points corresponding to $t > t_{bound}$. The values of t_{bound} , calculated for each stage, are given in the graph of each step. Values are included between 0.2 and 2 h, depending of the value of D . Note that step 2 was also considered here, so as to compare the data with that of Kunze and Kirkham's method, that is more appropriate, given possible impedance effects.

Figure 2.1-11 shows the hydraulic conductivities obtained using the three different methods: i) saturated hydraulic conductivity, using the constant-head permeability test, ii) unsaturated hydraulic conductivity at lower suctions, using Kunze and Kirkham's method (steps 1 and 2) and iii) unsaturated hydraulic conductivity at larger suctions, using Gardner's method (steps 2' and 5 to 13).

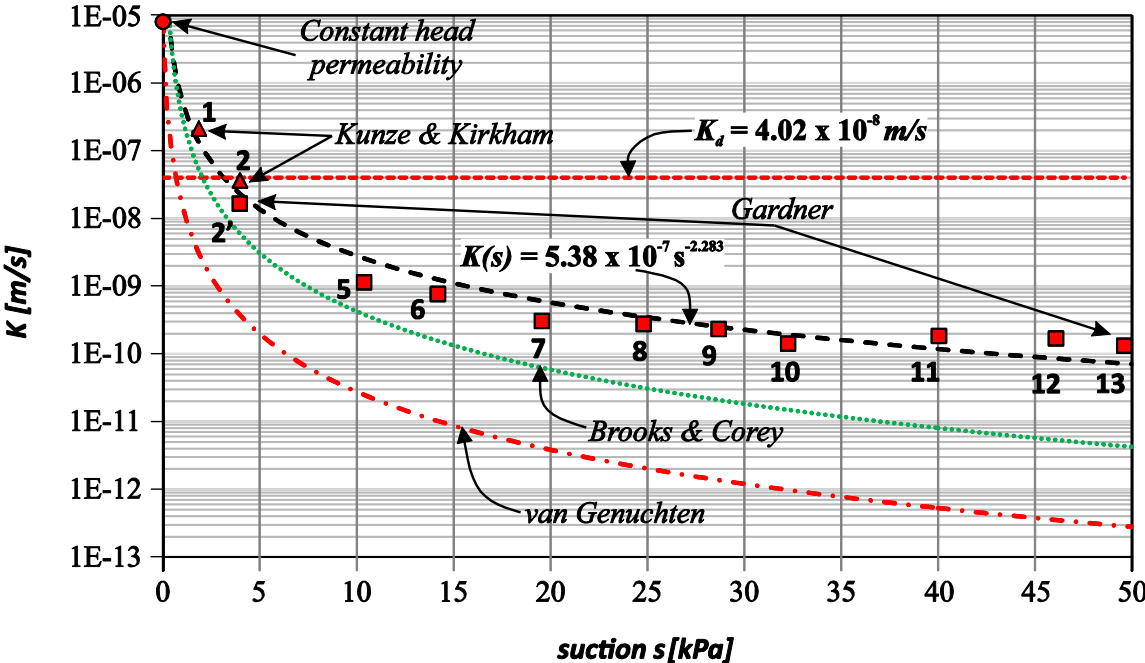


Figure 2.1-11. Hydraulic conductivity function (HCF)

One observes that the hydraulic conductivity at step 2' provided by Gardner's method is somewhat smaller than that (step 2) given by Kunze and Kirkham's method. This is compatible with the impedance effect due to the low permeability of the ceramic disk, which indicates that Gardner's method is not fully satisfactory for step 2. Note however that the difference in hydraulic conductivity is not that large (3.64×10^{-8} m/s for Kunze and Kirkham and 1.64×10^{-8} m/s for Gardner's method).

All the points obtained by the three methods are in reasonable agreement and provide the decrease in hydraulic conductivity with increased suction along the drying path. In the first 5 steps, a large decrease of 4 orders of magnitude is observed from 10^{-5} m/s (saturated state)

down to 10^{-9} m/s at a suction of 10.4 kPa, and the hydraulic conductivity then stays between 10^{-9} and 10^{-10} m/s for steps 5 to 13, corresponding to suctions between 10.4 and 49.6 kPa.

The results are also compared with the curves obtained by using the mathematical expressions of the relative hydraulic conductivity ($K_r(s) = K(s) / K_s$) derived from the WRC formulations of Brooks & Corey (1964) and van Genuchten (1980) according to Mualem (1976)'s approach (Equations 2.1-10 and 2.1-11), as follows:

$$\text{- van Genuchten: } K_r(s) = \frac{\left[1 - \left(\frac{s}{s_{ae}}\right)^{n_{vG}-1} \left(1 + \left(\frac{s}{s_{ae}}\right)^{n_{vG}}\right)^{-m_{vG}}\right]^2}{\left(1 + \left(\frac{s}{s_{ae}}\right)^{n_{vG}}\right)^{m_{vG}/2}} \quad (2.1-12)$$

$$\text{- Brooks & Corey: } K_r(s) = \left(\frac{s}{s_{ae}}\right)^{-2-5\Lambda_{BC}/2} \quad (2.1-13)$$

The curves obtained with the parameters obtained from the WRC curves, also represented in *Figure 2.1-11*, do not satisfactorily fit with the experimental data. Both formulations underestimate the hydraulic conductivity, with a better correspondence observed with the Brooks and Corey formulation. Indeed, the poor performance of the vG formulation is surprising, given that both the vG and BC expressions fitted quite nicely with the water retention curve, and that both permeability functions came through Mualem's approach. As explained above, the same physical parameters were adopted in both cases (air entry value s_{ae} , residual and saturated water content θ_r and θ_s , respectively), while the fitting parameters used for the water retention curve were n_{vG} (vG) and Λ_{BC} (BC), also linked together ($\Lambda_{BC} = n_{vG} - 1$). Actually, it seems that these permeability functions derived from the WRC curves are most often used in the literature without further experimental check. A possibility could be that we deal in this work with a rather specific coarse granular material. This poor performance of the vG HCF in such a coarse material certainly deserves further attention.

Because of this poor correspondence, it was decided to propose a power law, fitted by using the root-mean-square-deviation (RMSD) method. This solution can be written in the following form:

$$K(s) = a_1 \times s^{b_1} \quad (2.1-14)$$

with $a_1 = 5.38 \times 10^{-7}$ and $b_1 = -2.283$, giving:

$$K(s) = 5.38 \times 10^{-7} \times s^{-2.283} \quad (2.1-15)$$

The corresponding expression of the relative permeability is then:

$$\frac{K(s)}{K_s} = a_2 s^{b_1} = 6.63 \times 10^{-2} \times s^{-2.283} \quad (2.1-16)$$

In order to present the right side of Equation (2.1-16) in the relative form as well, coefficient a_2 can be written as follows:

$$a_2 = \left(\frac{1}{s_{ae}}\right)^{b_1} \rightarrow s_{ae} = a_2^{-\frac{1}{b_1}} = 0.305 \quad (2.1-17)$$

where the value of s_{ae} is expressed in [kPa]. The final form of the equation reads:

$$\frac{K(s)}{K_s} = \left(\frac{s}{s_{ae}}\right)^b \quad (2.1-18)$$

with $s_{ae} = 0.305 \text{ kPa}$ and $b = b_1 = -2.283$.

2.1.4. Conclusion

The new device developed in this work allowed to determine the water retention curve and the hydraulic conductivity function of a light coarse material used as substrate in an urban green roof. In a first estimation, it was estimated that the hanging column technique of controlling suction, with a maximum height of 3.2 m (suction 32 kPa) would have been satisfactory, but it was finally necessary to impose larger suctions by using the axis translation technique. This adaptation was rather simple to carry out, finally allowing us to run the whole test by using both techniques on the same specimen in the same cell, between the saturated state and a maximum suction of 49.6 kPa , with a good comparability between the experimental data obtained by the two techniques.

The advantage of the hanging column technique is to allow for a very good precision in the control of both the suction and the water exchanges, made possible by using a differential pressure sensor with an accuracy of 0.1 mm in height. A specific system based on the use of both an inner and an outer tube was also developed so as to improve the accuracy of the measurements along the range of the applied suctions. This good accuracy was necessary, given the significant changes in volumetric water content observed during the first application of a suction as low as 2.1 kPa that resulted in a significant decrease from 0.40 to 0.23.

Starting from a saturated state, the WRC exhibited a drastic decrease under a small suction of 2.1 kPa , in link with the coarse nature of the granular substrate, followed by a progressive decrease down to a water content of 0.11 at 49.6 kPa . Both the van Genuchten and Brooks and Corey mathematical expressions fitted quite nicely with the experimental data.

The good accuracy in the measurements of suction and water exchanges also allowed us to simultaneously determine, in a simple fashion, the hydraulic conductivity function from the monitoring of the water exchanges resulting from the step changes in suction. At lower suctions (2.1 and 4.2 kPa) and higher hydraulic conductivity, it was necessary to account for the impedance effects due to the 50 kPa air entry value ceramic disk by successfully using Kunze and Kirkham's method. Gardner's method was used at larger suctions, and a good comparability was observed from the experimental data from each technique. Another advantage of the device is to simply allow for the determination of both the water retention curve and the hydraulic conductivity function of the coarse material. Unsurprisingly, the HCF exhibited a trend similar to that of the WRC, with a decrease of around 3 orders of magnitude between the saturated state and that at a suction of 4.2 kPa , whereas all the data between 10.4 and 49.6 kPa were comprised between 10^{-9} and 10^{-10} m/s.

The experimental HCF data were compared with the analytical expressions derived from the WRC expressions of van Genuchten and Brooks and Corey, based on Mualem's approach. In both cases, these expressions appeared to significantly underestimate the experimental HCF, however with better results with BC's expression, which was less than one order of magnitude below the experimental data. These expressions of the HCF are often used in the lack of experimental data, and the difference observed in this work confirm the need of having operational devices for the simultaneous experimental determination of the water retention curve and the hydraulic conductivity function in granular materials, such as the green roof substrate investigated in this work.

To summarize, the main advantages of the presented device are i) its reliability for the simultaneous determination of both the WRC and the HCF, thanks to the robustness and precision of both the double tube system for monitoring water exchanges, and of the high precision differential pressure transducer for the measurement of suction; ii) its ability to accommodate both the hanging column and axis translation techniques of controlling suction, with the largest possible suction controlled by the air entry value of the porous stone, i.e. 1500 kPa for common ceramic porous stones; iii) its ability to provide relevant data within a reasonable period of time: 10 days were necessary to run 13 steps, a period that can be reduced by making less steps, resulting for instance in a time period of around 1 week for 7 steps.

Note that the technique developed in this work could be extended to larger suctions by using a ceramic disk with a larger air entry value, allowing it to reach drier states. Note however that the technique is more adapted for granular materials in which rather low suctions develop. It could exhibit some restrictions in terms of water retention properties in the case of finer soils. The range of unsaturated hydraulic permeability functions covered during our investigation is between 10^{-5} and 10^{-10} m/s. Again, it seems that the technique would be limited, for finer soils, at larger suctions resulting in smaller hydraulic conductivity functions.

2.1.5. References:

- AFNOR. 1992. *Analyse granulométrique des sols - Méthode par sédimentation*. NFP94-057(1992). Paris La Défense Cedex, approved May 20, 1992.
- AFNOR. 1996. *Analyse granulométrique - Méthode par tamisage à sec après lavage*. NFP94-056(1996). Paris La Défense Cedex, approved March 5, 1996.
- AFNOR. 1998. *Détermination de la teneur pondérale en matières organiques d'un matériau*. XPP94-047(1998). Paris La Défense Cedex, approved December, 1998.
- ASTM International. 2006. *Standard Practice for Classification of Soils for Engineering Purposes (Unified Soil Classification System)*. ASTM D2487-06(2006). West Conshohocken, PA: ASTM International, approved May 1, 2006.
- Blatz, J. A., Y. -J. Cui, and L. Oldecop. 2008. "Vapour Equilibrium and Osmotic Technique for Suction Control." *Geotech. Geol. Eng.* 26: 661–73. <https://doi.org/10.1007/s10706-008-9196-1>.
- Brooks, R. H., and A. T. Corey. 1964. "Hydraulic Properties of Porous Media." *Hydrology*

- Buckingham, E. 1907. *Studies on the Movement of Soil Moisture*, U. S. Department of Agriculture, Bureau of Soils, *Bulletin 38*. Washington DC.: U. S. Department of Agriculture.
- Corey, A. T. 1957. “Measurement of Water and Air Permeability in Unsaturated Soil.” *Soil Science Society of America Journal* 21 (1): 7–10.
<https://doi.org/10.2136/sssaj1957.03615995002100010003x>.
- Delage, P. 2002. “Experimental Unsaturated Soil Mechanics: State-of-Art-Report.” In *Third International Conference on Unsaturated Soils UNSAT (Vol. 3)*. Recife (Brazil).
- Delage, P., and Y. -J. Cui. 2008. “Geomechanics and Geoengineering : An International An Evaluation of the Osmotic Method of Controlling Suction.” *Geomechanics and Geoengineering: An International Journal* 3 (1): 1–11.
<https://doi.org/10.1080/17486020701868379>.
- Esteban, F. 1990. “Caracterizacion de La Expansividad de Una Roca Evaporítica. Identificacion de Los Mecanismos de Hinchamiento.” Universidad de Cantabria.
- Fredlund, D. G., H. Rahardjo, and M. D. Fredlund. 2012. *Unsaturated Soil Mechanics in Engineering Practice*. Hoboken, NJ: John Wiley & Sons.
- Gardner, W. R. 1956. “Calculation of Capillary Conductivity from Pressure Plate Outflow Data.” *Soil Science Society of America Journal* 20 (3): 317–20.
<https://doi.org/10.2136/sssaj1956.03615995002000030006x>.
- Genuchten, M. Th. van. 1980. “A Closed-Form Equation for Predicting the Hydraulic Conductivity of Unsaturated Soils.” *Soil Science Society of America Journal* 44 (5): 892–98. <https://doi.org/10.2136/sssaj1980.0A03615995004400050002x>.
- Klute, A. 1972. “The Determination of the Hydraulic Conductivity and Diffusivity of Unsaturated Soils.” *Soil Science* 113 (4): 264–76. <https://doi.org/10.1097/00010694-197204000-00006>.
- Kunze, R. J., and D. Kirkham. 1962. “Simplified Accounting for Membrane Impedance in Capillary Conductivity Determinations.” *Soil Science Society of America Journal* 26 (5): 421–26. <https://doi.org/10.2136/0A03615995002600050006x>.
- Masrouri, F., K. V. Bicalho, and K. Kawai. 2008. “Laboratory Hydraulic Testing in Unsaturated Soils.” *Geotech. Geol. Eng.* 26: 691–704. <https://doi.org/10.1007/s10706-008-9202-7>.
- Miller, E. E., and D. Elrick. 1958. “Dynamic Determination of Capillary Conductivity Extended for Non-Negligible Membrane Impedance.” *Soil Science Society of America Journal* 22 (6): 483–86.
<https://doi.org/10.2136/sssaj1958.03615995002200060002x>.
- Mualem, Y. 1976. “A New Model for Predicting the Hydraulic Conductivity of Unsaturated Porous Media.” *Water Resources Research* 12 (3): 513–22.
<https://doi.org/10.1029/WR012i003p00513>.
- Olsen, H. W., R. W. Nichols, and T. L. Rice. 1985. “Low Gradient Permeability Measurements in a Triaxial System.” *Géotechnique* 35 (2): 145–57.
<https://doi.org/10.1680/geot.1985.35.2.145>.
- Peters, A., W. Durner, and G. Wessolek. 2011. “Consistent Parameter Constraints for Soil Hydraulic Functions.” *Advances in Water Resources* 34 (10): 1352–65.

<https://doi.org/10.1016/j.advwatres.2011.07.006>.

- Richards, L. A. 1941. "A Pressure-Membrane Extraction Apparatus for Soil Solution." *Soil Science* 51 (5): 377–86. <https://doi.org/10.1097/00010694-194105000-00005>.
- . 1947. "Pressure-Membrane Apparatus – Construction and Use." *Agricultural Engineering* 28: 451–60.
- Vanapalli, S. K., M. V. Nicotera, and R. S. Sharma. 2008. "Axis Translation and Negative Water Column Techniques for Suction Control." *Geotech. Geol. Eng.* 26 (May): 645–60. <https://doi.org/10.1007/s10706-008-9206-3>.
- Versini, P. -A., A. Gires, I. Tchiguirinskaia, and D. Schertzer. 2018. "Toward an Assessment of the Hydrological Components Variability in Green Infrastructures: Pilot Site of the Green Wave (Champs-Sur-Marne)." *La Houille Blanche*, no. 4: 34–42. <https://doi.org/10.1051/lhb/2018040>.
- VulkaTec Riebensahm GmbH. 2016. "Vulkaplus Intensiv 0/12 / Vulkaplus Intensiv Typ Leicht." http://web.archive.org/web/%0A20190423142633/http://www.vulkatec.de/Begrueung/Dachbegrueung/Intensivbegrueung-bei-Substratstaerken-bis-50cm/%0AVulkaplus-Intensiv-0_12/?&d=1.
- Zur, B. 1966. "Osmotic Control the Matric Soil-Water Potential: I. Soil-Water System." *Soil Science* 102 (6): 394–98. <https://doi.org/10.1097/00010694-196612000-00007>.

2.2. Two improvements to Gardner's method of measuring the hydraulic conductivity of non-saturated media: accounting for impedance effects and non-constant imposed suction increment

(Published in *Water Resources Research*; DOI: 10.1029/2019WR026098)

2.2.1. Introduction

Gardner's method (Gardner, 1956) was the first analytical method of calculating the hydraulic conductivity of unsaturated porous media by measuring, in the pressure plate apparatus, the transient outflow resulting from a step increase in suction, applied to the unsaturated specimen through an increase in air pressure. This method is based on various assumptions, including the linearity of the water retention curve (WRC) and a constant value of the diffusivity D over the suction increment applied (both hypotheses are better fulfilled with small suction increments). Gardner's method does not account for the impedance effects of the plate (made up of a saturated ceramic porous disk with high air entry value) that may have a significantly lower hydraulic conductivity than that of the saturated specimen. This impedance effect was considered for first time by Miller & Elrick (1958), who proposed an analytical method to account for the flow resistance exerted by the disk, provided the disk hydraulic conductivity was known and the contact specimen/disk was perfect. Rijtema (1959) improved the method by developing a solution based on the hydraulic conductivity ratio between the soil and the disk, valid regardless of the quality of the specimen/disk contact. Finally, Kunze & Kirkham (1962) developed a graphical method based on Miller and Elrick's method, in which particular attention was focused on the accurate determination of initial outflow values, which is particularly important with respect to impedance effects. However, this method, based on fitting experimental data against normalized charts to obtain some specific parameters required to calculate the hydraulic conductivity, may present some degree of subjectivity and operator dependency (see Appendix A2). More recently, Valiantzas (1990) proposed an analytical method that was not based on the assumption of constant diffusivity. The method was applied on single-step outflow measurements (Doering, 1965) by using an iterative algorithm to determine the relationship between the diffusivity and the water content. The main disadvantage of this method is that the water retention curve, necessary to make the calculations, has to be determined independently of the hydraulic conductivity function (HCF).

In the past decades, numerical back analysis methods have been preferred to determine the HCF of unsaturated soils, through the simulation of water flow in unsaturated media by numerically solving Richards equation (Richards, 1931). When dealing with techniques in which ceramic stones are involved, numerical back analysis methods account for impedance effects by simulating transient water outflows from two-layered specimens (soil specimen and ceramic disk) subjected to suction increments (Eching & Hopmans, 1993; Eching et al., 1994;

van Dam et al., 1994; Durner & Iden, 2011; Schelle et al., 2011; Nasta & Hopmans, 2011; Wayllace & Lu, 2011). In these calculations, different functions are used to describe the hydraulic properties of the soils. Their parameter values are obtained by using different optimization algorithms for minimizing the deviation between measured and simulated outflows (Levenberg, 1944; Šimůnek et al., 2008). Since the WRC of the investigated materials cannot be always reliably interpreted with these functions that depend either on one (Brooks & Corey, 1964) or several semi-empirical parameters (van Genuchten, 1980; Fredlund & Xing, 1994; etc.), the HCF derived through Mualem (1976)'s approach does not necessarily provide realistic results (e.g. Khaleel & Relyea, 1995).

Given the advantages and drawbacks of existing methods, a new and simple analytical approach to account for impedance effects in the determination of the HCF of unsaturated soils is proposed in this paper, together with an approach to account for non-constant imposed suction increment. The validation of the method is carried out based on experimental data from three different materials, i.e. a coarse material used for covering Green Wave (Stanić et al., 2019), a poorly graded sand and an undisturbed silty clay (Wayllace & Lu, 2011). This analytical method is simpler than numerical back analysis methods since it does not require the use of any numerical code and sophisticated optimization tools. It is also not affected either by any subjective graphical method like in the traditional Kunze and Kirkham's method.

2.2.2. Methods

Analytical methods of determining the hydraulic conductivity of unsaturated materials

The methods developed in this work originate from an experimental investigation carried out by Stanić et al. (2019). The experimental device used for the determination of the HCF based on Gardner's and Kunze and Kirkham's methods is presented in a simplified way in *Figure 2.2-1* and *2* (see Stanić et al., 2019 for more details). It consists of a metal cylindrical cell in which specimen is placed on a high air entry value (HAEV) ceramic porous disk. In *Figure 2.2-1*, one observes that a suction step can be applied through a hanging column device, by moving down a mobile system in which the constant suction is controlled by the level of the top of the inner thin tube. The water extracted due to the suction step overflows in the outer tube and is determined by monitoring the change in water height by means of a high precision differential pressure gauge (Stanić et al., 2019).

In hanging column systems, it is convenient to express suction in water height $h_k(z, t)$, as the sum of the initially established hydrostatic suction profile $h_k(z, t=0)$ and the time depending change of suction $\Delta h_k(z, t)$. The imposed suction increment Δh_i [L] (index i for "imposed") impacts the gradient $\left. \frac{\partial h_k(z, t)}{\partial z} \right|_{z=0}$ that induces the outflow at the specimen bottom (see Appendix A1).

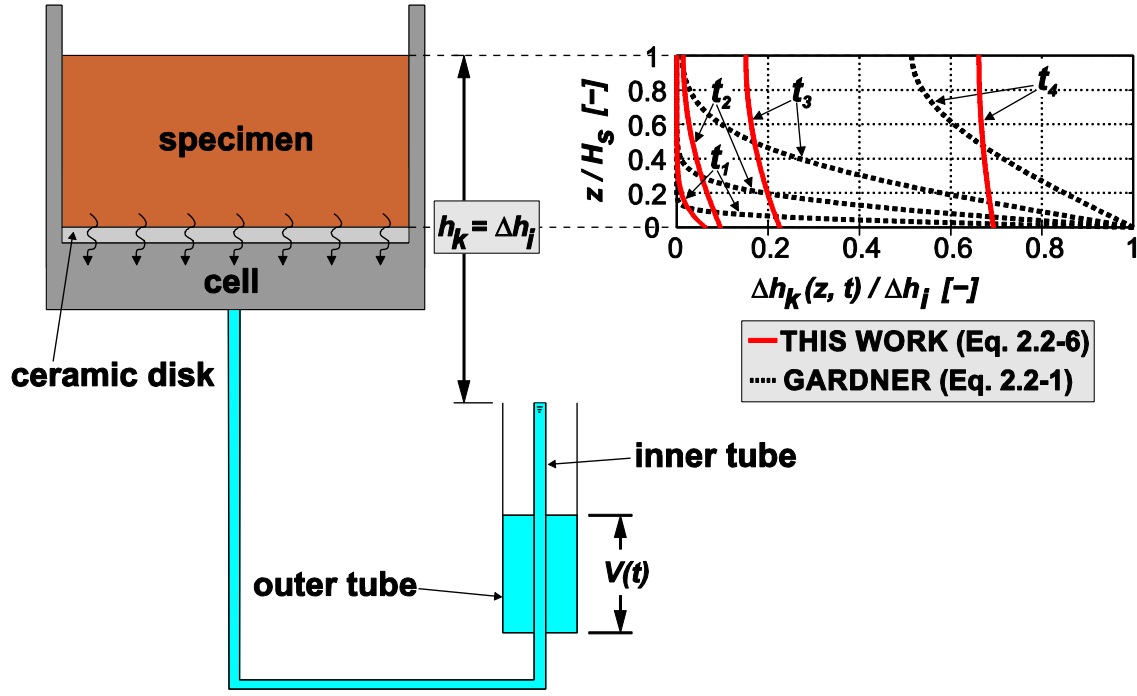


Figure 2.2-1. Simplified scheme of the hanging column apparatus of Stanić et al. (2019), where the water drained from the specimen overflows from the inner to the outer tube (initial suction equal to zero)

If the hydraulic conductivity of the ceramic disk is higher than that of the specimen (no impedance effects), the constant Δh_i is immediately transferred to the specimen bottom ($\Delta h_k(z=0, t) = \Delta h_i = const.$) – see dotted lines in Figure 2.2-1. In this case, the assumptions made by Gardner’s method (linearity of the WRC along the small suction step applied and constant diffusivity over the same Δh_i) allow to express $\Delta h_k(z, t)$ using Fourier’s series, based on the analogy with Terzaghi-Fröhlich consolidation equation (Terzaghi & Fröhlich, 1936) that governs the consolidation of saturated soils:

$$\Delta h_k(z, t) = \Delta h_i \left(1 - \frac{4}{\pi} \sum_{n=1,3,5,\dots}^{\infty} \frac{1}{n} e^{-\frac{(n/2)^2 \pi^2 t D(h_k)}{H_s^2}} \sin \frac{n\pi z}{H_s} \right) \quad (2.2-1)$$

where $D(h_k) = K(h_k)/C(h_k)$ is the (constant) diffusivity value [L^2/T] at suction h_k , where $K(h_k)$ [L/T] is the hydraulic conductivity and $C(h_k)$ [L^{-1}] the slope of the water retention curve along the applied suction step. Suction h_k is a reference value equal to the sum of the initial suction and Δh_i . Equation (2.2-1) concerns the outflow (see Appendix A1) which is integrated in time to obtain the changes in water volume:

$$V(t) = V_{\infty} \left(1 - \frac{8}{\pi^2} \sum_{n=1,3,5,\dots}^{\infty} \frac{1}{n^2} e^{-\frac{(n\pi/2)^2 t D(h_k)}{H_s^2}} \right) \quad (2.2-2)$$

where V_{∞} is the total volume [L^3] of the outflow drained from the soil specimen after imposing Δh_i .

Without considering the outflow at very small t , Gardner provided a convenient relation by keeping only the first term of Fourier series:

$$\ln(V_\infty - V(t)) = \ln\left(\frac{8V_\infty}{\pi^2}\right) - \left(\frac{\pi}{2H_s}\right)^2 D(h_k)t \quad (2.2-3)$$

Indeed, Gardner showed that the changes in the first term with respect to time become linear after a short time period (see Stanić et al., 2019), providing a reliable estimation of the diffusivity $D(h_k)$ from the slope of the $\ln(V_\infty - V(t))$ curve. The estimation is more accurate with small imposed suction increments, since $D(h_k)$ is the average diffusivity value along it. The hydraulic conductivity at suction h_k is derived as $K(h_k) = D(h_k)C(h_k)$.

When the hydraulic conductivity of the disk is significantly smaller than that of the specimen, the suction increment Δh_i imposed at the bottom of the porous disk is not immediately transferred to the specimen due to impedance effects. To cope with this issue, Kunze & Kirkham (1962) proposed a graphical method that is described in more details in Appendix A2. As commented in the Introduction, this graphical method is nowadays rarely used and has been replaced by numerical back analysis of water outflow under imposed suction increments.

A new method to account for impedance effects

As an alternative to existing methods of accounting for impedance effects, it is proposed to first apply Darcy's law to the saturated porous disk of thickness Δz_d , saturated hydraulic conductivity K_d and cross sectional area A , similarly as in Eching et al. (1994). One obtains the following expression of the drained outflow $Q(t)$ [L^3/T]:

$$Q(t) = -K_d \frac{\Delta h_k(z=0,t) - \Delta h_i}{\Delta z_d} A = \frac{\Delta V(t)}{\Delta t} \quad (2.2-4)$$

where ΔV [L^3] is the extracted water volume during the time interval Δt . The following relation gives the changes in the increment of suction at the specimen bottom:

$$\Delta h_k(z=0, t) = \Delta h_i - \Delta z_d \frac{Q(t)}{AK_d} \quad (2.2-5)$$

This relation indicates that the change with respect to time of the suction applied at the specimen bottom can be derived from the monitoring of the drained outflow $Q(t)$, that depends on both K_d and the combined effects of the water retention and transfer properties of the unsaturated specimen. Theoretically, the case with no impedance effect in which $\Delta h_k(z=0, t) = \Delta h_i$ is met with porous disks of large K_d , when $K_d \gg Q(t)/A$.

Based on the time superposition principle (Hantush, 1964; Stanić et al., 2017 among others), it is hence proposed: i) to decompose a suction increment at the specimen bottom $\Delta h_k(z=0, t)$ as the sum of a number N_s of very small successive suction increments $\Delta h_m = \Delta h_i/N_s$, occurring at time t_m , ii) to apply the analytical solution (Equation 2.2-1) to each suction increment and iii) to superpose in time all suction increments, giving the following expression of the suction changes:

$$\Delta h_k(z, t) = \sum_{m=1}^{N_s} \Delta h_m \left(1 - \frac{4}{\pi} \sum_{n=1,3,5,\dots}^{\infty} \frac{1}{n} e^{-(n\pi/2)^2(t-t_m)D(h_k)/H_s^2} \sin \frac{n\pi z}{2H_s} \right) \quad (2.2-6)$$

resulting in the following expression of extracted volume:

$$V(t) = \frac{V_\infty}{N_s} \sum_{m=1}^{N_s} \left(1 - \frac{8}{\pi^2} \sum_{n=1,3,5,\dots}^{\infty} \frac{1}{n^2} e^{-(n\pi/2)^2(t-t_m)D(h_k)/H_s^2} \right) \quad (2.2-7)$$

Note that larger N_s secures smoother curves obtained using Equations (2.2-6) and (2.2-7). Since the computation is not time consuming, $N_s = 1000$ is adopted for all cases. Also, for $N_s = 1$ Equation (2.2-7) becomes similar to standard Gardner's solution (Equation 2.2-2).

As in Gardner's method, $K(h_k)$ is calculated as $D(h_k)C(h_k)$, where $C(h_k) = \Delta\theta/\Delta h_i$ is determined from the measured WRC ($\Delta\theta$ is the measured change of water content over the suction step Δh_i). $D(h_k)$ is adjusted to obtain the best agreement between Equation (2.2-7) and the experimental points describing the water outflow, by optimizing the squared correlation coefficient R^2 . In *Figure 2.2-1*, the changes in suction along the specimen's height at different times are presented. Without any impedance effects (dotted lines), Equation (2.2-1) is used to calculate suction profiles (dotted lines), where the calculated Δh_k ($z=0, t$) immediately reaches Δh_i . In the case of impedance effects, the suction profiles (solid lines) are calculated using Equation (2.2-6). The calculated changes in suction with time at specimen bottom show how the boundary conditions progressively reach the Δh_i condition imposed at $t = 0$ at the bottom of the porous disk.

Given that the calculation of the Fourier series of Equations (2.2-1), (2.2-2), (2.2-6) and (2.2-7) may be found somewhat tedious, one tested the approximated empirical formula proposed by Sivaram & Swamee (1977) in their simplified approach to solve Terzaghi - Fröhlich's consolidation equation. This expression, that exhibits a difference with analytical solution smaller than 1% for $0\% < V(t)/V_\infty < 90\%$ and less than 3% for $90\% < V(t)/V < 100\%$, writes as follows:

$$\frac{V(t)}{V_\infty} = \left(\frac{4tD(h_k)}{\pi H_s^2} \right)^{0.5} \left(1 + \left(\frac{4tD(h_k)}{\pi H_s^2} \right)^{2.8} \right)^{-0.179} \quad (2.2-8)$$

Substituting in all equations where Fourier series appear, Equation (2.2-7) becomes:

$$V(t) = \frac{V_\infty}{\Delta h_i} \left[\sum_{m=0}^{N_s} \Delta h_m - \sum_{m=0}^{N_s} \Delta h_m \left(1 - \left(\frac{4(t-t_m)D(h_k)}{\pi H_s^2} \right)^{0.5} \left(1 + \left(\frac{4(t-t_m)D(h_k)}{\pi H_s^2} \right)^{2.8} \right)^{-0.179} \right) \right] \quad (2.2-9)$$

For sake of simplicity, it is proposed to adopt expression (2.2-9) instead of Equation (2.2-7).

A new method to account for non-constant imposed suction increment

As observed in Stanić et al. (2019), Gardner's method can be valid at lower water contents, if the hydraulic conductivity of the unsaturated soil becomes smaller than that of the ceramic disk, reducing impedance effects to zero. In Stanić et al. (2019)'s device, given that smaller water quantities are extracted from the specimen at higher suctions, it is necessary, for a better accuracy, to monitor the water exchanges through the changes in height of the inner thin tube used for imposing the suction increment $\Delta h_i = \Delta h_k$ ($z = 0, t = 0$), as seen in *Figure 2.2-2*.

Given that a gradual decrease in suction Δh_k ($z=0, t$) occurs once the mobile device has been lowered to water extraction, the standard Gardner's solution is valid only for sufficiently

small values of the ratio $\frac{\Delta h_i - \Delta h_k(z=0, t_\infty)}{\Delta h_i}$ (see Stanić et al., 2019). Otherwise, it is necessary to account for the change in $\Delta h_k(z=0, t)$.

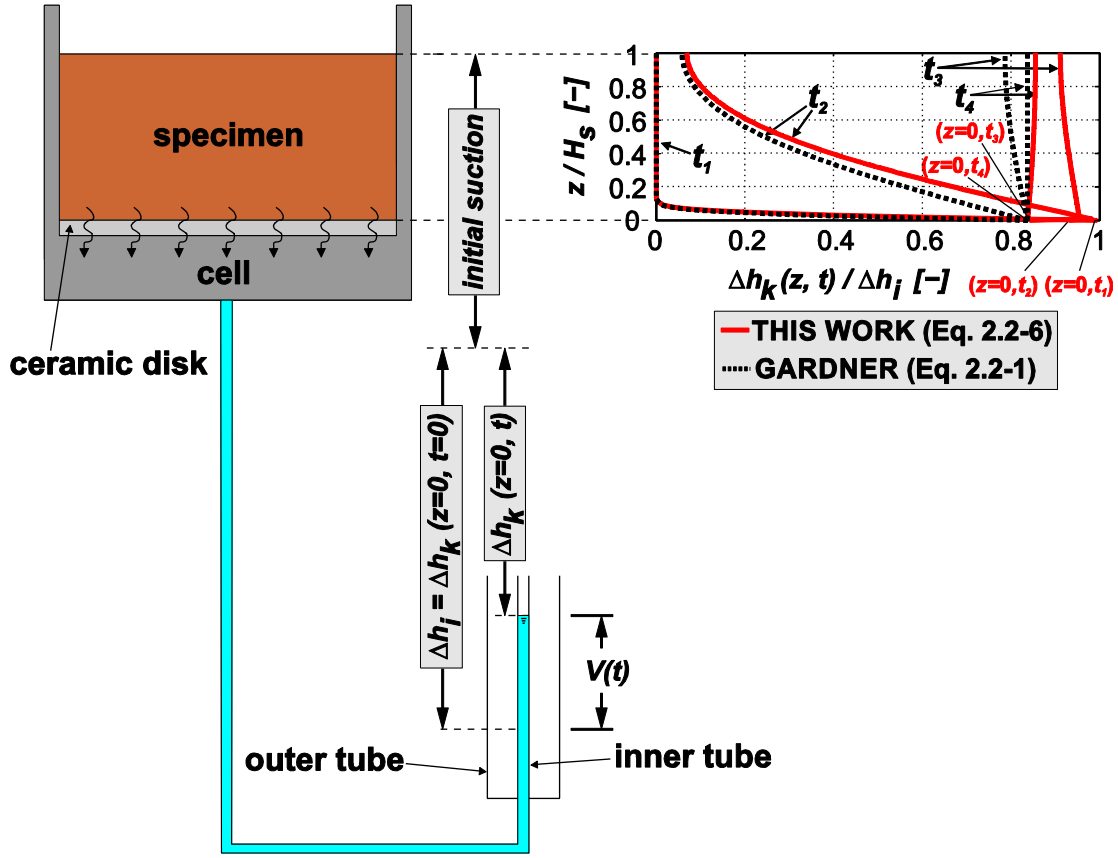


Figure 2.2-2. Simplified scheme of Stanić et al. (2019)'s device, in the case when the water extracted from the specimen is collected in the inner tube (no overflow), resulting in a non-constant suction step

Since the increase in water level is caused by the outflow drained from the specimen, the water balance equation can be written in the following way:

$$-\frac{d\Delta h_k(z=0, t)}{dt} a_{it} = Q(t) = \frac{dV(t)}{dt} \quad (2.2-10)$$

where a_{it} is the cross-section area [L²] of the small inner tube in which outflow is collected. Since there is no impedance effect, $V(t)$ can be substituted with Gardner's solution (Equation 2.2-2), by substituting V_∞ by $H_s A \Delta h_k(z=0, t) C(h_k)$, thus replacing the constant Δh_i by the non-constant $\Delta h_k(z=0, t)$. The outflow $Q(t)$ then becomes equal to:

$$Q(t) = \frac{dV(t)}{dt} = \frac{d\Delta h_k(z=0, t)}{dt} H_s A C(h_k) F(t) + H_s A \Delta h_k(z=0, t) C(h_k) F'(t) \quad (2.2-11)$$

where $F(t) = 1 - \frac{8}{\pi^2} \sum_{n=1,3,5,\dots}^{\infty} \frac{1}{n^2} e^{-(n\pi/2)^2 t D(h_k)/H_s^2}$ and $F'(t) = \frac{dF}{dt}$.

After introducing Equation (2.2-11) into Equation (2.2-10), the variables can be separated, leading to:

$$-\int_{\Delta h_i}^{\Delta h_k(z=0,t)} \frac{d\Delta h_k(z=0,t)}{\Delta h_k(z=0,t)} = \int_0^t \frac{F'(t)H_s C(h_k)A}{a_{it}+F(t)H_s C(h_k)A} dt \quad (2.2-12)$$

By integrating both sides of Equation (2.2-12), the following obtains:

$$\ln\left(\frac{\Delta h_i}{\Delta h_k(z=0,t)}\right) = \ln\left(1 + F(t) \frac{H_s C(h_k)A}{a_{it}}\right) \quad (2.2-13)$$

The expression of $\Delta h_k(z=0, t)$ is then derived as follows:

$$\Delta h_k(z=0, t) = \frac{\Delta h_i}{1+F(t) \frac{H_s C(h_k)A}{a_{it}}} \quad (2.2-14)$$

Since V_∞ is equal to the total volume of water collected in the tube between $t = 0$ and $t = t_\infty$, the following equation can be written:

$$V_\infty = a_{it}(\Delta h_i - \Delta h_k(z=0, t_\infty)) = H_s A \Delta h_k(z=0, t_\infty) C(h_k) \quad (2.2-15)$$

$$\frac{H_s C(h_k)A}{a_{it}} = \frac{\Delta h_i}{\Delta h_k(z=0, t_\infty)} - 1 \quad (2.2-16)$$

After introducing the last expression into Equation (2.2-14), the final forms of $\Delta h_k(z=0, t)$ and $V(t)$ are obtained:

$$\Delta h_k(z=0, t) = \frac{\Delta h_i}{1+F(t) \left(\frac{\Delta h_i}{\Delta h_k(z=0, t_\infty)} - 1 \right)} \quad (2.2-17)$$

$$V(t) = a_{it} \Delta h_i \left(1 - \frac{1}{1+F(t) \left(\frac{\Delta h_i}{\Delta h_k(z=0, t_\infty)} - 1 \right)} \right) \quad (2.2-18)$$

For $t = 0$, $F(t) = 0$, so $\Delta h_k(z=0, t=0) = \Delta h_i$ and $V(t) = 0$. On the contrary, for $t = t_\infty$, $F(t)=1$, leading to $\Delta h_k(z=0, t_\infty)$ and $V(t) = a_{it}(\Delta h_i - \Delta h_k(z=0, t_\infty)) = V_\infty$. Like in the standard Gardner's method, $K(h_k)$ is determined based on adjusting the value of $D(h_k)$ by comparing our solution (Equation 2.2-18) with experimental data. The value of $C(h_k) = \Delta\theta / \Delta h_k(z=0, t_\infty)$ is calculated based on the corresponding suction step on the measured $\Delta\theta$ taken from WRC. Unlike Equation (2.2-9) (or 2.2-7), Equation (2.2-18) cannot be mathematically reduced to standard Gardner's solution (Equation 2.2-2), since for $\Delta h_k(z=0, t_\infty) = \Delta h_i$ there will be no outflow - $V(t) = 0$. Please note that Fourier series $F(t)$ is identical as in Equation (2.2-2), thus it can be substituted using the empirical expression (2.2-8), as previously explained, and introduced into Equation (2.2-18) for sake of simplicity.

To calculate suction profiles, the non-constant boundary condition (Equation 2.2-17) is decomposed as in the case of the impedance effect, and Equation (2.2-6) is applied afterwards. *Figure 2.2-2* presents the calculated suction profiles at different times for 2 cases:

- i) constant suction step $\Delta h_i = \Delta h_k(z=0, t_\infty)$ described using Equation (2.2-1) – dotted line - and
 ii) non-constant suction increment $\Delta h_i = \Delta h_k(z=0, t)$ described with Equation (2.2-6) – solid line.

2.2.3. Experimental investigations

This work was initially developed when investigating the water retention and transfer properties of a volcanic coarse substrate used in an urban green roof in the Paris area, detailed in Stanić et al. (2019). The validity of the method is further established by also considering the experimental data obtained on two quite different materials (a poorly graded sand and an undisturbed silty clay) published by Wayllace & Lu (2011).

Data of Stanić et al. (2019)

In the device of Stanić et al. (2019) (Figures 1 and 2), a 70 mm diameter and 24 mm height specimen is placed on a $\Delta z_d = 5$ mm thick ceramic porous disk with an air entry value of 50 kPa, and a saturated hydraulic conductivity $K_d = 4.02 \times 10^{-8}$ m/s. Water exchanges are monitored by using an inner tube (inner diameter 5 mm, outer diameter 8 mm) and an outer tube (15 mm). The maximum height allowed by the system is equal to 5 m, corresponding to a maximum suction of 50 kPa. The material investigated was the volcanic substrate used for covering the “Green Wave” in the city of Champs-sur-Marne in France (Versini et al., 2018). The substrate is a coarse granular material with 4 % of organic matter, an average grain density of 2.35 Mg/m^3 and a bulk density of 1.42 Mg/m^3 (porosity of 0.395), with $D_{50} = 1.5$ mm, 15% particles smaller than $80 \mu\text{m}$ and a curvature coefficient ($D_{30}^2/(D_{10} D_{60})$) of 1.95. The saturated hydraulic conductivity of the substrate is $K_s = 8.11 \times 10^{-6}$ m/s, and its WRC is given in Figure 2.2-3a (Stanić et al., 2019).

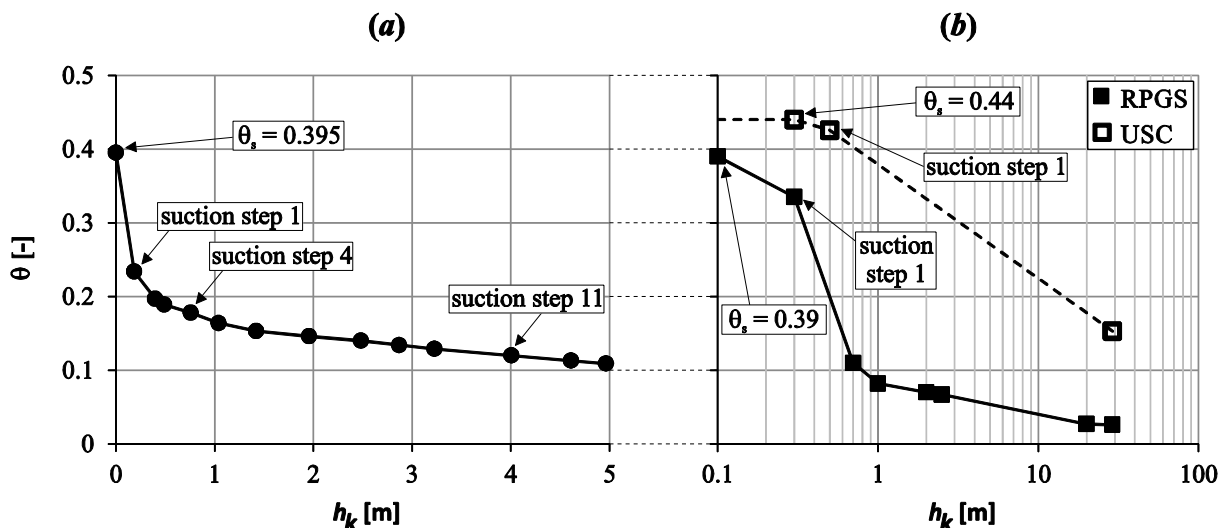


Figure 2.2-3. WRCs of (a) the coarse substrate determined by Stanić et al. (2019); (b) of the remolded poorly graded sand (RPGS) and undisturbed silty clay (USC) determined by Wayllace & Lu (2011). Saturated water content (θ_s) is indicated in each graph

Data of Wayllace & Lu (2011)

Wayllace & Lu (2011) developed a transient water release and imbibition (TWRI) method for determining the WRC and HCF of two materials along the drying and wetting paths, by imposing, through the axis translation method, two suction increments for draining water from the soil specimen, followed by a suction decrease allowing subsequent water imbibition. The TWRI apparatus consisted of i) a flow cell accommodating a soil specimen of 60.7 mm diameter placed on 300 kPa HAEV ceramic disk (saturated hydraulic conductivity $K_d = 2.5 \times 10^{-9}$ m/s, thickness $\Delta z_d = 3.2$ mm), ii) a pressure regulator connected to cell top and iii) a water jar placed on a weight scale connected to cell bottom to collect the drained outflow (more details in Wayllace and Lu, 2011). During drainage, a first imposed suction increment was fixed (2 kPa), just above the specimen air entry values, small enough to just initiate the outflow from the specimen, while the second step was significantly larger (about 300 kPa).

Wayllace and Lu investigated two different soils: a remoulded poorly graded sand compacted to a porosity of 0.39 and an undisturbed silty clay with a porosity 0.44. The values of the saturated hydraulic conductivities of these soils are $K_s = 2.1 \times 10^{-6}$ m/s and 1.1×10^{-7} m/s, respectively, and their WRCs are presented in *Figure 2.2-3b*. The significantly lower saturated hydraulic conductivity of the ceramic disk clearly indicates that impedance effects have to be accounted for when analyzing the outflow data.

2.2.4. Determination of hydraulic conductivity values

Coarse volcanic substrate of the Green Wave (Stanić et al., 2019)

By analyzing the evolution of drained outflow for different suction steps, the change in hydraulic conductivity with respect to increased suction is obtained. Thirteen suction steps were carried out, where steps 1 and 2 were constant suction steps (with the overflow system of *Figure 2.2-1*) whereas the remaining steps correspond to non-constant suction increments (see *Figure 2.2-2*). The saturated hydraulic conductivities of both the specimen (K_s) and the ceramic disk (K_d) were determined using a constant head hydraulic conductivity test described in details in Stanić et al. (2019).

In the top graph of *Figure 2.2-4a* is illustrated the evolution of $\Delta h_k (z = 0, t)$ for step 1 (connected filled dots), calculated using measured volumes and Darcy's law (Equation 2.2-5), that gradually reaches Δh_i imposed at the disk bottom. It can be noticed that the ratios $\Delta h_k (z=0, t)/\Delta h_i$ at different times (t_1 to t_4) correspond to those in *Figure 2.2-1* (x axis) for the same t .

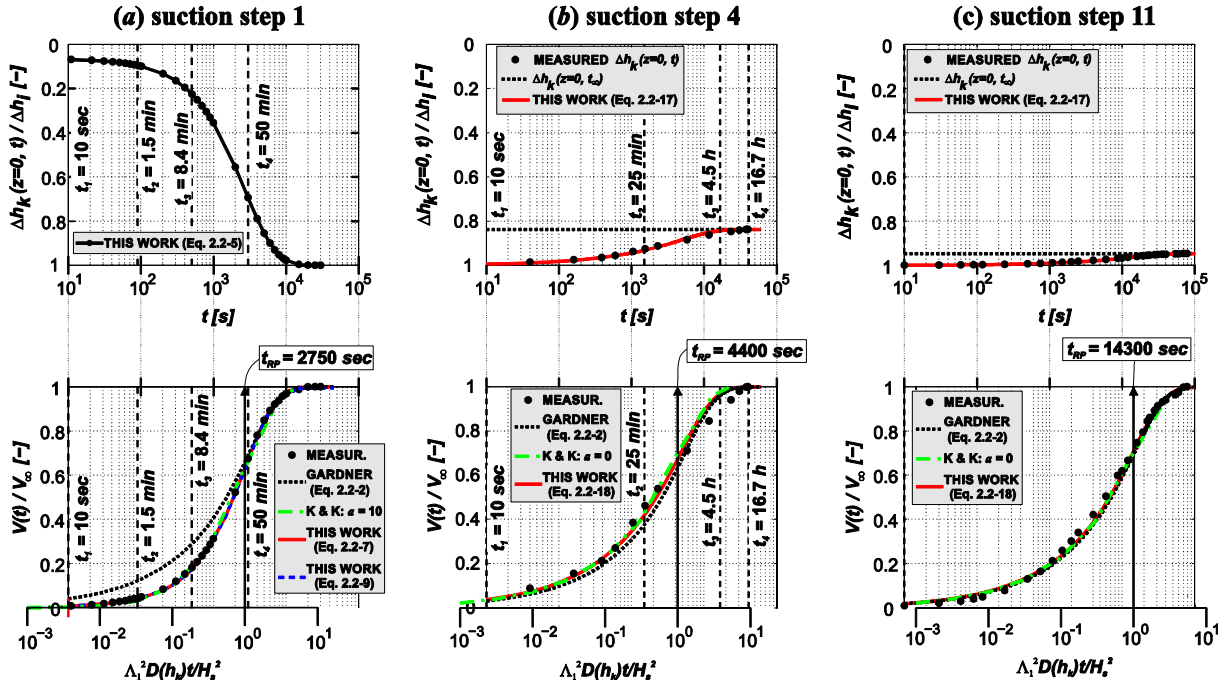


Figure 2.2-4. Green Wave substrate; top graphs - suction change at specimen bottom, at contact with ceramic disk; bottom graphs - measured outflow (circles) compared with calculated values from different methods (indicated on the Figure); (a) suction step 1 - impedance effect; (b) suction step 4 – non-constant suction increment; (c) suction step 11 – same as in (b)

The bottom graph of Figure 2.2-4a presents a comparison of the calculated values of $V(t)/V_\infty$ (in a time logarithmic scale) using Gardner's method, Kunze and Kirkham's method and that developed in this work. The best fit between Equation (2.2-9) and experimental data is obtained for $D(h_k = 18.5 \text{ cm}) = 1.2 \times 10^{-6} \text{ m}^2/\text{s}$, where $C(h_k = 18.5 \text{ cm}) = 0.16 / 0.185 = 0.86 \text{ m}^{-1}$ (see Figure 2.2-3a), which finally gives $K(h_k = 18.5 \text{ cm}) = 1.04 \times 10^{-6} \text{ m/s}$. Fitting our experimental data following Kunze and Kirkham's method (non-dimensional time variable $\Lambda_1^2 D(h_k) t_{RP} / H_s^2$ is also reported on the bottom x-axis, see Appendix A2) provided $\Lambda_1 = 0.097$ and $t_{RP} \approx 2750 \text{ s}$, with $a = 10$. The case of suction step 1 is described in details in Appendix A2 to point out the difficulties typical of graphical methods. Finally, the best overall agreement with measurements is obtained for $a = 10$ (having on mind that $a = 1000$ provides a hydraulic conductivity higher than the saturated one). The Figure shows excellent agreement between experimental data and both Kunze & Kirkham and the proposed method. Unsurprisingly, the extracted volume estimated by Gardner's method ($D(h_k) = 7.5 \times 10^{-8} \text{ m}^2/\text{s}$) for times smaller than 1 h is higher than the measured one and that calculated with the two other methods.

In case of step 4 (initial suction 0.489 m and $\Delta h_i = 0.321 \text{ m}$ with 17 % of suction step change), calculated changes in $\Delta h_k(z=0, t)$ (Equation 2.2-17 - solid line) are compared with the measured changes in water level in the top graph of Figure 2.2-4b, whereas calculated (Equation 2.2-18) and measured drained volumes are compared in the bottom graph. In this case $C(h_k) = \Delta\theta / \Delta h_k(z=0, t_\infty) = 0.04 \text{ m}^{-1}$, where $\Delta\theta = 0.011$ and $\Delta h_k(z=0, t_\infty) = (1 - 0.17) \times \Delta h_i = 0.266 \text{ m}$ (see Figure 2.2-3a). The difference between the non-constant ($\Delta h_k(z=0, t)$) and

constant ($\Delta h_k(z=0, t_\infty)$) suction increment is more significant at initial time, right after imposing Δh_i , while the largest difference in drained volumes between our method and Gardner's method is observed after $t_2 = 25$ min. The method proposed in this work shows the best agreement for $D(h_k) = 4.3 \times 10^{-8} \text{ m}^2/\text{s}$ (the same value is adopted for Gardner's method), while Kunze & Kirkham's theoretical curve with parameters $a = 0$, $t_{RP} \approx 4400 \text{ s}$ and $A_I^2 = 2.467$ also shows satisfying agreement at small times. All three methods show almost identical agreement with measured volumes when the overall suction step change is negligible, like in step 11 (initial suction 3.227 m and $\Delta h_i = 0.822 \text{ m}$ with 5 % of suction step change) presented in *Figure 2.2-4c* (Gardner's and our method - $D(h_k) = 1.6 \times 10^{-8}$, Kunze & Kirkham's method - $a = 0$, $t_{RP} \approx 14300 \text{ s}$ and $A_I^2 = 2.467$). Concerning the methods proposed in this work, $R^2 > 0.99$ for all three steps presented.

The accuracy of the determined $K(h_k)$ value depends on the accuracies of both the WRC measurements (parameter $C(h_k)$) and the outflow measurements (fitted value of $D(h_k)$), both governed by the precision of the differential pressure transducer ($\pm 0.05 \text{ mm}$). The relative uncertainty of $K(h_k)$ can be expressed as follows:

$$\frac{\delta K(h_k)}{K(h_k)} = \sqrt{\left(\frac{\delta D(h_k)}{D(h_k)}\right)^2 + \left(\frac{\delta C(h_k)}{C(h_k)}\right)^2} \quad (2.2-19)$$

The uncertainty of $C(h_k) = \Delta\theta/\Delta h_i = V_\infty/(H_s A \Delta h_i)$ depends on the uncertainties of V_∞ , H_s and Δh_i , and it can be expressed as:

$$\frac{\delta C(h_k)}{C(h_k)} = \sqrt{\left(\frac{\delta V_\infty}{V_\infty}\right)^2 + \left(\frac{\delta H_s}{H_s}\right)^2 + \left(\frac{\delta \Delta h_i}{\Delta h_i}\right)^2} \quad (2.2-20)$$

where $\delta V_\infty = \pm 6.32 \times 10^{-9} \text{ m}^3$ ($\pm 9.82 \times 10^{-10} \text{ m}^3$) when measuring in the outer (inner) tube, $\delta H_s = \pm 0.1 \text{ mm}$ and $\delta \Delta h_i = \pm 0.5 \text{ mm}$. In case of all three suction steps presented, $\frac{\delta C(h_k)}{C(h_k)} \approx 0.5 \%$. Furthermore, it appears that the uncertainties of the outflow measurements (few percent at small times, and less than 1 % for $t > 5 \text{ min}$) have no significant impact on $D(h_k)$ value, adjusted based on the R^2 criterion ($\frac{\delta D(h_k)}{D(h_k)} \approx \frac{\delta C(h_k)}{C(h_k)} \approx 0.5 \%$). Finally, the relative uncertainty of hydraulic conductivity can be calculated based on Equation (2.2-19) as $\frac{\delta K(h_k)}{K(h_k)} \approx \sqrt{2 \left(\frac{\delta C(h_k)}{C(h_k)}\right)^2} \approx \sqrt{2} \times 0.5 \% \approx 0.71 \%$. Given that the hydraulic conductivity changes over 5 orders of magnitude in the case of the coarse volcanic material (see *Figure 2.2-5*), this value is satisfactory.

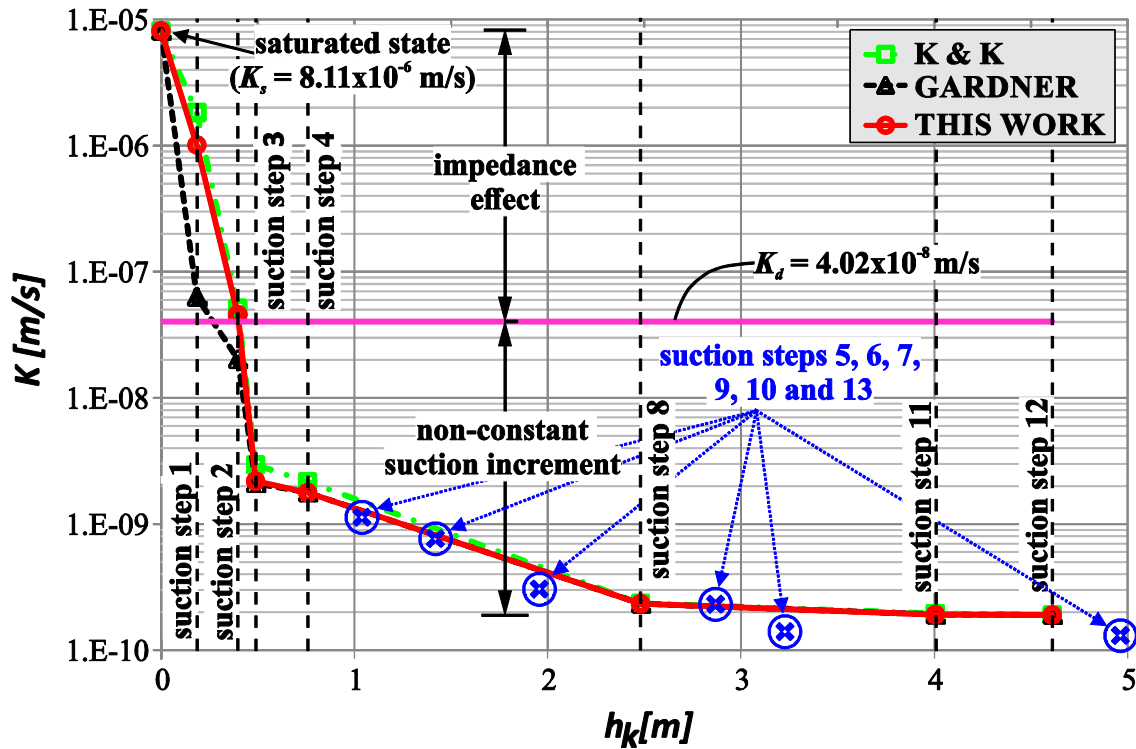


Figure 2.2-5. Change of hydraulic conductivity of the coarse substrate with respect to increased suction obtained using 3 different methods: Kunze & Kirkham's method (squares), Gardner's method (triangles) and methods developed in this work (circles). Hydraulic conductivity values obtained by analyzing volume change measurements at larger times (Equation 2.2-3) are presented with blue symbols

Figure 2.2-5 shows the changes in hydraulic conductivity obtained by using the three different approaches: Gardner's method (triangles), Kunze & Kirkham's method (squares) and the methods proposed in this work (circles). All 3 methods are applied on steps 1, 2, 3, 4, 8, 11 and 12, for which stable and reliable volume change measurements are obtained at small times. Note that we also present in the *Figure* the hydraulic conductivity values for steps 5, 6, 7, 9, 10 and 13, that were obtained by using the standard Gardner's method, based on volume change measurements at larger times (Equation 2.2-3).

Figure 2.2-5 shows that both our method and Kunze & Kirkham's one provide very similar results for the first two steps, where significant impedance effect occurs. In this range, Gardner's method unsurprisingly provides significantly lower $K(h_k)$ values because it integrates the effect of the low hydraulic conductivity of the disk. However, the difference between the three methods decreases quite rapidly, with convergence observed at $K(h_k) = 2 \times 10^{-8}$ m/s, to compare to the twice larger K_d value of the ceramic disk (4.02×10^{-8} m/s). In case of steps 8, 11 and 12, where the imposed suction step changes less than 5 % with no impedance effect, all methods provide comparable results.

From a hydrological point of view, the values of $K(h_k)$ in the low suction regime are of the greatest interest, since they have the most significant influence on the hydrological responses of the soil (substrate). As shown in *Figure 2.2-5*, this zone (first 4 steps) is precisely that in which the most significant differences are observed between the methods used, showing the

advantage of our method, that is less operator-dependent compare to that of Kunze and Kirkham.

Poorly graded sand and silty clay (Wayllace & Lu, 2011)

Among the transient outflow data from Wayllace & Lu (2011), only the first and smallest of the two applied suction steps was considered on both specimens because: i) our method assumes constant diffusivity, a hypothesis only acceptable for small suction increments and ii) the impedance effect is more significant at initial steps, when the hydraulic conductivity of the soil is significantly larger than that of the ceramic disk.

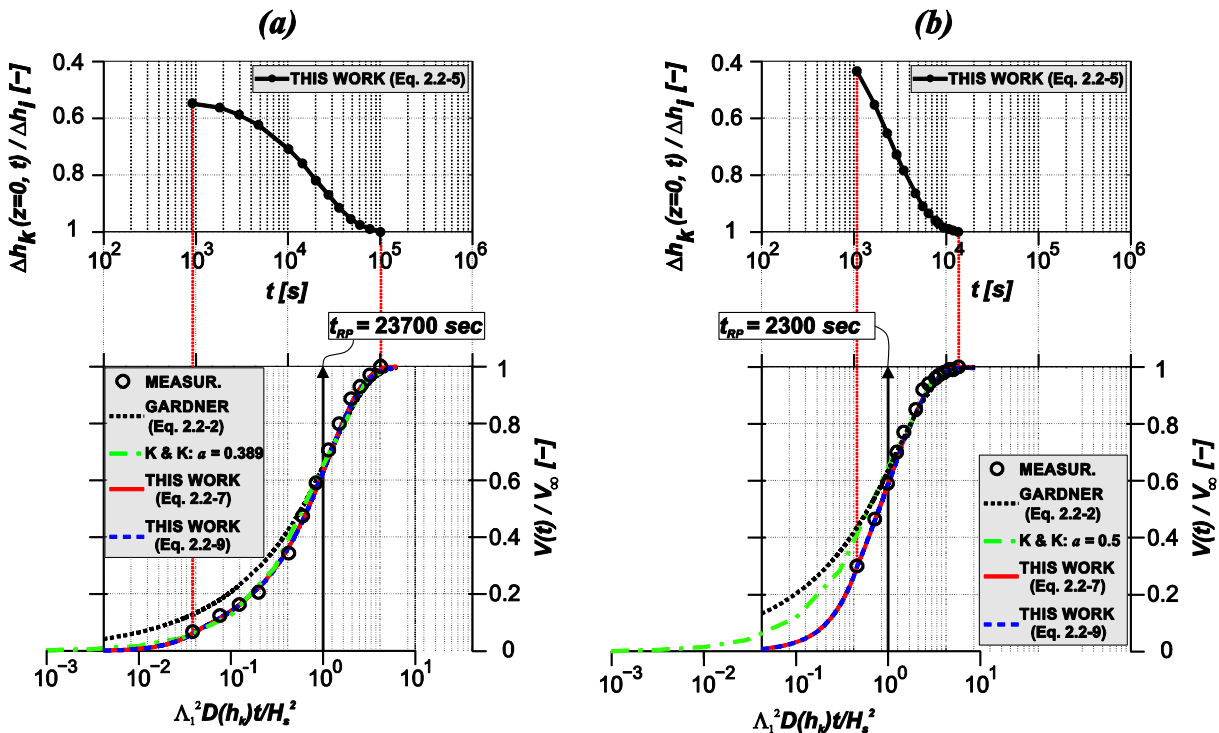


Figure 2.2-6. (a) Poorly graded sand (data from Wayllace & Lu, 2011); top - Suction change at specimen bottom, at contact with ceramic disk, bottom – measured outflow (circles) compared with calculated values from different methods (indicated on the Figure); (b) Undisturbed silty clay (data from Wayllace & Lu, 2011): same as in (a)

In Figure 2.2-6 are presented the same kind of data as in Figure 2.2-4 for the poorly graded sand (Figure 2.2-6a) and the silty clay specimens (Figure 2.2-6b). In the first case $H_s = 2.67$ cm, $\Delta h_i = 0.2$ m and $V_\infty = 4.66 \times 10^{-6}$ m³, while in the case of silty clay $H_s = 2.41$ cm, $\Delta h_i = 0.2$ m and $V_\infty = 1 \times 10^{-6}$ m³. The bottom graphs in Figure 2.2-6a show that our method and Kunze & Kirkham’s method compare quite well, whereas Gardner’s method overestimates the outflow values at small times, like for the Green Wave substrate (Figure 2.2-4a). On the contrary, for the silt clay specimen (Figure 2.2-6b-bottom) both Gardner’s and Kunze & Kirkham’s methods overestimate the outflows at small times, whereas our method shows excellent agreement with measurements along the whole time range. Due to the poor

agreement at small times, Kunze & Kirkham's analytical curve was fitted with measurements at larger times (the parameters for this method are presented in *Table 2.2-1*).

Table 2.2-1. Parameters used and hydraulic conductivity values obtained for Gardner's method, our method and Kunze & Kirkham's method for the poorly graded sand and the undisturbed silt clay investigated in Wayllace & Lu (2011)

| | <i>Gardner</i> | | <i>This Work</i> | | <i>Kunze & Kirkham</i> | | | |
|-------------------------------|------------------------------|-----------------------|------------------------------|-----------------------|----------------------------|----------------------------|--|-----------------------|
| | <i>D</i> [m ² /s] | <i>K</i> [m/s] | <i>D</i> [m ² /s] | <i>K</i> [m/s] | <i>a</i> [-] | <i>t</i> _{RP} [s] | <i>A</i> _I ² [-] | <i>K</i> [m/s] |
| Poorly graded sand | 1.0x10 ⁻⁸ | 3.01x10 ⁻⁹ | 1.8x10 ⁻⁸ | 5.43x10 ⁻⁹ | 0.389 | 23700 | 1.3228 | 6.87x10 ⁻⁹ |
| Undisturbed silty clay | 8.0x10 ⁻⁸ | 5.73x10 ⁻⁹ | 5.0x10 ⁻⁷ | 3.58x10 ⁻⁸ | 0.5 | 2300 | 1.1596 | 1.59x10 ⁻⁸ |

Based on the adjusted $D(h_k)$ values in the case of Gardner's and our method, and on parameters a , t_{RP} and A_I^2 in case of Kunze & Kirkham's method, the values of the hydraulic conductivity for the first step were determined (see *Table 2.2-1*). Based on the data from both our method and Kunze & Kirkham's one, it can be concluded that the impedance effect occurs for both soils ($K(h_k) > K_d$), especially in case of silty clay where calculated $K(h_k)$ values are about an order of magnitude larger than K_d for both methods. As in case of the coarse substrate, Gardner's method provides significantly lower $K(h_k)$ values compared to those determined using our and Kunze & Kirkham's method.

On the occurrence of impedance effects

The most convenient way to clarify the importance of impedance effects is by analyzing the evolution of the ratio $\Delta h_k(z=0,t) / \Delta h_i$, calculated by using Equation (2.2-5). The faster the ratio gets close to 1, the less significant impedance effects are, and vice versa. It seems reasonable in this regard to define a criterion based on the relative time t / t_∞ (t_∞ is the time at which equilibrium is reached) at which $\Delta h_k(z=0, t) / \Delta h_i$ gets close enough to 1 (ex. 0.95). Based on experience, we believe that impedance can be ignored if $\Delta h_k(z=0,t) / \Delta h_i$ reaches 0.95 within the first 5 % of the step duration, leading to a criterion $t_c / t_\infty = 0.05$. After dividing both sides of Equation (2.2-5) by Δh_i and introducing the proposed criterion, the following is obtained:

$$\frac{V(t_c)}{t_c A} < 0.05 \frac{\Delta h_i}{\Delta z_d} K_d, \quad t_c = 0.05 t_\infty \quad (2.2-21)$$

Equation (2.2-21) shows that, besides the hydraulic conductivity K_d of the ceramic disk, the values of imposed suction increment Δh_i and stone thickness Δz_d also affect the impedance. For the data presented in *Figure 2.2-4a* (coarse material), *Figure 2.2-6a* (sand) and *Figure 2.2-6b* (silty clay), the values of the left side of Equation (2.2-21) are 1.2×10^{-6} , 6.8×10^{-8} and 9.6×10^{-8} m/s, respectively, while the values on the right side are 1.5×10^{-7} , 7.81×10^{-9} and 7.81×10^{-9} m/s. Equation (2.2-21) is hence not satisfied in none of the three cases, meaning that impedance effects cannot be neglected. In case of step 2 of the coarse substrate, the left

and right side of Equation (2.2-21) are almost identical, which is in agreement with the obtained $K(h_k)$ value that is rather close to K_d (see *Figure 2.2-5*).

2.2.5. Conclusion

This paper presented two improvements to Gardner's method that were carried out i) to account for impedance effect in a simpler and more objective way than in Kunze and Kirkham's graphical method and ii) to account for conditions in which non-constant suction increment is applied, as is often the case in hanging column techniques.

The experimental data from various materials analyzed (coarse substrate, poorly graded sand and undisturbed silty clay) in this work showed that the proposed simple analytical method fairly well accounts for the impedance effects of the ceramic disk. This method is believed to be more reliable than Kunze & Kirkham's graphical method, especially in the case of significant impedance effect, because it is not dependent of the difficulty in choosing the best fitting theoretical curve, among the family of curves provided by Kunze & Kirkham. The proposed method, based on the analytical resolution of the water transfer equations in the different parts of the system, only requires the accurate monitoring of outflow measurements, a requirement that is typical for any method for determining the hydraulic conductivity of multiphase porous material. The boundary condition in which a non-constant suction increment is applied, which is often the case when using the hanging column technique, was also treated analytically to be applied in the (larger) suction area in which no impedance effect has to be considered, with also good agreement between measured and calculated values. It has also been shown, that the simplified equation of Sivaram & Swamee (1977) could successfully replace the analytical solution in Fourier series, which simplifies the use and improves the efficiency of the method. Compared to numerical back analyses method, this method provides point values of hydraulic conductivity without the need to assume a parametric expression for the conductivity function. Thus, it is not confronted with the issue of model selection. Also, this method is considered simpler in the sense that it does not require the use of any numerical simulations with optimization algorithms, since the analysis of outflow data and the derivation of hydraulic conductivity value is much more straightforward.

2.2.6. References:

- Brooks, R. H., and A. T. Corey. 1964. "Hydraulic Properties of Porous Media." *Hydrology Papers*, no. 3: 1–27.
- Dam, J. C. van, J. N. M. Stricker, and P. Droogers. 1994. "Inverse Method to Determine Soil Hydraulic Functions from Multistep Outflow Experiments." *Soil Science Society of America Journal* 58: 647–52.
- Doering, E. J. 1965. "Soil-Water Diffusivity by the One-Step Method." *Soil Science* 99: 322–26.
- Durner, W., and S. C. Iden. 2011. "Extended Multistep Outflow Method for the Accurate Determination of Soil Hydraulic Properties near Water Saturation." *Water Resources*

Research 47 (W08526): 1–13. <https://doi.org/10.1029/2011WR010632>.

- Eching, S. O., and J. W. Hopmans. 1993. "Soil Science Society of America." *Soil Science Society of America Journal* 57 (5): 1167–75.
- Eching, S. O., J. W. Hopmans, and O. Wendroth. 1994. "Unsaturated Hydraulic Conductivity from Transient Multistep Outflow and Soil Water Pressure Data." *Soil Science Society of America Journal* 58: 687–95.
- Fredlund, D. G., and A. Xing. 1994. "Equations for the Soil-Water Characteristic Curve." *Canadian Geotechnical Journal* 31: 521–32.
- Gardner, W. R. 1956. "Calculation of Capillary Conductivity from Pressure Plate Outflow Data." *Soil Science Society of America Journal* 20 (3): 317–20. <https://doi.org/10.2136/sssaj1956.03615995002000030006x>.
- Genuchten, M. Th. van. 1980. "A Closed-Form Equation for Predicting the Hydraulic Conductivity of Unsaturated Soils." *Soil Science Society of America Journal* 44 (5): 892–98. <https://doi.org/10.2136/sssaj1980.%0A03615995004400050002x>.
- Hantush, M. S. 1964. "Hydraulics of Wells." In *Advances in Hydroscience* (ISSN: 0065-2768, Vol. 1, pp. 281-432). Socorro, New Mexico: New Mexico Institute of Mining and Technology.
- Khaleel, R., and J. F. Relyea. 1995. "Evaluation of van Genuchten-Mualem Relationships to Estimate Unsaturated Hydraulic Conductivity at Low Water Contents." *Water Resources Research* 31 (11): 2659–68.
- Kunze, R. J., and D. Kirkham. 1962. "Simplified Accounting for Membrane Impedance in Capillary Conductivity Determinations." *Soil Science Society of America Journal* 26 (5): 421–26. <https://doi.org/10.2136/%0Assaj1962.03615995002600050006x>.
- Levenberg, K. 1944. "A Method for the Solution of Certain Non-Linear Problems in Least Squares." *Applications of Mathematics* 2 (164–168).
- Miller, E. E., and D. Elrick. 1958. "Dynamic Determination of Capillary Conductivity Extended for Non-Negligible Membrane Impedance." *Soil Science Society of America Journal* 22 (6): 483–86. <https://doi.org/10.%0A2136/sssaj1958.03615995002200060002x>.
- Mualem, Y. 1976. "A New Model for Predicting the Hydraulic Conductivity of Unsaturated Porous Media." *Water Resources Research* 12 (3): 513–22. <https://doi.org/10.1029/WR012i003p00513>.
- Nasta, P., and J. W. Hopmans. 2011. "Simplified Multistep Outflow Method to Estimate Unsaturated Hydraulic Functions for Coarse-Textured Soils." *Soil Science Society of America Journal* 75: 418–25. <https://doi.org/10.2136/sssaj2010.0113>.
- Richards, L. A. 1931. "Capillary Conduction of Liquids through Porous Media." *Physics* 1: 318–33.
- Rijtema, P. E. 1959. "CALCULATION OF CAPILLARY CONDUCTIVITY FROM PRESSURE PLATE OUTFLOW DATA WITH NON-NEGLIGIBLE MEMBRANE IMPEDANCE." *Netherlands Journal of Agricultural Science* 7 (3): 209–15.
- Schelle, H., S. C. Iden, and W. Durner. 2011. "Combined Transient Method for Determining Soil Hydraulic Properties in a Wide Pressure Head Range." *Soil Science Society of America Journal* 75 (5): 1681–94. [https://doi.org/10.2136/5553\)2010.0374](https://doi.org/10.2136/5553)2010.0374).

-
- Šimůnek, J., M. Th. van Genuchten, and M. Šejna. 2008. "Released Online." *Vadose Zone Journal* 7 (2): 587–600. <https://doi.org/10.2136/vzj2007.0077>.
- Sivaram, B., and K. Swamee. 1977. "A COMPUTATIONAL METHOD FOR CONSOLIDATION-COEFFICIENT." *Soils Found. Tokyo* 17 (2): 48–52.
- Stanić, F., Y.-J. Cui, P. Delage, E. De Laure, P.-A. Versini, D. Schertzer, and I. Tchiguirinskaia. 2019. "A Device for the Simultaneous Determination of the Water Retention Properties and the Hydraulic Conductivity Function of an Unsaturated Coarse Material ; Application to a Green- Roof Volcanic Substrate." *Geotechnical Testing Journal*. <https://doi.org/10.1520/GTJ20170443>.
- Stanić, F., N. Jaćimović, A. Randelović, and J. Despotović. 2017. "Laboratory Investigation of Hydraulic Characteristics of Fly Ash as a Fill Material from the Aspects of Pollutant Transport." *Water Science & Technology* 76 (4): 976–82. <https://doi.org/10.2166/wst.2017.243>.
- Terzaghi, K., and O. K. Fröhlich. 1936. "Theorie der Setzung von Tonschichten." Leipzig: Wien, Franz Deuticke.
- Valiantzas, J. D. 1990. "Analysis of Outflow Experiments Subject to Significant Plate Impedance." *Water Resources Research* 26 (12): 2921–29.
- Versini, P. -A., A. Gires, I. Tchiguirinskaia, and D. Schertzer. 2018. "Toward an Assessment of the Hydrological Components Variability in Green Infrastructures: Pilot Site of the Green Wave (Champs-Sur-Marne)." *La Houille Blanche*, no. 4: 34–42. <https://doi.org/10.1051/lhb/2018040>.
- Wayllace, A., and N. Lu. 2011. "A Transient Water Release and Imbibitions Method for Rapidly Measuring Wetting and Drying Soil Water Retention and Hydraulic Conductivity Functions." *Geotechnical Testing Journal* 35 (1): 1–15.

3. Soil properties models

In order to assess the heterogeneity of the Green Wave substrate and to further use it for developing new soil properties functions, X-ray CT scanner was used. By reducing the resolution of the scanned grey-scale soil image(s), the cumulative representation of solid particles (grains) and pores equal to or larger than the actual discretization element can be determined and described analytically. Due to the variable grain densities, described through different shades of grey color on a scanned image, the UM (Universal Multifractals) theoretical framework has been used to develop the grain size distribution (GSD) model (Chapter 3.1). Comparison between the proposed model and the standard dry sieving experimental data confirms that the GSD curve can be reasonably well predicted from the scanned soil image. If those images are not available, the proposed model can be used for interpreting the experimental data by adjusting the parameter values, as demonstrated on case of two soils taken from the literature. Even though it requires more parameters than the well-known fractal-based PSF (Pore-Solid-Fractal) model, the proposed UM-based model has stronger physical-basis, while its parameters are closely related to the gradation of granular material.

Compared to the multifractal GSD model, the proposed PSD model is based on a simpler fractal approach, where the fixed value of fractal dimension, related to the minimal grain size, is used instead of a continual set of fractal dimensions describing the GSD. Even though the PSD model is simplified compared to the GSD, the fixed value of the fractal dimension conserves the link between two distributions. The fractal-based PSD model has been used for practical reasons, to develop a simple and robust physically-based model of the water retention and transfer properties in non-saturated soils valid from saturation to oven-dryness (Chapter 3.2). To do so, new capillary-based water retention and hydraulic conductivity functions founded on the fractal approach have been derived from the PSD, by means of the Young-Laplace law and Mualem's model. To describe adsorption phenomena, these functions are combined with those used in the Peter-Iden-Durner (PID) model, providing a model along the full-range of suctions, with less parameters than the existing models. This work also shows that some parameters are directly determined from the experimental GSD (the fractal dimension), or from the water retention data (air entry suction and residual water content), leaving only two parameters to be optimized. The model was successfully validated with respect to published experimental data from 10 different coarse, sandy and clayey soils, confirming it is convenient for simulating the water movements in unsaturated porous medium.

3.1. A new physically-based Grain Size Distribution model based on the application of the Universal Multifractals on the results provided by the X-ray Computed Tomography

(Ready for submission)

3.1.1. Introduction

The grain size distribution (GSD) is one of the fundamental properties of granular soils that, besides the influence on mechanical characteristics, also affects the packing arrangement of grains (Nolan & Kavanagh, 1993; He et al., 1999 among the others), and thus the distribution of pores and hence hydraulic properties of the porous medium (Segal et al., 2009). The GSD curve is experimentally determined by using the dry sieving method that is based on the determination of the mass fractions of grains of different sizes (AFNOR, 1996). By using numerous sieves with different void diameters, grains are classified in the same number of groups according to their size, where the representation of each group is determined based on the measured mass fraction that stays on the corresponding sieve. After aggregating, the cumulative mass distribution (or the GSD) curve is obtained. However, the mentioned mass fractions are non-homogeneously distributed, which provides complex GSD curves that need to be modeled.

Detailed overview of different approaches used for describing the mentioned complexity of GSD curves can be found in Ghanbarian-Alavijeh & G.Hunt (2017). One of them is the self-similarity principle which is included in fractal-based models and which assumes occurrence of the same pattern of the soil structure at all scales. According to Ghanbarian-Alavijeh et al. (2011), the three-phase PSF (pore-solid-fractal) approach (Perrier et al., 1999; Bird et al., 2000) is the most consistent and with the strongest physical-basis among the fractal-based approaches. Besides pores and grains, it assumes one additional “fictive” type of soil elements – fractals - that are successively broken at smaller scales in a self-similar way, leading finally to the structure consisting of fractal-distributed pore and grain sizes. Thus, the GSD can be represented by means of a power (fractal) law, where the fractal coefficient is included in the exponent. However, unlike assumed in the PSF model, grain densities are non-homogeneous, which also contributes to the complexity of distribution of different mass fractions.

Multifractal formalism, that takes into account different fractal coefficients for different threshold values, was also used for analyzing the complexity of GSD. Grout et al., (1998) and Posadas et al., (2001) used Renyi dimensions, one of the multifractal parameters, to characterize the heterogeneous distribution of different mass fractions. Besides this type of multifractal analysis, the singularity spectra analysis is also applied for analyzing the dry soil volume-size distribution obtained by using a laser distraction method (Martín & Montero, 2002). Recently, Torre et al., (2016) used a X-ray CT, a non-destructive technique for obtaining a three-dimensional grey-scale image of a porous material (Hseih, 2003; Banhart, 2008), in order to compare the three-dimensional structural complexity of spatial arrangement of grains and pores, with that of differently oriented two-dimensional planes. The multifractal

analysis has also proved to be convenient in this case. Even though the multifractal theory brings great potential to better understand the complexity of GSD (Ghanbarian & Hunt, 2017), up to date this kind of analysis has not found practical application. In other words, the multifractal theory has not been used for developing a GSD model, as done in case of the fractal approach (e.g. PSF model).

This work is focused on development of a new physically-based GSD model founded on the Universal Multifractal (UM) framework (Schertzer & Lovejoy, 1987; Schertzer & Lovejoy, 1997). Based on a grey-scale soil image scanned by means of X-ray CT, it is possible to recognize solid particles of different sizes by progressively decreasing the resolution of the image while keeping the fixed value of the threshold. Change of the representation of solid particles with the resolution of the image can be directly linked with the grain size distribution, and described analytically in a mathematically-elegant way by means of the UM framework. Compared to Lai & Chen (2018), where a specific machine learning tool was used for particle recognition, this approach is much simpler and more convenient for practical application.

The approach presented was firstly validated by using the scanned structure of the artificial volcanic substrate (Stanić et al., 2019) used for covering green roof named Green Wave (Versini et al., 2018; Versini et al., 2020). Results of the model, whose parameters are directly determined from scanned images, are compared with the experimental data obtained by means of the standard dry sieving method (AFNOR, 1996) and sedimentation test (AFNOR, 1992). Furthermore, the model was tested on two additional soils taken from the literature (Bird et al., 2000), Ariana silty clay loam (ASCL) and Yolo clay loam (YCL), whose scanned images are not available. In this case the proposed model was used only for interpreting the experimental data, while the model parameters were manually adjusted to obtain a credible description of the experimental points. Finally, the model was compared with the fractal-based PSF model, and a physically-based explanation of the model behavior was given.

3.1.2. Universal Multifractal (UM) framework (Schertzer & Lovejoy, 1987)

Contrary to the fractal approach that assumes a fixed fractal dimension, the multifractal formalism uses a continual set of fractal dimensions for estimating the probability that the value of the investigated field exceeds different resolution dependent thresholds. In the context of this work, the field of interest is a soil density indicator field $\rho^{ind}(\lambda)$ [-] proportional to the ratio ρ / ρ_{bulk} , where ρ_{bulk} is the dry bulk density [M/L³] of the material. $\rho^{ind}(\lambda)$ field is presented in the form of two- or three-dimensional scanned soil image, and hence it depends on the resolution λ . In such case, the multifractal-based probability function is expressed as the following:

$$P(\rho^{ind}(\lambda) \geq \lambda^\gamma) = \frac{N(\rho^{ind}(\lambda) \geq \lambda^\gamma)}{\lambda^E} \approx \lambda^{-c(\gamma)} \quad (3.1-1)$$

$$c(\gamma) = C_1 \left(\frac{\gamma}{C_1 \alpha'} + \frac{1}{\alpha} \right)^{\alpha'} ; \quad \alpha' = \left(1 - \frac{1}{\alpha} \right)^{-1}, \quad \alpha \neq 1 \quad (3.1-2)$$

where E is Euclidian dimension [-] (in this case $E = 2$ or 3 for two- and three-dimensional fields, respectively), $\lambda = \frac{L}{l(\lambda)}$ is a resolution of $\rho^{ind}(\lambda)$ field equal to the ratio between the size of the field L [L] and the size of a single discretization element $L_l(\lambda)$ [L] (pixel or voxel for $E = 2$ or 3 , respectively). Note that λ needs to be a power of an integer λ_l (usually equal 2). Furthermore, dimensionless singularity γ [-] defines a resolution dependent threshold λ^γ for which the probability of exceedance is calculated, while $c(\gamma)$ is the co-dimension function that describes how the fractal dimension changes depending on the value of threshold (or γ).

Note that for conservative fields $c(\gamma)$ is described by means of parameters C_l and α , describing the sparseness of the mean value of the field and the change of sparseness for values around the mean, respectively. According to Schertzer & Lovejoy (1987), C_l takes values between 0 (mean value is ubiquitous - homogeneous field) and E (mean value is too sparse to be observed), while α takes values between 0 (no occurrence of extremes – fractal field) and 2 (maximal occurrence of extremes – log-normal field). For $\gamma = C_l$ the fixed point of the co-dimension function $c(C_l) = C_l$ is obtained (see Equation 3.1-2), whereas for $\gamma = \gamma_s$ the co-dimension function reaches dimension of the investigated field, $c(\gamma_s) = E$. Value of γ_s is known as the most probable singularity that can be computed from Equation (3.1-2) as the following:

$$\gamma_s = C_l \alpha' \left(\left(\frac{E}{C_l} \right)^{1/\alpha'} - \frac{1}{\alpha} \right) \quad (3.1-3)$$

Note that Equation (3.1-3) is written for a single data set analyzed. The two UM parameters can be determined from the real data sets by applying different techniques (Schertzer & Lovejoy, 1993). In this work the Trace Moment (TM) technique (Schertzer & Lovejoy, 1987) based on the scaling behavior of the statistical moments of order p is used.

$$\langle (\rho^{ind}(\lambda))^p \rangle \approx \lambda^{K(p)} \quad (3.1-4)$$

where $\langle (\rho^{ind}(\lambda))^p \rangle$ is the average statistical moment of an order p ($\langle \rangle$ indicates average value) and $K(p)$ is the moment scaling function described as following:

$$K(p) = \frac{C_l}{\alpha-1} (p^\alpha - p); \quad \alpha \neq 1 \quad (3.1-5)$$

Note that both $c(\gamma)$ and $K(p)$ functions are convex, they increase with no upper limit and they are linked by Legendre transform (Frisch & Parisi, 1985), meaning that for each γ there is a corresponding p (i.e. for $\gamma = C_l$ and $\gamma = \gamma_s$ the corresponding values are $p = 1$ and $p = p_s$, respectively). More details about the UM theoretical framework can be found in Chapter 4.2.

3.1.3. Methodology

X-ray CT (Computed Tomography)

Previously mentioned $\rho^{ind}(\lambda)$ field is obtained from the grey-scale soil image scanned by means of X-ray CT scanner. In this work, an UltraTom microtomograph from Laboratoire

Navier was used, where a 10 cm diameter and 15 cm height specimen of the Green Wave substrate (Stanić et al., 2019) was placed on the rotation table located between the X-ray source and the flat panel detector (more details on the principle and the device in Bruchon et al., 2013). The obtained three-dimensional grey-scale image consists of 1785x1785x3072 50 μm size voxels, carrying the information about different intensities of grey level GL (bright shades of grey represent high, and dark shades low density zones). Based on the proved linear correlation between GL and soil density (Taina et al., 2008), ρ^{ind} can be obtained by:

- subtracting the GL_0 threshold value from the original GL values.
- setting to zero all GL values lower than GL_0 .
- renormalizing the modified GL field.

$$\rho^{ind} = \begin{cases} GL > GL_0, & \frac{GL - GL_0}{\langle GL - GL_0 \rangle} \\ GL \leq GL_0, & 0 \end{cases} \quad (3.1-6)$$

where notation $\langle \rangle$ indicates the mean value. GL_0 is adjusted based on the locations of pores that can be reliably identified on the image. By using *Fiji*, an open source Java-based image processing package, it was possible to estimate the value of GL_0 .

Preliminary investigation confirmed the existence of the statistical isotropy within the investigated specimen (explained later in the text), allowing not to analyze the full three-dimensional $\rho^{ind}(\lambda_n)$ field, but only several horizontal planes ($E = 2$) extracted from it. This is rather significant for saving computational time and memory. In *Figure 3.1-1* are presented eight horizontal $\rho^{ind}(\lambda_n)$ planes that are further analyzed, where $\lambda_n = 2^{10} = 1024$ is the highest resolution considered. These fields are located within central 10 cm of the specimen height (the top and the bottom 2.5 cm are ignored due to technical reasons), with an equal distance (1.6 cm) between two consecutive images.

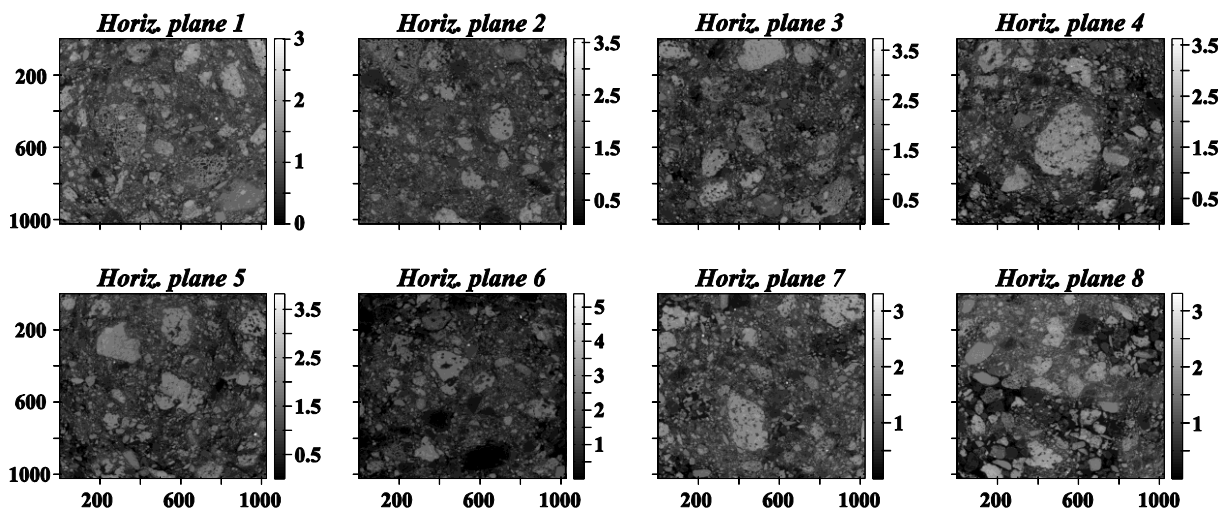


Figure 3.1-1. Eight horizontal $\rho^{ind}(\lambda_n = 1024)$ fields analyzed in this work (vertical distance between two consecutive planes is ≈ 1.6 cm)

A New GSD Model

In order to develop a GSD model it is necessary to find a way to reliably recognize grains and pores based on the ρ^{ind} field obtained, and to classify them according to their sizes. The approach proposed in this work is based on the up-scaling procedure (decreasing the resolution of $\rho^{ind}(\lambda)$ field), which is due to the secured statistical isotropy explained on the example of two-dimensional $\rho^{ind}(\lambda)$ field ($E = 2$). The same procedure can be applied for $E = 3$.

Starting from λ_n , it is assumed that $\rho^{ind}(\lambda) \geq \rho_{s,min}^{ind}$ values indicate grains, where $\rho_{s,min}^{ind}$ is a threshold related to the minimal grain density, while $\rho^{ind} = 0$ indicate pores. Intermediate values of the field ($0 < \rho^{ind}(\lambda) < \rho_{s,min}^{ind}$) represent mixtures of grains and pores of sizes smaller than the actual pixel size $L_I(\lambda)$, and thus they cannot be classified neither as grains nor pores at λ . Since λ is a power of λ_I ($=2$), pixels are merged in groups by λ_I^2 and their values are averaged, creating that way one out of λ_I^2 pixels. Thus, λ is decreased λ_I times, while $L_I(\lambda)$ is increased by the same factor. By averaging, $\rho^{ind}(\lambda)$ values are mitigated and the representation of those above $\rho_{s,min}^{ind}$ is decreased compared to that met at λ_n . Mostly individual grain-pixels of size $L_I(\lambda)$, that are surrounded by zero or intermediate $\rho^{ind}(\lambda)$ values, disappear after averaging because larger pixels replacing them do not satisfy the criterion for grains ($\rho^{ind}(\lambda) \geq \rho_{s,min}^{ind}$). Therefore, the representation of grain-pixels at different λ ($P_{grains}(\lambda)$) corresponds to a cumulative representation of grains that are equal to or larger than $L_I(\lambda)$. The up-scaling procedure is repeated iteratively, and grain-pixels gradually disappear as λ decreases, until even the largest grain-pixels vapor (see *Figure 3.1-2*).

In *Figure 3.1-2* is illustrated the $\rho^{ind}(\lambda)$ field (horizontal plane 4 in *Figure 3.1-1*) at different λ , where each bar presents $\rho^{ind}(\lambda)$ value, while the horizontal platform presents value of $\rho_{s,min}^{ind} = 1.55$. Fluctuation of the field is clearly reduced as λ decreases, as well as the representation of pixels above the platform. However, pixels grouped in the central part of the field resist longer to the up-scaling process (up to $\lambda = 8$ – see *Figure 3.1-2e*), indicating the presence of a large grain on that location.

$P_{grains}(\lambda)$ describes how the probability of exceeding a fixed threshold ($\rho_{s,min}^{ind}$ in this case) changes with λ , and it can be expressed as the following:

$$P_{grains}(\lambda) = P(\rho^{ind}(\lambda) \geq \rho_{s,min}^{ind}) = \frac{N(\rho^{ind}(\lambda) \geq \rho_{s,min}^{ind})}{\lambda^E} \quad (3.1-7)$$

where λ^E is the total number of discretization elements (pixels in case of $E = 2$) at λ , while $N(\rho^{ind}(\lambda) \geq \rho_{s,min}^{ind})$ is the number of discretization elements at λ , whose values are equal to or larger than $\rho_{s,min}^{ind}$. The probability that a size of a grain exceeds $L_I(\lambda)$, $P(d \geq L_I(\lambda))$, is obtained by renormalizing Equation (3.1-7) with respect to $P_{grains}(\lambda_n)$. Thus, $P(d < L_I(\lambda)) = 1 - P(d \geq L_I(\lambda))$ can be expressed as the following:

$$P(d < L_I(\lambda)) = 1 - \frac{P_{grains}(\lambda)}{P_{grains}(\lambda_n)} = 1 - \frac{N(\rho^{ind}(\lambda) \geq \rho_{s,min}^{ind})}{N(\rho^{ind}(\lambda_n) \geq \rho_{s,min}^{ind})} \left(\frac{\lambda_n}{\lambda}\right)^E \quad (3.1-8)$$

Compared to the standard dry sieving method where grains are classified in groups according to the sizes of voids on the sieves, and hence the total mass representation of each group is used for determining a GSD curve, the approach presented in this work takes into account densities of individual grains. However, the analogy between the dry sieving method and the approach proposed here (Equation 3.1-8) can be derived under certain simplifications, as presented in the Appendix A3.

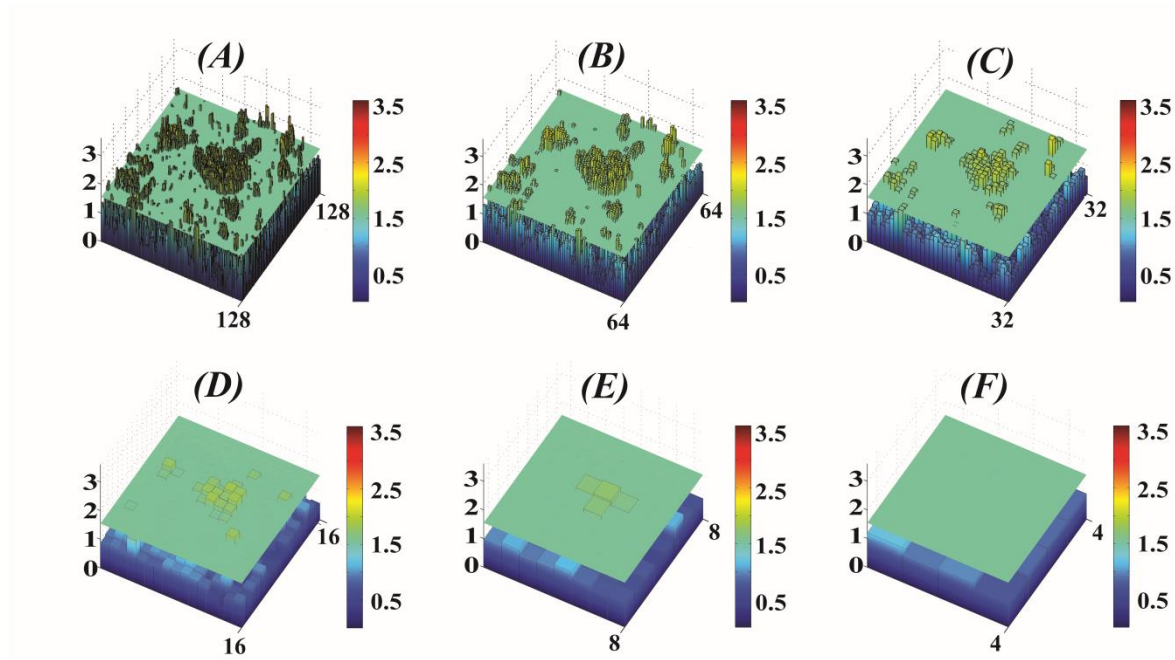


Figure 3.1-2. Change of the two-dimensional $\rho^{ind}(\lambda)$ field (Horiz. plane 4 in Figure 3.1-1) with λ at: (A) $\lambda = 128$; (B) $\lambda = 64$; (C) $\lambda = 32$; (D) $\lambda = 16$; (E) $\lambda = 8$; (F) $\lambda = 4$.

The approach proposed here is facing certain issues that are mostly related to the way pixels are grouped. Thus, it is possible to have λ_I^2 neighbor pixels that belong to a grain of larger size, but since they are distributed in different groups there is a “good” chance that this larger grain will not be recognized after the aggregation. On the contrary, those pixels can signify separated grains, but if they are aggregated as a part of the same group of λ_I^2 pixels, they will be recognized as a part of the larger grain. The same issues appear when applying the presented approach on the three-dimensional image, where λ_I^3 voxels are grouped instead of pixels. Nevertheless, these special cases seem not to have significant influence on the proposed algorithm if applied on sufficiently large λ_n . This has been confirmed by moving the frame of pixels at the initial resolution by one up to a few pixels to the left, right, bottom or the top in order to impact the way pixels are grouped.

Adaptation of the UM framework

To describe Equation (3.1-8) analytically, it is necessary to adapt the UM framework to the approach proposed in this work. As previously explained, UM assume a resolution dependent

threshold λ^γ , while here the emphasis is put on the fixed threshold value $\rho_{s,min}^{ind}$. Therefore, it is necessary to express $\rho_{s,min}^{ind}$, which is independent of λ , through λ .

$$\rho_{s,min}^{ind} = \lambda^{\gamma(\lambda)} \quad (3.1-9)$$

where $\gamma(\lambda)$ is determined at each λ in order to maintain constant value of $\rho_{s,min}^{ind}$. Thus, $\gamma(\lambda)$ is calculated from Equation (3.1-9) as the following:

$$\gamma(\lambda) = \frac{\ln(\rho_{s,min}^{ind})}{\ln(\lambda)} \quad (3.1-10)$$

By introducing Equation (3.1-10) into Equation (3.1-2), $P_{grains}(\lambda)$ (Equation 3.1-7) can be expressed analytically in the following form:

$$P_{grains}(\lambda) = \frac{N(\rho^{ind}(\lambda) \geq \rho_{s,min}^{ind})}{\lambda^E} \approx \lambda^{-c_1 \left(\frac{\ln(\rho_{s,min}^{ind})/\ln(\lambda)}{c_1 \alpha'} + \frac{1}{\alpha} \right)^{\alpha'}} \quad (3.1-11)$$

In *Figure 3.1-3* is presented comparison between Equation (3.1-11) (solid line) and Equation (3.1-1) (dashed lines) for the same values of UM parameters that are related to the horizontal plane 4 in *Figure 3.1-1* ($C_1 = 2.23 \times 10^{-2}$, $\alpha = 1.67$). Different dashed lines shows how the probability of exceeding a scale dependent threshold λ^γ changes with λ for different values of γ (indicated in the Figure), while solid line describes how the probability of exceeding a fixed value of $\rho_{s,min}^{ind} = 1.55$ changes with λ .

As illustrated in *Figure 3.1-3*, Equation (3.1-11) is valid for λ between the lower (λ_{low}) and the upper (λ_{up}) resolution limit. According to Equation (3.1-9), $\lambda_{low} = (\rho_{s,min}^{ind})^{1/\gamma(\lambda)}$, where $\gamma(\lambda) = \gamma_s$ is the previously introduced maximal observable singularity value (see *Figure 3.1-3*). $P_{grains}(\lambda)$ reaches its maximal value for $\lambda = \lambda_{up}$ which is computed the same way as λ_{low} just for $\gamma(\lambda) = C_1$. Therefore, $P_{grains}(\lambda_{up}) = (\rho_{s,min}^{ind})^{-c(C_1)/C_1} = 1/\rho_{s,min}^{ind}$ due to the fact that $c(C_1) = C_1$ (see Equation 3.1-2).

Finally, after renormalizing Equation (3.1-11) with respect to $P_{grains}(\lambda_n)$, the following is obtained:

$$P(d < L_1(\lambda)) = 1 - \frac{\lambda^{-c_1 \left(\frac{\ln(\rho_{s,min}^{ind})/\ln(\lambda)}{c_1 \alpha'} + \frac{1}{\alpha} \right)^{\alpha'}}}{\lambda_n^{-c_1 \left(\frac{\ln(\rho_{s,min}^{ind})/\ln(\lambda_n)}{c_1 \alpha'} + \frac{1}{\alpha} \right)^{\alpha'}}} \quad (3.1-12)$$

Please note that, in order to avoid negative values of Equation (3.1-12), it is necessary for λ_n to be equal to or lower than the upper resolution limit λ_{up} .

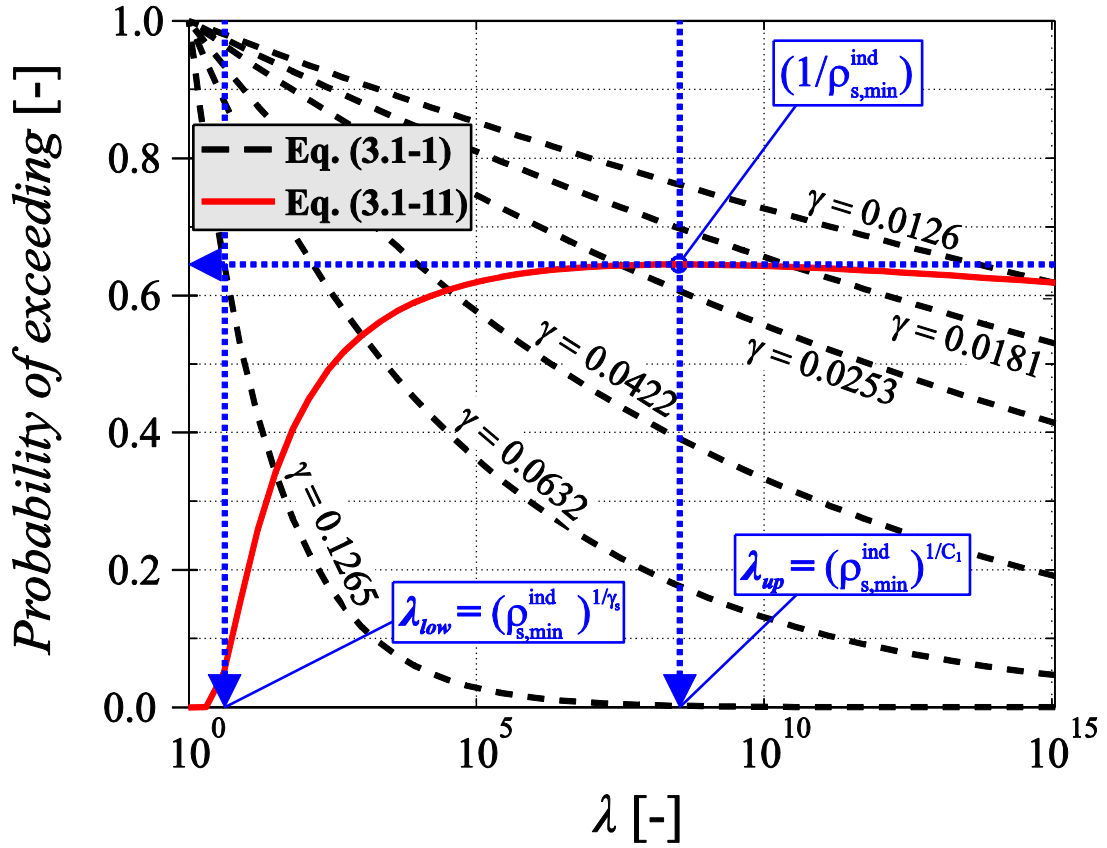


Figure 3.1-3. Comparison between the probability of exceeding i) a resolution dependent threshold λ^γ (Equation (3.1-1) – different dashed lines for different γ values) and ii) a fixed threshold value $\rho_{s,min}^{ind} = 1.55$ (Equation (3.1-11)- solid line). UM parameter values are related to the Horizontal plane 4 (see Table 3.1-1 later in the text): $C_1 = 2.23 \times 10^{-2}$, $\alpha = 1.67$

Equation (3.1-12) is a function of image resolution λ , and thus it is rather convenient for predicting the GSD based on grey-scale images obtained by means of X-ray CT. However, sometimes it is preferable to express GSD curve as a function of grain size instead of image resolution. Having on mind that the actual grain size d_g corresponds to the actual size of a pixel $L_I(\lambda)$, it is clear that λ can be expressed as the ratio (L / d_g) . Furthermore, based on Equation (3.1-10) $\gamma_\lambda = \frac{\ln(\rho_{s,min}^{ind})}{\ln(L/d_g)}$, and thus Equation (3.1-12) can be finally presented in the following form:

$$P(d < d_g) = 1 - \frac{\left(\frac{L}{d_g}\right)^{-c_1 \left(\frac{\ln(\rho_{s,min}^{ind})}{c_1 \alpha'} + \frac{1}{\alpha} \right)^{\alpha'}}{\left(\frac{L}{d_{g,min}}\right)^{-c_1 \left(\frac{\ln(\rho_{s,min}^{ind})}{c_1 \alpha'} + \frac{1}{\alpha} \right)^{\alpha'}} \quad (3.1-13)$$

where $\lambda_n = L / d_{g,min}$, and $d_{g,min}$ is the minimal grain diameter [L]. L is the size of the investigated $\rho^{ind}(\lambda)$ field (grey-scale image), which can be also understood as the size of a cubic shape specimen that contains a material whose GSD needs to be determined. L can be also expressed through the maximal grain diameter $d_{g,max}$ [L], as $L = \lambda_{low} d_{g,max}$.

Determination of model parameters

The model proposed in this work (Equation 3.1-12 and Equation 3.1-13) uses four parameters: $\rho_{s,min}^{ind}$, $d_{g,min}$ (or λ_n in case of Equation 3.1-12), C_1 and α . Value of $\rho_{s,min}^{ind} = \rho_{s,min} / \rho_{bulk}$ can be determined as the ratio between the minimal grain density and the dry bulk density of the material investigated, while λ_n is the highest resolution of the image ($d_{g,min} = L / \lambda_n$).

Finally, α and C_1 are determined by analyzing the scaling behavior of two-dimensional $\rho^{ind}(\lambda)$ field by means of the Trace Moment (TM) technique (Schertzer & Lovejoy, 1987).

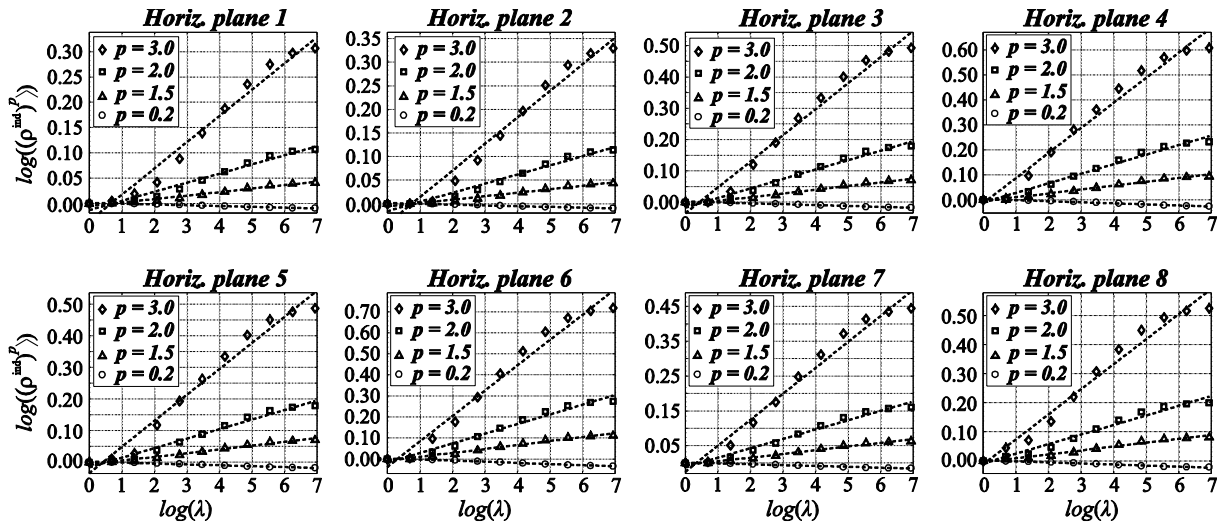


Figure 3.1-4. Scaling of statistical moments for eight $\rho^{ind}(\lambda)$ fields presented in Figure 3.1-1

Firstly, $\rho^{ind}(\lambda)$ field is up-scaled and at each resolution λ it is raised on the power p . Then, $\langle (\rho^{ind}(\lambda))^p \rangle$ (the average statistical moment of an order p) is calculated. For different p values, change of $\langle (\rho^{ind}(\lambda))^p \rangle$ with respect to λ is plotted in log-log scale. In Figure 3.1-4 the scaling behavior is presented only for four different p values, for each of the eight $\rho^{ind}(\lambda)$ fields illustrated in Figure 3.1-1. Different slopes of the obtained linear regressions are related to different $K(p)$ values that are plotted against p in order to form the moment scaling function (see Figure 3.1-5 – different solid lines correspond to eight analyzed fields). Based on Equation (3.1-5), the first derivative of the obtained $K(p)$ function at $p = 1$ is equal to $C_1 = \frac{dK(p)}{dp} \Big|_{p=1}$ (calculated numerically), while the ratio between the second and the first derivative at $p = 1$ is $\alpha = \frac{1}{C_1} \frac{d^2K(p)}{dp^2} \Big|_{p=1}$.

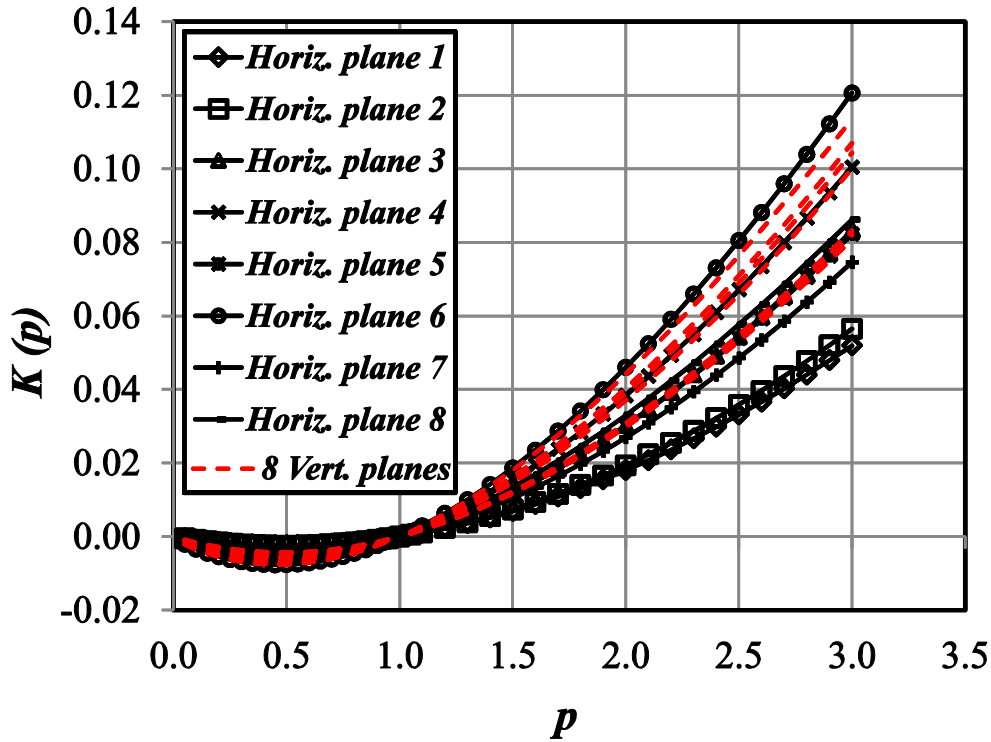


Figure 3.1-5. Moment scaling functions $K(p)$ obtained by applying TM technique on eight horizontal $\rho^{ind}(\lambda)$ fields presented in Figure 3.1-1 (different solid lines) and eight vertically oriented $\rho^{ind}(\lambda)$ fields (dashed lines)

Compared to Equation (3.1-12), Equation (3.1-13) is more convenient for application when the scanned soil images are not available. In that case, α and C_1 cannot be determined as explained above, but manually adjusted for a certain range of scales ($L / d_{g,min}$) so that the best possible agreement between Equation (3.1-13) and experimental GSD data is obtained. Clearly, this procedure is less reliable than the former one, but might be helpful if X-ray CT is not available.

Influence of model parameters

In order to better understand the influence of the four parameters on the model behavior, Equation (3.1-13) has been tested on different values of each parameter, as illustrated in Figure 3.1-6. For all cases presented in Figure 3.1-6, value of $L = 100$ mm is kept constant while changing values of the four model parameters.

The impact of C_1 on the GSD is illustrated in Figure 3.1-6a by increasing (dash-dotted line) / decreasing (dashed line) its initial value (solid line) by 50 % while preserving values of the three remaining parameters. Similarly, in Figure 3.1-6b value of α is changed by 50 % in both ways. Figure 3.1-6a shows that parameter C_1 mostly affects the break onto the finer particles and the shape of that part of the curve in a way that smaller C_1 secures higher contribution of fine grains (dashed line), while the case is opposite for higher C_1 (dash-dotted line). On the contrary, the change of parameter α (Figure 3.1-6b) is less affecting the representation of small grains, but it is mainly responsible for the slope of the central part of the GSD curve, where smaller α provides steeper curve. Thus, in case of granular soils higher α and smaller

C_I values describe well-graded, while smaller α and higher C_I describe poorly (uniformly) graded materials. Indeed, well-graded materials usually have lower total porosity due to the better spatial packing of grains, meaning the lower representation of zeros in ρ^{ind} field that causes stronger variability of the field (higher α) and lower intermittency of its mean value (lower C_I).

The impacts of $\rho_{s,min}^{ind}$ and $d_{g,min}$ on the GSD curve are also tested by varying one of the parameters while maintaining the rest. As illustrated in *Figure 3.1-6c*, the higher $\rho_{s,min}^{ind}$ (more strict threshold value), the higher values of $P(d < d_g)$ (Equation 3.1-13), and vice versa. Unlike the three other parameters, $d_{g,min}$ dictates the total range of scales ($L / d_{g,min}$) by affecting mostly the distribution of small grains (tail of the GSD) - see *Figure 3.1-6d*.

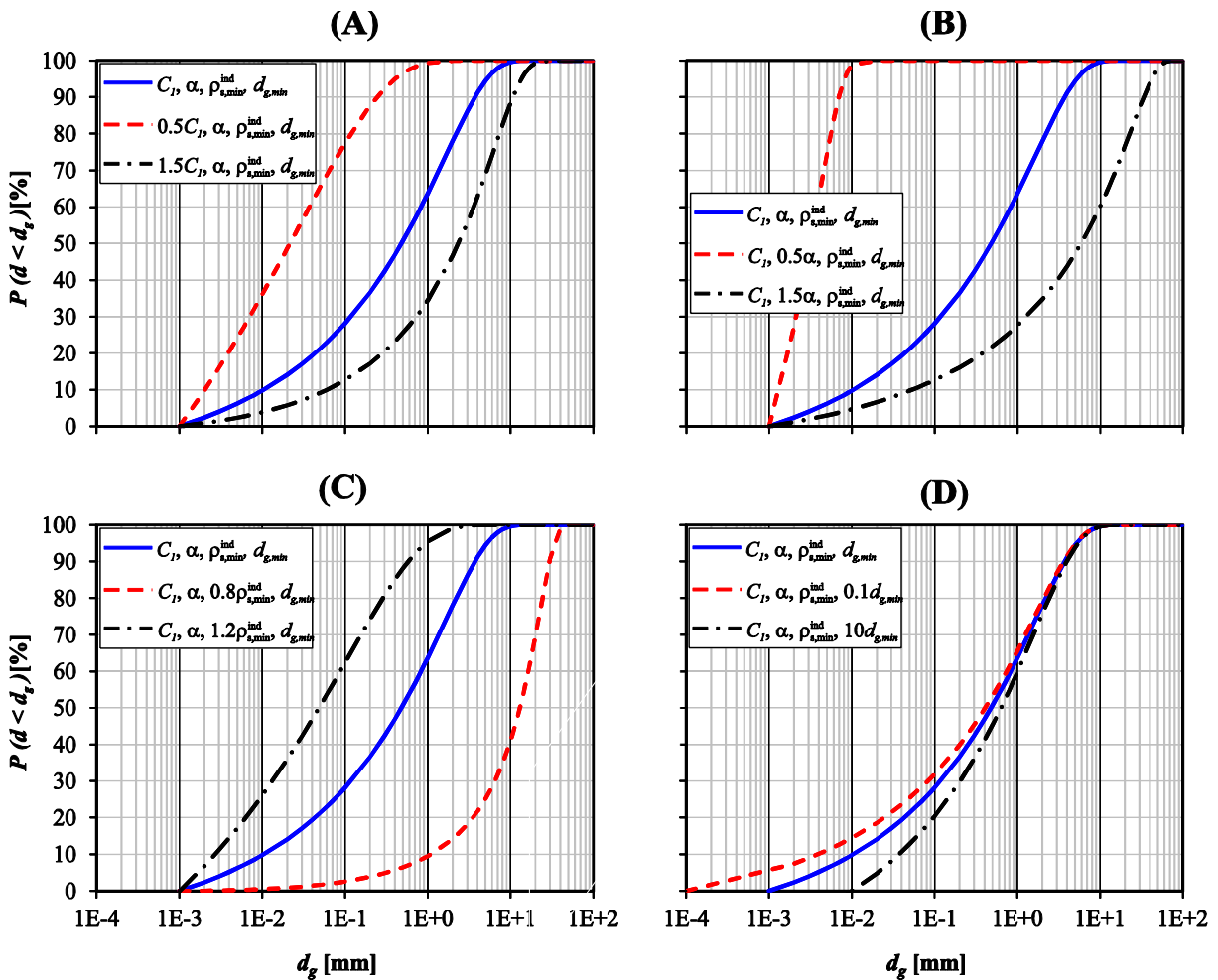


Figure 3.1-6. Behavior of the proposed GSD model when changing values of: a) C_I ; b) α ; c) $\rho_{s,min}^{ind}$; d) $d_{g,min}$. Initial parameter values (solid line in each graph) are $C_I = 1.85 \times 10^{-2}$, $\alpha = 1.3$, $\rho_{s,min}^{ind} = 1.55$ and $d_{g,min} = 1 \times 10^{-3}$ mm

3.1.4. Results and Discussion

The approach presented in this work is firstly validated through the comparison between Equation (3.1-12), applied on the scanned soil images of the Green Wave (GW) substrate, and

the experimental GSD data of the same material. In this case, the UM parameters are estimated based on the scanned soil images following the previously described methodology. The model (Equation 3.1-13) is further applied on two additional soils (Ariana silty clay loam and Yolo clay loam) taken from the literature (Bird et al., 2000), for which scanned images are not available. The comparison with the fractal-based PSF model (Perrier et al., 1999; Bird et al., 2000) is also presented.

Prediction model

Before applying Equation (3.1-12) on ρ^{ind} fields presented in *Figure 3.1-1*, the model parameters need to be determined. As previously explained, $\lambda_n = 1024$ ($d_{g,min} = L_I(\lambda_n) = 50 \mu\text{m}$) and $\rho_{s,min}^{ind} = \frac{\rho_{s,min}}{\rho_{bulk}} = \frac{2.2}{1.42} = 1.55$, where both $\rho_{s,min}$ and ρ_{bulk} were determined experimentally. Finally, α and C_I are determined by applying the TM analysis on both horizontally- and vertically-oriented ρ^{ind} fields (only horizontal planes are presented in *Figure 3.1-1*) in order to check the statistical isotropy within the specimen. Note that $\lambda_n = 1024$ for vertically-oriented planes as well, and they occupy the central part of the specimen with an equal distance between two consecutive images.

Figure 3.1-4 shows that the scaling quality of statistical moments of order p is satisfactory for all horizontal fields, whereas the quality of scaling is even better in case of vertical fields (not presented in the *Figure*). Note that $\lambda_n = 2^{10} = 1024$ is considered as sufficiently high so that the obtained values of UM parameters can be assumed as valid even for higher λ_n .

Figure 3.1-5 illustrates $K(p)$ functions obtained for each analyzed vertical (red dashed lines) and horizontal (different solid lines) image, while the values of the determined UM parameters are presented in *Table 3.1-1*. Obtained moment scaling functions for vertical and horizontal planes $K(p)$ are overlapping (UM parameters cover similar range of values), which indicates the statistical isotropy (homogeneity) that was previously mentioned. Low obtained values of C_I (between 0.01 and 0.027) can be explained by the relatively narrow range of ρ^{ind} values varying between 0 and several units (see grey-scale-bar in *Figure 3.1-1*). Values of this parameter should be approximately the same order of magnitude for majority of soils, since the ratio between the grain density and the bulk density cannot change significantly, regardless of the soil type. On the contrary, high α values (between 1.6 and 2) point out that fluctuations of densities around the bulk density are rather significant, which indicates the presence of various grain sizes of different densities. This is in agreement with the initially made correlation between the high α values and the well-graded materials. As previously mentioned, the characteristic of well-graded materials is the absence of large pores, which seems to be the case here since the majority of pores are smaller than $l(\lambda_n = 1024) = 50 \mu\text{m}$ and cannot be observed on the presented images.

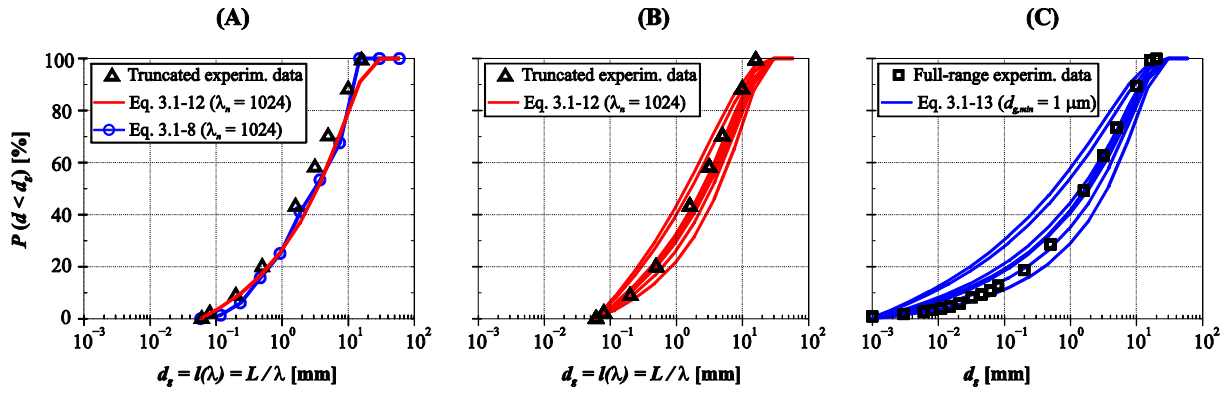


Figure 3.1-7. Comparison between: A) Equation (3.1-12) applied on the Horizontal plane 4 ($L = 60$ mm, $\rho_{s,min}^{ind} = 1.55$, $\lambda_n = 1024$, $C_1 = 2.23 \times 10^{-2}$, $\alpha = 1.67$), Equation (3.1-8) applied on the same field ($\rho_{s,min}^{ind} = 1.55$, $\lambda_n = 1024$), and truncated experimental GSD data ($d_g \geq 50$ μm); B) Equation (3.1-12) applied on eight $\rho^{ind}(\lambda)$ fields presented in Figure 3.1-1 ($L = 60$ mm, $\rho_{s,min}^{ind} = 1.55$, $\lambda_n = 1024$, while α and C_1 are presented in Table 3.1-1), and truncated experimental GSD data ($d_g \geq 50$ μm); C) Equation (3.1-12) (same as in B) just for $d_{g,min} = 1$ μm and the full-range experimental GSD data ($d_g \geq 1$ μm)

Table 3.1-1. Determined UM parameters for eight analyzed ρ^{ind} fields

| Horizontal plane | | | | | | | | |
|------------------|----------|----------|----------|----------|----------|----------|----------|----------|
| | 1 | 2 | 3 | 4 | 5 | 6 | 7 | 8 |
| C_1 | 9.34E-03 | 9.93E-03 | 1.64E-02 | 2.23E-02 | 1.66E-02 | 2.72E-02 | 1.45E-02 | 1.93E-02 |
| α | 1.93 | 1.96 | 1.83 | 1.67 | 1.80 | 1.61 | 1.85 | 1.66 |
| Vertical plane | | | | | | | | |
| | 1 | 2 | 3 | 4 | 5 | 6 | 7 | 8 |
| C_1 | 2.66E-02 | 2.21E-02 | 1.74E-02 | 1.72E-02 | 1.67E-02 | 1.63E-02 | 2.06E-02 | 2.37E-02 |
| α | 1.56 | 1.72 | 1.75 | 1.75 | 1.76 | 1.82 | 1.78 | 1.60 |

After determining values of the four model parameters, Equation (3.1-12) is firstly tested on one of the ρ^{ind} fields presented in Figure 3.1-1 (Horiz. plane 4). Figure 3.1-1a illustrates comparison between Equation (3.1-12) (solid line), Equation (3.1-8) (connected dots) that uses the counted number of $\rho^{ind}(\lambda) \geq \rho_{s,min}^{ind}$ values at different λ , and the truncated experimental GSD data of the GW substrate (triangles). Note that truncated data consider only grains equal to or larger than $d_{g,min} = 50$ μm . Good agreement between different curves presented verifies the approach proposed.

In Figure 3.1-1b is presented comparison between the truncated experimental data (triangles) and Equation (3.1-12) applied on every ρ^{ind} field presented in Figure 3.1-1 (different solid lines). Moreover, in Figure 3.1-1c the full range experimental data (squares) are compared with Equation (3.1-12) by using the same parameter values as in Figure 3.1-1b, with only difference that $d_{g,min}$ is adopted to the minimal measured grain diameter (1 μm). The agreement between Equation (3.1-12) and both truncated and full-range experimental data is considered as satisfactory. Also, the results presented confirm that the change of $d_{g,min}$ impacts mostly the tail of the analytical function. The obtained family of curves creates reasonably narrow confidential zone around experimental points, verifying that way the proposed analytical model.

Application of the model without using X-ray CT

Alternatively, this model can be also applied when the scanned soil images are not available. In such case, the model proposed can be used only to interpret the measured GSD curve, and not to predict it. Values of $\rho_{s,min}^{ind}$ and $d_{g,min}$ are determined as described, while α and C_l are manually adjusted for a given range of scales ($L / d_{g,min}$) so that the best possible agreement between Equation (3.1-13) and measured points is obtained. Besides the GW substrate, this procedure has been tested on Ariana silty clay loam (ASCL) and Yolo clay loam (YCL) taken from Bird et al. (2000).

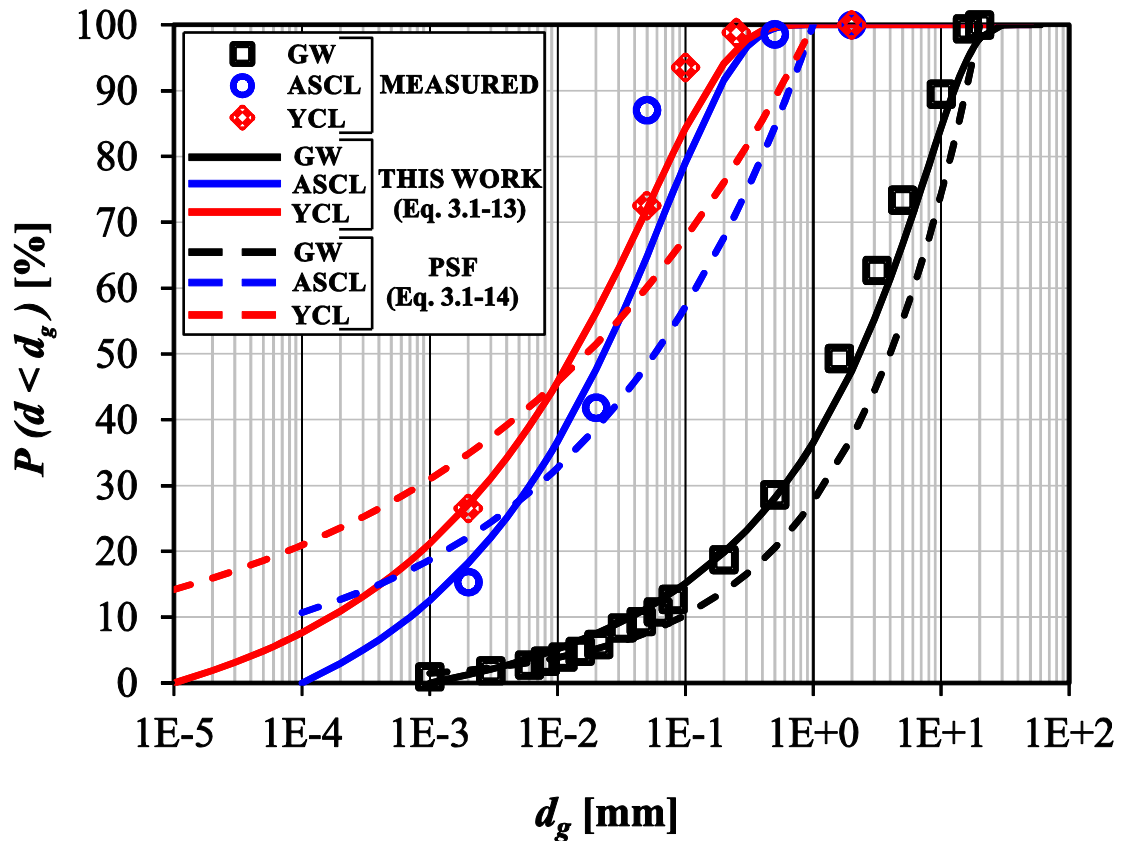


Figure 3.1-8. Comparison between the experimental GSD data (GW substrate – squares; ASCL – circles; YCL - diamonds) and Equation (3.1-13) (solid lines) and Equation (3.1-14) (dashed lines). The adjusted values of C_l and α (Equation 3.1-13) and $D_{f,PSF}$ (Equation 3.1-14) are presented in Table 3.1-2

In case of the GW substrate (squares in Figure 3.1-8), $L = 60$ mm, $\rho_{s,min}^{ind} = 1.55$ and $d_{g,min} = 1$ μ m are kept identical as in the previous section, while $C_l = 2.25 \times 10^{-2}$ and $\alpha = 1.6$ are manually adjusted. The optimal values of UM parameters are rather close to those determined through the application of TM technique on Horizontal plane 4 (see Table 3.1-1). This confirms the physical basis of the proposed approach, having on mind that the analytical curve related to plane 4 provides the best (among the eight planes investigated) agreement with measured data.

In case of the ASCL (circles in Figure 3.1-8) and YCL (diamonds in Figure 3.1-8) there are much more uncertainties due to the not so detailed information about these materials. Since

only the average grain densities (ρ_s) are provided, $\rho_{s,min}^{ind}$ is calculated as $\frac{\rho_s}{\rho_{bulk}} = \frac{2.61}{1.409} = 1.85$ in case of ASCL, and as $\frac{\rho_{bulk}}{\rho_{bulk}(1-\varphi)} = \frac{1}{1-0.434} = 1.77$ in case of YCL, where $\rho_s = \frac{\rho_{bulk}}{1-\varphi}$ and φ is the total porosity [-]. Furthermore, values of $d_{g,min}$ are approximately estimated from the measurements presented in *Figure 3.1-8* (see *Table 3.1-2*), while L is estimated based on the total volume of the material used for the experimental determination of the GSD. By assuming that the standard empirical equation was used for estimating the total mass of the material $M_{total} = 300d_{g,max}$ [g] ($d_{g,max}$ is expressed in [mm]), its volume can be estimated as $L^3 = M_{total} / \rho_{bulk}$, and finally $L = (M_{total} / \rho_{bulk})^{1/3}$. Based on the adopted value of $d_{g,max} = 1$ mm for both ASCL and YCL, value of L is computed as 59.70 cm and 60.72 cm, respectively, while the optimal values of α and C_1 are presented in *Table 3.1-2*.

Table 3.1-2. Basic physical parameters related to the GW substrate, ASCL and YCL, together with the manually adjusted values of UM parameters (THIS WORK) and fractal coefficient (PSF MODEL)

| Soil type | $d_{g,min}$ [mm] | $d_{g,max}$ [mm] | L [mm] | ρ_{bulk} [g/cm ³] | $\rho_{s,min}$ [g/cm ³] | α | C_1 | $D_{f,PSF}$ |
|---------------------|---------------------|---------------------|-------------|---------------------------------------|--|----------|---------|-------------|
| GW substrate | 1E-3 | 18 | 60.00 | 1.42 | 2.20* | 1.60 | 2.25E-2 | 2.57 |
| ASCL | 1E-4 | 1 | 59.70 | 1.41 | 2.61 | 0.98 | 2.76E-2 | 2.76 |
| YCL | 1E-5 | 1 | 60.72 | 1.34 | 2.37 | 1.02 | 2.26E-2 | 2.83 |

*Value 2.20 g/cm³ is the minimal grain density of GW substrate measured by means of the standard pycnometer procedure, while the average one is 2.35 g/cm³. In case of the ASCL and YCL, there is no information about the $\rho_{s,min}$, but only ρ_s which is used instead

The PSF approach, a three-phase fractal-based GSD model firstly introduced by Perrier et al. (1999), is also used for interpreting the three experimental GSD curves. According to this model, the GSD can be described using the following expression (Bird et al., 2000):

$$P(d < d_g) = \left(\frac{d_g}{d_{g,max}} \right)^{3-D_{f,PSF}} \quad (3.1-14)$$

where $D_{f,PSF}$ is the fractal coefficient [-] whose optimal value can be determined from the slope of the best fitting linear regression in logarithmic scale that goes through the experimental GSD data and reaches 100 % at $d_{g,max}$. In *Table 3.1-2* are presented the optimal values of $D_{f,PSF}$ for all three investigated materials, while the values of $d_{g,max}$ are those used for estimating M_{total} in case of ASCL and YCL ($d_{g,max} = 18$ mm is adopted for the GW substrate).

Compared to Equation (3.1-14) which considers the fixed fractal dimension $D_{f,PSF}$, Equation (3.1-13) takes into account the fractal dimension that changes with d_g (the co-dimension function). Therefore, for the multifractal-based approach it is quite important to know the quantity of the material investigated, defined through L , in order to estimate properly the total range of scales ($L / d_{g,min}$). Even though the PSF model (Equation 3.1-14) is more convenient for practical application, since it requires only two parameters that can be determined quite easily, the model proposed in this work (Equation 3.1-13) shows better agreement with

experimental data for all three materials investigated (see *Figure 3.1-8*). If having more detailed information about ASCL and YCL, Equation (3.1-13) could fit even better.

3.1.1. Conclusion

This work shows that the proposed multifractal-based analytical model can be used for predicting the GSD of a certain material based on its scanned micro-structure which represents a density indicator field. By reducing the resolution of the scanned image, density indicator values above the fixed threshold are treated at each resolution as a cumulative representation of solid particles of diameter equal to or larger than the corresponding pixel size. The quantity of values above the threshold at different resolutions can be described by means of Universal Multifractals (UM), leading to the new multifractal-based GSD model. The model uses four parameters, where two of them are related to physical properties of the material (the minimal grain diameter and the ratio between the minimal grain density and dry bulk density), while the remaining ones (UM parameters) characterize the spatial heterogeneity of the soil density field.

An innovative approach proposed in this work was firstly tested on an unconventional volcanic granular material used for covering green roofs. Based on the Trace Moment analysis of its two-dimensional scanned soil images (density indicator field), UM parameter (C_1 and α) values were determined and a family of analytical GSD curves was obtained, showing a good agreement with dry sieving / sedimentation test data. In order to save computational time and memory, the analysis was performed on eight two-dimensional horizontal slices extracted from the full three-dimensional image, which is legit if the statistical isotropy within the specimen is secured.

Alternatively, if the scanned soil image(s) is not available the proposed model can be used for interpreting, instead of predicting, the GSD data. This was tested on two materials taken from literature (Ariana silty clay loam and Yolo clay loam), where C_1 and α values were manually adjusted to secure the best possible agreement between the model and experimental data. Even though the model applied in this form is less reliable compared to the analysis of scanned soil images, results confirm that values of UM parameters can be correlated with the gradation of granular materials. Lower C_1 and higher α describe materials with wide range of grain sizes (well-graded materials such as the Green Wave substrate), while lower α and higher C_1 are related to the steeper GSD curve in its central part and stronger curvature close to the break onto the finer particles (two other soils). Also, values of C_1 are proved to be the same order of magnitude for different soils (10^{-2}) due to the fact that density of an individual grain cannot be significantly larger than the dry bulk density, regardless of the soil type.

Finally, compared to the fractal-based PSF model that requires only two parameters, the proposed multifractal-based model requires four. However, the proposed model uses different fractal dimensions for different grain sizes, providing better match with experimental data than the PSF model.

3.1.2. References:

- AFNOR. 1992. *Analyse Granulométrique Des Sols - Méthode Par Sédimentation*. France: Association Française de Normalisation.
- . 1996. *Analyse Granulométrique - Méthode Par Tamisage à Sec Après Lavage*. France: Association Française de Normalisation.
- Banhart, J. 2008. *Advanced Tomographic Methods in Materials Research and Engineering*. New York: Oxford University Press.
- Bird, N. R. A., E. Perrier, and M. Rieu. 2000. “The Water Retention Function for a Model of Soil Structure with Pore and Solid Fractal Distributions.” *European Journal of Soil Science* 51 (1): 55–63. <https://doi.org/10.1046/j.1365-2389.2000.00278.x>.
- Bruchon, J. F., J. M. Pereira, M. Vandamme, N. Lenoir, P. Delage, and M. Bornert. 2013. “Full 3D Investigation and Characterisation of Capillary Collapse of a Loose Unsaturated Sand Using X-Ray CT.” *Granular Matter* 15 (6): 783–800. <https://doi.org/10.1007/s10035-013-0452-6>.
- Frisch, U., and G. Parisi. 1985. “A Multifractal Model of Intermittency.” *Turbulence and Predictability in Geophysical Fluid Dynamics and Climate Dynamics*, 84–88.
- Ghanbarian-Alavijeh, B., H. Millán, and G. Huang. 2011. “A Review of Fractal, Prefractal and Pore-Solid-Fractal Models for Parameterizing the Soil Water Retention Curve.” *Canadian Journal of Soil Science* 91 (1): 1–14. <https://doi.org/10.4141/cjss10008>.
- Ghanbarian, B., and A. G. Hunt. 2017. *Fractals - Concepts and Applications in Geoscience*. Edited by Behzad Ghanbarian and Allen G. Hunt. Boca Raton: CRC Press.
- Grout, H., A. M. Tarquis, and M. R. Wiesner. 1998. “Multifractal Analysis of Particle Size Distributions in Soil.” *Environmental Science and Technology* 32 (9): 1176–82. <https://doi.org/10.1021/es9704343>.
- He, D., N. N. Ekere, and L. Cai. 1999. “Computer Simulation of Random Packing of Unequal Particles.” *Physical Review E* 60 (6 Pt B): 7098–7104. <http://www.ncbi.nlm.nih.gov/pubmed/11970649>.
- Hsieh, J. 2003. *Computed Tomography: Principles, Design, Artifacts, and Recent Advances*. 114th ed. Society of Photo Optical.
- Lai, Z., and Q. Chen. 2018. “Reconstructing Granular Particles from X-Ray Computed Tomography Using the TWS Machine Learning Tool and the Level Set Method.” *Acta Geotechnica* 3456789. <https://doi.org/10.1007/s11440-018-0759-x>.
- Martín, M. Á., and E. Montero. 2002. “Laser Diffraction and Multifractal Analysis for the Characterization of Dry Soil Volume-Size Distributions.” *Soil and Tillage Research* 64 (1–2): 113–23. [https://doi.org/10.1016/S0167-1987\(01\)00249-5](https://doi.org/10.1016/S0167-1987(01)00249-5).
- Nolan, G. T., and P. E. Kavanagh. 1993. “Computer Simulation of Random Packings of Spheres with Log-Normal Distributions.” *Powder Technology* 76 (3): 309–16. [https://doi.org/10.1016/S0032-5910\(05\)80012-9](https://doi.org/10.1016/S0032-5910(05)80012-9).
- Perrier, E., N. Bird, and M. Rieu. 1999. “Generalizing the Fractal Model of Soil Structure: The Pore-Solid Fractal Approach.” *Developments in Soil Science* 27 (C): 47–74. [https://doi.org/10.1016/S0166-2481\(00\)80005-7](https://doi.org/10.1016/S0166-2481(00)80005-7).
- Posadas, A. N. D., D. Giménez, M. Bittelli, C. M. P. Vaz, and M. Flury. 2001. “Multifractal Characterization of Soil Particle-Size Distributions.” *Soil Science Society of America*
-

Journal 65 (5): 1361. <https://doi.org/10.2136/sssaj2001.6551361x>.

Schertzer, D., and S. Lovejoy. 1987. "Physical Modeling and Analysis of Rain and Clouds by Anisotropic Scaling Multiplicative Processes." *Journal of Geophysical Research* 92: 9693–9714.

———. 1993. "Nonlinear Variability in Geophysics 3 - Scaling and Multifractal Processes." In *AGU Chapman / EGS Richardson Memorial Conference*.

———. 1997. "Universal Multifractals Do Exist!: Comments on 'A Statistical Analysis of Mesoscale Rainfall as a Random Cascade.'" *Journal of Applied Meteorology* 36: 1296–1303.

Segal, E., P. J. Shouse, S. A. Bradford, T. H. Skaggs, and D. L. Corwin. 2009. "Measuring Particle Size Distribution Using Laser Diffraction : Implications for Predicting Soil Hydraulic Properties." *Soil Science* 174 (12): 639–45.
<https://doi.org/10.1097/SS.0b013e3181c2a928>.

Stanić, F., Y.-J. Cui, P. Delage, E. De Laure, P.-A. Versini, D. Schertzer, and I. Tchiguirinskaia. 2019. "A Device for the Simultaneous Determination of the Water Retention Properties and the Hydraulic Conductivity Function of an Unsaturated Coarse Material ; Application to a Green- Roof Volcanic Substrate." *Geotechnical Testing Journal*. <https://doi.org/10.1520/GTJ20170443>.

Taina, I. A., R. J. Heck, and T. R. Elliot. 2008. "Application of X-Ray Computed Tomography to Soil Science : A Literature Review." *Can. J. Soil Sci.* 88: 1–20.

Torre, I. G., J. C. Losada, and A. M. Tarquis. 2016. "Multiscaling Properties of Soil Images." *Biosystems Engineering* 168: 133–41.
<https://doi.org/10.1016/j.biosystemseng.2016.11.006>.

Versini, P. -A., A. Gires, I. Tchiguirinskaia, and D. Schertzer. 2018. "Toward an Assessment of the Hydrological Components Variability in Green Infrastructures: Pilot Site of the Green Wave (Champs-Sur-Marne)." *La Houille Blanche*, no. 4: 34–42.
<https://doi.org/10.1051/lhb/2018040>.

Versini, P. -A., F. Stanic, A. Gires, D. Schertzer, and I. Tchiguirinskaia. 2020. "Measurements of the Water Balance Components of a Large Green Roof in the Greater Paris Area." *Earth Syst. Sci. Data* 12: 1025–35.
<https://doi.org/https://doi.org/10.5194/essd-12-1025-2020>.

3.2. A new (multi)fractal approach to account for capillary and adsorption phenomenon in the water retention and transfer properties of unsaturated soils

(Under revision in Water Resources Research)

3.2.1. Introduction

The most widely used water retention curves (WRC) (e.g. Brooks & Corey (1964), van Genuchten (1980), Fredlund & Xing (1994) or Kosugi (1996)) are semi-empirical relations fitted from experimental data. As recalled in Rahardjo and Leung (1997), hydraulic conductivity functions have been derived from WRCs through statistical models (Hoffmann-Riem et al. 1999), among which Burdine (1953)'s and Mualem (1976)'s are the most widely-used. These models consider unsaturated soils as a bunch of parallel capillary tubes of various diameters, with water saturation governed by Young-Laplace's capillary law that distinguishes, at a given suction, smaller saturated tubes from larger unsaturated ones. Water flux through the saturated tubes is controlled by the Hagen-Poiseuille law. This empirical approach of WRCs has been completed by more physically-based models based on the fractal theory (Ghanbarian-Alavijeh et al., 2011) and accounting for capillary effects within the pores of the partially saturated specimens (e.g. Bird et al., 2000; Russell & Buzzi, 2012, etc). The Pore-Solid-Fractal (PSF) model (Bird et al., 2000) is closely related to the grain size distribution (GSD) that is assumed to follow the same fractal law as the pore size distribution (PSD) (Perrier et al., 1999). Russell & Buzzi (2012) proposed a model based on two different fractal dimensions for pores and grains, respectively, that also accounts for the hysteresis of the WRCs. Hydraulic conductivity models have also been completed based on the fractal theory. Xu (2004) developed a hydraulic conductivity function based on the PSF approach, while Yang et al. (2014) extended a fractal-based hydraulic conductivity model to the hydraulic hysteresis of the WRC.

Capillary models assume water to be immobile at water contents lower than the residual one, which is not in agreement with some studies (Li & Wardlaw, 1986; Lenormand, 1990; Wang et al., 2013) that showed that the movement of the thin liquid films of water adsorbed along the clay particles cannot be neglected in clayey soils. The different mechanisms affecting the soil-water interaction in clayey soils can be found in Lu & Zhang (2019) and Zhang & Lu (2019, 2020). Campbell & Shiozawa (1992) proposed a water retention function for the adsorbed water, that decreases linearly towards zero in a semi-log scale. Various hydraulic conductivity functions for the film flow were proposed by Tuller & Or (2001) and Tokunaga (2009), and various models accounting for both capillary and adsorbed phenomena along the whole range of suction between saturated and dry states have been developed. Peters (2013) used the water retention models of both van Genuchten (1980) and Kosugi (1996), in combination with Mualem's model for the capillary-dominated suction zone, completed by using Campbell & Shiozawa (1992) and Tokunaga (2009)'s functions in the high suction zone, where film-dominated flow occurs. To cope with mathematical discontinuity at the air-

entry suction met in Campbell & Shiozawa (1992)'s function, Iden & Durner (2014) proposed, in the so-called PID (Peter-Iden-Durner) model, a continuously differentiable function. This approach was upgraded by Rudyanto et al. (2015) to account for hysteresis, while a mathematically continuous model based on Fredlund & Xing (1994)'s function has been recently proposed by Wang et al. (2016).

All these models have shown rather good agreement with published data for a variety of soils along the full-range of suction. However, optimization tools are necessary to properly model experimental data, mostly because of the poor physical basis of the water retention functions in the capillary range. The existing fractal-based capillary models can be used as an alternative, but they suppose a fractal GSD, which is not in agreement with the work presented in Chapter 3.1 showing its multifractal nature.

In this work, we are going back from a multifractal to a simplified fractal-based approach in order to obtain a capillary model for soil hydraulic properties (WRC and HCF) which is more convenient for practical application. Compared to the existing fractal capillary models whose fractal dimension is related to the pore size distribution, the model proposed here uses fractal dimension related to grains, preserving that way the link between the soil hydraulic properties and the multifractal-based GSD function presented in Chapter 3.1. Finally, the capillary model developed here is combined with the PID model to account for retention and transfer properties of both sandy and clayey soils along the whole suction range. The performance of this model is tested by considering published data of 10 different soils.

3.2.2. Methodology

Pore Size Distribution – Reduction from a multifractal to a fractal-based approach

In Chapter 3.1 is explained in details how are the raw grey-level data, obtained by means of X-ray CT scanner, transformed into the density indicator $\rho^{ind} \geq 0$ values (see Equation 3.1-6 in Chapter 3.1), where $\rho^{ind} = 0$ corresponds to pores full of air. It was shown that the representation of $\rho^{ind}(\lambda) \geq \rho_{s,min}^{ind}$ values changes with the image resolution λ following the multifractal law, which was used to develop the multifractal-based GSD function. However, in this work a simpler fractal law is used for describing the link between the representation of $\rho^{ind}(\lambda) > 0$ values and λ , which is further used to analytically interpret distribution of pores ($\rho^{ind}(\lambda) = 0$ values). Such a reduction from a multifractal to a fractal-based approach is applied due to more convenient practical application, having on mind the main idea of this work, to develop a simple and robust hydraulic properties model.

The fractal-based approach is explained on the example of two-dimensional grey-scale image (Horiz. plane 4 from *Figure 3.1-1*) that has been previously modified in order to increase the number of $\rho^{ind} = 0$ values, which was originally negligible. To do so, the value of parameter GL_0 in Equation 3.1-6 (Chapter 3.1) has been increased compared to the original value used in Chapter 3.1. Please note that such a modification was done only for illustration purposes, and has no impact on the results presented later in the text.

As explained in Chapter 3.1, starting from the initial resolution λ_n , one applies the standard up-scaling procedure on a $\rho^{ind}(\lambda)$ field by reducing λ stepwise. By averaging groups of four neighbor pixels distributed in square, λ decreases by a factor $\sqrt[4]{4} = 2$, while the pixel size increases by the same factor. The procedure is repeated until λ_{min} , the lowest λ containing black pixels, is reached.

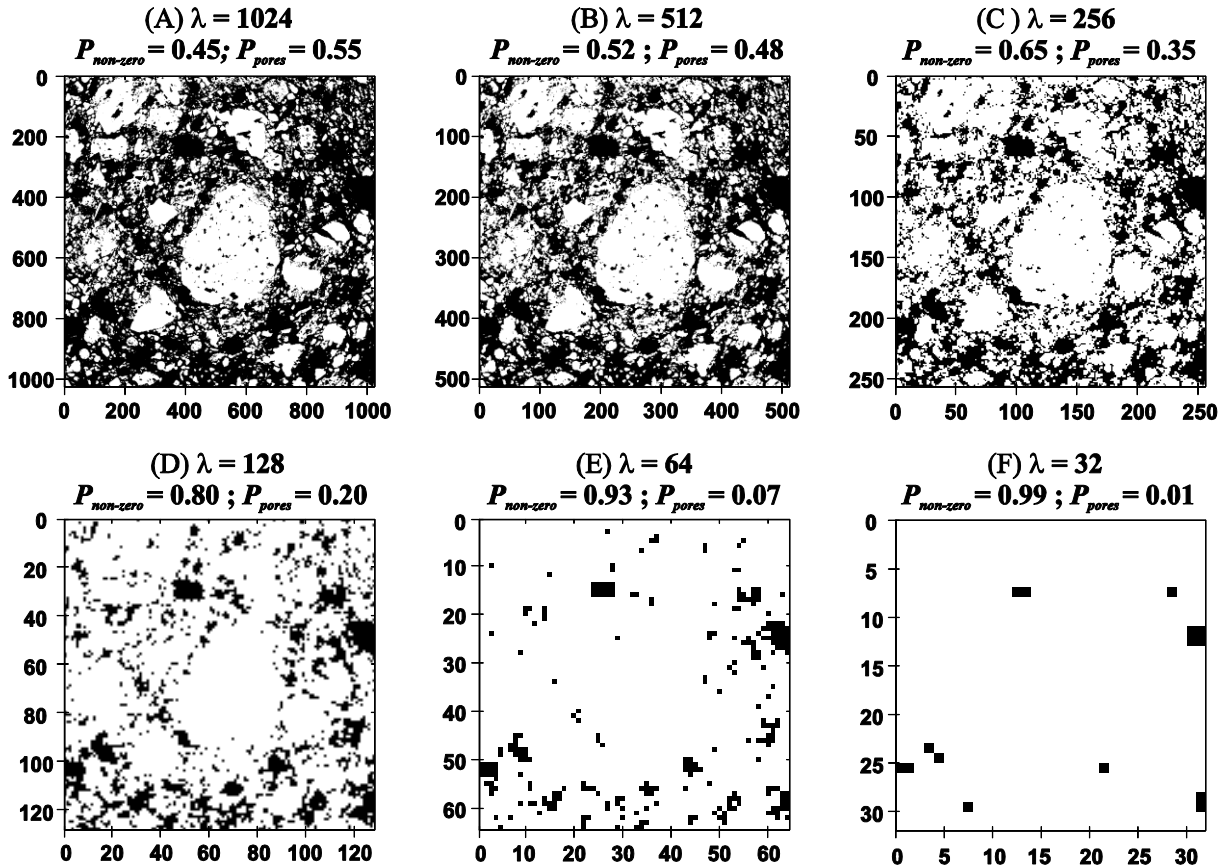


Figure 3.2-1. Procedure for determination of the fractal dimension of white pixels ($\rho^{ind} = \text{const.} > 0$). Resolution λ of the binary image decreases starting from (A) to (F) by factor 2. Axis of each image indicates the number of pixels in two orthogonal directions that correspond to λ

If at each λ , all $\rho^{ind}(\lambda) > 0$ values are set to a constant positive value (white) while keeping all $\rho^{ind}(\lambda) = 0$ (black areas), the grey-level image (Horiz. plane 4 from Figure 3.1-1) is transformed into the binary black-white image of Figure 3.2-1. This Figure shows that as λ decreases from $\lambda_n = 1024$ to $\lambda_{min} = 32$, the pores (black areas) smaller than the actual pixel size $L_1(\lambda)$ vanish, while those equal to or larger remain. Thus, solely the largest pores are recognized at the minimal resolution λ_{min} ($\lambda_{min} = 32$ in Figure 3.2-1), providing the link between the actual pore diameter d_p and $L_1(\lambda)$ ($d_p = L_1(\lambda)$), that is further used in the development of the fractal-based PSD model.

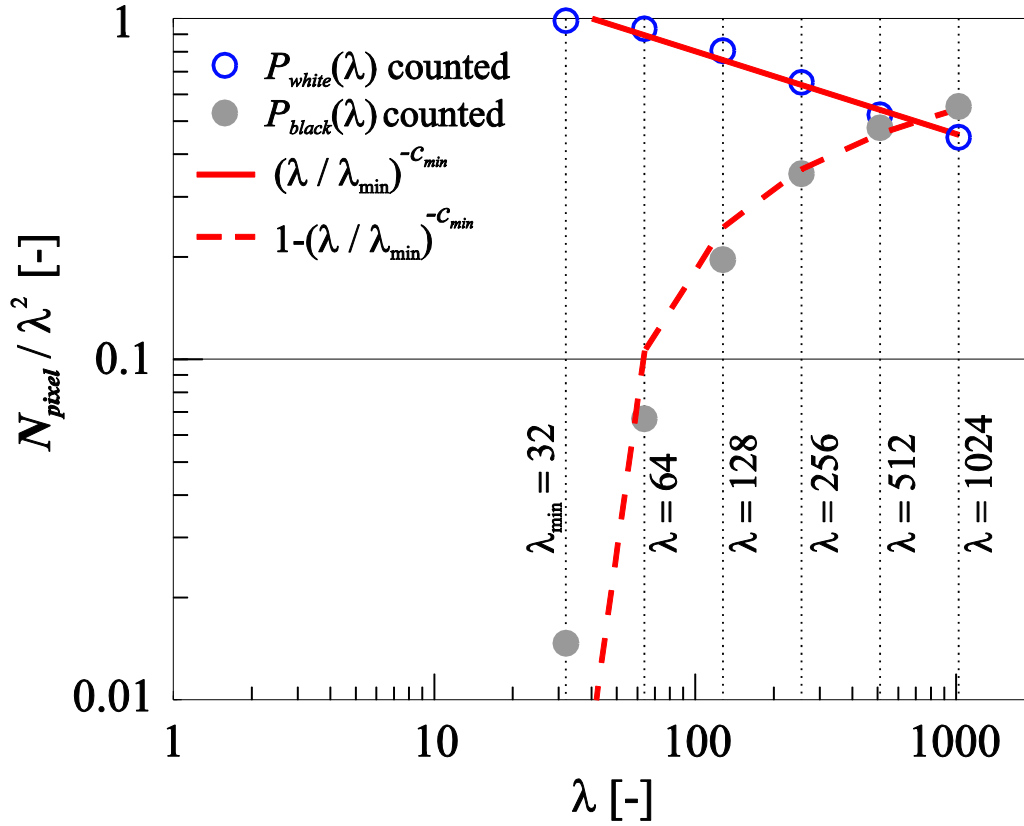


Figure 3.2-2. Empty and filled dots illustrate the representations of white and black pixels that are counted at different λ of Figure 3.2-1; Solid and dashed lines illustrate the change of white and black pixels, respectively, according to the fractal-based approach presented

By counting separately the white ($N_{white}(\lambda)$) and black ($N_{black}(\lambda)$) pixels at each value of λ , their representations are calculated with respect to the total number of pixels at that resolution (λ^2) as indicated in Figure 3.2-1 ($P_{white}(\lambda) = \frac{N_{white}(\lambda)}{\lambda^2}$, $P_{black}(\lambda) = \frac{N_{black}(\lambda)}{\lambda^2}$ and $P_{white}(\lambda) + P_{black}(\lambda) = 1$). In Figure 3.2-2, the counted values of $P_{white}(\lambda)$ (empty dots) and $P_{black}(\lambda)$ (filled dots) are plotted against λ in log-log scale, showing a fractal behavior of white pixels that follow a linear regression for $\lambda \geq \lambda_{min} = 32$. Therefore, a power (fractal) law can be used over this range to express $P_{white}(\lambda)$:

$$P_{white}(\lambda) = \left(\frac{\lambda}{\lambda_{min}}\right)^{-c_{min}} \quad (3.2-1)$$

where $c_{min} = (E - D_f)$ is the exponent, corresponding to the slope of the solid line. Note that D_f is the fractal dimension [-] of white pixels, while E is the Euclidian dimension ($E = 2$ for two-dimensional image as in Figure 3.2-1, and $E = 3$ for a three-dimensional space). Black pixels ($P_{black}(\lambda) = P_{pores}(\lambda)$) are complementary to white ones ($P_{white}(\lambda)$), resulting in the following expression:

$$P_{pores}(\lambda) = 1 - \left(\frac{\lambda}{\lambda_{min}}\right)^{-c_{min}} \quad (3.2-2)$$

Given that $L_I(\lambda) = d_p$, the ratio $\frac{\lambda}{\lambda_{min}} = \frac{L/d_p}{L/d_{p,max}}$ is equal to $\frac{d_{p,max}}{d_p}$, where $d_{p,max}$ is the maximal pore diameter [L] related to λ_{min} . Thus, Equation (3.2-2) describes the representation of pores with diameter equal to or larger than d_p .

Similarly as in Chapter 3.1, the representation function (Equation 3.2-2) needs to be renormalized with respect to the initial representation of pores met at λ_n ($P_{pores}(\lambda_n)$) in order to obtain a cumulative distribution function describing the probability of exceeding $d_p = L_I(\lambda)$. Therefore, $P(d \geq d_p) = \frac{P_{pores}(\lambda)}{P_{pores}(\lambda_n)}$, while $P(d < d_p) = 1 - \frac{P_{pores}(\lambda)}{P_{pores}(\lambda_n)}$. At sufficiently high λ_n , it can be assumed that $P_{pores}(\lambda_n)$ is equal to the experimentally determined porosity φ . Hence, the pore size distribution expressing the cumulative distribution of pores smaller than d_p can finally be written as follows:

$$P(d < d_p) = 1 - \frac{1 - \left(\frac{d_{p,max}}{d_p}\right)^{-c_{min}}}{\varphi} \quad (3.2-3)$$

Since $\lambda_n = L/d_{p,min}$, where $d_{p,min}$ is the minimal pore diameter [L], representation of pores at λ_n can be expressed by means of Equation (3.2-2) as $P_{pores}(\lambda_n) = 1 - \left(\frac{d_{p,max}}{d_{p,min}}\right)^{-c_{min}} = \varphi$.

Therefore, porosity can be calculated as $\varphi = 1 - \left(d_{p,max}/d_{p,min}\right)^{-c_{min}}$. Note that c_{min} is the fixed minimal value of the co-dimension function used for describing the GSD, which is related to the minimal grain diameter $d_{g,min}$ (c_{min} is equal to the value of the exponent below the division sign in Equation 3.1-13 - Chapter 3.1). This provides the link between the PSD and the GSD. Since the PSD is based on the representation of pore volumes ($E = 3$), $c_{min} = 3 - D_f$. Note that $D_f = 3$ (or $c_{min} = 0$) describes the case when grain pixels are ubiquitous at λ_n , leading to zero porosity ($\varphi = 0$).

In the case of well-graded materials, smaller grains fill the voids between larger ones, creating pores of different sizes. This causes the black areas in the black-white soil image to resist longer to the up-scaling procedure, securing less steep linear regression of white pixels (see *Figure 3.2-2*), and hence lower c_{min} (higher D_f). On the contrary, grains of uniform size create narrow spectrum of pore sizes that vanish rather rapidly once the up-scaling procedure is started. This results in a steeper slope of the linear regression, and hence higher c_{min} (lower D_f). Finally, it can be concluded that a lower D_f is related to poorly graded materials like clean sands with a narrow range of grain sizes, while higher D_f (closer to E) is related to well-graded materials.

Water retention

When accounting for the water content change along the drying path of the water retention curve from saturation to oven-dryness, both capillary and adsorptive water need to be considered. In this case, the total water content $\theta^{tot}(h_k)$ can be written, as proposed by Iden & Durner (2014):

$$\theta^{tot}(h_k) = (\theta_s - \theta_r)S_e^{cap}(h_k) + \theta_r S_e^{ads}(h_k) \quad (3.2-4)$$

where $S_e^{cap}(h_k)$ and $S_e^{ads}(h_k)$ are the relative saturations [0 - 1] of capillary and adsorptive water, respectively, θ_s and θ_r are the saturated and residual water contents [-], respectively, and h_k is the suction expressed in terms of water height (pressure head) [L]. Equation (3.2-4) indicates that capillary water is dominant at lower h_k ($\theta_s < \theta < \theta_r$), while for significantly higher h_k values ($\theta < \theta_r$), mainly the adsorptive water remains.

To date, semi-empirical water retention functions (Brooks & Corey (1964), van Genuchten (1980), Fredlund & Xing (1994), Kosugi (1996), etc.) are most often used to account for water retention effects in the capillary range, with no consideration of the residual adsorbed water at high suction. In this study, a new physically-based function based on Equation (3.2-3) and the Young-Laplace law is proposed in the capillary range. Following Young-Laplace's law, once suction h_k is imposed to an initially saturated porous medium, all pores with diameters smaller than $d_p = C / h_k$ cm ($C \approx 0.28$ expresses Young-Laplace's law and is a function of water/solid interaction properties) are emptied. Thus, $S_e^{cap}(h_k)$ can be simply obtained from Equation (3.2-3):

$$S_e^{cap}(h_k) = \frac{\theta^{cap}(h_k) - \theta_r}{\theta_s - \theta_r} = \begin{cases} 1, & h_k < h_{k,a} \\ 1 - \frac{1 - \left(\frac{h_k}{h_{k,a}}\right)^{D_f - 3}}{\theta_s - \theta_r}, & h_{k,a} \leq h_k \leq h_{k,r} \end{cases} \quad (3.2-5)$$

where $h_{k,a}$ is the air entry value suction [L], a maximal h_k corresponding to full saturation.

The suction $h_{k,r}$ corresponding to the extraction of all capillary water and to $\theta = \theta_r$ is obtained by writing $S_e^{cap}(h_{k,r}) = 0$, giving $h_{k,r} = h_{k,a} [1 - (\theta_s - \theta_r)]^{\frac{1}{D_f - 3}}$.

Thus, both S_e^{cap} and S_e^{ads} condition the value of θ^{tot} for $h_{k,a} \leq h_k < h_{k,r}$, while only S_e^{ads} remains for $h_k \geq h_{k,r}$ (see Equation 3.2-4). Note that Equation (3.2-5) does not account for the total porosity ϕ , but for its part $(\theta_s - \theta_r)$ full of capillary water. This implies that Equation (3.2-5) is not differentiable for $h_k = h_{k,a}$ and $h_k = h_{k,r}$, unlike standard water retention functions. But it provides a better insight into the impact of the pore size distribution on the retention properties, as pointed out in the Results Section, later on.

Based on the fact that adsorptive water linearly decreases towards zero in semi log scale (Campbell & Shiozawa, 1992), Peters (2013) proposed an equation describing S_e^{ads} , that has been later replaced with a smoothed piecewise linear function proposed by Iden & Durner, (2014), as follows:

$$S_e^{ads}(h_k) = \frac{\theta^{ads}(h_k)}{\theta_r} = 1 + \left(\log_{10} \left(\frac{h_{k,a}}{h_0} \right) \right)^{-1} \left\{ \log_{10} \left(\frac{h_k}{h_{k,a}} \right) + b \ln \left[1 + e^{\log_{10} \left(\frac{h_{k,a}}{h_k} \right) / b} \right] \right\} \quad (3.2-6)$$

where b is a smoothing parameter that impacts $S_e^{ads}(h_k)$ near $h_k = h_{k,a}$ (see Iden & Durner, 2014 for more details), and h_0 is the suction [L] value (about 10^7 cm) related to totally dry conditions $\theta^{tot}(h_0) = 0$. In this work, $h_0 = 6.3 \times 10^6$ cm has been adopted as suggested by Peters (2013). The higher the value of b , the smoother the $S_e^{ads}(h_k)$ function, with a limitation that b should take a value between 0.1 and 0.3, as proposed by Iden & Durner (2014) based on a sensitivity analysis. They also proposed empirical expressions for determining b as function

of the parameters of van Genuchten, (1980) or Kosugi (1996)'s equations. Since Equation (3.2-5) is not differentiable for $h_k = h_{k,a}$, Equation (3.2-4) cannot be mathematically continuous regardless of b value. However, Equation (3.2-6), with a maximum value of $b = 0.3$, has been finally adopted to smooth θ^{tot} as much as possible in the zone around $h_k = h_{k,a}$, allowing better interpretation of measured data. Note that Equation (3.2-4) can be reduced to solely capillary model ($\theta^{tot} = \theta^{cap}$) if water is considered to be immobile for $\theta < \theta_r$ ($\theta^{ads} = \theta_r$ for every h_k).

Hydraulic conductivity

According to Peters (2013), the hydraulic conductivity K^{tot} along the whole suction range can be presented as the sum of two components K^{cap} and K^{film} , if isothermal vapor conductivity is neglected:

$$K^{tot} = K^{cap} + K^{film} = K_s^{cap} K_r^{cap} + K_s^{film} K_r^{film} \quad (3.2-7)$$

where K_s^{cap} and K_s^{film} are the saturated hydraulic conductivities [L/T] for capillary and adsorptive (film) water, respectively, while K_r^{cap} and K_r^{film} are the corresponding relative hydraulic conductivity functions [-], respectively. Note that K^{film} is several orders of magnitude lower than K^{cap} , and thus has a negligible influence on K^{tot} for $\theta > \theta_r$. If the film flow is ignored ($K^{film} = 0$), Equation (3.2-7) is reduced to a capillary hydraulic conductivity function.

As previously explained, the bulk hydraulic conductivity can be calculated by integrating the contributions of water fluxes through the saturated capillary tubes of different sizes that correspond to the actual water content or saturation degree. Based on the assumption that the water movement through straight capillary tubes follows Hagen-Poiseuille's law, and that exponent l can account for the tortuosity effect, a general analytical form of the relative hydraulic conductivity of capillary water has been given by Hoffmann-Riem et al. (1999):

$$K_r^{cap}(S_e^{cap}) = (S_e^{cap})^l \left(\frac{\int_0^{S_e^{cap}} h_k^{-k} dS_e^{cap}}{\int_0^1 h_k^{-k} dS_e^{cap}} \right)^\beta \quad (3.2-8)$$

where parameters l , k and β vary for different models. The commonly used Mualem (1976) model can be obtained for $k = 1$ and $\beta = 2$, while l remains a fitting parameter, as proposed by many authors (Yates et al., 1991; Schaap & Leij, 1999; Neto et al., 2011; Peters et al., 2011, among others). In this case, it is more convenient to integrate Equation (3.2-8) with respect to

h_k , which can be done by introducing the derivative of Equation (3.2-5) $\left(dS_e^{cap} = \frac{D_f - 3}{h_{k,a}(\theta_s - \theta_r)} \left(\frac{h_k}{h_{k,a}} \right)^{D_f - 4} dh_k \right)$ and by changing the boundaries of the integration with respect to the boundaries in Equation (3.2-5):

$$K_r^{cap}(h_k) = (S_e^{cap})^l \left(\frac{\int_{h_{k,r}}^{h_k} h_k^{D_f-5} dh_k}{\int_{h_{k,r}}^{h_{k,a}} h_k^{D_f-5} dh_k} \right)^2 \quad (3.2-9)$$

Finally, $K_r^{cap}(h_k)$ can be re-written as follows:

$$K_r^{cap}(h_k) = \begin{cases} 1, & h_k < h_{k,a} \\ \left(1 - \frac{1 - \left(\frac{h_k}{h_{k,a}}\right)^{D_f-3}}{\theta_s - \theta_r} \right)^l \left(\frac{\left(\frac{h_k}{h_{k,a}}\right)^{D_f-4} - \left(\frac{h_{k,r}}{h_{k,a}}\right)^{D_f-4}}{1 - \left(\frac{h_{k,r}}{h_{k,a}}\right)^{D_f-4}} \right)^2, & h_{k,a} \leq h_k \leq h_{k,r} \end{cases} \quad (3.2-10)$$

where the values of the expression in the second brackets is included between 0 and 1, null for $h_k = h_{k,r}$ and equal to 1 for $h_k = h_{k,a}$.

Tokunaga (2009) showed that the hydraulic conductivity of the film decreases almost linearly with increasing suction in log-log scale, with a slope $a = -1.5$. Based on that, Peters (2013) proposed a simple function describing the film flow:

$$K_r^{film}(S_e^{ads}) = \left(\frac{h_0}{h_{k,a}} \right)^{-1.5(1-S_e^{ads})} \quad (3.2-11)$$

Besides Peters (2013), Zhang (2011) also proposed an analytical function that depends on many physical constants and hence brings additional uncertainties into the calculation. This is why this function was not adopted in this work. Note that parameter a can deviate from -1.5 (Equation 3.2-11) since this value was derived from the case of smooth spherical grains. Some authors, such as Rudiyanto et al. (2015) included parameter a into the optimization process. In this work, $a = -1.5$ was adopted, as in Peters (2013) and Wang et al. (2016).

3.2.3. Results

The proposed model was validated with literature data for 10 different soils, presented in *Table 3.2-1*, that also provides for each soil the values of the 5 physically-based model parameters (θ_r , $h_{k,a}$, D_f , K_s^{film} and l), together with the squared correlation coefficient (R^2) used to rate the agreement between model and measurements. Among them, the Green wave coarse granular material (Stanić et al., 2019a) has a particular status. Indeed, it does not present any significant adsorption effect, but it is the only material for which the complete set of parameters needed is available, including the grain size distribution curve that has not been provided for the other soils.

Table 3.2-1. Measured (θ_s , K_s^{cap}) and determined / adjusted values (highlighted in grey) of the model parameters

| Soil | Reference | θ_s [-] | K_s^{cap} [cm/day] | D_f [-] | $h_{k,a}$ [cm] | θ_r [-] | K_s^{film} [cm/day] | l [-] | R^2 WRC | R^2 HCF |
|---------------------------------|--|----------------|-------------------------|-----------|-------------------|----------------|--------------------------|---------|--------------|--------------|
| Shonai sand | <i>Mehta et al. 1994</i> ¹ | 0.431 | 941.76 | 2.680 | 120.00 | 0.064 | 1.50E-02 | 1.10 | 0.98 | 0.80 |
| Rehovot sand | <i>Mualem 1976b</i> ¹ | 0.400 | 1100.00 | 2.725 | 120.00 | 0.021 | 4.50E-03 | 0.30 | 0.99 | 0.99 |
| Gilat loam | <i>Mualem 1976b</i> ¹ | 0.440 | 17.28 | 2.790 | 330.00 | 0.168 | 4.50E-02 | 1.00 | 0.99 | 0.97 |
| Pachappa loam | <i>Jackson et al., 1965</i> ¹ | 0.460 | 17.28 | 2.860 | 500.00 | 0.138 | 8.00E-02 | 1.20 | 0.99 | 0.98 |
| Pachappa fine sandy clay | <i>Mualem 1976b</i> ¹ | 0.330 | 12.10 | 2.873 | 500.00 | 0.111 | 2.00E-02 | 0.20 | 0.99 | 0.98 |
| Adelanto loam | <i>Jackson et al., 1965</i> ¹ | 0.430 | 3.89 | 2.905 | 1500.00 | 0.261 | 2.50E-02 | 0.30 | 0.99 | 1.00 |
| Sandy loam | <i>Pachepsky et al., 1984</i> ¹ | 0.425 | 7.78 | 2.930 | 180.00 | 0.091 | 8.00E-02 | -0.50 | 0.99 | 0.96 |
| GW substrate | <i>Stanic et al., 2019b</i> | 0.395 | 70.07 | 2.950 | 9.00 | 0.045 | 1.00E-01 | -1.35 | 0.99 | 1.00 |
| Okcheon 2 | <i>Oh et al., 2015</i> ² | 0.435 | 20.56 | 2.960 | 450.00 | 0.200 | 1.00E-01 | -1.35 | 0.99 | 0.99 |
| Seochang | <i>Oh et al., 2015</i> ² | 0.379 | 7.89 | 2.965 | 180.00 | 0.050 | 1.20E-01 | -1.30 | 0.96 | 0.99 |

¹ taken from Rudiyanto et al. (2015)

² taken from Oh et al. (2015), where θ_s is calculated based on the void ratio e [-] as $\theta_s = \varphi = \frac{1}{1+e}$

Figure 3.2-3 shows, for the Green Wave substrate the water retention (top graph) and the hydraulic conductivity function (bottom graph).

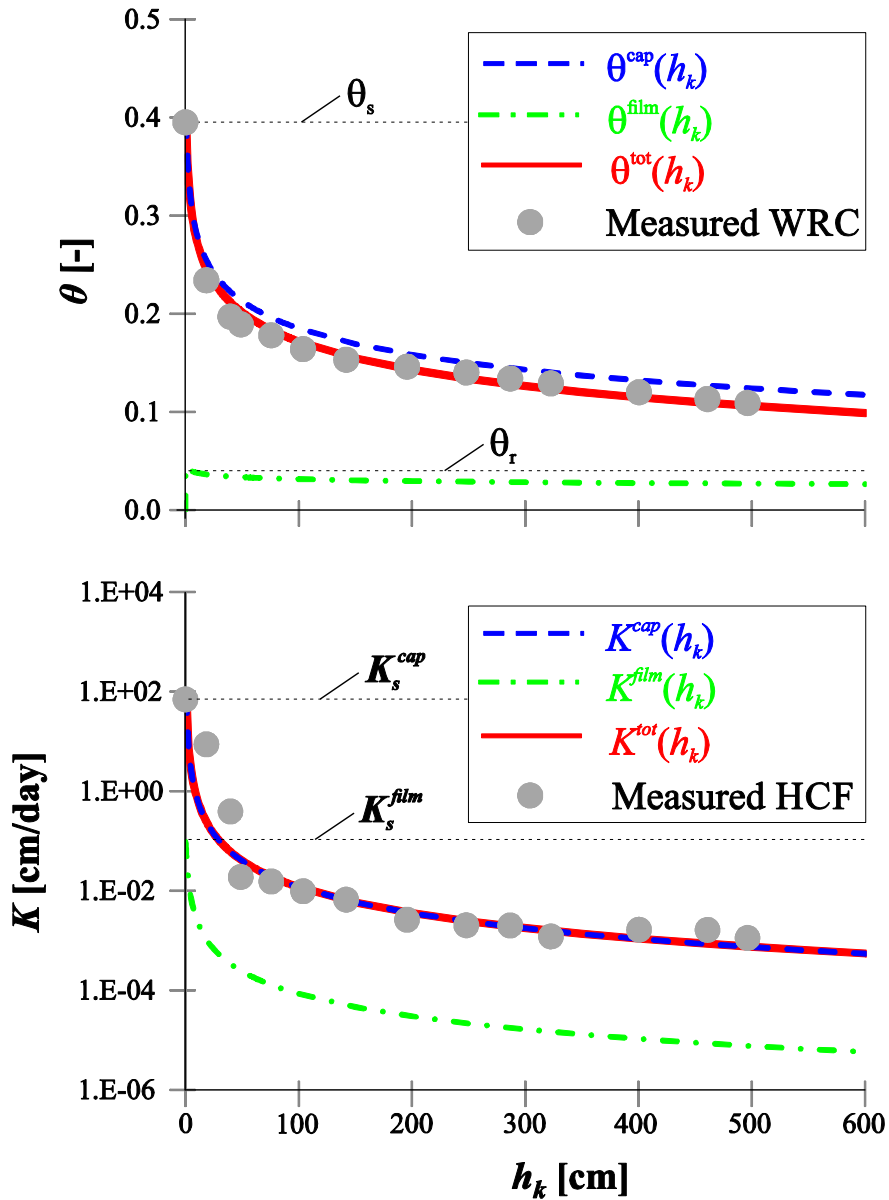


Figure 3.2-3. Comparison between the proposed model and the water retention (top graph) and hydraulic conductivity (bottom graph) experimental data taken from Stanić et al. (2019b)

The other soils, for which only the hydraulic properties data were available, are divided into two groups. Figure 3.2-4 compares, for 6 soils, the modeled water retention and hydraulic conductivity function with experimental data. The same is presented in Figure 3.2-5 for 3 soils where the measured hydraulic conductivity was related to changes in water content.

In Figure 3.2-3 to 3.2-5, computed θ^{tot} values (solid line - Equation 3.2-4) are compared with measured water retention data (filled dots). On the same Figures, calculated values of θ^{cap} (dashed line – Equation 3.2-5) and θ^{ads} (dash-dot line – Equation 3.2-6) are also presented. Similarly, computed K^{tot} values (solid line - Equation 3.2-7) are compared with measured hydraulic conductivity data (filled dots), together with the individual contributions of K^{cap} (dashed line) and K^{film} (dash-dot line) calculated by using Equations (3.2-10) and (3.2-11), respectively.

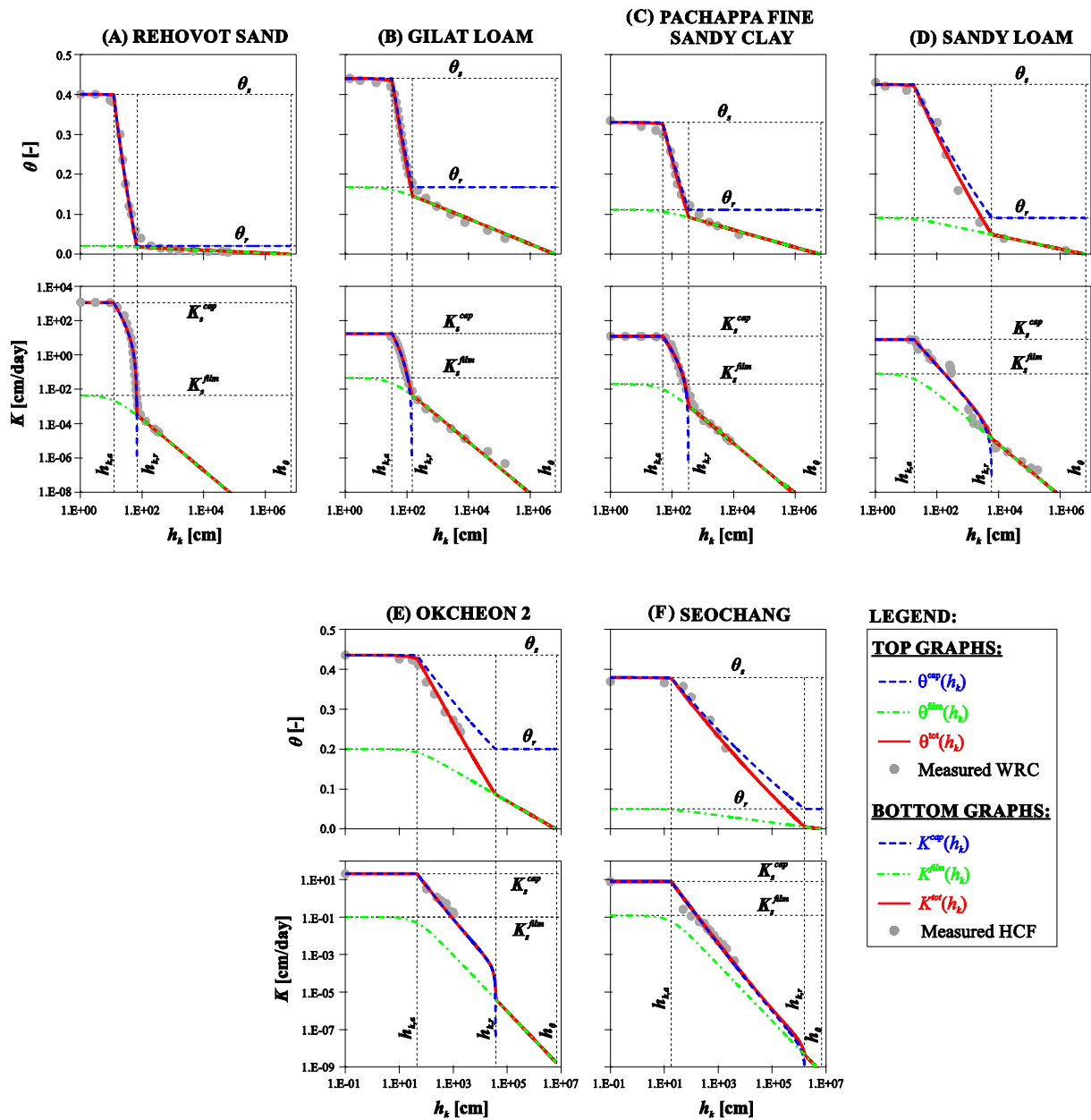


Figure 3.2-4. Comparison between the proposed model and 6 data sets from the literature. Top graphs present water retention data, bottom graphs hydraulic conductivity functions, all with respect to suction changes

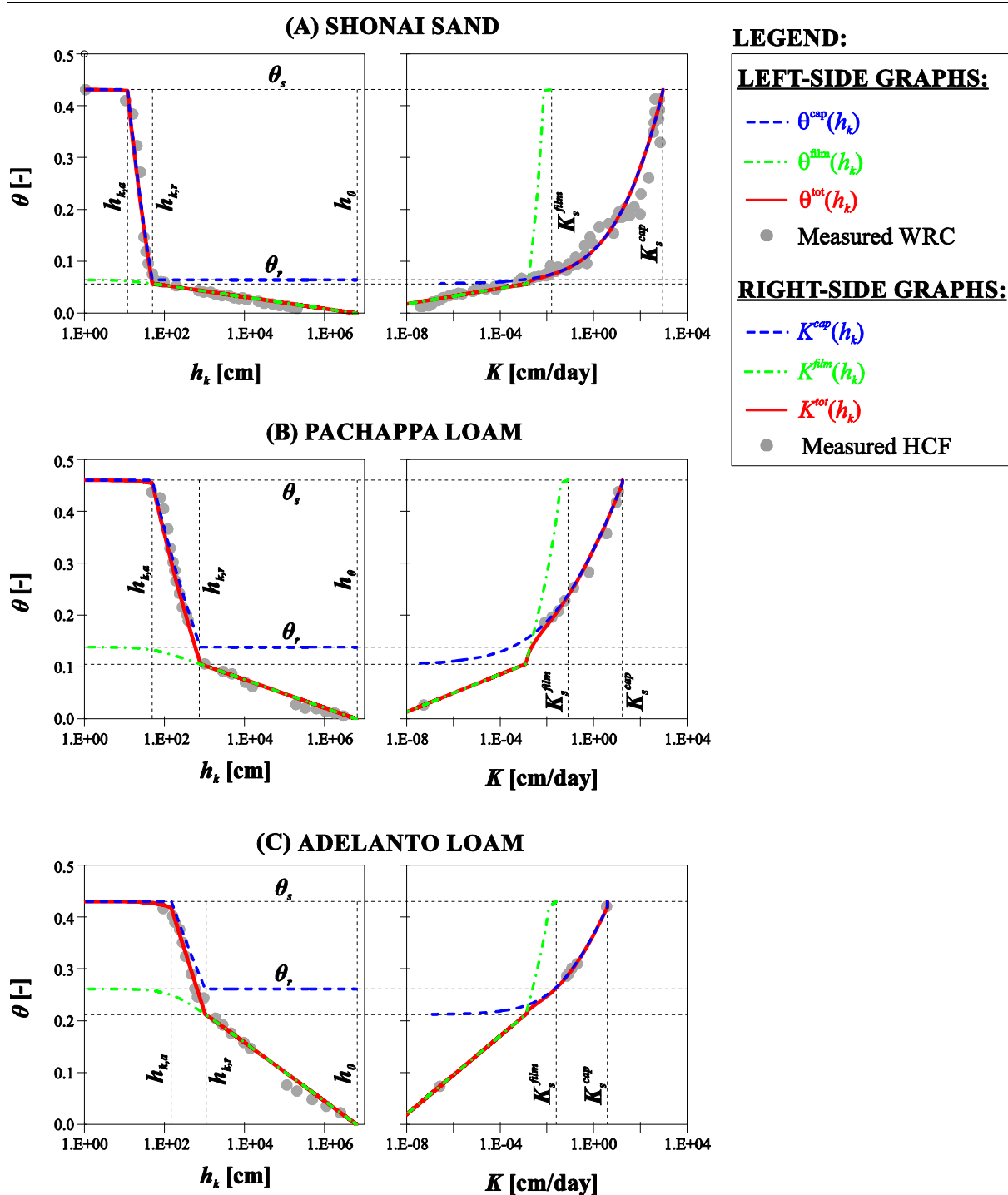


Figure 3.2-5. Comparison between the proposed model and 3 additional data sets from the literature. Left-side graphs deal with water retention data, whereas right-side graphs deal with hydraulic conductivity functions with respect to changes in water content

3.2.4. Discussion

Figure 3.2-3 to 3.2-5 show that, unsurprisingly, K^{film} has a negligible effect on K^{tot} in the lower range of suctions ($h_k < h_{k,r}$), since K_s^{film} is several orders of magnitude lower than K_s^{cap} .

For $h_k \geq h_{k,r}$, θ^{cap} becomes constant and equal to θ_r , resulting in having θ^{tot} only controlled by θ^{ads} , with no effect of K^{cap} on K^{tot} ($K^{tot} = K^{film}$).

The data of the Green Wave substrate (*Figure 3.2-3*) show the relation between the material GSD and its hydraulic properties in unsaturated state. Based on the best fitting parameters of the GSD model presented in Chapter 3.1 ($L = 60$ mm, $d_{g,min} \approx 1$ μ m, $\rho_{s,min}^{ind} = 1.55$, $C_1 = 2.25 \times$

10^{-2} and $\alpha = 1.6$), $c_{min} = c \left(\frac{L}{d_{g,min}} \right) = -C_1 \left(\frac{\ln(\rho_{s,min}^{ind})}{\frac{\ln(L/d_{g,min})}{C_1 \alpha'} + \frac{1}{\alpha}} \right)^{\alpha'}$ can be computed (value of the

exponent below the division sign in Equation 3.1-13 in Chapter 3.1), hence providing the value of $D_f = 3 - c_{min} = 2.950$. The D_f value is further used in Equations (3.2-5) and (3.2-10) for comparison with the water retention and transfer properties in *Figure 3.2-3*. The possibility to determine D_f from GSD data confirms the relevance of our physically based model. Note that the Green Wave experimental data are related solely to small suctions ($h_k < 5$ m), which it is not enough to estimate the rest of parameter values. Hence, in this case four parameters ($h_{k,a}$, $h_{k,r}$ (or θ_r), K_s^{film} and l) are manually adjusted to provide the best agreement between the model and the experimental points.

For the other soils, the GSD curves were not available, and hence D_f was manually adjusted based on water retention data. By means of these detailed experimental data that cover full range of matric suctions, it was possible to determine most of the remaining parameter values without using any optimization tools. The value of $h_{k,a}$ can be easily estimated from water retention data, since the water content for $h_k < h_{k,a}$ remains almost constant, while for $h_k > h_{k,a}$ it starts to decrease more significantly depending on the value of D_f (see Equation 3.2-5). Also, the value of θ_r can be computed from Equation (3.2-5) by estimating the residual $h_{k,r}$, after which water content starts to decrease less significantly ($S_e^{cap}(h_{k,r}) = 0$):

$$\theta_r = \theta_s - 1 + \left(\frac{h_{k,r}}{h_{k,a}} \right)^{D_f - 3} \quad (3.2-12)$$

Finally, K_s^{film} and l were adjusted based on the agreement between Equation (3.2-7) and the experimental hydraulic conductivity data. Parameter l affects the regression of K^{cap} together with D_f , in such a way that smaller l (including negative values), ensure less significant decrease of K^{cap} with suction increase, and vice versa. Also, the value of K_s^{film} only moves the K^{film} curve upwards or downwards, without affecting its regression (Equation 3.2-11). The values of l and K_s^{film} cannot be predefined or determined based on the water retention curve, which means that the hydraulic conductivity function cannot be reliably predicted without measurements, as already observed for any analytical hydraulic conductivity function. Unsurprisingly, the water retention curves appear to be steeper in the case of sands (*Figure 3.2-4A* and *Figure 3.2-5A*), which corresponds to lower D_f values and indicates that the sands tested are poorly graded, with a narrow range of pore sizes. This results in having the most significant change in water content and hydraulic conductivity over the smallest ratio of suctions ($h_{k,r} / h_{k,a}$). A lower ratio ($h_{k,r} / h_{k,a}$) in combination to a lower D_f value results in a lower θ_r (see Equation 13). This is characteristic of sands with a small percentage of fine particles and no adsorption properties, as confirmed by the results of *Figure 3.2-4A* and

Figure 3.2-5A, where θ^{tot} is almost equal to θ^{cap} for $h_k < h_{k,r}$. In this case, it is possible to totally separate capillary and adsorptive mechanisms, without affecting the parameter values. Thus, $\theta^{tot} = \theta^{cap}$ for $h_k < h_{k,r}$ and $\theta^{tot} = \theta^{ads}$ for $h_k \geq h_{k,r}$. Moreover, the difference between K_s^{cap} and K_s^{film} is the most significant for these two soils (around 5 orders of magnitude).

Compared to sands, higher values of D_f are used to describe the hydraulic properties of loams and clay soils (Figure 3.2-4B, C, D and Figure 3.2-5B, C). Larger θ_r values evidence the influence of adsorptive water. In the cases of Sandy loam (Figure 3.2-4D) and Adelanto loam (Figure 3.2-5C), θ^{cap} clearly deviates from θ^{tot} , even at lower suctions, which is directly related to the higher values of θ_r and D_f . This means that a water retention function accounting solely for capillarity ($\theta^{tot} = \theta^{cap}$) is not satisfactory. In this case, a smaller D_f value is necessary to obtain good agreement between θ^{cap} and the water retention data. Furthermore, the difference between K_s^{cap} and K_s^{film} is about 2 orders of magnitude lower than in the case of sands, confirming the stronger impact of adsorption mechanism. As commented before, the highest values of D_f are related to well graded granular materials with 5 to 15 % of fine particles ($< 75 \mu\text{m}$), presented in Figure 3.2-3 and Figure 3.2-4E, F. Again, significant deviation between θ^{ads} and θ^{tot} at low suctions is related to the combination of high D_f and θ_r values, as it is the case of Okcheon 2 and Seochang soils (Figure 3.2-4E and F, respectively). Also, the Green Wave substrate, Okcheon 2 and Seochang soils show less significant decrease in hydraulic conductivity with respect to suction increase, which is described by negative l values (see Equation 3.2-10). The values of l have been adjusted by respecting the criterion that K^{cap} needs to be a decreasing and concave function (Peters et al., 2011). Note that no measurements at high suctions were available for these three materials, so parameters calibration was done based on the available data range.

Most of the data presented here have already been compared with different published models (Peters (2013), Iden & Durner (2014), Rudiyanto et al. (2015), Wang et al. (2016)), with satisfactory agreements. However, usually more than 5 parameters, with some empirical ones, have to be considered in the optimization process. In our model, two out of five parameters (D_f and θ_r) can be derived from soil properties. Thus, the determination of the 3 remaining parameters can be achieved manually in a rather simpler way, due to their strong physical basis.

3.2.5. Conclusion

The main objective of this work was to develop a simple and robust physically-based model of the water retention and transfer properties of unsaturated soils over the entire range of matric suctions, including both capillary and adsorption effects. This was done by introducing new capillary-based water retention and hydraulic conductivity functions based on a fractal approach, and by adopting the Peters-Iden-Durner (PID) model to account for adsorption effects. Compared to available models, these functions depend on a smaller number of physically-based parameters, ensuring simple computations of their values by manual adjustment.

In Chapter 3.1 it has been shown that the grain size distribution of material with various grain densities can be described by using a continual set of fractal dimensions related to different

grain sizes. This multifractal approach has been reduced to the fractal-based one by using a fixed fractal dimension, related to the minimal grain diameter, for characterizing the pore size distribution. The water retention and hydraulic conductivity functions for capillary water were derived based on this pore size distribution through Young-Laplace's law and Mualem's model whereas adsorption effects were based on the PID model. Our model confirms that, in fine grained soils, both capillary and adsorptive water affect the hydraulic properties at water content higher than residual, whereas solely the effect of adsorptive water remains at smaller water content.

The model is based on 5 physically-based parameters: the air-entry value $h_{k,a}$, the residual water content θ_r , the fractal dimension of the grains D_f , the saturated film hydraulic conductivity K_s^{film} , and a parameter l accounting for the tortuosity and pore connectivity. The value of D_f can be computed based on the grain size distribution, while $h_{k,a}$ and θ_r can be determined from water retention data. Finally, as in other models, solely K_s^{film} and l values need to be adjusted, based on hydraulic conductivity data.

The model has been tested on published data sets of 10 different soils. The example of the Green Wave substrate confirms that good agreement with experimental data can be obtained when D_f is determined based on the grain size distribution. For the 9 remaining soils, the grain size distribution was not available, so D_f was adjusted based on water retention data. Smaller values of D_f appeared to be related to materials with more uniform grain and pore size distribution, such as sands, while higher D_f values were related to well-graded granular materials with non-negligible percentage of clay particles. Higher values of θ_r are also related to materials with significant amount of fine particles. In this case, the adsorptive water has a more significant impact, especially on the water retention properties. In terms of the hydraulic conductivity, particularly in the low suction range, the contribution of adsorptive water is always negligible comparing to capillary water, with lower values by two to five orders of magnitude. In the case of the well-graded granular materials with 5 to 15 % fines, the change in hydraulic conductivity with respect to suction is less significant, resulting in negative l values. It is thought that the strong physical basis of the model proposed here makes it convenient for water flow simulation through fine-grained soils along the full range of matric suctions.

3.2.6. References:

- Bird, N. R. A., E. Perrier, and M. Rieu. 2000. "The Water Retention Function for a Model of Soil Structure with Pore and Solid Fractal Distributions." *European Journal of Soil Science* 51 (1): 55–63. <https://doi.org/10.1046/j.1365-2389.2000.00278.x>.
- Brooks, R. H., and A. T. Corey. 1964. "Hydraulic Properties of Porous Media." *Hydrology Papers*, no. 3: 1–27.
- Campbell, G. S., and S. Shiozawa. 1992. "Prediction of Hydraulic Properties of Soils Using Particle-Size Distribution and Bulk Density Data." In *Proceedings of the International Workshop on Indirect Methods for Estimating the Hydraulic Properties of Unsaturated Soil*, 317–328.

-
- Fredlund, D. G., and A. Xing. 1994. "Equations for the Soil-Water Characteristic Curve." *Canadian Geotechnical Journal* 31: 521–32.
- Genuchten, M. Th. van. 1980. "A Closed-Form Equation for Predicting the Hydraulic Conductivity of Unsaturated Soils." *Soil Science Society of America Journal* 44 (5): 892–98. <https://doi.org/10.2136/sssaj1980.%0A03615995004400050002x>.
- Ghanbarian-Alavijeh, B., H. Millán, and G. Huang. 2011. "A Review of Fractal, Prefractal and Pore-Solid-Fractal Models for Parameterizing the Soil Water Retention Curve." *Canadian Journal of Soil Science* 91 (1): 1–14. <https://doi.org/10.4141/cjss10008>.
- Hoffmann-Riem, H., M. Th. van Genuchten, and H. Flühler. 1999. "A General Model for the Hydraulic Conductivity of Unsaturated Soils." In *Proceedings of the International Workshop on Characterization and Measurement of the Hydraulic Properties of Unsaturated Porous Media*, 31–42.
- Iden, S. C., and W. Durner. 2014. "Comment on "Simple Consistent Models for Water Retention and Hydraulic Conductivity in the Complete Moisture Range" by A. Peters." *Water Resources Research* 50 (1): 7530–34. <https://doi.org/10.1002/2014WR015937>.Received.
- Kosugi, K. 1996. "Lognormal Distribution Model for Unsaturated Soil Hydraulic Properties." *Water Resources Research* 32 (9): 2697–2703.
- Lenormand, R. 1990. "Liquids in Porous Media." *J. Phys.: Condens. Matter* 2 79.
- Li, Y., and N. C. Wardlaw. 1986. "Mechanisms of Nonwetting Phase Trapping during Imbibition at Slow Rates." *Journal of Colloid and Interface Science* 109 (2): 473–86.
- Lu, N., and C. Zhang. 2019. "Soil Sorptive Potential : Concept, Theory, and Verification." *J. Geotech. Geoenviron. Eng.* 145 (4): 1–13. [https://doi.org/10.1061/\(ASCE\)GT.1943-5606.0002025](https://doi.org/10.1061/(ASCE)GT.1943-5606.0002025).
- Mualem, Y. 1976. "A New Model for Predicting the Hydraulic Conductivity of Unsaturated Porous Media." *Water Resources Research* 12 (3): 513–22. <https://doi.org/10.1029/WR012i003p00513>.
- Neto, D. D., Q. J. van Lier, M. Th. van Genuchten, K. Reichardt, K. Metselaar, and D. R. Nielsen. 2011. "Alternative Analytical Expressions for the General van Genuchten – Mualem and van Genuchten – Burdine Hydraulic Conductivity Models." *Vadose Zone Journal* 10: 618–23. <https://doi.org/10.2136/vzj2009.0191>.Received.
- Oh, S., Y. K. Kim, and J. -W. Kim. 2015. "A Modified van Genuchten-Mualem Model of Hydraulic Conductivity in Korean Residual Soils." *Water* 7: 5487–5502. <https://doi.org/10.3390/w7105487>.
- Perrier, E., N. Bird, and M. Rieu. 1999. "Generalizing the Fractal Model of Soil Structure: The Pore-Solid Fractal Approach." *Developments in Soil Science* 27 (C): 47–74. [https://doi.org/10.1016/S0166-2481\(00\)80005-7](https://doi.org/10.1016/S0166-2481(00)80005-7).
- Peters, A. 2013. "Simple Consistent Models for Water Retention and Hydraulic Conductivity in the Complete Moisture Range." *Water Resources Research* 49 (April): 6765–80. <https://doi.org/10.1002/wrcr.20548>.
- Peters, A., W. Durner, and G. Wessolek. 2011. "Consistent Parameter Constraints for Soil Hydraulic Functions." *Advances in Water Resources* 34 (10): 1352–65. <https://doi.org/10.1016/j.advwatres.2011.07.006>.
- Rudiyanto, M. Sakai, M. Th. van Genuchten, A. A. Alazba, B. I. Setiawan, and B. Minasny.
-

-
2015. "A Complete Soil Hydraulic Model Accounting for Capillary and Adsorptive Water Retention, Capillary and Film Conductivity, and Hysteresis." *Water Resources Research* 51: 1–16. <https://doi.org/10.1002/2015WR017703>.Received.
- Russell, A. R., and O. Buzzi. 2012. "A Fractal Basis for Soil-Water Characteristics Curves with Hydraulic Hysteresis." *Géotechnique* 62 (3): 269–74. <https://doi.org/http://dx.doi.org/10.1680/geot.10.P.119>.
- Schaap, M. G., and F. J. Leij. 1999. "Improved Prediction of Unsaturated Hydraulic Conductivity with the Mualem-van Genuchten Model." *Soil Science Society of America Journal* 64: 843–51.
- Stanić, F., Y.-J. Cui, P. Delage, E. De Laure, P.-A. Versini, D. Schertzer, and I. Tchiguirinskaia. 2019a. "A Device for the Simultaneous Determination of the Water Retention Properties and the Hydraulic Conductivity Function of an Unsaturated Coarse Material ; Application to a Green- Roof Volcanic Substrate." *Geotechnical Testing Journal*. <https://doi.org/10.1520/GTJ20170443>.
- Stanić, F., P. Delage, Y. -J. Cui, E. De Laure, P. -A. Versini, D. Schertzer, and I. Tchiguirinskaia. 2019b. "Two Improvements to Gardner’s Method of Measuring the Hydraulic Conductivity of Non-saturated Media: Accounting for Impedance Effects and Non-constant Imposed Suction Increment." *Water Resources Research* 56: 1–15. <https://doi.org/10.1029/2019WR026098>.
- Tokunaga, T. K. 2009. "Hydraulic Properties of Adsorbed Water Films in Unsaturated Porous Media." *Water Resources Research* 45 (March): 1–9. <https://doi.org/10.1029/2009WR007734>.
- Tuller, M., and D. Or. 2001. "Hydraulic Conductivity of Variably Saturated Porous Media : Film and Corner Flow in Angular Pore Space." *Water Resources Research* 37 (5): 1257–76.
- Wang, Y., J. Ma, and H. Guan. 2016. "A Mathematically Continuous Model for Describing the Hydraulic Properties of Unsaturated Porous Media over the Entire Range of Matric Suctions." *Journal of Hydrology* 541 (July): 873–88. <https://doi.org/10.1016/j.jhydrol.2016.07.046>.
- Wang, Y., J. Ma, Y. Zhang, M. Zhao, and W. M. Edmunds. 2013. "A New Theoretical Model Accounting for Film Flow in Unsaturated Porous Media." *Water Resources Research* 49 (February): 5021–28. <https://doi.org/10.1002/wrcr.20390>.
- Xu, Y. 2004. "Calculation of Unsaturated Hydraulic Conductivity Using a Fractal Model for the Pore-Size Distribution." *Computers and Geotechnics* 31: 549–57. <https://doi.org/10.1016/j.compgeo.2004.07.003>.
- Yang, H., A. Khoshghalb, and A. R. Russell. 2014. "Fractal-Based Estimation of Hydraulic Conductivity from Soil – Water Characteristic Curves Considering Hysteresis." *Géotechnique Letters* 4: 1–10. <https://doi.org/http://dx.doi.org/10.1680/geolett.13.00071>.
- Yates, S. R., A. W. Warrick, and F. J. Leij. 1991. "Analysis of Measured, Predicted, and Estimated Hydraulic Conductivity Using the RETC Computer Program." *Soil Science Society of America Journal* 56: 347–54.
- Zhang, C., and N. Lu. 2019. "Unitary Definition of Matric Suction." *J. Geotech. Geoenviron. Eng.* 145 (2): 1. [https://doi.org/10.1061/\(ASCE\)GT.1943-5606.0002004](https://doi.org/10.1061/(ASCE)GT.1943-5606.0002004).
- . 2020. "Soil Sorptive Potential : Its Determination and Predicting Soil Water Density." *J. Geotech. Geoenviron. Eng.* 146 (1): 1–10.
-

[https://doi.org/10.1061/\(ASCE\)GT.1943-5606.0002188](https://doi.org/10.1061/(ASCE)GT.1943-5606.0002188).

Zhang, Z. F. 2011. "Soil Water Retention and Relative Permeability for Conditions from Oven-Dry to Full Saturation." *Vadose Zone Journal* 10: 1299–1308.
<https://doi.org/10.2136/vzj2011.0019>.

4. In situ investigation carried out on Green Wave

For analyzing performances of Green Wave at roof scale, it was necessary to install detailed monitoring system that covers three water balance components: rainfall intensity, change of water content, and drained discharge. These data are multifunctional, since they can be used for detailed investigation of green roofs from multiple aspects, going beyond the standard investigation of rainfall-runoff measurements.

In Chapter 4.1 the emphasis is put on different techniques used for measuring three mentioned water balance components. For measuring rainfall rate, an optical disdrometer is used, while the wireless network of 32 TDR sensors is spread over a part of Green Wave for monitoring the change of water content at different locations along the roof inclination. Drained discharge is monitored by means of ultrasonic displacement sensors that are installed inside the sewer pipe and in the storage unit that collects water drained from one part of Green Wave. Based on the water level change inside the pipe it is possible to calculate flow using Manning's equation, thanks to the reasonably uniform flow secured, while a more reliable method is the one based on the change of water level in the storage unit. For verifying the data collected, a 3 months long continuous time series of monitored data are presented.

In order to assess the behaviour of Green Wave beyond the standard investigation of the cumulative quantities of rainfall and drained discharge (rainfall-runoff coefficient), the temporal variabilities of the three measured water balance components are analysed in Chapter 4.2 by means of UM framework. This approach has been applied on the data monitored during three characteristic rainfall events, and results confirmed the ability of the substrate layer to provide mitigated fluctuations in the drainage network compared to those coming from the rainfall. Furthermore, this kind of analysis appeared as convenient for verifying the impact of roof inclination on the water movement in lateral direction, showing that the infiltration is dominantly vertical and that slope does not affect the outflow drained. However, it seems that the roof inclination impacts redistribution of the retained water in the downstream direction during dry periods, which is the reason why after the rainfall higher water contents can be observed at slope bottom.

4.1. Measurement of the water balance components of a large green roof in Greater Paris Area

(Published in *Earth System Science Data*, DOI: 10.5194/essd-12-1025-2020)

4.1.1. Introduction

For a green roof, the water balance during a rainfall event can be reduced to 3 components (see Equation 4.1-1), as evapotranspiration can be neglected:

$$IN = OUT + \Delta W \quad (4.1-1)$$

Where IN is the precipitation, OUT the discharge flowing out of the structure, and ΔW the variation of water stored in the substrate conducting both retention and detention properties. All quantities are expressed in $[m^3]$.

Many experimental set-up have been implemented to monitor, assess and understand the hydrological behavior of green roofs (see Berndtsson (2010) for a review). Most of them were conducted on small green roof modules or plots (Getter et al., 2007; Berretta et al., 2014; Locatelli et al., 2014; Li & Babcock, 2015; Poë et al., 2015; Stovin et al., 2015; Wong & Jim, 2015; Zhang et al., 2015; do Nascimento et al., 2018) characterized by an area ranging 0.5 to 3 m^2 . These modular structures make possible the modification of green roof configuration and study of the effects of substrate (depth and nature), vegetation type, slope, or climate conditions on their performances. Some of them were also monitored in controlled conditions (Ouldboukhitine et al., 2011; Poë et al., 2015) to assess the respective impacts of temperature, irrigation, and light on green roof behavior for instance.

In addition, few studies were conducted at full-scale green roofs. Indeed, such large infrastructures are harder to monitor, as this operation was not generally planned during their construction. For instance, once built, electric connection is rarely compatible with the conservation of the roof sealing. To the knowledge of the authors, only the following works can be mentioned.

Palla et al. (2009) studied an instrumented portion (170 m^2) of a green roof in Genoa (Italy) under Mediterranean climate. This pilot site was equipped to monitor the different components of the water balance with: a meteorological station for rainfall, several Time Domain Reflectometry probes installed horizontally along a vertical profile for retention in the substrate, and a triangular weir and a tipping bucket devices to follow the outflowing discharge.

Hakimdavar et al. (2016) used the data collected on three full-scale extensive green roofs in New York City (USA) to validate a modeling approach based on the Soil Water Apportioning Method (SWAM). Under a humid continental climate, these monitored drainage areas were comprised between 310 and 940 m^2 . The three main components of the water balance were measured: rainfall with a weather station, water content with soil moisture and water content reflectometer sensors, and discharge with a custom designed weir placed in the drain of the

green roof.

Fassman-Beck et al. (2013) assessed several green roofs in Auckland (New Zealand) under sub-tropical climate. Their areas were comprised between 17 and 171 m². As the experimental setup was focused on rainfall-runoff relationship, only these components were measured: rainfall with a tipping bucket rain gauge and discharge (deduced from water level) from a water pressure transducer and a custom-designed orifice restricted device.

Cipolla et al. (2016) analyzed runoff from a 60 m² extent green roof in Bologna (Italy) characterized by a humid temperate sub-continental climate. Continuous weather data and runoff were especially monitored for modeling development. Runoff was estimated by using an in-pipe flow meters consisting of a runoff chamber with an outlet weir and an ultrasonic sensor (to detect water level). The site was also equipped with a weather station measuring several meteorological variables (rainfall, wind speed, wind direction, relative humidity, atmospheric temperature, etc.).

Although these works were focused on the hydrological behavior of green roofs, few of them have actually monitored the 3 components of the water balance. Rainfall and discharge were generally considered as sufficient to assess their performances. Some additional studies can also be mentioned, but as they were focused on other topics (evapotranspiration processes Feng et al., 2018, or water quality Buffam et al., 2016), only one component on the water balance was assessed.

The full-scale monitoring experiments mentioned above also suffer from two limitations. First, they are still dedicated to rather small green roof areas. As the hydrological performance of a green roof is influenced by the size of the plot (water detention depends on water routing in the structure for instance), larger infrastructure should be studied. Second, very few measurements are performed (usually only one!) to assess water content on the whole vegetated surface. Indeed, green roof substrates –which are usually largely composed of mineral components – are very heterogeneous, causing variability in their infiltration and retention capacities. Therefore, large-scale monitoring set-ups able to capture this heterogeneity are required to better understand green roof hydrological behavior and to study the space-time variability of the involved processes.

Based on these considerations, this paper aims to present and make available the water balance data collected on Green Wave in order to study its hydrological behavior and its ability to be used as stormwater management tool. The monitoring set-up has been particularly tailored to take into account the space-time variability of the water balance components.

4.1.2. Materials and method

The Blue Green Wave

From a technical point of view, Green Wave is covered by two types of vegetation: green grass that represents the large majority of its area and a mix of perennial planting, grasses and bulbous (see *Figure 4.1-1*). They are based on a substrate layer of about 20 cm depth, a filter

layer made of synthetic fiber, and a drainage layer made of expanded polystyrene securing free drainage condition. The vertical profile of the structure is presented in *Figure 4.1-2*. The substrate is composed of volcanic soil completed by organic matter and is characterized by a total porosity of 40 % and a density of 1.42 g/cm^3 (see Chapter 2.1 for a detailed description).

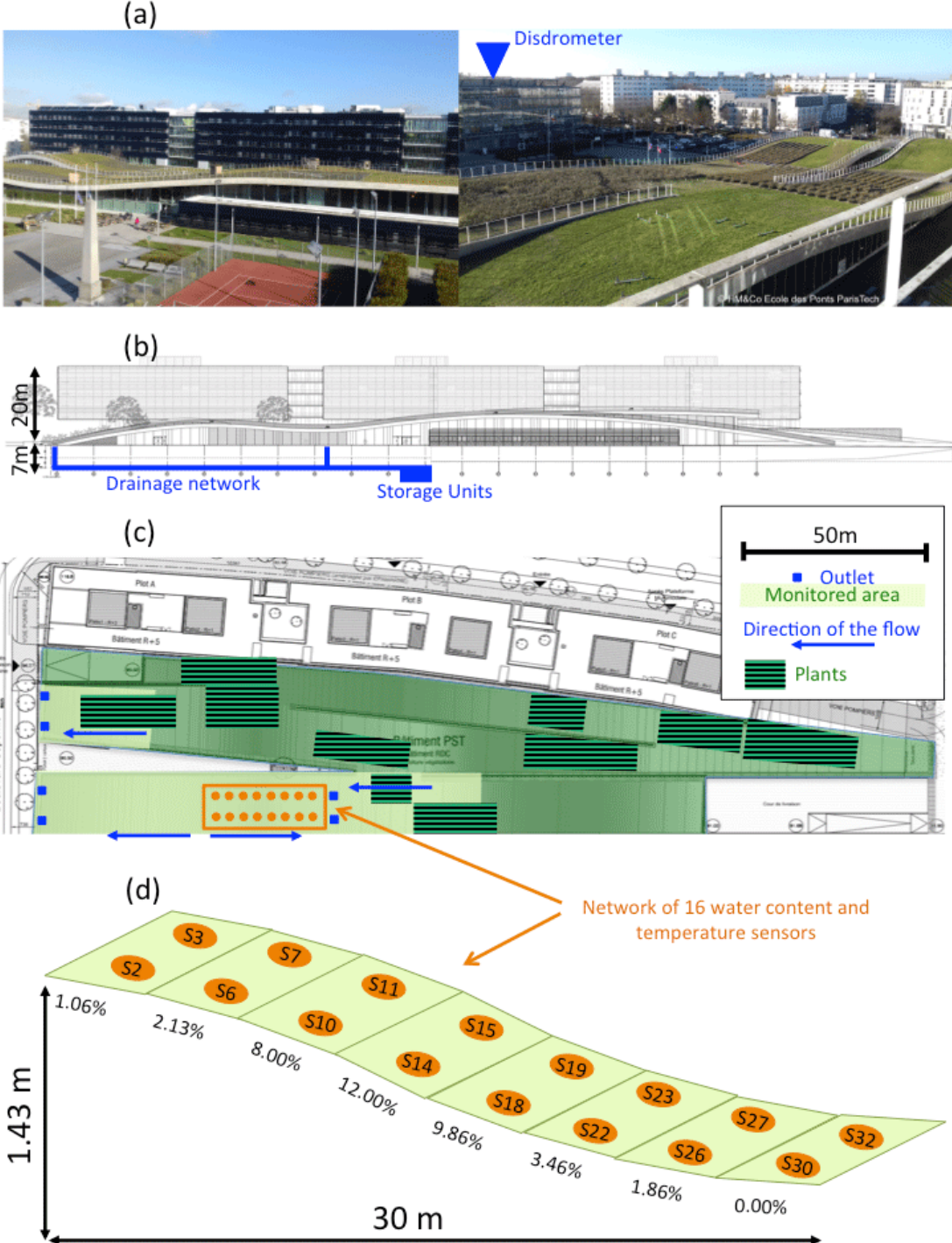


Figure 4.1-1. The Blue Green Wave monitoring site of ENPC: (a) pictures, (b) vertical representation and flow path lengths, (c) aerial representation showing the monitored area, and (d) profile of the section where the water content sensors were implemented indicating the slopes

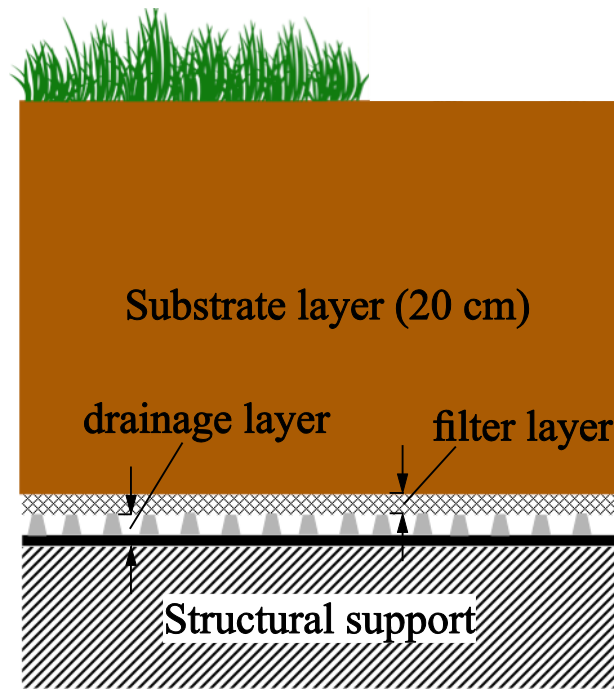


Figure 4.1-2. Vertical profile of the Green Wave structure

From a hydrological point of view, Green Wave is connected to three storage units that collect rainwater coming from the roof (with pipes) but also from several impervious parts around the greened building. One of the storage units is preceded by a smaller unit dedicated to irrigation. The water is then routed to a large retention basin to collect excess volumes of water during a rainfall event before being routed to the rainwater network. This retention basin has been designed (and oversized) as it was considered that the green roof (representing 50% of the total contributive area) was totally impervious without any retention capacity. Until now in France, there is no rule or guideline devoted to retention basin sizing and taking into account the retention properties of green areas. That is why the follow-up of such infrastructure is particularly important to develop new guidelines or legislations. For this purpose, the 3 components of the water balance have been monitored on Green Wave. The implemented set-up is described in the following.

Devices

Rainfall measurement

Local rainfall is analysed with the help of an optical disdrometer Campbell Scientific® PWS100. This device is made of two receivers, which are not aligned with a transmitter generating four laser sheets. By analyzing the signals received from the light refracted by each drop passing through the 40 cm² sampling area, their size and velocity are estimated. A rain rate can then be derived. Disdrometers are now considered as a reliable rainfall measurement instrument (Frasson et al., 2011; Gires et al., 2015; Thurai et al., 2011). The device is installed since September 2013 on the roof of the Ecole des Ponts ParisTech building (see *Figure 4.1-1*). This disdrometer and its corresponding data have already been presented in details in a

previous data paper (Gires et al., 2018) that summarizes a measurement campaign that took place in January-February 2016. Here, the rainfall data provided by this disdrometer and characterized by a time step of 30 seconds is used.

Water content measurement

Estimation of soil moisture represents a difficult challenge, as it deals with a highly spatially and temporally variable process (Lakshmi et al., 2003), essentially due to soil type and depth. Hence, suitable systems are required to properly assess soil moisture. Nowadays a large number of sensors based on different methods are available for this purpose (Jackson et al., 2008). Among them, indirect methods based on electromagnetic (EM) principles have gained wide acceptance over the last decades. They have the advantage to deliver fast, in-situ, non-destructive and reliable measurements with acceptable precision (Stacheder et al., 2009).

Here Time Domain Reflectometry technique (TDR also known as capacitance) has been selected. It is an EM moisture measurement that determines an electrical property called electrical conductivity or dielectric constant (k_a). It is based on the interaction of an EM field and the water by using capacitance/frequency domain technology (Stacheder et al., 2009). The TDR sensor measures the propagation time of an EM pulse, generated by a pulse generator and containing a broad range of different measurement frequencies. The electrical pulse is applied to the waveguides (traditionally a pair of parallel metallic rods) inserted in the soil. The incident EM travels across the length of the waveguides and then is reflected back when it reaches the end of the waveguides. The travel time required for the pulse to reach the end of the waveguides and come back depends on the dielectric constant of the soil.

$$k_a = \left(\frac{c_{EM} \times \Delta t}{2 \times L_{ep}} \right) \quad (4.1-2)$$

where k_a is the bulk soil dielectric permittivity [-], L_{ep} the effective probe length [m] Δt is the two-way travel time along the probe (s), and c_{EM} the velocity of EM wave in free space ($c_{EM} = 2.298 \times 10^8$ m/s).

Based on k_a it is possible to estimate a volumetric water content θ [-] of the soil. The usual relationship between the two is known as Topp's equation (Topp et al., 1980), adapted to a homogeneous conventional soil:

$$\theta = -5.3 \times 10^{-2} + 2.92 \times 10^{-2} k_a - 5.5 \times 10^{-4} k_a^2 + 4.3 \times 10^{-6} k_a^3 \quad (4.1-3)$$

However, this expression is found inappropriate for applying on an unconventional volcanic material such as that placed on Green Wave. In order to calibrate TDR sensors specifically for the Green Wave substrate, the correlation between θ and k_a has been experimentally determined in laboratory conditions. By controlling different water quantities in various cylindrical specimens of known dimensions, it is possible to calculate corresponding θ values, while values of k_a are measured using a TDR sensor. The results obtained are presented in *Figure 4.1-3*, where experimentally determined (k_a , θ) values (circles in *Figure 4.1-3*) are compared with Topp equation (Equation 4.1-3). Experimental results show

significant deviation from Equation (4.1-3), confirming that Topp equation is inappropriate for this kind of material. Since the relationship between k_a and volumetric water content is of interest, it is clear that the compaction level of the soil, and hence the soil bulk density (porosity), strongly affects the correlation between the two. This has been confirmed by repeating the calibration procedure for two additional levels of compaction obtained by applying vibrations during 1 min (squares) and 2 min (triangles). Having on mind the results presented in *Figure 4.1-3*, and the fact that bulk densities at different locations in situ are unknown, it was concluded that transformation from k_a into θ brings a lot of uncertainties, and thus the original k_a data are further considered as an indicator of water content.

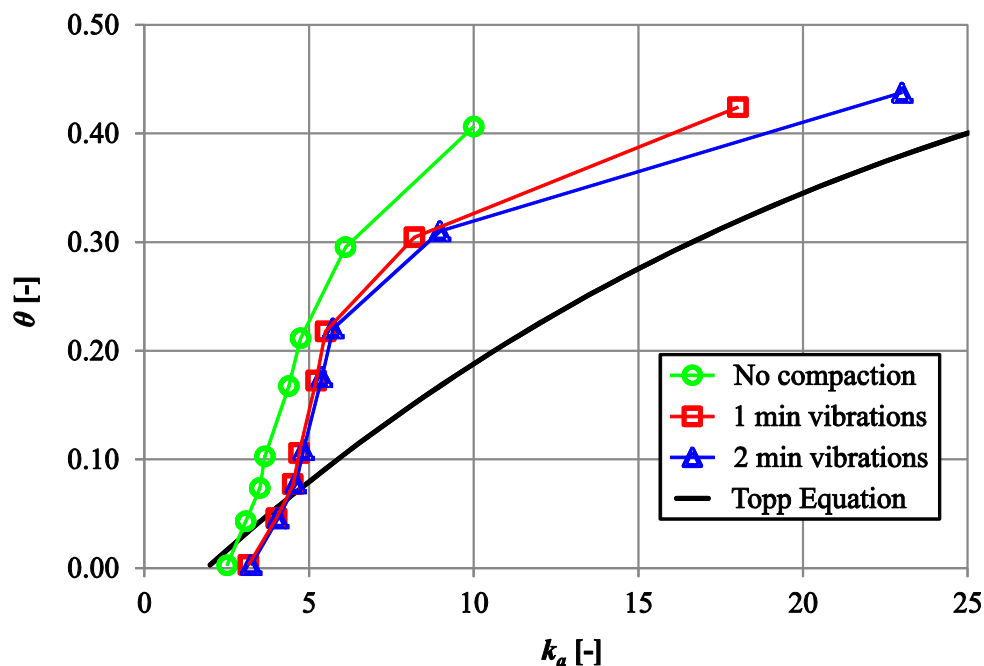


Figure 4.1-3. Comparison between Topp Equation (black solid line) and experimentally determined correlations between k_a and θ , for the Green Wave substrate, for different levels of compaction obtained in laboratory conditions

An ubiquitous wireless TDR sensors network has been implemented on the ENPC Blue Green Wave to measure both water content indicator and temperature. For this purpose 32 CWS665 wireless TDR sensors (produced by Campbell Scientific[®]) were initially installed. The data were collected by 4 CWB100 wireless bases, able to store each the data of 8 sensors. Then the data was transferred to a data-logger CR6 from Campbell Scientific[®]. The initial selected time step was 1 minute. It appeared that this first configuration was responsible of many gaps in the time series due to interferences between the different TDR sensors and the bases. To avoid this problem, only 16 TDR sensors were used, all of them connected to the same CWB100 base. For this same reason of possible interferences between the sensors, the time interval has been enlarged to 4 minutes. Indeed, it is recommended to let 15 seconds by sensor to ensure its connection to the base. The final network aimed to capture the space-time variability of water content in a heterogeneous soil as the Green Wave substrate. It was particularly adapted to assess the influence of the slope on infiltration and evapotranspiration processes.

Discharge measurement

Direct discharge measures are difficult to obtain in drainage pipes. For this reason, indirect measures using water level measurements are usually carried out. Here, water level inside the pipes was measured by a UM18 ultrasonic sensor (SICK, 2018) produced by SICK®. This sensor has been especially developed to perform non-contact distance measurement or detection of objects. The sensor head emits an ultrasonic wave and receives the wave reflected back from the target. Ultrasonic sensors measure the distance to the target by measuring the time between the emission and reception. Implemented face to the water surface, it also measures the variation of the water level. The UM18 sensor is characterized by a nominal range of 250 mm, and an accuracy of 1% on this measurement range.

One UM18 sensor has been implemented inside a pipe located in the garage in the building basement (see *Figure 4.1-1*). With a diameter of 300 mm, this pipe collects the water coming from a large part of Green Wave (approximately 1143 m²). A standard 4–20 mA current loop is used to monitor or control remotely these analogue sensors. The current is then transformed in voltage by a resistance of 100 Ω. The resulting transmitted signal also ranges 400-2000 mV. In order to translate the electric signal in water level values, the following relationship has been applied:

$$H_0 = (U - 460) \times \frac{250}{1600} \quad (4.1-4)$$

where H_0 is the water level in [mm], U the measured voltage in [mV], 460 represents the offset, 250 the modified nominal range in [mm], 1600 the nominal range in [mV].

The water level is then transformed into discharge by means of Manning-Strickler equation (Equation 4.1-5). This formula is usually used to estimate the average velocity (and discharge) of water flowing in an open channel. It is commonly applied in sewer design containing circular pipes.

$$Q_0 = v \times A_W = \kappa \times A_W \times R^{2/3} \times I_p^{1/2} \quad (4.1-5)$$

where v is the average water velocity [m.s⁻¹], κ the friction coefficient [m^{1/3}s⁻¹] adopted to 85 for cast iron pipe, A_W is the wet surface [m²], R the hydraulic radius [m], and I_p the inclination of the pipe [m/m]. R and A_W are directly linked to the water level:

$$R = \frac{A_W}{r \times \delta} \quad (4.1-6)$$

$$A_W = \frac{(\delta - \sin(\delta)) \times r^2}{2} \quad (4.1-7)$$

$$\delta = 2 \times \arccos\left(\frac{r - H_0}{r}\right) \quad (4.1-8)$$

where δ is the central angle for partially water filled pipe [rad]. Note that Equation (4.1-5) is valid for uniform flow which is assumed to occur on the location where UM18 sensor is installed. Having on mind the sufficiently high value of $I_p = 1$ %, the location is chosen to be

far enough from any upstream obstacle (elbow curve in this case), but also to secure long enough and aligned downstream section that prevents from propagation of any disturbance in upstream direction. In order to check the reliability of assumptions made, discharge calculated by means of Equation (4.1-5) is compared with that calculated based on the measurements of water level and water velocity, for one rainfall event occurred between 8th and 10th of November 2016 (see *Figure 4.1-4*). In this case, the average water velocity has been measured with Doppler Flow Meter (Greyline DFM 5.1) that was temporary installed on the exterior bottom face of the pipe. Agreement between the two types of discharge data is reasonably good (see *Figure 4.1-4*), having on mind that the comparison is relevant mostly for peak values when water velocity measurements are reliable.

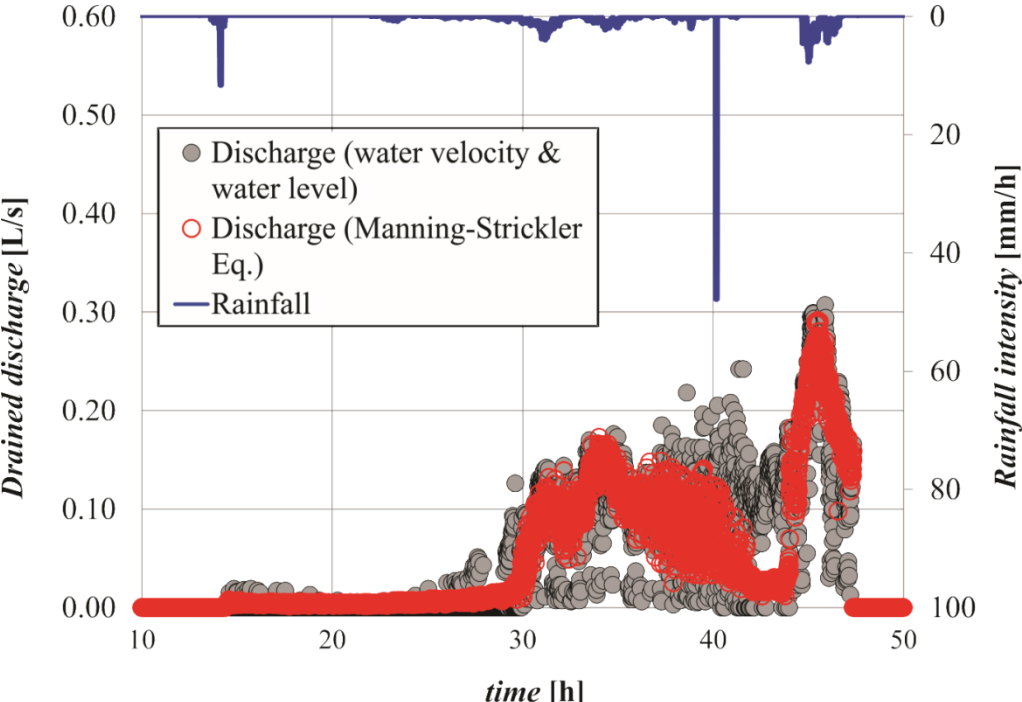


Figure 4.1-4. Validation of the application of Manning-Strickler equation for estimating drained discharge based on the measurements of water level inside the drainage pipe

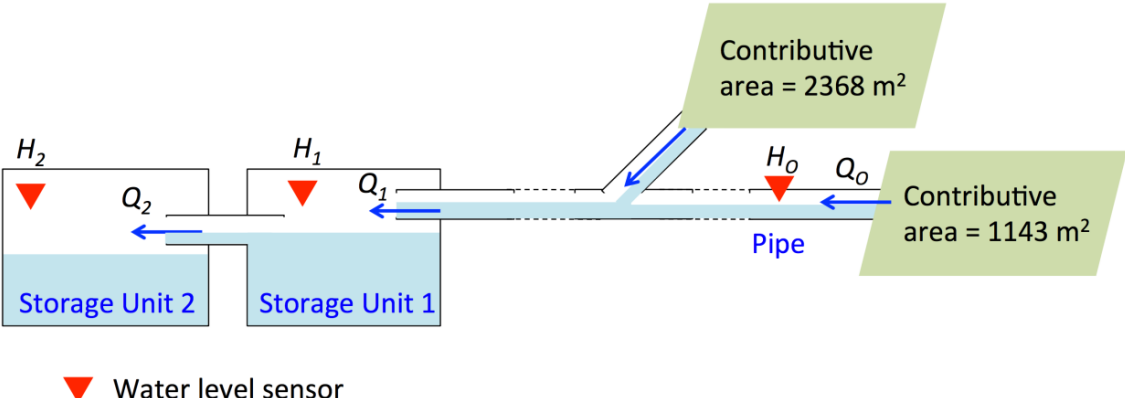


Figure 4.1-5. Location of the water level sensors in the stormwater network

Two additional UM18 sensors have been implemented in the two consecutive storage units collecting the rainwater drained by a large contributive area of 3511 m², and including the previous monitored area (*Figure 4.1-5*). The first storage unit is a rainwater tank (characterized by a floor area of 32.2 m²) devoted to irrigation. Filled most of the time, the excess water is routed by a pipe toward the second unit (floor area of 22.5 m²). A similar relationship to Equation 4.1-4 between the voltage measurement and the water level has been adjusted for both units:

$$H_i = (U - 0.38) \times \frac{20}{1.62} - dh \quad (4.1-9)$$

Here U the measured voltage in [V], the nominal range is 20 cm and dh (equal to 1.06 cm) corresponds to an additional offset due to the elevation of the sensor.

By studying both water level variations, a relationship between the water level measured in the first unit (H_1) and the outflow routing to the second unit Q_2 (and related to H_2) has been established (see *Figure 4.1-6*). Finally, the total discharge reaching the first unit and collecting the downstream rainfall can be assessed by the following equation depending only on H_1 :

$$Q_1 = Q_2 + \frac{dH_1}{dt} \times A_1 = f(H_1) + \frac{dH_1}{dt} \times A_1 \quad (4.1-10)$$

where Q_1 is the discharge reaching the first unit and Q_2 the second respectively, $A_1 = 33.2$ m² is floor area of the first unit.

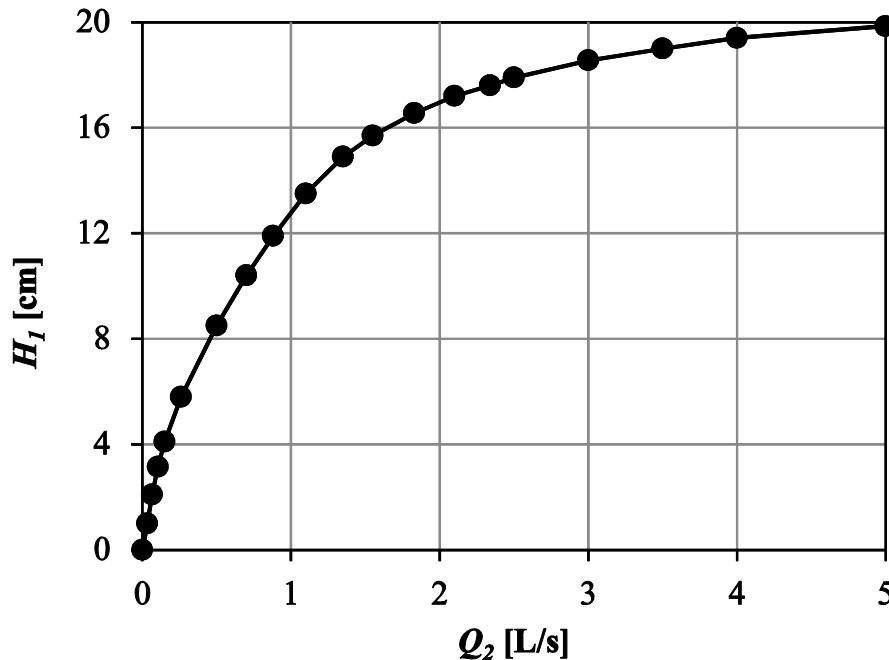


Figure 4.1-6. Relationship adjusted between the water level H_1 and the downstream discharge Q_2

Finally, discharge data was recorded with a time step of 30 seconds for the sensor implemented in the conduit, and 15 seconds for the one in the storage unit.

Available output, data processing and period of study

As already presented in details in Gires et al. (2018), precipitation data is collected in real time and stored through daily files. Here, these files for 30 s time step rain rate have been gathered with the help of a Python script to create a long time series covering the whole period of study. Each line contains the time step expressed as YYYY-MM-DD HH:MM:SS and the corresponding rainfall intensity (in mm/h) separated by a coma.

Water content and water level data inside the pipe are collected and stored every night on the HM&Co server in two different files. For this purpose, the Loggernet software produced by Campbell Scientific® has been used. It supports programming, communication, and data retrieval between data loggers and a PC. Concerning the water level file, each line corresponds to a time step for which the following information is recorded (in each line, these values are separated by a coma):

- Exact definition of the time step expressed as YYYY-MM-DD HH:MM:SS
- Item number
- Voltage indicator to ensure the quality of the measurement (it should be close to 12 V)
- Internal temperature of the datalogger box
- Unused data coming from a non-operational sensor
- Water level measured inside the pipe (U in Equation (4.1-4), expressed in mV)
- Unused data coming from a non-operational sensor
- Unused data coming from a non-operational sensor

Similar format has been chosen for volumetric water content data (note that names of the 16 VWC sensors are indicated in the header and also are reported on *Figure 4.1-1*):

- Exact definition of the time step expressed in YYYY-MM-DD HH:MM:SS
- Item number
- Voltage indicator to ensure the quality of the measurement (it should be close to 12 V)
- Internal temperature of the datalogger box
- Volumetric water content (expressed as k_a) for the 16 TDR sensors
- STT_B3: Summary Transfer Time for basis, which is related to the total time required for collecting information from all the sensors that are collected to that base.

Water level data inside the storage units have been collected by using the open-source Arduino Uno microcontroller board that works in the offline regime. Data are continuously stored on the 64 MB memory card implemented on the board, and copied manually to the HM&Co server once per week. Data contain the following information (in each line, these values are separated by a space):

-
- Item number
 - Voltage values for the first storage unit – U_1 (in mV)
 - Voltage values for the second storage unit – U_2 (in mV)
 - Exact definition of the time step expressed in YYYY-MM-DD HH:MM:SS

By using Equation (4.1-9) U_1 values are transformed into H_1 as a part of post-processing. Note that U_2 data have been used only for a short period of time after the implementation of UM18 sensors, until $Q_2 = f(H_1)$ functionality has been obtained. After that they were no longer necessary.

4.1.3. Data availability

Conversely to rainfall and discharge, which are measured continuously at the same locations, water content sensors can be moved from a location to another on Green Wave. Moreover they were rarely conserved during the night for security reason. Nevertheless, during several months at the beginning of 2018, they were maintained on the same section of Green Wave (that showed in *Figure 4.1-1*). This time period corresponds to 78 days, from February 19th to May 7th 2018. It has been selected to provide water balance components measurements to potential users. This data set is available for download from the following web page (Versini et al., 2019): <https://doi.org/10.5281/zenodo.3467300>

Presentation of the available data set

This data set presented in details in the next section contains the following files:

- A rainfall file: 2018_0219-0507_Data_rainfall.dat
- A water content file: 2018_0219-0507_VWC.dat
- A water level inside the pipe file: 2018_0219-0507_Data_discharge.dat
- A water level in the storage file: 2018_0219-0507_Data_Arduino.dat
- A python script to select the data, transform the raw data in physical measurements and carry out some initial analysis.

In details, the python script is structured as follow:

- Time period selection: this part could be changed to select a study time period by choosing an initial and final date.
- Data selection and transformation: the data corresponding to this time period are selected in the different files. Electric signals measured by the water level sensors are converted in water level (by using Equation 4.1-4 and 4.1-10), then in discharge by using Manning-Strickler equation (Equation 4.1-5) for the pipe and Equation (4.1-11) for the storage unit. In order to smooth the erratic 15s-signal produced by storage unit measurements, the computed discharge data are averaged on a moving window, whose number of time steps can be modified. As previously mentioned, dielectric constant measurements monitored by the 16 TDRs are used in their original form as water content indicators.

-
- Representation of the computed data: Several Figures are drawn to illustrate the variation of the hydrological components in time. The first one represents the corresponding hydrographs for both discharges computed inside the pipe and in the storage unit. The second one synthesizes the dielectric constant measured by the 16 TDR sensors. In each Figure, the precipitation is drawn on an invert y-axis.
 - Computation of runoff coefficients: runoff coefficient is the ratio between the total amount of precipitation (computed by multiplying the rain depth by the corresponding contributive area) and the total volume of water flowing through the monitored pipe or the storage unit. This value ranging 0 to 100% illustrates the capacity of the green roof to retain rainwater.

Presentation of the time series

During the available time period including half of winter and half of spring, it rained a total amount of 123.1 mm (see *Figure 4.1-7*). The rainfall file has no missing value, and at least 7 rainfall events can be defined. They correspond to a precipitation higher than 5 mm that caused discharge in both pipe and storage unit: 7th march (9 mm), 10 and 11th March (14 mm), 17th March (7.5 mm), 27th march (6.5 mm), 28th March (8.5 mm), 9th April (9.5 mm), 29 and 30th April (24.5 mm).

Concerning the 16 VWC sensors, 5.6% of the time steps are considered as missing data. This is essentially due to 2 particular sensors that were out of service from 16th March to the end of the study time period. The 16 sensors follow the same dynamic, responding to the several rainfall events (see *Figure 4.1-8*). Dielectric constant measurements show different absolute values, but they change similarly during the observed period, remaining almost parallel during the rainfall, while getting closer during dry periods (end of February and from mid-April to the beginning of May). Besides the spatial heterogeneity of water content, these differences also indicate that the roof inclination does not affect peaks of drained outflow, but mostly the redistribution of retained water along the slope during dry periods. That way higher water contents appear at slope's bottom compared to those at the top.

Discharge data are almost complete. Only two data are missing for the measure in the pipe and 0.2% of total amount of time steps for the storage unit. These missing data correspond to the short periods during which the manually collection of the data is carried out. Note that in order to avoid the loss of relevant data, this operation is done during a dry period. On this time period of 78 days, runoff coefficient computed for both pipe and storage unit are equal to 70.6% and 71.1% respectively. These close values demonstrate the relevance of the monitored set-up, and the missing water corresponds to the water retained by the substrate and the vegetation.

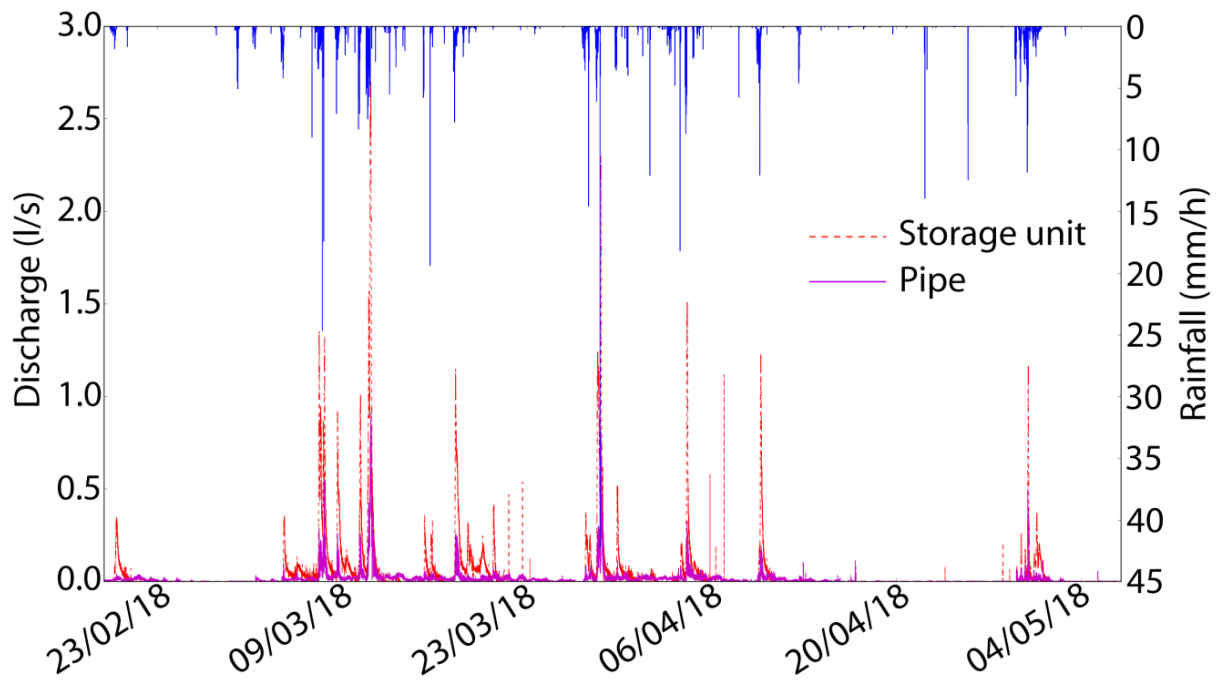


Figure 4.1-7. Rainfall and computed discharges for the whole time period

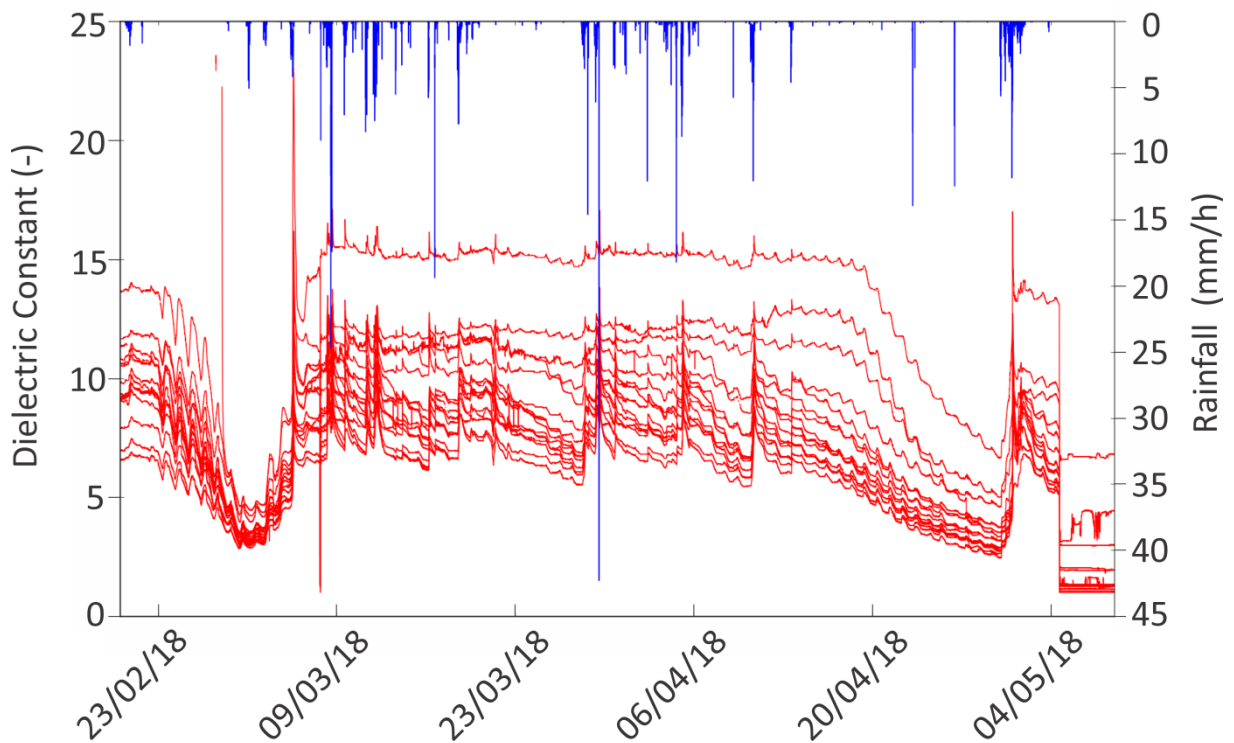


Figure 4.1-8. Rainfall and Dielectric Constant for 16 TDR sensors

4.1.4. Conclusion

This paper presents the data collected by several devices devoted to the assessment of the water balance of a particular green roof located close to Paris. The dataset made available for research purposes contain 3 types of data, representing the relevant components of the water balance during a rainfall event: rainfall, water content in the substrate and the discharge flowing out of the infrastructure. They were collected during 78 days between February and May 2018. These measurements are useful to study the capacity of such vegetated infrastructures to store rainwater and act as stormwater management tool. They could also be useful to develop and validate some appropriate modeling approaches (Stovin et al., 2013; Versini et al., 2016).

This data set is available for download free of charge from the following web page (Versini et al., 2019): <https://doi.org/10.5281/zenodo.3467300>

It is provided by the Hydrology, Meteorology, and Complexity laboratory of École des Ponts ParisTech (HM&Co-ENPC). The following references should be cited for every use of the data:

Versini, P.-A., Stanic, F., Gires, A., Scherzer, D., and Tchiguirinskaia, I. (2019). Measurement of the water balance components of a large green roof in Greater Paris Area. Earth System Science Data. XXXXX

Versini, P.-A., Stanic, F., Gires, A., Scherzer, D., Tchiguirinskaia, I.: Data for "Measurement of the water balance components of a large green roof in Greater Paris Area", <https://doi.org/10.5281/zenodo.3467300>, 2019

Researches focused on the assessment of ecosystem services provided by Blue Green Solutions is continuing at HM&Co-ENPC, and particularly on the BGW. The monitoring set-up has been recently extended to the energy balance measurement. The objective is to assess its different components (radiation balance, conduction, sensitive and latent heat flux). Such data will be particularly useful to study the ability of Blue Green Solutions to mitigate urban heat islands. The French ANR EVNATURB project (<https://hmco.enpc.fr/portfolio-archive/evnaturb/>), that aims to develop a platform to assess some of the eco-system services (i.e stormwater management, cooling effect, or biodiversity conservation) provided by BGS is now pursuing this work of monitoring (Versini et al., 2017).

4.1.5. References:

Berndtsson, J. C. 2010. "Green Roof Performance towards Management of Runoff Water Quantity and Quality : A Review." *Ecological Engineering* 36 (4): 351–60. <https://doi.org/10.1016/j.ecoleng.2009.12.014>.

-
- Berretta, C., S. Poë, and V. Stovin. 2014. “Moisture Content Behaviour in Extensive Green Roofs during Dry Periods : The Influence of Vegetation and Substrate Characteristics.” *JOURNAL OF HYDROLOGY* 511: 374–86.
<https://doi.org/10.1016/j.jhydrol.2014.01.036>.
- Buffam, I., M. E. Mitchell, and R. D. Durtsche. 2016. “Environmental Drivers of Seasonal Variation in Green Roof Runoff Water Quality.” *Ecological Engineering* 91: 506–14.
<https://doi.org/10.1016/j.ecoleng.2016.02.044>.
- Cipolla, S. S., M. Maglionico, and I. Stojkov. 2016. “A Long-Term Hydrological Modelling of an Extensive Green Roof by Means of SWMM.” *Ecological Engineering* 95: 876–87.
<https://doi.org/10.1016/j.ecoleng.2016.07.009>.
- Fassman-Beck, E., E. Voyde, R. Simcock, and Y. Sing. 2013. “4 Living Roofs in 3 Locations : Does Configuration Affect Runoff Mitigation ?” *Journal of Hydrology* 490: 11–20. <https://doi.org/10.1016/j.jhydrol.2013.03.004>.
- Feng, Y., S. J. Burian, and E. R. Pardyjak. 2018. “Observation and Estimation of Evapotranspiration from an Irrigated Green Roof in A.” *Water* 10 (262).
<https://doi.org/10.3390/w10030262>.
- Frasson, R. P. De M., L. K. Cunha, and W. F. Krajewski. 2011. “Assessment of the Thies Optical Disdrometer Performance.” *Atmospheric Research* 101 (1–2): 237–55.
<https://doi.org/10.1016/j.atmosres.2011.02.014>.
- Getter, K. L., D. B. Rowe, and J. A. Andresen. 2007. “Quantifying the Effect of Slope on Extensive Green Roof Stormwater Retention.” *Ecological Engineering* 3 (1): 225–31.
<https://doi.org/10.1016/j.ecoleng.2007.06.004>.
- Gires, A., I. Tchiguirinskaia, and D. Schertzer. 2015. “Multifractal Comparison of the Outputs of Two Optical Disdrometers.” *Hydrological Sciences Journal*.
<https://doi.org/10.1080/02626667.2015.1055270>.
- . 2018. “Two Months of Disdrometer Data in the Paris Area.” *Earth System Science Data* 10: 941–50. <https://doi.org/10.5194/essd-10-941-2018>.
- Hakimdavar, R., P. J. Culligan, A. Guido, and W. R. McGillis. 2016. “The Soil Water Apportioning Method (SWAM): An Approach for Long-Term , Low-Cost Monitoring of Green Roof Hydrologic Performance.” *Ecological Engineering* 93: 207–20.
<https://doi.org/10.1016/j.ecoleng.2016.05.023>.
- Jackson, T., K. Mansfield, M. Saafi, T. Colman, and P. Romine. 2008. “Measuring Soil Temperature and Moisture Using Wireless MEMS Sensors.” *Measurement* 41: 381–90.
<https://doi.org/10.1016/j.measurement.2007.02.009>.
- Lakshmi, V., T. J. Jackson, and D. Zehrhuhs. 2003. “Soil Moisture – Temperature Relationships : Results from Two Field Experiments.” *Hydrological Processes*, 3041–57.
<https://doi.org/10.1002/hyp.1275>.
- Li, Y., and R. W. Jr. Babcock. 2015. “Modeling Hydrologic Performance of a Green Roof System with HYDRUS-2D.” *Journal of Environmental Engineering*, 1–9.
[https://doi.org/10.1061/\(ASCE\)EE.1943-7870.0000976](https://doi.org/10.1061/(ASCE)EE.1943-7870.0000976).
- Locatelli, L., O. Mark, P. Steen, K. Arnbjerg-Nielsen, M. Bergen, and P. John. 2014. “Modelling of Green Roof Hydrological Performance for Urban Drainage Applications.” *JOURNAL OF HYDROLOGY*. <https://doi.org/10.1016/j.jhydrol.2014.10.030>.
- Nascimento, C. M. L. do, W. Mary, and L. P. da Silva. 2018. “Hydrological Performance of
-

-
- Modular-Tray Green Roof Systems for Increasing the Resilience of Mega-Cities to Climate Change.” *Journal of Hydrology*. <https://doi.org/10.1016/j.jhydrol.2018.01.004>.
- Ouldboukhitine, S. -E., I. Jaffal, and A. Trabelsi. 2011. “Assessment of Green Roof Thermal Behavior : A Coupled Heat and Mass Transfer Model.” *Building and Environment* 46: 2624–31. <https://doi.org/10.1016/j.buildenv.2011.06.021>.
- Palla, A., I. Gnecco, and L. G. Lanza. 2009. “Unsaturated 2D Modelling of Subsurface Water Flow in the Coarse-Grained Porous Matrix of a Green Roof.” *Journal of Hydrology* 379 (1–2): 193–204. <https://doi.org/10.1016/j.jhydrol.2009.10.008>.
- Poë, S., V. Stovin, and C. Berretta. 2015. “Parameters Influencing the Regeneration of a Green Roof ’ s Retention Capacity via Evapotranspiration.” *Journal of Hydrology* 523: 356–67. <https://doi.org/10.1016/j.jhydrol.2015.02.002>.
- Stacheder, M., F. Koeniger, and R. Schuhmann. 2009. “New Dielectric Sensors and Sensing Techniques for Soil and Snow Moisture Measurements.” *Sensors* 9: 2951–67. <https://doi.org/10.3390/s90402951>.
- Stovin, V., S. Poë, and C. Berretta. 2013. “A Modelling Study of Long Term Green Roof Retention Performance.” *Journal of Environmental Management* 131: 206–15. <https://doi.org/10.1016/j.jenvman.2013.09.026>.
- Stovin, V., S. Poë, S. De-ville, and C. Berretta. 2015. “The Influence of Substrate and Vegetation Configuration on Green Roof Hydrological Performance.” *Ecological Engineering* 85: 159–72. <https://doi.org/10.1016/j.ecoleng.2015.09.076>.
- Thurai, M., W. A. Petersen, A. Tokay, C. Schultz, and P. Gatlin. 2011. “Drop Size Distribution Comparisons between Parsivel and 2-D Video Disdrometers.” *Adv. Geosci.* 30: 3–9. <https://doi.org/10.5194/adgeo-30-3-2011>.
- Topp, G. C., J. L. Davis, and A. P. Annan. 1980. “Electromagnetic Determination of Soil Water Content:” *Water Resources Research* 16 (3): 574–82.
- Versini, P. -A., A. Gires, I. Tchinguirinskaia, and D. Schertzer. 2016. “Toward an Operational Tool to Simulate Green Roof Hydrological Impact at the Basin Scale: A New Version of the Distributed Rainfall–Runoff Model Multi-Hydro.” *Water Science & Technology* 74 (8): 1845–54. <https://doi.org/10.2166/wst.2016.310>.
- Versini, P. -A., F. Stanić, A. Gires, D. Schertzer, and I. Tchinguirinskaia. 2019. “Data for ‘Measurement of the Water Balance Components of a Large Green Roof in Greater Paris Area.’” <https://doi.org/10.5281/zenodo.3467300>.
- Wong, G. K. L., and C. Y. Jim. 2015. “Landscape and Urban Planning Identifying Keystone Meteorological Factors of Green-Roof Stormwater Retention to Inform Design and Planning.” *Landscape and Urban Planning* 143: 173–82. <https://doi.org/10.1016/j.landurbplan.2015.07.001>.
- Zhang, Qi., L. Miao, X. Wang, D. Liu, L. Zhu, B. Zhou, J. Sun, and J. Liu. 2015. “Landscape and Urban Planning The Capacity of Greening Roof to Reduce Stormwater Runoff and Pollution.” *Landscape and Urban Planning* 144: 142–50. <https://doi.org/10.1016/j.landurbplan.2015.08.017>.
-

4.2. Application of Universal Multifractals (UM) on monitored data of water balance components of Green Wave for assessing its hydrological performances

(Ready for submission)

4.2.1. Introduction

Implementation of green roofs in highly urbanized areas is becoming more and more required in recent years for variety of reasons. Besides the urban heat island (UHI), effect that is characteristic for large metropolitan areas where temperature can be significantly higher compared to surrounding rural areas (Francis & Jensen, 2017), there is one more important aspect of green roofs utilization - mitigation and delay of urban runoff peak (Stovin et al., 2012; Versini et al., 2016). The retention and detention capacities of green roof substrate and vegetation layer were proved to be the main advantage of this particular type of Nature Based Solutions (NBS) for cities. Besides the investigation of green roofs from the aspect of modelling, where different conceptual (Versini et al., 2016) and physically-based hydrological models (Palla et al., 2009; Yang & Wang, 2014; Li & Babcock, 2016) are used to simulate different scenarios at different scales, impact of different roof configuration (Fassman-Beck et al., 2013), substrate and vegetation type (Stovin et al., 2015), drainage area (Hakimdavar et al., 2014), etc., are also analyzed based on monitored rainfall-runoff data. Good overview of different investigations in terms of green roofs can be found in Berndtsson (2010) and Li & Babcock, (2014).

In most of the studies a rainfall-runoff coefficient is used to rate the retention capacity of a green roof. However, this approach takes into account only cumulative quantities of rainfall and runoff, while their temporal variabilities, as well as the temporal variability of the water retained in the substrate, are not considered. For analyzing and characterizing temporal variabilities of different geophysical fields, a theoretical Universal Multifractals (UM) framework (Schertzer & Lovejoy, 1987; Schertzer & Lovejoy, 1997) was proved as convenient. This scientific approach enables describing statistical properties of an investigated field by means of solely 2 relevant parameters (in case of conservative fields) that can be determined using two techniques, Trace moment and Double trace moment (Lavallée et al., 1992; Schmitt et al., 1993). These techniques rely on the analysis of change of average statistical moments of different orders while changing the resolution of the field, which is described by means of moment scaling function. Up to date, UM framework was proved as successful in characterizing rainfall intensity (Lovejoy & Schertzer, 1995; Olsson & Niemczynowicz, 1996; Tchiguirinskaia et al., 2011 ; Paz et al., 2016), river discharge (Tessier et al., 1996 ; Kantelhardt et al., 2003), soil hydraulic conductivity (Liu & Molz, 1997), porosity and gravimetric water content (Morató et al., 2016), etc. However, to the knowledge of the authors, this approach has not been used to assess the behavior of green roofs, or other types of NBS.

The idea of this work is to assess the hydrological behavior of green roofs by comparing moment scaling functions of three water balance components relevant for green roofs: rainfall intensity, water content and drained discharge, where the obtained moment scaling functions are characterized by means of UM parameters. Also, it is believed that in case of inclined roofs, a comparison between these functions for the rainfall intensity and for the water content change at slope's bottom can provide certain information concerning the impact of roof inclination on the lateral water movement within the substrate. Clearly, such investigation requires detailed monitoring system, such as the one installed on Green Wave (Chapter 4.1), where the three mentioned water balance components are measured.

4.2.2. Pilot Site

In Chapter 4.1 is introduced the monitoring system installed on Green Wave, with detailed explanation of different techniques used for measuring rainfall intensity, water content change of the roof substrate and discharged drained from the substrate. In this work are analyzed data (time series) of these three water balance components, measured respectively by means of: an optical disdrometer (Campbell Scientific - PWS100), wireless network of 32 TDR sensors (Campbell Scientific - CWS665), and an ultrasonic displacement sensor (SICK - UM18) that measures water level change in the drainage pipe.

TDR sensors provide values of dielectric constant k_a as an output, which is obtained based on the travel time required for electro-magnetic signal to cross the length of sensor waveguides. Topp et al., (1980) have reported that k_a is strongly correlated with volumetric water content by means of the polynomial expression of third order, in case of conventional soils. However, due to the fact that substrate used for covering Green Wave (Stanić et al., 2019) is a volcanic material with several percent of organic matters, Topp's equation is found inappropriate. Thus, the original values of k_a are further analyzed and treated solely as an indicator of water content. In order to analyze the impact of roof inclination on a hydrological behavior of Green Wave, numerous TDRs are distributed along a single slope of Green Wave.

Hydraulic conditions in the pipe that collects outflow drained from Green Wave are such that a reasonably uniform flow on the location of the displacement sensor can be assumed (sufficient value of the pipe slope, long and aligned downstream section that prevents from any disturbance propagation in the upstream direction, and long enough distance from any upstream obstacles). Thus, discharge can be computed by means of Manning equation, based solely on the information about pipe material, pipe geometry and measured water layer thickness inside the pipe (see Chapter 4.1 for more details).

4.2.3. Universal Multifractal (UM) framework

Time series of the three mentioned water balance components are analyzed in this work by means of UM framework. Thus, an overview of this approach is given in the following sections, more detailed than done in Chapter 3.1.

Brief overview of the theoretical framework

If certain field ε_λ at a given resolution λ (ratio between the outer scale L and the observation scale $L_I(\lambda)$) is considered to be multifractal (Figure 4.2-1), then the probability of exceeding a scale depending threshold λ^γ can be expressed using the following equation:

$$P(\varepsilon_\lambda \geq \lambda^\gamma) \approx \lambda^{-c(\gamma)} \quad (4.2-1)$$

where γ is the scale invariant singularity and $c(\gamma)$ is the co-dimension function which is convex and increasing with no upper limit.

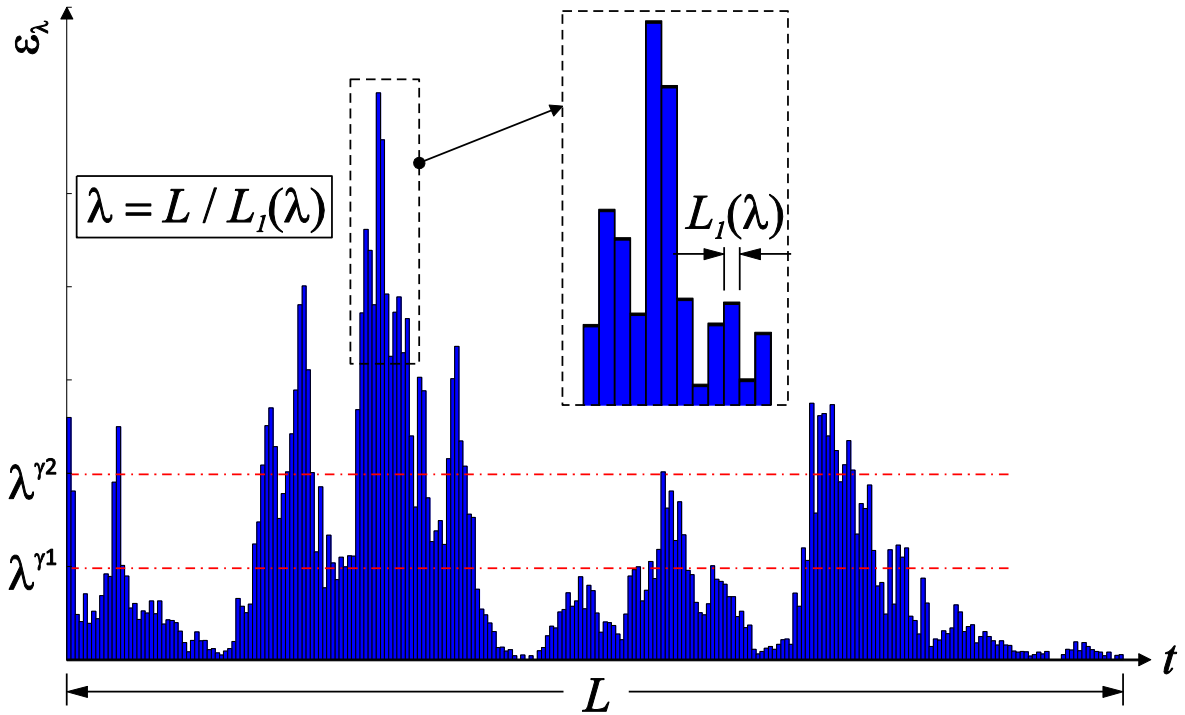


Figure 4.2-1. Example of an one-dimensional multifractal field (time series)

By means of UM framework (Schertzer & Lovejoy, 1987; Schertzer & Lovejoy, 1997), $c(\gamma)$ can be expressed using only 2 relevant parameters, C_1 (mean intermittency) and α (multifractality index), in case of a conservative field:

$$c(\gamma) = \begin{cases} C_1 \left(\frac{\gamma}{C_1 \alpha'} + \frac{1}{\alpha} \right)^{\alpha'} & \alpha \neq 1 \\ C_1 e^{\left(\frac{\gamma}{C_1} - 1 \right)} & \alpha = 1 \end{cases} \quad (4.2-2)$$

where $\alpha' = (1 - 1/\alpha)^{-1}$. The main properties of $c(\gamma)$ function are illustrated in Figure 4.2-2 (top row). Equation (4.2-2) is valid for $c(\gamma) \leq E + E_s$, where E is Euclidian dimension (equal to 1 for time series) and $E_s = \log(N_{sample}) / \log(\lambda) \geq 0$ is called sampling dimension and it represents an additional portion of the probability space that is explored (Schertzer & Lovejoy, 2011). If there is only one data sample ($N_{sample} = 1$), $E_s = 0$ thus $c(\gamma) \leq E$. For $c(\gamma) =$

E (or $E + E_s$), maximal observable singularity $\gamma = \gamma_s$ can be determined from Equation (4.2-2). Also, $\gamma = C_1$ is the singularity corresponding to the mean value of the field, and thus $c(C_1) = C_1$ (see Equation 4.2-2 and Figure 4.2-2c - top).

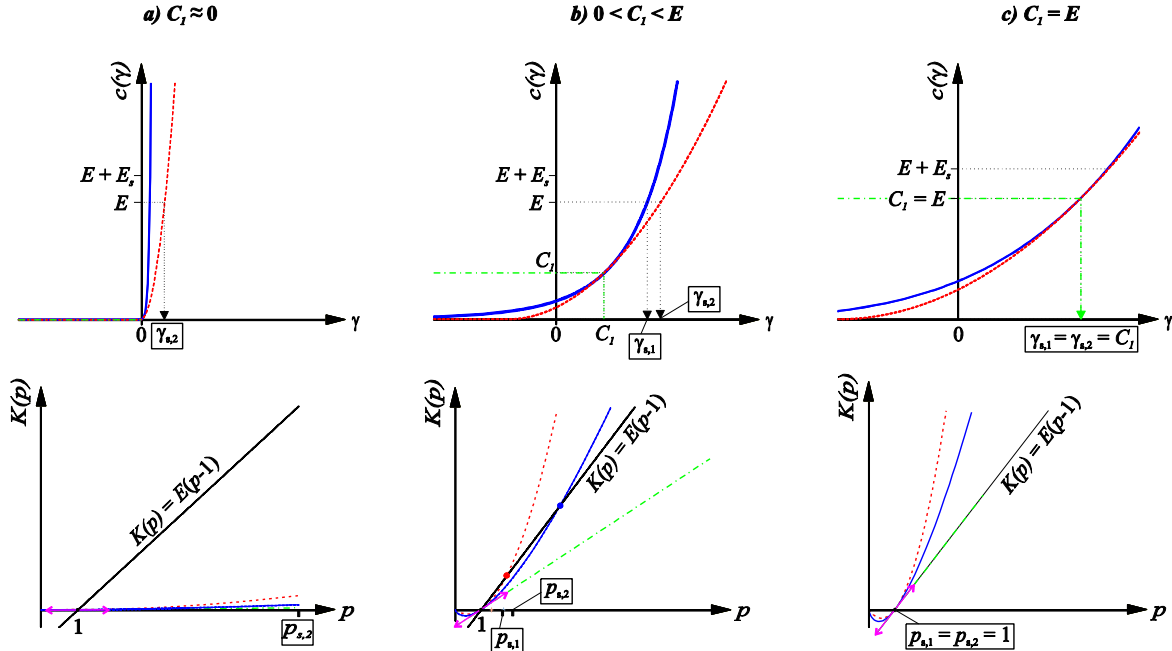


Figure 4.2-2. Dependence of $c(\gamma)$ (top row) and $K(p)$ (bottom row) on UM parameters α and C_1 . Dashed line is related to $\alpha = 2$, solid line to $0 < \alpha < 2$ and dash-dotted line to $\alpha = 0$. Concerning parameter C_1 , three cases are presented: a) C_1 is approximately zero; b) C_1 takes value between 0 and E ; c) C_1 takes maximal value E . Values of the maximal observable singularity γ_s and the corresponding p_s are marked in the graphs

Another, equivalent way of describing statistical properties of the multifractal field was introduced by Schertzer & Lovejoy (1987). This approach is based on scaling of the statistical moments of order p :

$$\langle \varepsilon_\lambda^p \rangle \approx \lambda^{K(p)} \quad (4.2-3)$$

where $\langle \varepsilon_\lambda^p \rangle$ is the average statistical moment of order p ($\langle \rangle$ indicates average value) and $K(p)$ is the moment scaling function which is also convex, and can be described through parameters C_1 and α by means of the following expression:

$$K(p) = \begin{cases} \frac{C_1}{\alpha-1} (p^\alpha - p) & \alpha \neq 1 \\ C_1 p \ln p & \alpha = 1 \end{cases} \quad (4.2-4)$$

Functions $K(p)$ and $c(\gamma)$ are linked by Legendre transform (Frisch & Parisi, 1985), which means that every moment order p has the corresponding singularity γ and vice versa.

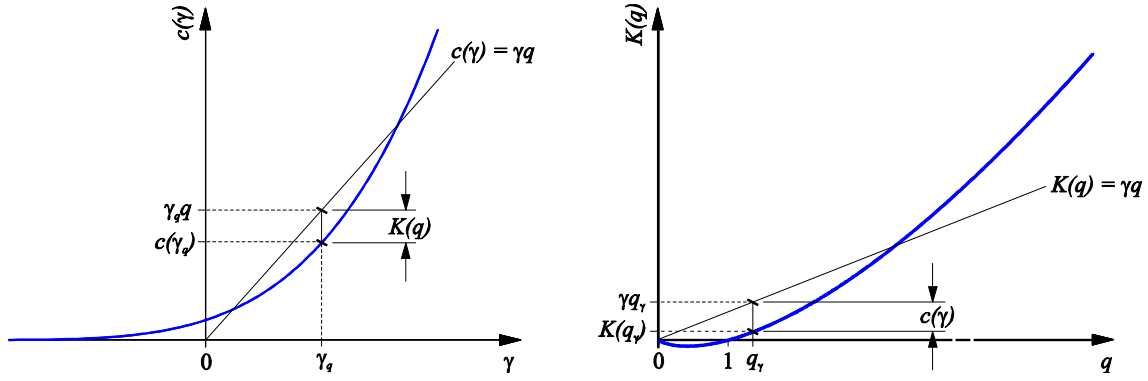


Figure 4.2-3. Legendre transform

This is illustrated in *Figure 4.2-3* where:

$$c(\gamma) = \max_p(p\gamma - K(p)) = p_\gamma \gamma - K(p_\gamma) \quad (4.2-5)$$

$$K(p) = \max_\gamma(p\gamma - c(\gamma)) = p\gamma_p - c(\gamma_p) \quad (4.2-6)$$

$K(p)$ function is mostly used for determination of UM parameters (C_1 and α) due to its characteristics. In *Figure 4.2-2* (bottom row) are presented $K(p)$ functions obtained using the same combinations of UM parameters as used for the corresponding $c(\gamma)$ functions presented in the left column. It can be observed that for a single value of C_1 , slope of $K(p)$ function for $p = 1$ remains the same regardless of α value (two side arrow indicates slope), which can be proved by calculating the first derivative of Equation (4.2-4) at $p = 1$:

$$\frac{dK(p)}{dp} \Big|_{p=1} = C_1 \quad (4.2-7)$$

On the contrary, if varying only value C_1 , both the first and the second derivative at $p = 1$ change (see *Figure 4.2-2*), which can be confirmed by calculating the second derivative of Equation (4.2-4) at $p = 1$:

$$\frac{d^2K(p)}{dp^2} \Big|_{p=1} = \alpha C_1 \quad (4.2-8)$$

These characteristics of $K(p)$ function are used in different techniques for determination of UM parameters, as described later on.

Critical value of moment order

Theoretical $K(p)$ function (Equation 4.2-4) is valid only up to the certain critical value of moment order p_c . This critical value is associated with multifractal phase transition (Schertzer et al., 1993) and it is estimated as $p_c = \min(p_s, p_D)$, where p_s is the maximal order moment estimated with a finite number of samples N_{sample} , while p_D is the critical moment order of divergence. Value of p_s is linked with the maximal observable singularity γ_s by means of Legendre transform (illustrated in *Figure 4.2-2*), and it can be determined using following equation:

$$p_s = \left(\frac{E+E_s}{C_1} \right)^{1/\alpha} \quad (4.2-9)$$

In case of one-dimensional field ($E = 1$) when only one data sample is used ($N_{sample} = 1$, thus $E_s = 0$) critical value of moment order is usually $p_c = p_s$, which is manifested as a linear behavior of the empirical $K(p)$ for $p \geq p_s$.

On the other hand, moment order p_D represents the critical value of p for which extreme values of the field are becoming so dominant that the average statistical moment of order $p \geq p_D$ approaches to infinity:

$$\langle \varepsilon_\lambda^p \rangle = \infty, \quad p \geq p_D \quad (4.2-10)$$

Moment order p_D can be determined from the following equation:

$$K(p_D) = (p_D - 1)D \quad (4.2-11)$$

Value of p_D is a point where Equation (4.2-4) intersects the linear regression $K(p) = E(p-1)$ obtained by means of Equation (4.2-4) for $C_I = E$ and $\alpha = 0$ (see bottom graph of *Figure 4.2-2b* – filled circles). In case that $p_c = p_D$, the empirical $K(p)$ function starts rapidly approaching infinity for $p > p_D$.

Value of p_s can be increased by increasing the number of data samples ($N_{sample} > 1$, $E_s > 0$), which enables Equation (4.2-4) to be valid over a larger range of p . Thus, the theoretical framework is able to simulate investigated field more accurately. However, limitation related to p_D remains an obstacle that still has not been overcome.

Physical basis of UM parameters

Based on the presented characteristics of $c(\gamma)$ and $K(p)$ functions, the physical meaning of UM parameters can be introduced.

Mean intermittency C_I describes the sparseness of the mean value of the field. From *Figure 4.2-2* (top row) it is evident that for low values of C_I (*Figure 4.2-2a*) $c(\gamma)$ function gradually increases up to the value C_I , after which it starts rapidly to approach infinity. Since C_I is low, values equal to or lower than the mean value are “ubiquitous” (low $c(C_I)$ secures high probability of exceedance – Equation 4.2-1), while values higher than the mean are very sparse ($c(\gamma > C_I)$ secures low probability of exceedance). This leads to conclusion that $C_I = 0$ corresponds to a homogeneous field with $P(\varepsilon_\lambda \geq \lambda^{C_1}) = 1$. On the contrary, high C_I value provides much smoother $c(\gamma)$ which enables presence of very high extremes, but in the same time secures high sparseness of most of the values (including mean value) – see *Figure 4.2-2c*. This means that for $C_I = E$, mean value is too sparse to be observed, leading to $P(\varepsilon_\lambda \geq \lambda^{C_1}) = 0$. Thus, C_I takes values between 0 and E (=1 in case of time series).

Multifractality index α describes how much sparseness varies as we go away from the mean value of the field. In other words, two $c(\gamma)$ functions with the same C_I but different α parameter secure the same sparseness of the mean value, but different sparseness of low and high intensities (see *Figure 4.2-2b*). Unlike low α , high α value secures lower $c(\gamma)$ values

(higher probability of exceedance) for very low and very high singularities γ , meaning that variability of the field is strong. Log-normal field secures the highest variability ($\alpha = 2$; $c(\gamma)$ is parabola), while fractal field corresponds to no variability ($\alpha = 0$; $c(\gamma) = C_I$ for all γ). More details can be found in Schertzer & Lovejoy (1992).

Non-conservation parameter H indicates whether the investigated field is conservative or not. For conservative renormalized fields ($H = 0$) mean value remains constant independently of the resolution λ ($\langle \varepsilon_\lambda \rangle = 1$), while for non-conservative fields ($H \neq 0$) it is not the case. Parameter H can be determined with help of the slope of energy spectrum of the field (slope > 1 – non-conservative field; check Tessier et al. (1993) among others), but in this study is used more convenient approach given by Lavallée et al. (1993). According to the author, original non-conservative field can be transformed into conservative one if considering the absolute values of data increments instead of the original data themselves. This approach was proved to work even for strongly non-conservative fields that are rather inert, such as discharge, hydraulic conductivity, etc.

From the description of α and C_I parameters, it is evident that the biggest extremes are associated with high values of both parameters. For better understanding the impact UM parameters, check examples of simulated multifractal fields obtained with different combinations of α and C_I values - Schertzer & Lovejoy (1993).

Determination of the UM parameters from real data

As previously mentioned, $K(p)$ function (Equation 4.2-4) is, due to its characteristics, found as rather convenient for determining values of C_I and α from real data. Two techniques founded on $K(p)$ function can be found in the literature - Trace Moment (TM) and Double Trace Moment (DTM), that are also applied in this work.

TM technique

Trace Moment (TM) technique is based on scaling behavior of average statistical moments of order p (also done in Chapter 3.1 but for $E = 2$). This technique relies on Equation (4.2-3) and the assumption that the investigated field is conservative. Application of TM technique is illustrated in *Figure 4.2-4*. The field is firstly renormalized as the following:

$$\varepsilon_\lambda = \frac{\varepsilon_\lambda}{\langle \varepsilon_\lambda \rangle} \quad (4.2-12)$$

In this case it is evident that mean value of the renormalized field becomes equal to 1. By averaging λ_I (most commonly $\lambda_I = 2$) neighbor values of the field, resolution λ gradually decreases with factor λ_I up to the uniform field ($\lambda = 1$). At each resolution λ field is raised on the power p (example of 3 different p values - *Figure 4.2-4*) and the average statistical moment of a given order p (dashed line in *Figure 4.2-4*) is calculated as following:

$$\langle \varepsilon_\lambda^p \rangle = \frac{\sum_1^{\lambda^E} \varepsilon_\lambda^p}{\lambda^E} \quad (4.2-13)$$

where $E = 1$ for one-dimensional field (time series in this study).

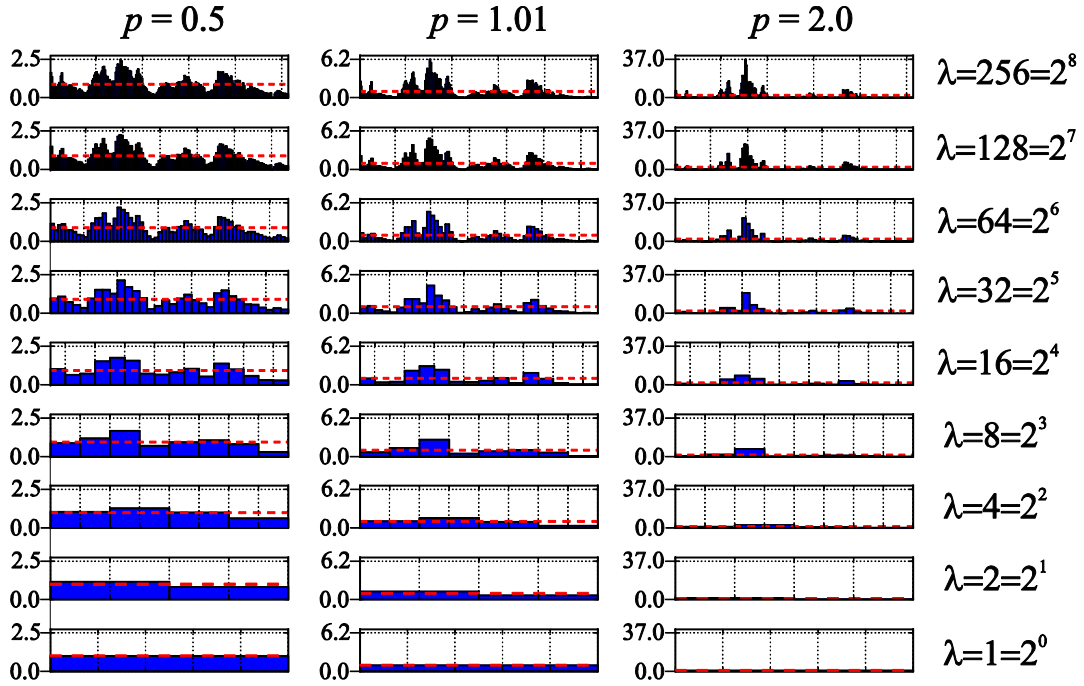


Figure 4.2-4. Trace Moment (TM) technique (dashed line represents the mean value)

After reaching $\lambda = 1$, average statistical moments computed at each resolution λ ($\langle \varepsilon_\lambda^p \rangle$) are plotted versus the corresponding λ in logarithmic scale. This is repeated for different p values. Values of $\langle \varepsilon_\lambda^p \rangle$ determined for one p value should scale linearly with respect to λ in logarithmic scale, where slope of the linear regression is equal to $K(p)$. After determining values of slopes for variety of p , the empirical $K(p)$ function is obtained. Finally, values of C_1 and α are determined by means of Equations (4.2-7) and (4.2-8), respectively, where both the first and the second derivative are calculated numerically.

DTM technique

Double Trace Moment (DTM - Lavallée et al., 1992; Schmitt et al., 1993) technique, which also relies on the assumption that investigated field is conservative, enables direct estimation of parameters C_1 and α under the assumption that Equation (4.2-4) reliably interprets empirical $K(p)$ function. The main idea of DTM method is that the average statistical moment $\langle \varepsilon_\lambda^{(\eta)p} \rangle$ also scales with λ in the following way:

$$\langle \varepsilon_\lambda^{(\eta)p} \rangle = \lambda^{K(p,\eta)} \quad (4.2-14)$$

$$K(p, \eta) = K(\eta p) - pK(\eta) \quad (4.2-15)$$

After combining Equations (4.2-4) and (4.2-15), $K(p, \eta)$ can be presented as following:

$$K(p, \eta) = \eta^\alpha K(p) = \eta^\alpha \frac{C_1}{\alpha - 1} (p^\alpha - p) \quad (4.2-16)$$

Figure 4.2-5 illustrates the application of DTM technique.

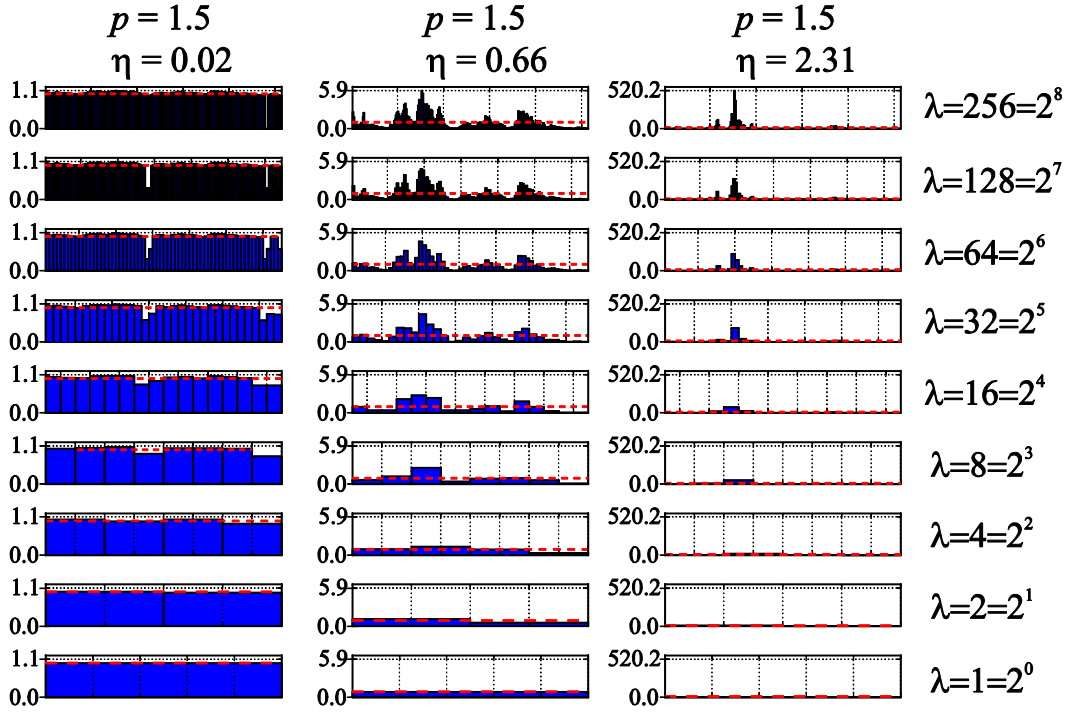


Figure 4.2-5. Double Trace Moment (DTM) technique (dashed line represents the mean value)

Original field is firstly renormalized (Equation 4.2-12) and raised afterwards to the power η (three different values of η are presented in Figure 4.2-5). TM technique is applied on such a modified field, but only a single value of exponent p is used (usually $p = 0.5 \div 2$, $p = 1.5$ in this study). This is sufficient since different p values are solely shifting $K(\eta, p)$ function in vertical direction, without changing its characteristics. Average moments $\langle \varepsilon_\lambda^{(\eta)p} \rangle$ scale linearly with resolution λ in logarithmic scale, where $K(\eta, p)$ is the slope of linear regression for certain η (and $p = 1.5$). By plotting different slope values versus η , $K(\eta, p)$ function is obtained and presented in logarithmic scale (presented later in Results section), where the slope of the linear section on the graph corresponds to parameter α , while its intercept b is used for calculating C_I :

$$\alpha_{DTM} = SLOPE \quad (4.2-17)$$

$$C_{1,DTM} = e^b \frac{\alpha_{DTM}^{-1}}{p^{\alpha_{DTM}-p}} \quad (4.2-18)$$

Notations α_{DTM} and $C_{1,DTM}$ are used to indicate technique that was used. Note that Equation (4.2-16) is valid only for the limited range of η that corresponds to a linear part of $K(\eta, p)$ (when presented in logarithmic scale). Theoretically, Equation (4.2-16) breaks down when $\max(p\eta, p) > \min(p_s, p_D)$ due to the already mentioned multifractal phase transition, leading to $K(p, \eta)$ function becoming independent of η . On the other hand, flat part of the graph related to small η values is associated with the numerous zeros (Gires et al., 2013) or extremely low values of the field that can be overcome by the noise of the measuring device (Tessier et al., 1993). Application of both TM and DTM techniques is described in details in Results section.

4.2.4. Results

Presented methodology is applied on the in-situ measurements of rainfall intensity, water content (dielectric constant) and drained discharge, carried out on Green Wave. In the following text are analyzed 3 rainfall events occurred in March 2018 (event 1), November 2017 (event 2) and August 2017 (event 3), that show rather interesting results from the aspect of application of UM for assessing behavior of green roofs.



Figure 4.2-6. Configuration of TDR sensors in case of: a) events 1 and 2; b) event 3

In *Figure 4.2-6* are illustrated different configurations of TDR sensors network used in case of events 1 and 2 (*Figure 4.2-6a*) and event 3 (*Figure 4.2-6b*). Note that the number of TDR sensors contained in a network dictates the time discretization, adopted to be large enough (4 min) to avoid communication problems between TDRs and the base-station. On the contrary, finer time discretization for both rainfall intensity and discharge measurements is adopted (30 s).

Event 1 (07.03.2018)

The first event investigated in this work occurred on 07.03.2018, and in *Figure 4.2-7* are presented measurements of 3 water balance components. Top subplot represents rainfall intensity, 15 small subplots in the center illustrate monitored dielectric constant data by means of 15 TDR sensors distributed along the slope of Green Wave, while the bottom subplot represents discharge data obtained. The total amount of rainfall during this event was 20.63 mm.

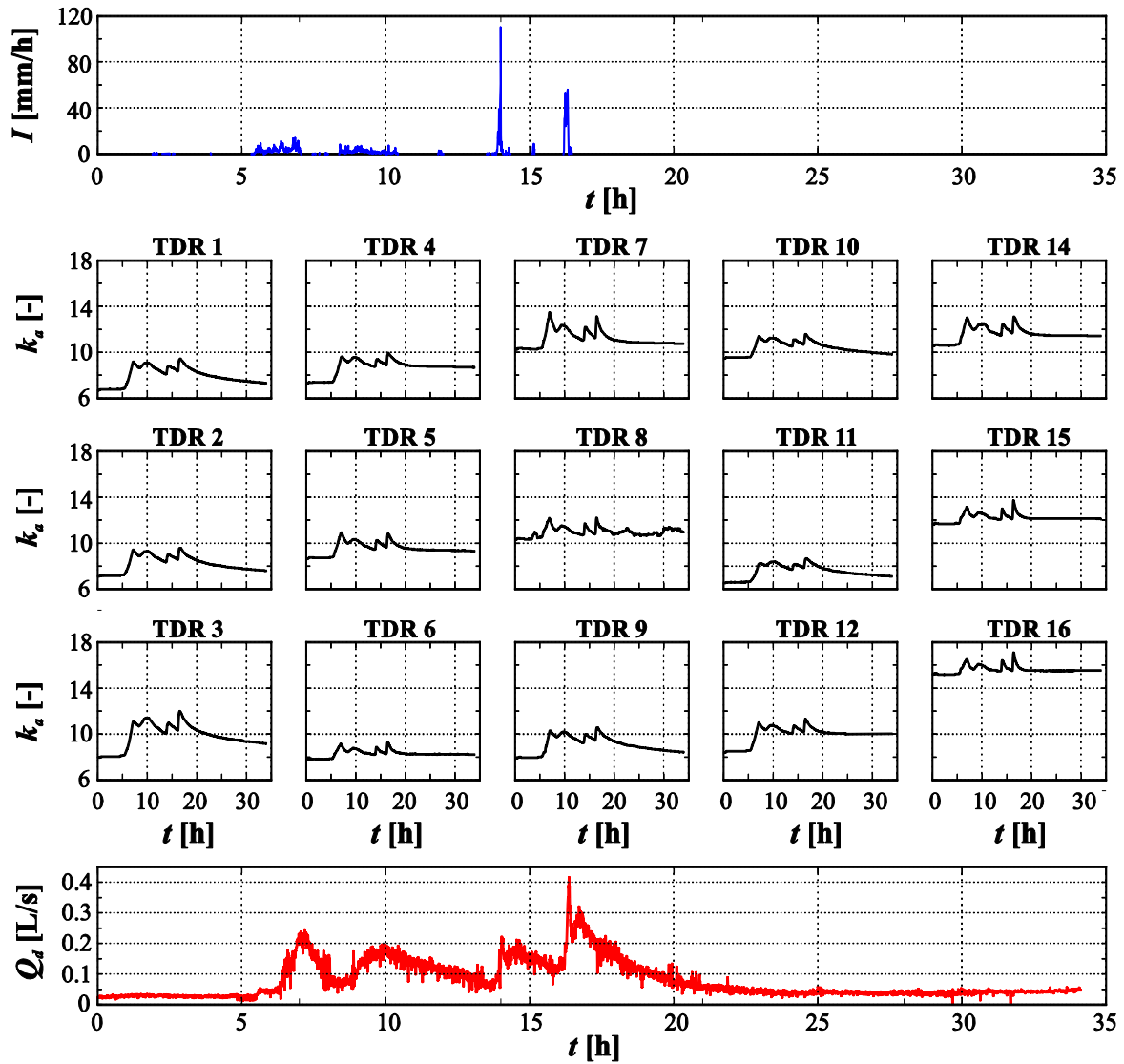


Figure 4.2-7. Data of the rainfall intensity I (top subplot), dielectric constant k_a (15 subplots in the center corresponding to 15 TDR sensors) and drained discharge Q_d (bottom subplot) captured during event 1 (07.03.2018)

By analyzing energy spectrum of all water balance components, it was shown that water content (dielectric constant) and discharge measurements are strongly non-conservative, and thus they are further analyzed in the form of absolute increments (as discussed in the Methodology section). It can be observed that rainfall occurs only within the first 17 h, and thus only this period is analyzed. As already explained, the number of data required for multifractal analysis needs to be a power of 2, and thus the number of data used in case of rainfall intensities, dielectric constant increments and discharge increments is respectively 2048, 512 and 4096.

Table 4.2-1. Event 1 - values of UM parameters obtained by both TM (α_{TM} and $C_{I, TM}$) and DTM (α_{DTM} and $C_{I, DTM}$) techniques, values of p_D and p_s calculated based on α_{DTM} and $C_{I, DTM}$, and the maximal and the minimal values of R^2 parameter related to the scaling of $\langle \varepsilon_\lambda^p \rangle$

| | | α_{TM} | $C_{I, TM}$ | α_{DTM} | $C_{I, DTM}$ | p_D | p_s | R^2_{max} | R^2_{min} |
|---------------------------------------|---------------|---------------|-------------|----------------|--------------|-------|-------|-------------|-------------|
| Rainfall intensity | | 0.91 | 0.31 | 0.89 | 0.32 | 38.29 | 3.55 | 0.96 | 0.95 |
| Discharge increments | | 1.70 | 0.05 | 1.76 | 0.05 | 33.89 | 5.23 | 0.93 | 0.84 |
| Dielectric constant increments | TDR 1 | 2.04 | 0.10 | 1.92 | 0.10 | 10.97 | 3.25 | 0.97 | 0.66 |
| | TDR 2 | 1.28 | 0.16 | 1.33 | 0.16 | 27.98 | 3.99 | 0.98 | 0.62 |
| | TDR 3 | 1.15 | 0.17 | 1.42 | 0.17 | 18.08 | 3.52 | 0.98 | 0.74 |
| | TDR 4 | 1.08 | 0.16 | 1.30 | 0.16 | 32.11 | 4.12 | 0.98 | 0.75 |
| | TDR 5 | 0.88 | 0.18 | 1.25 | 0.17 | 34.65 | 4.12 | 0.99 | 0.82 |
| | TDR 6 | 1.57 | 0.11 | 1.81 | 0.11 | 12.26 | 3.35 | 0.96 | 0.58 |
| | TDR 7 | 1.23 | 0.18 | 1.28 | 0.18 | 25.39 | 3.78 | 0.98 | 0.73 |
| | TDR 8 | 1.23 | 0.12 | 1.56 | 0.11 | 22.45 | 4.03 | 0.93 | 0.62 |
| | TDR 9 | 1.15 | 0.17 | 1.28 | 0.18 | 27.33 | 3.87 | 0.98 | 0.64 |
| | TDR 10 | 0.63 | 0.21 | 1.07 | 0.19 | 85.41 | 4.72 | 0.98 | 0.77 |
| | TDR 11 | 1.39 | 0.13 | 1.32 | 0.14 | 41.48 | 4.52 | 0.97 | 0.59 |
| | TDR 12 | 1.29 | 0.16 | 1.32 | 0.16 | 28.43 | 3.99 | 0.98 | 0.61 |
| | TDR 14 | 1.00 | 0.18 | 1.32 | 0.17 | 24.15 | 3.77 | 0.98 | 0.87 |
| | TDR 15 | 0.87 | 0.24 | 1.18 | 0.23 | 21.15 | 3.42 | 0.98 | 0.94 |
| | TDR 16 | 0.91 | 0.21 | 1.22 | 0.21 | 22.72 | 3.56 | 0.98 | 0.85 |

In Figure 4.2-8 is presented scaling of $\langle \varepsilon_\lambda^p \rangle$ for different values of p (0.1, 1.01, 1.5, 2.0, 2.5) and for all measurements obtained. Dielectric constant increments and discharge increments data are calculated from the original measurements presented in Figure 4.2-7. Figure 4.2-8 shows satisfactory scaling for all measurements presented, which is rated by means of the best and the worst R^2 parameters related to different values of p (see Table 4.2-1). In all cases the worst scaling corresponds to $p = 0.1$ due to the numerous zeros or rather small values of the investigated field.

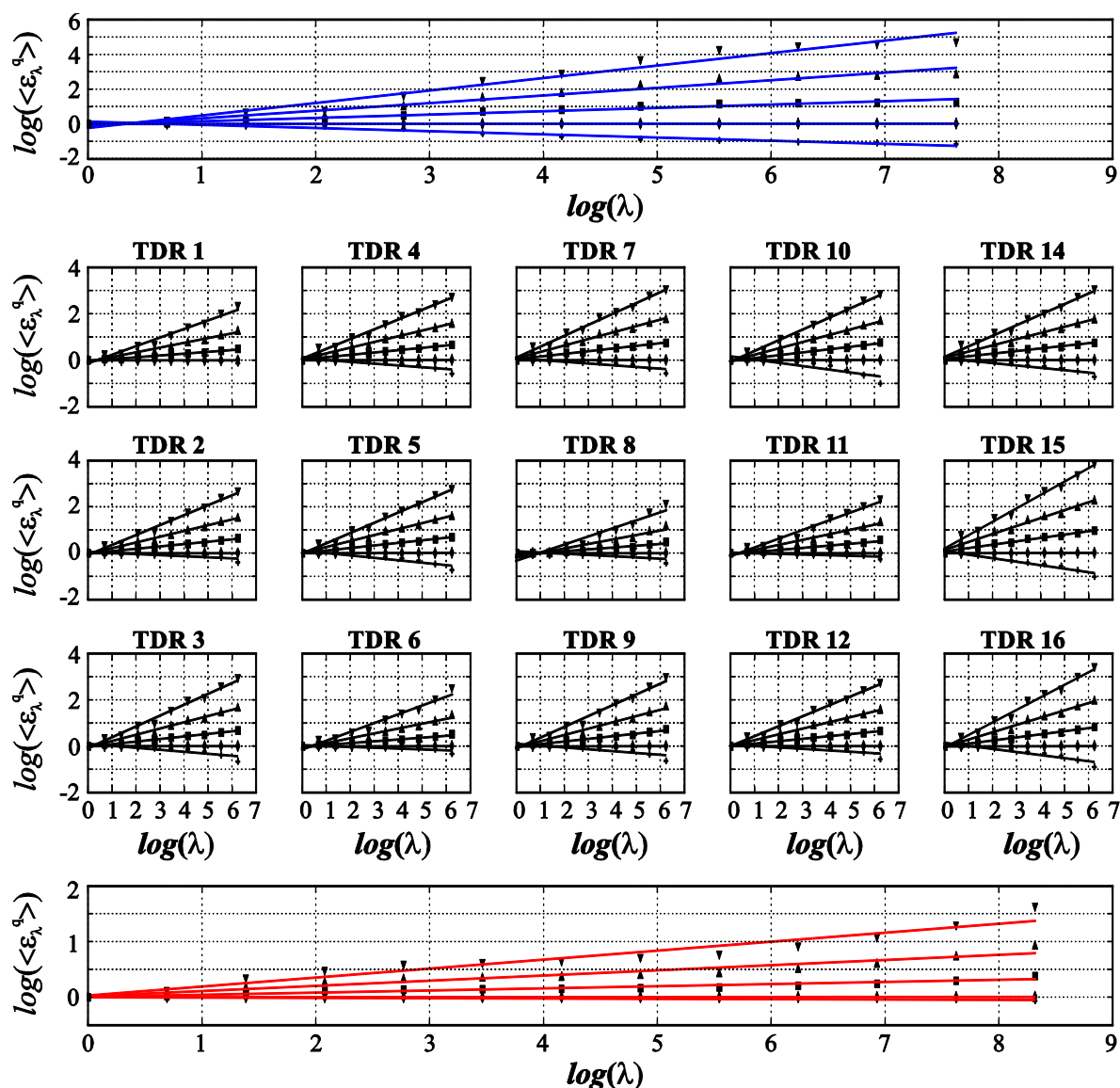


Figure 4.2-8. Scaling of the average statistical moments of order p ($\langle \varepsilon_\lambda^p \rangle$) applied on data of event 1. Subplots are distributed the same way as in Figure 4.2-7, with the following symbols representing values of $\langle \varepsilon_\lambda^p \rangle$ for: \blacktriangledown ($p = 3.0$), \blacktriangle ($p = 2.5$), \blacksquare ($p = 1.5$), \blacklozenge ($p = 1.01$), $+$ ($p = 0.1$)

Following the TM procedure, based on the slopes of linear regressions presented in Figure 4.2-8 the empirical $K(p)$ functions are obtained in Figure 4.2-9. Unsurprisingly, the strongest variability corresponds to rainfall measurements, intermediate variabilities correspond to dielectric constant increments, while the lowest variability is related to discharge increments. In this case green roof behaves as a filter that mitigates strong fluctuations of rainfall, providing attenuated fluctuations of discharge increments by draining the water through the substrate layer. By means of Equations (4.2-7) and (4.2-8) that are applied on the obtained empirical $K(p)$ curves, values of α_{TM} and $C_{I,TM}$ are determined (see Table 4.2-1), and thus the obtained $K(p)$ functions can be characterized using the analytical curve (Equation 4.2-4).

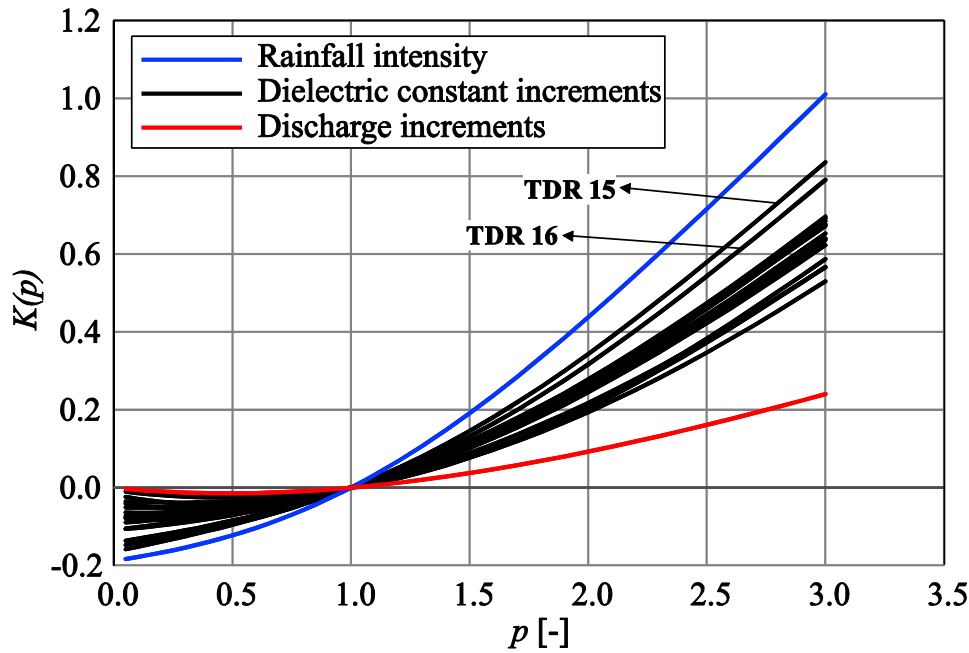


Figure 4.2-9. Empirical $K(p)$ functions obtained for rainfall intensity, dielectric constant increments and discharge increments data (event 1)

Based on the curves presented in Figure 4.2-9, one can also try to make some conclusions concerning the lateral water movement along the roof inclination. It is rather difficult to predict the impact of the lateral water exchange on the variabilities of water content increments along the slope, due to the fact that besides the inflow coming from the rainfall, there is an inflow coming from the higher roof altitudes as well as the outflow towards the lower roof altitudes. Thus, the fluctuations of water content increments can be both amplified or mitigated by the green roof substrate, depending on the inflow-outflow dynamics. However, it seems reasonable to expect that this variability should be closer to that of the rainfall at the flat part of the roof, compared to locations on the slope. Thus, if $K(p)$ function related to the dielectric constant increments at roof's bottom is similar to that of the rainfall, it can be concluded that the lateral water flow within the substrate layer is not important. This is exactly the case in Figure 4.2-9, where $K(p)$ functions for TDR sensors located at the bottom of the slope (TDR 15 and 16) are the closest to that of the rainfall.

In order to determine UM parameters by means of another technique (DTM), the scaling behavior of average moments $\langle \varepsilon_{\lambda}^{(\eta)p} \rangle$ for 4 different η values (0.81, 1.23, 1.87, 2.84) is presented in Figure 4.2-10, where $p = 1.5$ is adopted. Rather good scaling is obtained for all measurements. Following the DTM procedure, based on the slopes of linear regressions presented in Figure 4.2-10, $K(p, \eta)$ function is obtained in Figure 4.2-11. Solid line in each subplot of Figure 4.2-11 indicates the linear section of the graph used for calculating UM parameters by means of Equations (4.2-17) and (4.2-18). Values of determined $C_{1,DTM}$ and α_{DTM} are presented in Table 4.2-1.

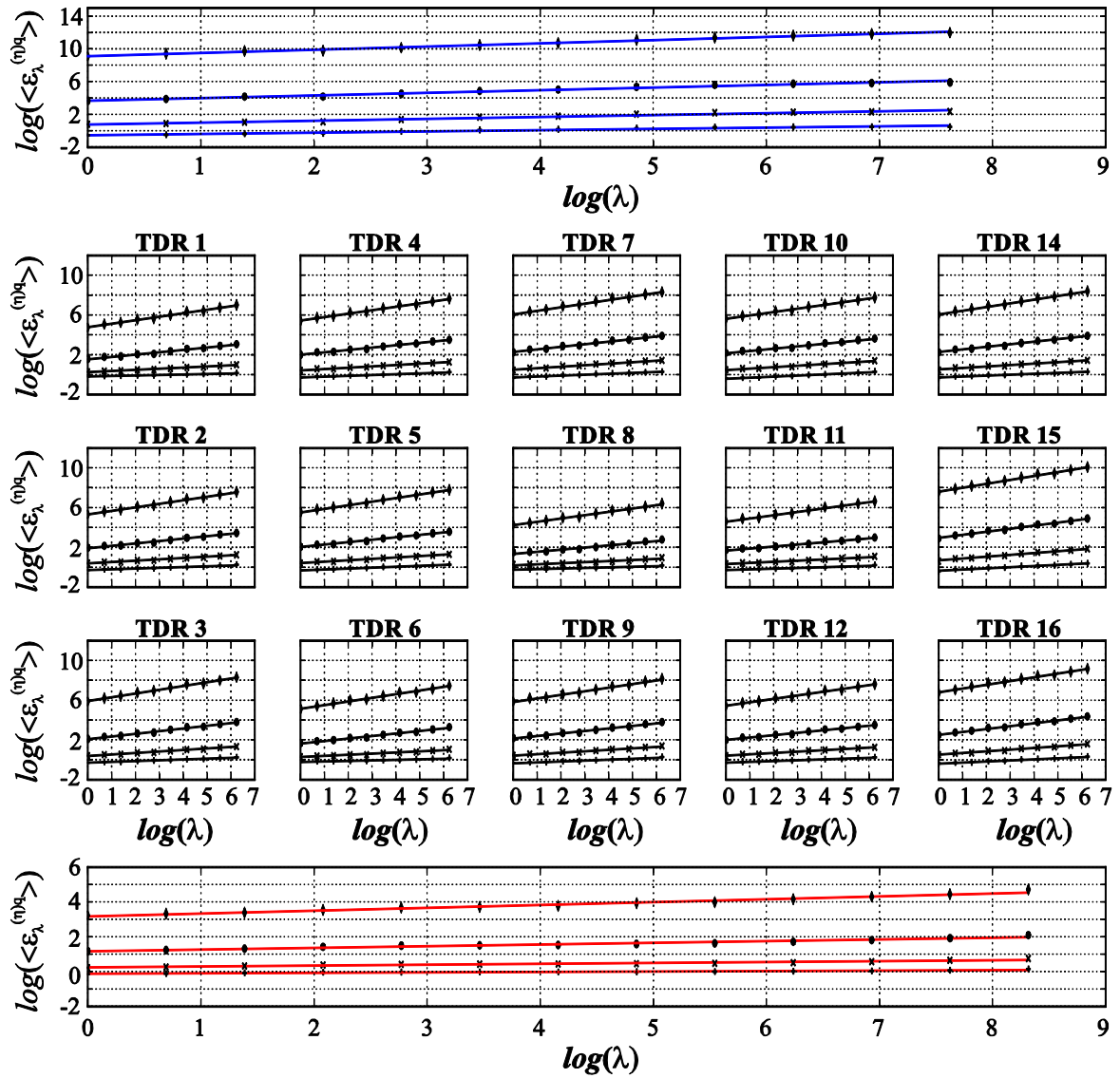


Figure 4.2-10. Results of DTM technique applied on data of event 1 – $\log(\langle \varepsilon_\lambda^{(n)p} \rangle)$ versus $\log(\lambda)$. Subplots are distributed the same was as in Figure 4.2-7, with the following symbols representing values of $\langle \varepsilon_\lambda^{(n)p} \rangle$ for $p = 1.5$ and: \blacklozenge ($\eta = 2.84$), \bullet ($\eta = 1.87$), \times ($\eta = 1.23$), $+$ ($\eta = 0.81$)

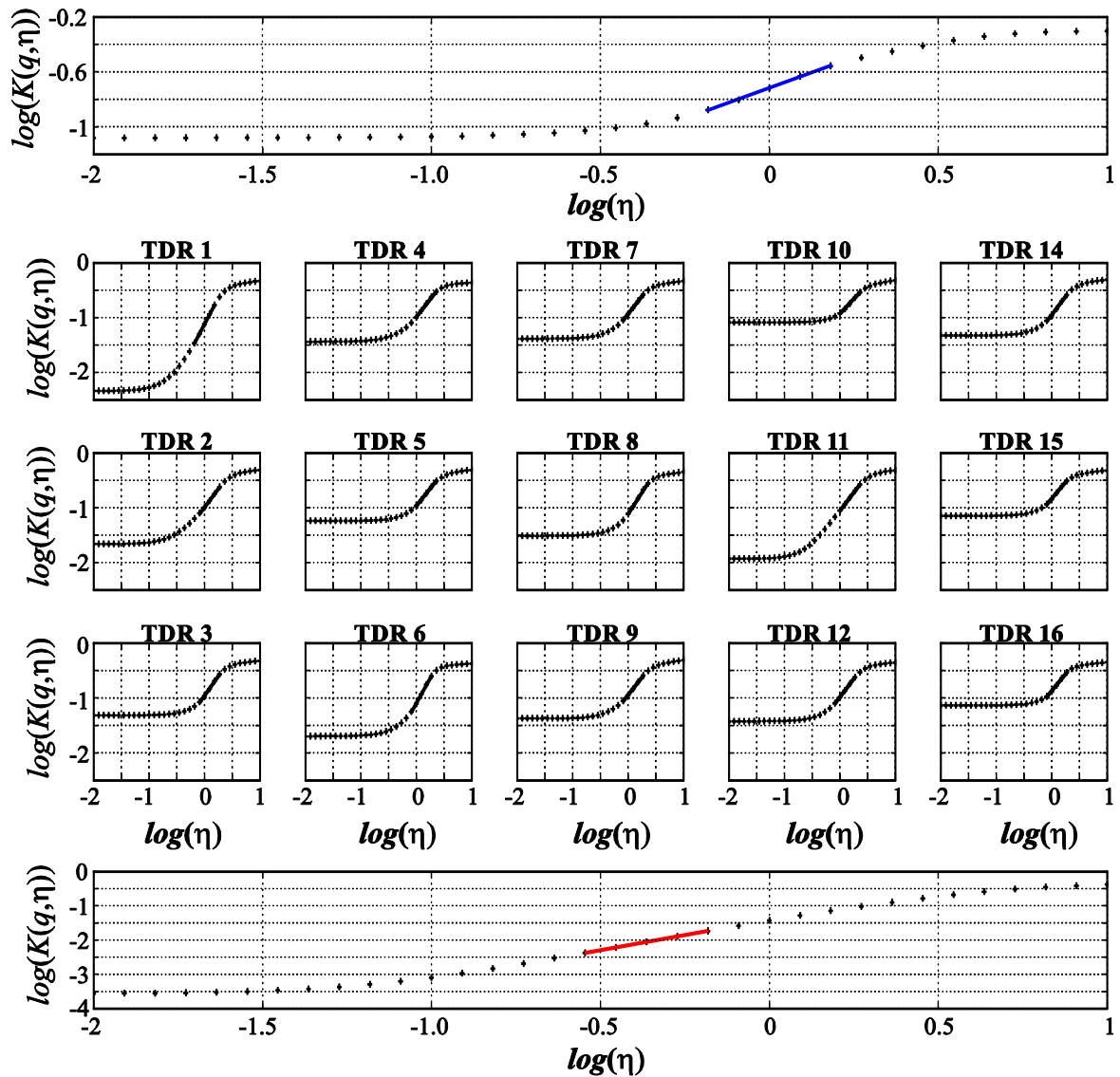


Figure 4.2-11. Results of DTM technique applied on data of event 1 - $\log(K(p, \eta))$ versus $\log(\eta)$ obtained from results presented in Figure 4.2-10. Subplots are distributed the same as in Figure 4.2-7, where solid line in each subplot indicates linear part of the graph from which characteristics UM parameters are determined

Finally, in Figure 4.2-12 are presented empirical $K(p)$ curves from Figure 4.2-9 versus the theoretical ones (Equation 4.2-4) computed by means of α_{TM} , $C_{1, TM}$ (dashed line) and α_{DTM} , $C_{1, DTM}$ (dash-dotted line). Clearly, DTM technique provides more reliable values of UM parameters since the corresponding curves ($K(p)_{DTM}$ - dash-dotted lines) show better agreement with empirical ones. Thus, values of α_{DTM} and $C_{1, DTM}$ are considered as more reliable for calculating critical value p_c by means of Equation (4.2-9) and (4.2-11). As expected, $p_c = p_s$ for all the measurements presented (see Table 4.2-1), since only a single data sample per measurement is used ($N_{sample} = 1$). Also, following the previously made explanation, a good agreement between theoretical $K(p)_{DTM}$ (dash-dotted line) and empirical $K(p)$ (solid line) functions is obtained for $p < p_s$ for most of the measurements. However, due to the presence of zeros or rather small values of investigated field, majority of empirical $K(p)$

functions do not reach zero for $p = 0$, causing deviation from theoretical curves at small p values.

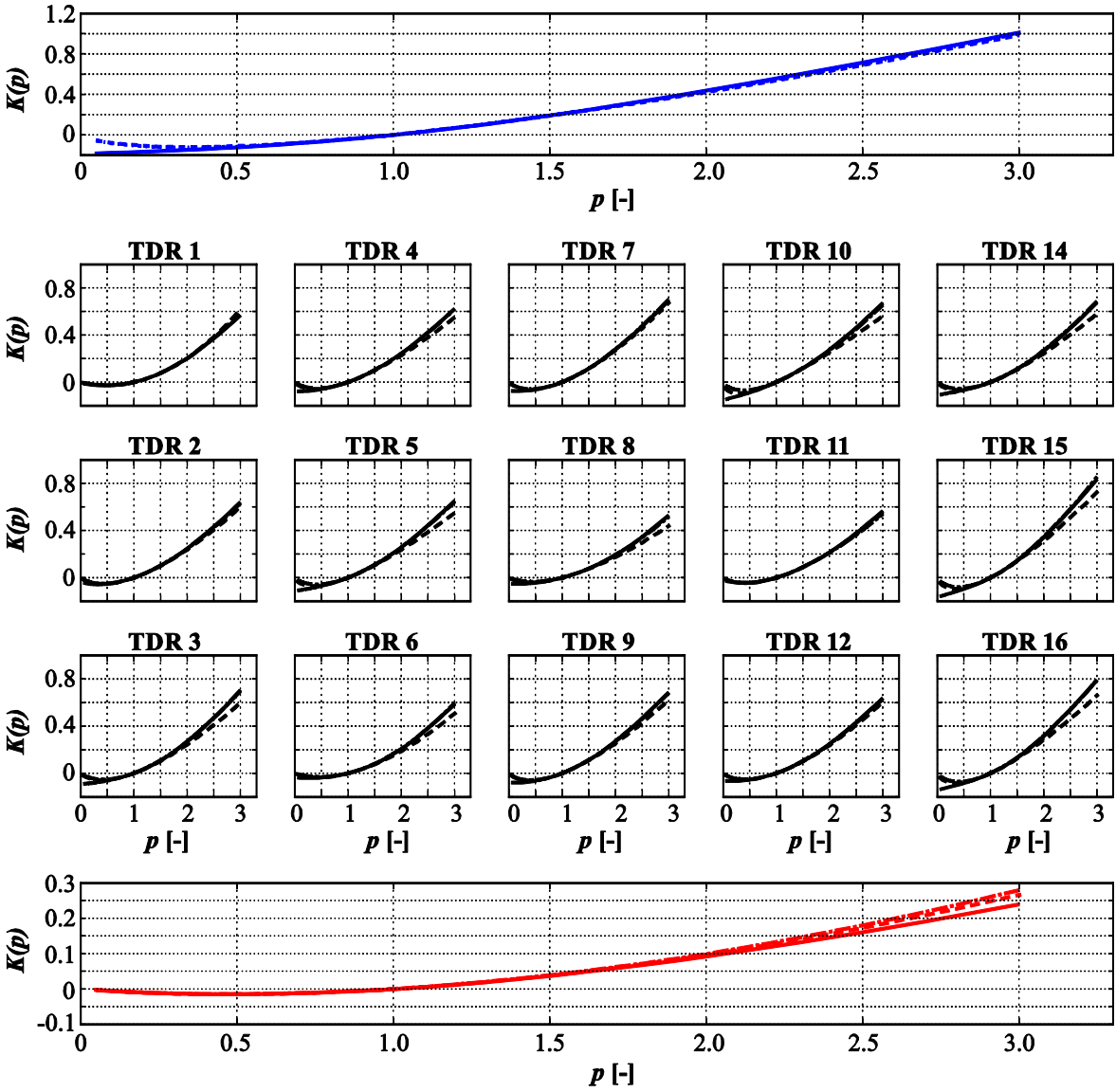


Figure 4.2-12. Comparison between the empirical $K(p)$ curves (solid lines) taken from Figure 4.2-9, and Equation (4.2-4) computed by means of α_{TM} , $C_{1,TM}$ (dashed line) and α_{DTM} , $C_{1,DTM}$ (dash-dotted line). Subplots are distributed the same as in Figure 4.2-7

Event 2 (11.11.2017)

The second event investigated in this study occurred on 11.11.2017 and measurements obtained during this period are presented in Figure 4.2-13 in the same way as done for the first event. In this case only 8 TDR sensors are considered due to the communication issues between the data-logger and the rest of TDRs. Duration of the rainfall event is about 34 h, and thus the total number of data used is 4096, 512 and 4096 for the rainfall, dielectric constant increments and discharge increments, respectively. The total amount of rainfall is 14 mm.

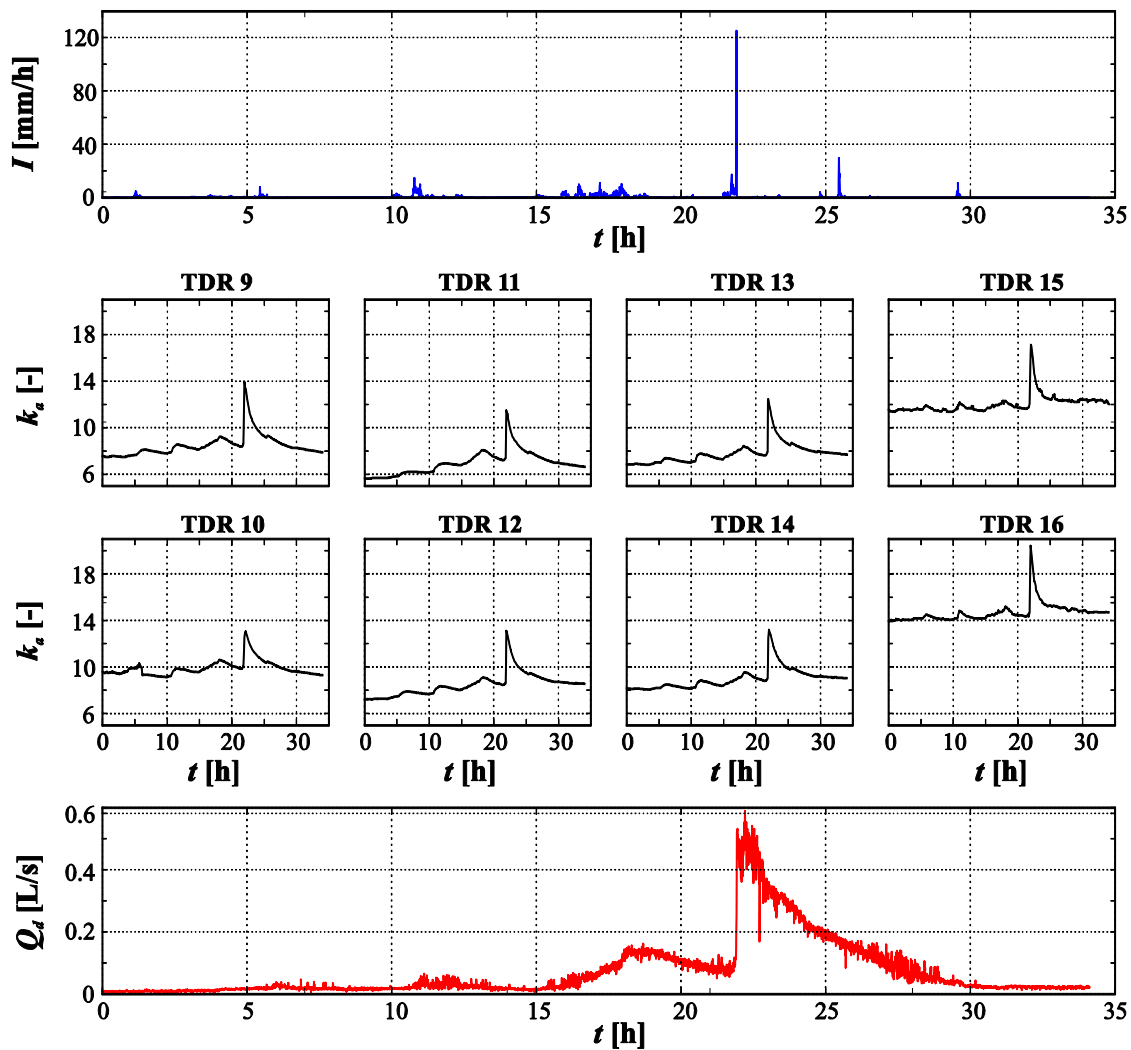


Figure 4.2-13. Data of the rainfall intensity (top subplot), dielectric constant (8 subplots in the center corresponding to 8 TDR sensors) and drained discharge (bottom subplot) captured during event 2 (11.11.2017)

In this case the quality of scaling is satisfactory as for event 1 (Figure 4.2-8), and thus the empirical $K(p)$ functions are obtained following the previously made explanation – see Figure 4.2-14. Again, $K(p)$ of discharge increments is significantly below that of rainfall, while $K(p)$ functions related to dielectric constant increments are mostly located between the two, with exception of one curve that is even above that of rainfall. $K(p)$ functions linked to TDRs located at the bottom (TDR 16) and the top flat part of the slope (TDR 9) show rather similar behavior as $K(p)$ for the rainfall, indicating once again insignificant impact of the roof inclination on the lateral water flow.

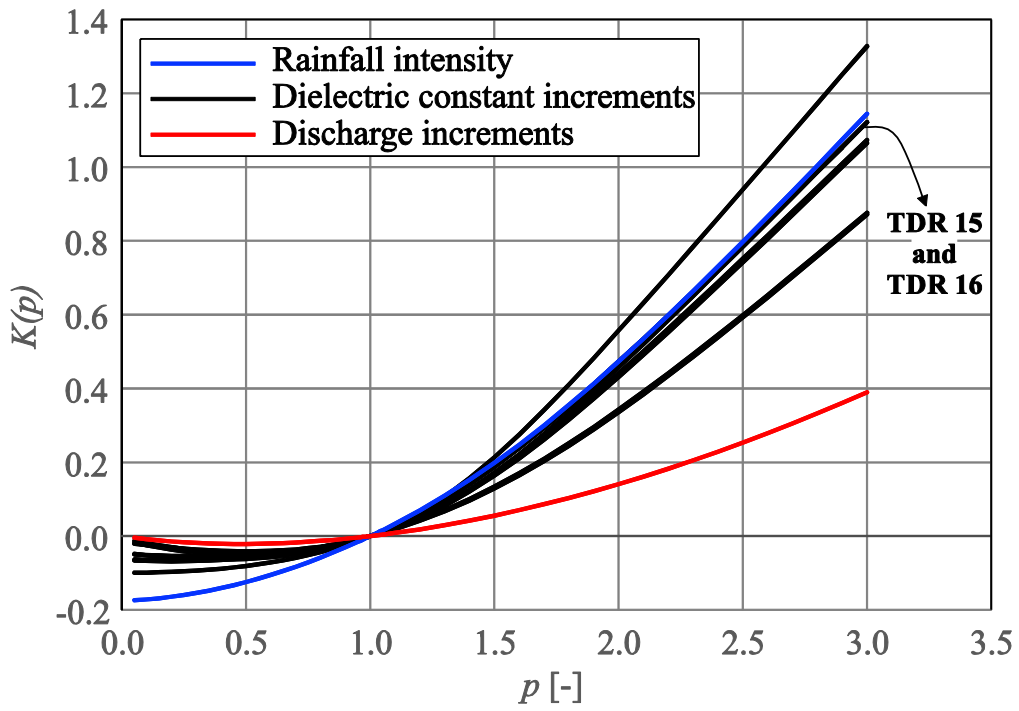


Figure 4.2-14. Empirical $K(p)$ functions obtained for rainfall intensity, dielectric constant increments and discharge increments data (event 2)

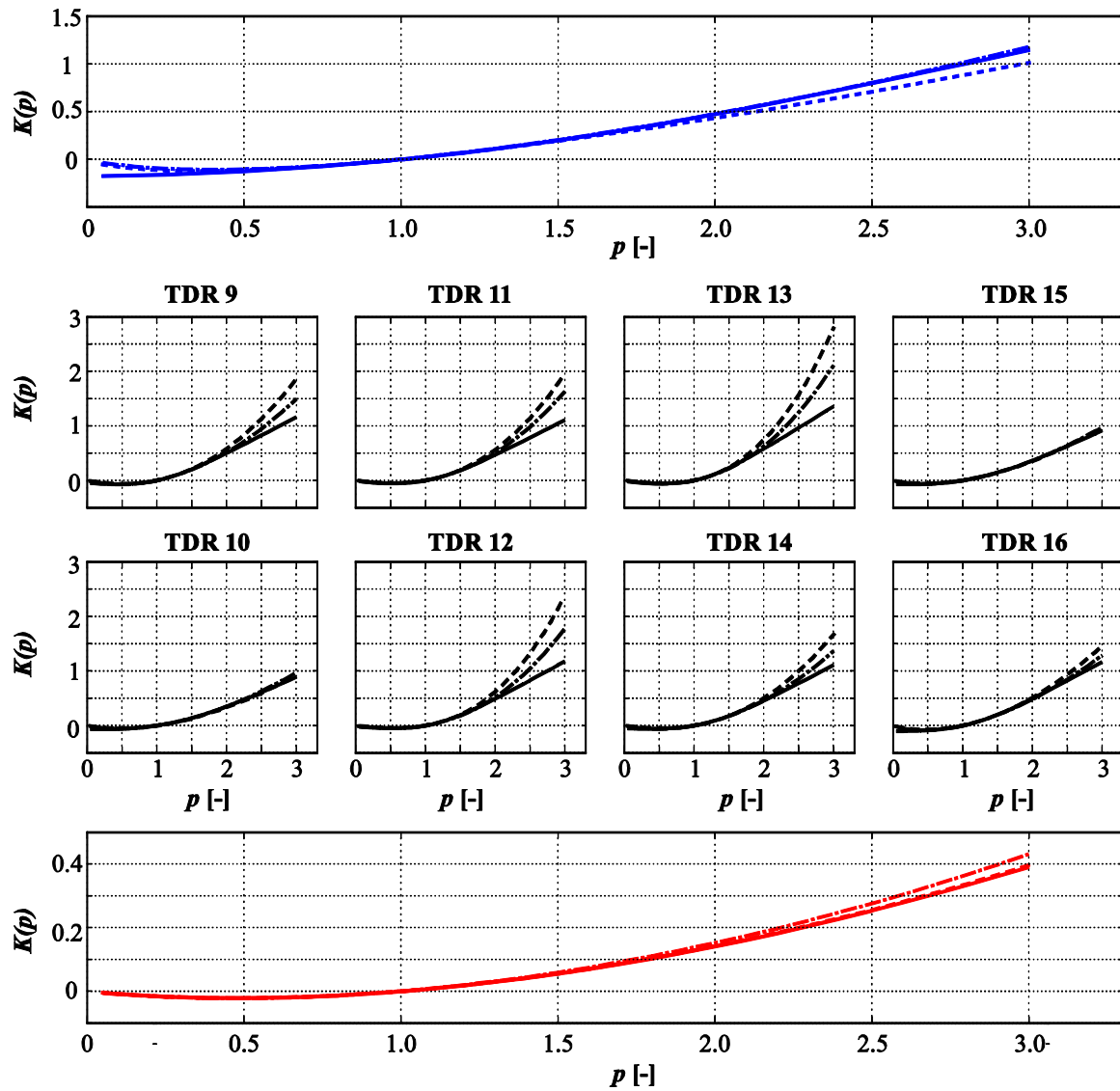


Figure 4.2-15. Comparison between the empirical $K(p)$ curves (solid lines) taken from Figure 4.2-14, and Equation (4.2-4) computed by means of α_{TM} , $C_{1,TM}$ (dashed line) and α_{DTM} , $C_{1,DTM}$ (dash-dotted line). Subplots are distributed the same as in Figure 4.2-13

By computing UM parameters using both TM (Equations 4.2-7 and 4.2-8) and DTM (Equations 4.2-17 and 4.2-18) techniques, it has been shown that parameter α is higher than 2 (the theoretical maximum) for 5/8 and 3/8 of TDRs, respectively (see Table 4.2-2). This shows that the two mentioned techniques are facing some issues when applied on a field with a single dominant extreme, such as the case with the dielectric constant increments of event 2. Based on the obtained values of α_{DTM} that are smaller than 2, it is possible to compute p_c which appears to be equal to p_s for all measurements presented (see Table 4.2-2). Values of p_s are lower than those in case of event 1, and thus the deviation between theoretical and empirical $K(p)$ functions is observable in Figure 4.2-15 for $p \approx 2 \div 2.5$ in case of dielectric constant increment data. Note that empirical $K(p)$ becomes linear for $p > p_s$.

Table 4.2-2. The same as in Table 4.2-1, just for event 2

| | | a_{TM} | $C_{I,TM}$ | a_{DTM} | $C_{I,DTM}$ | p_D | p_s | R^2_{max} | R^2_{min} |
|-----------------------------|---------------|----------|------------|-----------|-------------|-------|-------|-------------|-------------|
| Rainfall intensity | | 0.92 | 0.32 | 1.19 | 0.32 | 9.38 | 2.60 | 0.98 | 0.97 |
| Discharge increments | | 1.72 | 0.08 | 1.79 | 0.08 | 18.66 | 4.04 | 0.97 | 0.91 |
| Dielectric constant | TDR 9 | 2.25 | 0.26 | 1.87 | 0.27 | 4.14 | 2.01 | 0.98 | 0.70 |
| | TDR 10 | 1.72 | 0.18 | 1.70 | 0.20 | 7.51 | 2.61 | 0.97 | 0.56 |
| | TDR 11 | 2.53 | 0.23 | 2.27 | 0.23 | 3.57 | 1.92 | 0.98 | 0.84 |
| | TDR 12 | 2.88 | 0.22 | 2.48 | 0.22 | 3.28 | 1.86 | 0.98 | 0.70 |
| | TDR 13 | 2.81 | 0.27 | 2.44 | 0.26 | 2.88 | 1.73 | 0.98 | 0.78 |
| | TDR 14 | 2.38 | 0.22 | 1.98 | 0.23 | 4.42 | 2.10 | 0.99 | 0.65 |
| | TDR 15 | 1.68 | 0.20 | 1.58 | 0.21 | 8.29 | 2.67 | 0.99 | 0.65 |
| | TDR 16 | 1.81 | 0.27 | 1.53 | 0.29 | 5.73 | 2.26 | 0.99 | 0.72 |

Event 3 (25.08.2017)

The third event occurred on 25.08.2017 and the corresponding measurements are presented in *Figure 4.2-16*. Nine TDRs, distributed as illustrated in *Figure 4.2-6b*, are used in this case. The event lasted only couple of hours, with the total amount of rainfall equal to 28 mm. Characteristic for this event is the non-conservative rainfall intensity field (*Figure 4.2-16* top), confirmed by means of the energy spectrum analysis. Thus, in order to obtain a conservative field, rainfall intensities were analyzed in the form of increments, as done with dielectric constant and discharge measurements. Furthermore, rainfall intensity increments and discharge increments are analyzed only during the first 2.5 h (256 data), while the dielectric constant increments are analyzed during a longer time period (9 h - 128 data).

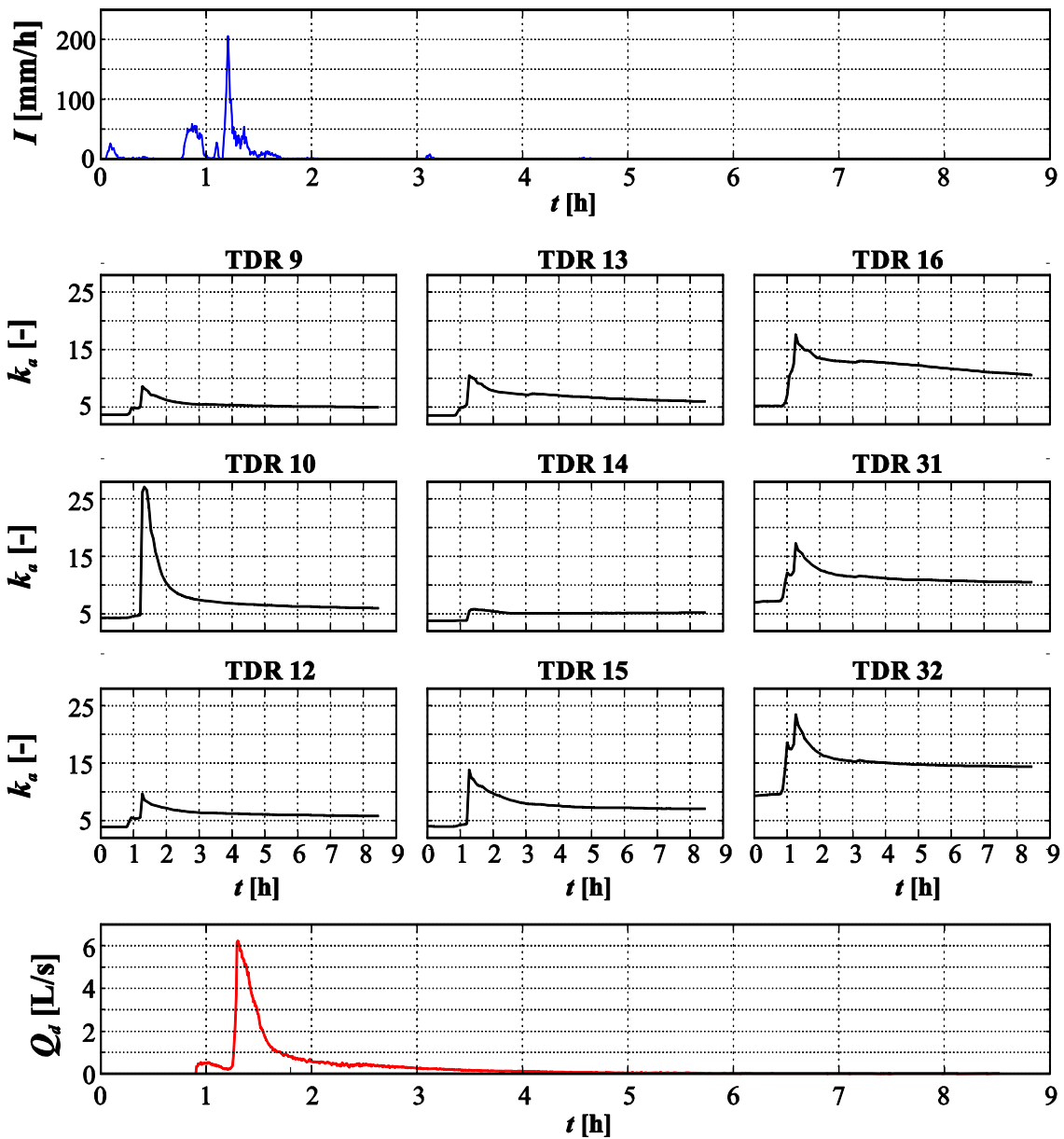


Figure 4.2-16. Data of the rainfall intensity (top subplot), dielectric constant (9 subplots in the center corresponding to 9 TDR sensors) and drained discharge (bottom subplot) captured during event 3 (25.08.2017)

As for the two previous events, scaling quality of $\langle \varepsilon_\lambda^p \rangle$ is considered as satisfactory, and thus the empirical $K(p)$ functions are obtained – see Figure 4.2-17. In this case it is not relevant to compare $K(p)$ functions of discharge and dielectric constant increments with that of the rainfall, due to the fact that rainfall increments are analyzed instead of the original data. However, due to the fact that change of water content is analyzed over a 9 h period, within which 6.5 h is without rainfall (> 70 %), it is possible to make some conclusions based on the draining process. During the dry period, if the lateral water movement exists, it is reasonable to expect that the fluctuations of water content (dielectric constant) increments are progressively attenuated in downstream direction due to the drainage process, securing that way the smoothest fluctuations at slope’s bottom. Figure 4.2-17 shows that TDRs located at

the bottom of the slope (TDR 31 and TDR 32) show the most attenuated fluctuations, and thus their $K(p)$ curves are the closest to that of the discharge increments. Having on mind the two previous events (1 and 2), and the fact that both rainfall and drained discharge are almost zero for $t > 2.5$ h in event 3, it can be concluded that the roof inclination does not affect the peak outflow from the substrate bottom, but it impacts the redistribution of the water quantity retained in the substrate along the roof inclination. This mostly occurs during the period with no rainfall, which is why initially, before each event, higher values of water content can be observed at slope's bottom compared to those at the top (see *Figure 4.2-7*, *Figure 4.2-13*, *Figure 4.2-16*). Similar conclusions concerning the impact of roof inclination on water movement were made by Bengtsson (2005), among the others.

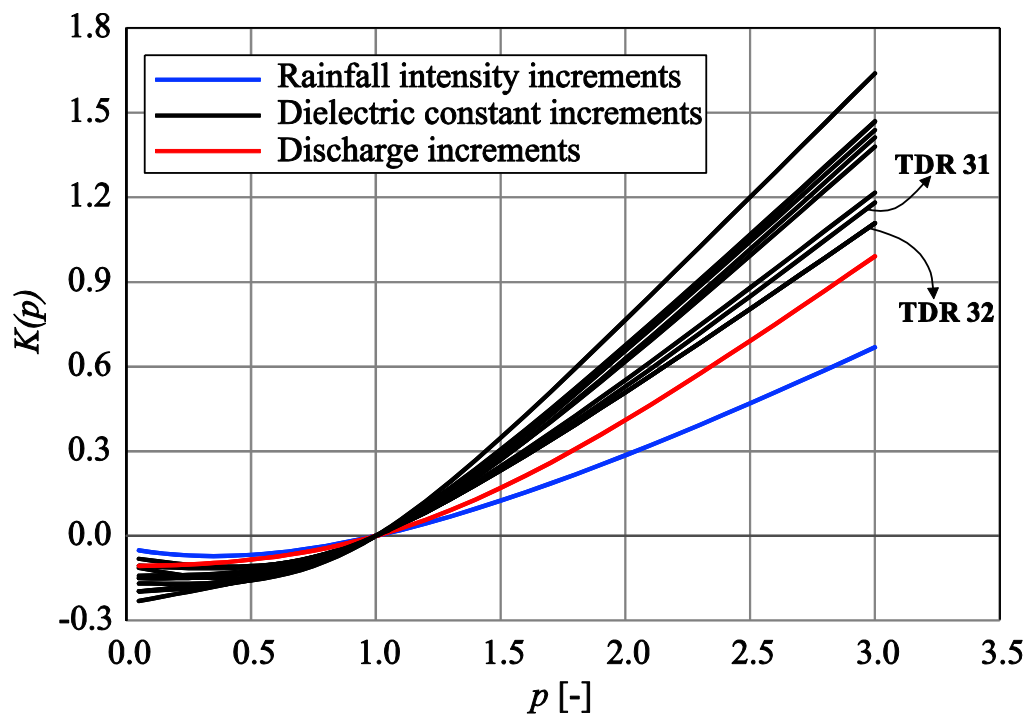


Figure 4.2-17. Empirical $K(p)$ functions obtained for rainfall intensity, dielectric constant increments and discharge increments data (event 3)

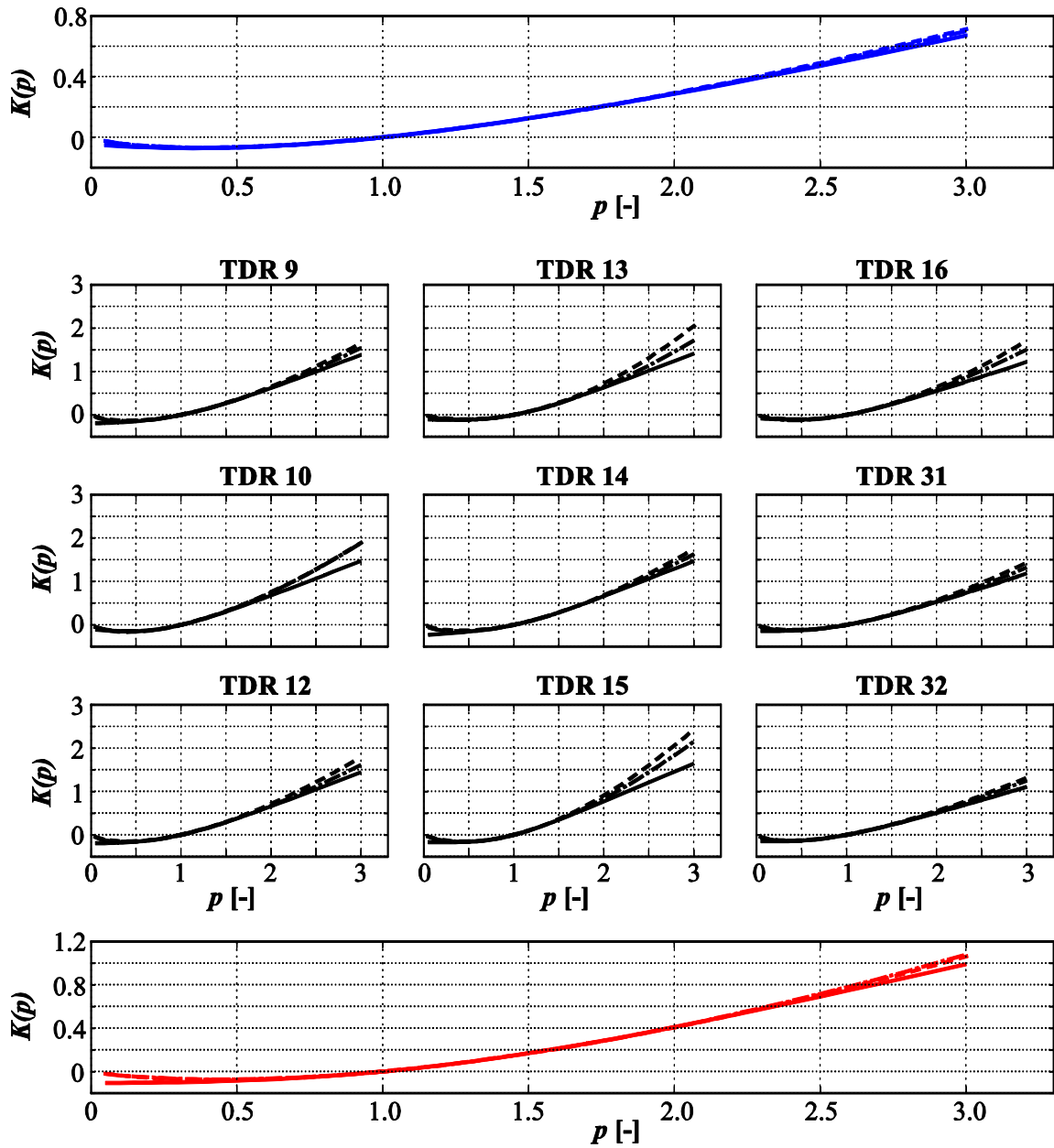


Figure 4.2-18. Comparison between the empirical $K(p)$ curves (solid lines) taken from Figure 4.2-17, and Equation (4.2-4) computed by means of α_{TM} , $C_{1,TM}$ (dashed line) and α_{DTM} , $C_{1,DTM}$ (dash-dotted line). Subplots are distributed the same as in Figure 4.2-16

In case of event 3, UM parameters and p_c (equal to p_s) are determined following the same procedures as for the two remaining events, and their values are presented in Table 4.2-3. Again, the deviation between theoretical and empirical $K(p)$ functions is observable in Figure 4.2-18 for $p \approx 1.5 \div 2.5$ and $p \approx 2.5$ in case of dielectric constant increments and discharge increments, respectively.

Table 4.2-3. The same as in Table 4.2-1 and Table 4.2-2, just for event 3

| | | α_{TM} | $C_{L,TM}$ | α_{DTM} | $C_{L,DTM}$ | p_s | p_D | R^2_{max} | R^2_{min} |
|-----------------------------|---------------|---------------|------------|----------------|-------------|-------|-------|-------------|-------------|
| Rainfall intensity | | 1.13 | 0.20 | 1.12 | 0.20 | 48.72 | 4.24 | 0.99 | 0.92 |
| Discharge increments | | 1.43 | 0.25 | 1.48 | 0.25 | 7.86 | 2.56 | 0.98 | 0.83 |
| Dielectric constant | TDR 9 | 1.30 | 0.42 | 1.17 | 0.43 | 5.19 | 2.08 | 0.99 | 0.87 |
| | TDR 10 | 1.26 | 0.50 | 1.32 | 0.48 | 3.33 | 1.75 | 0.98 | 0.88 |
| | TDR 12 | 1.26 | 0.47 | 1.08 | 0.47 | 4.97 | 2.02 | 0.99 | 0.87 |
| | TDR 13 | 1.79 | 0.39 | 1.51 | 0.39 | 3.75 | 1.87 | 0.99 | 0.75 |
| | TDR 14 | 1.36 | 0.43 | 1.17 | 0.45 | 4.60 | 1.98 | 0.99 | 0.92 |
| | TDR 15 | 1.55 | 0.54 | 1.39 | 0.52 | 2.67 | 1.60 | 0.99 | 0.93 |
| | TDR 16 | 1.54 | 0.38 | 1.31 | 0.38 | 5.02 | 2.08 | 0.98 | 0.72 |
| | TDR 31 | 1.27 | 0.37 | 1.14 | 0.37 | 7.59 | 2.39 | 0.98 | 0.84 |
| | TDR 32 | 1.07 | 0.38 | 0.99 | 0.38 | 11.42 | 2.66 | 0.97 | 0.85 |

4.2.5. Conclusion

In this work a new application of Universal Multifractals is presented. It has been shown that this theoretical framework can be rather convenient for assessing behavior of green roofs based on the analysis of in-situ measurements of three water balance components: rainfall intensity, water content and drained discharge. The methodology has been performed on Green Wave, for three different rainfall events.

By using monitored data of the three water balance components, the moment scaling functions $K(p)$ are obtained based on the scaling behavior of average statistical moments of order p . In this work it has been shown that a comparison between $K(p)$ curves related to different components of water balance helps assessing the hydrological behavior of green roofs. It was confirmed that green roof behaves as a filter that mitigates strong variability of the rainfall, providing attenuated fluctuations of the outflow drained from its bottom. Concerning the variabilities of water content increments, results show that they can be used for checking the influence of the roof inclination on the lateral water movement by comparing $K(p)$ related to the water content increments at slope's bottom with $K(p)$ for the rainfall. If those two functions are relatively close, it is reasonable to assume that solely rainfall affects the change of water content, and there is no lateral inflow coming from the higher altitudes of the roof. This is the case for events 1 and 2 analyzed in this work. Furthermore, the impact of roof's inclination has been also analyzed during the dry period right after the high intensity rainfall of short duration – event 3. Results showed that $K(p)$ functions related to the water content increments at slope's bottom are the most attenuated and the closest to $K(p)$ of drained

discharge increments, indicating that the roof inclination gradually mitigates the fluctuations of the water content increments in the downstream direction. Finally, based on the three events analyzed, it was concluded that the infiltration through Green Wave substrate layer is dominantly vertical, with negligible influence of roof's inclination on the lateral flow and hence outflow drained from the substrate, but with more significant impact on the redistribution of retained water along the slope during the dry period.

Concerning the techniques for determination of UM parameters that characterize mentioned empirical $K(p)$ functions (obtained from measurements), it was confirmed that DTM technique provides more reliable estimation than TM. Also, determination of the critical moment order p_c based on the values of UM parameters determined through DTM, appeared to be in agreement with the point where theoretical and empirical $K(p)$ curves deviate. However, in most of the cases neither DTM nor TM are able to interpret properly empirical $K(p)$ curve for small p values, due to the non-negligible presence of zeros or rather small values of the investigated field. Also, the both techniques are facing some difficulties in case of strongly variable fields that have one dominant extreme, as the case of dielectric constant increments in event 2. As a result, the estimated values of α overcome the maximal theoretical value of 2, for about 50 % of TDR sensors used. In order to improve the reliability of the UM framework as a statistical tool and further consolidate physically-based conclusions presented in this work, more data samples and more characteristic rainfall events should be analyzed.

4.2.6. References:

- Bengtsson, L. 2005. "Peak Flows from Thin Sedum-Moss Roof." *Nordic Hydrology* 36 (3): 269–80.
- Berndtsson, J. C. 2010. "Green Roof Performance towards Management of Runoff Water Quantity and Quality : A Review." *Ecological Engineering* 36 (4): 351–60. <https://doi.org/10.1016/j.ecoleng.2009.12.014>.
- Fassman-Beck, E., E. Voyde, R. Simcock, and Y. Sing. 2013. "4 Living Roofs in 3 Locations : Does Configuration Affect Runoff Mitigation ?" *Journal of Hydrology* 490: 11–20. <https://doi.org/10.1016/j.jhydrol.2013.03.004>.
- Francis, L. F. M., and M. B. Jensen. 2017. "Benefits of Green Roofs : A Systematic Review of the Evidence for Three Ecosystem Services." *Urban Forestry & Urban Greening*. <https://doi.org/10.1016/j.ufug.2017.10.015>.
- Frisch, U., and G. Parisi. 1985. "A Multifractal Model of Intermittency." *Turbulence and Predictability in Geophysical Fluid Dynamics and Climate Dynamics*, 84–88.
- Gires, A., I. Tchiguirinskaia, D. Schertzer, and S. Lovejoy. 2013. "Development and Analysis of a Simple Model to Represent the Zero Rainfall in a Universal Multifractal Framework." *Nonlinear Processes in Geophysics* 20: 343–56. <https://doi.org/10.5194/npg-20-343-2013>.
- Hakimdavar, R., P. J. Culligan, M. Finazzi, S. Barontini, and R. Ranzi. 2014. "Scale Dynamics of Extensive Green Roofs : Quantifying the Effect of Drainage Area and Rainfall Characteristics on Observed and Modeled Green Roof Hydrologic Performance." *Ecological Engineering* 73: 494–508.

-
- <https://doi.org/10.1016/j.ecoleng.2014.09.080>.
- Kantelhardt, J. W., D. Rybski, S. A. Zschiegner, P. Braun, E. Koscielny-Bunde, V. Livina, S. Halvin, and A. Bunde. 2003. "Multifractality of River Runoff and Precipitation : Comparison of Fluctuation Analysis and Wavelet Methods." *Physica A* 330: 240–45. <https://doi.org/10.1016/j.physa.2003.08.019>.
- Lavallée, D., S. Lovejoy, D. Schertzer, and P. Ladoy. 1993. "Nonlinear Variability and Landscape Topography: Analysis and Simulation." In *Fractals in Geography*, 158 – 192.
- Lavallée, D., S. Lovejoy, D. Schertzer, and F. Schmitt. 1992. "ON THE DETERMINATION OF UNIVERSAL MULTIFRACTAL PARAMETERS IN TURBULENCE." In *Topological Aspects of the Dynamics of Fluids and Plasmas*, edited by H. K. Moffatt, G. M. Zaslavsky, P. Comte, and M. Tabor, 463–78. Springer, Dordrecht. https://doi.org/10.1007/978-94-017-3550-6_27.
- Li, Y., and R. W. Jr. Babcock. 2014. "Green Roof Hydrologic Performance and Modeling: A Review." *Water Science & Technology* 69 (4): 727–38. <https://doi.org/10.2166/wst.2013.770>.
- . 2016. "A Simplified Model for Modular Green Roof Hydrologic Analyses and Design." *Water* 8 (343): 1–13. <https://doi.org/10.3390/w8080343>.
- Liu, H. H., and F. J. Molz. 1997. "Multifractal Analyses of Hydraulic Conductivity Distributions." *Water Resources Research* 33 (11): 2483–88. <https://doi.org/10.1029/97WR02188>.
- Lovejoy, S., and D. Schertzer. 1995. "Multifractals and Rain." In *New Uncertainty Concepts in Hydrology and Water Resources*, edited by Z. Kundzewicz, 61–103. Cambridge University Press. <https://doi.org/10.1017/CBO9780511564482.009>.
- Morató, M. C., M. T. Castellanos, N. R. Bird, and A. M. Tarquis. 2016. "Geoderma Multifractal Analysis in Soil Properties : Spatial Signal versus Mass Distribution." *Geoderma*. <https://doi.org/10.1016/j.geoderma.2016.08.004>.
- Olsson, J., and J. Niemczynowicz. 1996. "Multifractal Analysis of Daily Spatial Rainfall Distributions." *Journal of Hydrology* 187: 29–43.
- Palla, A., I. Gnecco, and L. G. Lanza. 2009. "Unsaturated 2D Modelling of Subsurface Water Flow in the Coarse-Grained Porous Matrix of a Green Roof." *Journal of Hydrology* 379 (1–2): 193–204. <https://doi.org/10.1016/j.jhydrol.2009.10.008>.
- Paz, I., A. Gires, I. Tchiguirinskaia, D. Schertzer. 2016. "Quantitative comparison of the rainfall data resulting from C-band and X-band radar measurements to study the impact of small scale rainfall variability over the SIAVB catchement." Report for Veolia.
- Schertzer, D., and S. Lovejoy. 1987. "Physical Modeling and Analysis of Rain and Clouds by Anisotropic Scaling Multiplicative Processes." *Journal of Geophysical Research* 92: 9693–9714.
- . 1992. "Hard and Soft Multifractal Processes." *Physica A* 185: 187–94.
- . 1993. "Nonlinear Variability in Geophysics 3 - Scaling and Multifractal Processes." In *AGU Chapman / EGS Richardson Memorial Conference*.
- . 1997. "Universal Multifractals Do Exist!: Comments on 'A Statistical Analysis of Mesoscale Rainfall as a Random Cascade.'" *Journal of Applied Meteorology* 36: 1296–1303.
-

-
- . 2011. “MULTIFRACTALS , GENERALIZED SCALE INVARIANCE AND COMPLEXITY IN GEOPHYSICS.” *International Journal of Bifurcation and Chaos* 21 (12): 3417–56. <https://doi.org/10.1142/S0218127411030647>.
- Schertzer, D., S. Lovejoy, and D. Lavallée. 1993. “Generic Multifractal Phase Transitions and Self-Organized Criticality.” *Phys. Rev. Lett.*, 216–27.
- Schmitt, F. G., D. Schertzer, S. Lovejoy, and Y Brunet. 1993. “Estimation of Universal Multifractal Indices for Atmospheric Turbulent Velocity Fields.” *Fractals* 1 (3): 568–75. <https://doi.org/10.1142/S0218348X93000599>.
- Stanić, F., Y.-J. Cui, P. Delage, E. De Laure, P.-A. Versini, D. Schertzer, and I. Tchiguirinskaia. 2019. “A Device for the Simultaneous Determination of the Water Retention Properties and the Hydraulic Conductivity Function of an Unsaturated Coarse Material ; Application to a Green- Roof Volcanic Substrate.” *Geotechnical Testing Journal*. <https://doi.org/10.1520/GTJ20170443>.
- Stovin, V., S. Poë, S. De-ville, and C. Berretta. 2015. “The Influence of Substrate and Vegetation Configuration on Green Roof Hydrological Performance.” *Ecological Engineering* 85: 159–72. <https://doi.org/10.1016/j.ecoleng.2015.09.076>.
- Stovin, V., G. Vesuviano, and H. Kasmin. 2012. “The Hydrological Performance of a Green Roof Test Bed under UK Climatic Conditions.” *Journal of Hydrology* 414–415: 148–61. <https://doi.org/10.1016/j.jhydrol.2011.10.022>.
- Tchiguirinskaia, I., D. Schertzer, C. T. Hoang, and S. Lovejoy. 2011. “Multifractal Study of Three Storms with Different Dynamics over the Paris Region.” In *12nd International Conference on Urban Drainage*. Porto Alegre (Brazil).
- Tessier, Y., S. Lovejoy, P. Hubert, D. Schertzer, and S. Pecknold. 1996. “Multifractal Analysis and Modeling of Rainfall and River Flows and Scaling , Causal Transfer Functions.” *Journal of Geophysical Research* 101 (D21): 426–40. <https://doi.org/10.1029/96JD01799>.
- Tessier, Y., S. Lovejoy, and D. Schertzer. 1993. “Universal Multifractals: Theory and Observations for Rain and Clouds.” *Journal of Applied Meteorology* 32: 223–50.
- Topp, G. C., J. L. Davis, and A. P. Annan. 1980. “Electromagnetic Determination of Soil Water Content:” *Water Resources Research* 16 (3): 574–82.
- Versini, P. -A., A. Gires, I. Tchinguirinskaia, and D. Schertzer. 2016. “Toward an Operational Tool to Simulate Green Roof Hydrological Impact at the Basin Scale: A New Version of the Distributed Rainfall–Runoff Model Multi-Hydro.” *Water Science & Technology* 74 (8): 1845–54. <https://doi.org/10.2166/wst.2016.310>.
- Yang, J., and Z. -H. Wang. 2014. “Physical Parameterization and Sensitivity of Urban Hydrological Models : Application to Green Roof Systems.” *Building and Environment* 75: 250–63. <https://doi.org/10.1016/j.buildenv.2014.02.006>.

5. Hydrological Modeling

The objective of Chapter 5 is to provide reliable substitution for numerical models founded on Richards law, in terms of their physical basis, in order to improve the computational efficiency of hydrological models. Further application of this model, primarily for treating the spatial heterogeneity of green roofs at different scales, remains to be done in near future.

A new analytical and physically-based hydrological model which can be reliably and efficiently applied at different scales (from REV to catchment) is presented in Chapter 5.1. It appears that for coarse materials, such as those used in green roofs, with usual - small thickness and free drainage conditions at the bottom, it is possible to derive through the simplified Richards equation the analytical expression describing the leakage from the non-linear reservoir. The obtained analytical solution is derived by using the new fractal-based hydraulic conductivity function presented in Chapter 3.2, and by assuming dominantly vertical flow, as observed in green roofs (Chapter 4). This confirms the physical-basis of the non-linear reservoir concept, but also gives further insight into its limitations.

As an improvement of the standard non-linear reservoir concept, in Chapter 5.1 is presented a cascade of non-linear reservoirs that are located one below another, where the leakage from one reservoir is the inflow into the one below. The adequate number of reservoirs simulates the dynamics of water release that is not taken into account in standard (non-linear) reservoir-based concepts. Furthermore, results show that the model enables rather reliable and accurate interpretation of the outflows computed by numerically solving Richards equation, if the water drains freely from the bottom side of porous medium. A significant advantage of this concept over standard numerical models is its efficiency. The model also appears to be rather fast and reliable in simulating the long-time series of drained outflows measured on Green Wave.

5.1. A cascade of non-linear reservoirs concept and proof of its physical basis through comparison with Richards equation; application on green roofs

(Ready for submission)

5.1.1. Introduction

One of the main purposes of green roofs is the mitigation of the urban runoff peak (Stovin et al., 2012; Versini et al., 2016). The effectiveness depends on different factors such as: roof configuration (Fassman-Beck et al., 2013), drainage area (Hakimdavar et al., 2014), vegetation type (Stovin et al., 2015), and most importantly, the hydraulic properties of the substrate. This implies that physically-based rainfall-runoff models are necessary to reliably assess the hydrological impacts of green roofs.

Physically-based models, such as HYDRUS 1D (Šimůnek et al., 2008) used by Hilten et al., (2008) and Hakimdavar et al., (2014), or SWMS_2D (Palla et al., 2009; Palla et al., 2011), rely on Richards equation (Richards, 1931), usually in combination with van Genuchten – Mualem functions (van Genuchten, 1980), which is solved numerically. This kind of approach is considered to be the most reliable, and as such, rather useful for designing green roofs. However, it appears extremely time-consuming for performing continuous simulations (long rainfall series) on larger (catchment) scales, if the domain investigated is not homogenized, but treated as a grid of certain resolution, where the hydrological response is calculated for each cell of the grid. This kind of spatial discretization is characteristic for fully distributed hydrological models (Ichiba et al., 2018) that are used to treat the spatial heterogeneity of (sub)catchment, which is of particular interest for the urban storm water management.

Besides the mentioned physically-based models, conceptual models are also used for estimating green roof hydrological impacts. These models are very efficient and can be used for estimating hydrological response of green roofs on a catchment or sub-catchment scale. SCS-CN method is common example of such simple model. It is based on the assumption that actual retention/potential retention is equal to actual runoff/total rainfall (Getter et al., 2007), and is used in SWMM (Carter & Jackson, 2007; Alfredo et al., 2010; Burszta-Adamiak & Mrowiec, 2015), etc. Green Ampt is another widely used method (She & Pang, 2010), also implemented in SWMM, but not quite suitable for modeling green roofs due to the physical assumptions that are found inappropriate for green roof materials. The main assumption of this method is a steep wetting front that is not common for highly permeable coarse materials. In addition, due to high Darcy filtration coefficients of green roof substrates, saturation is rarely reached (for some roofs it is almost impossible), which questions the use of this method for such purposes.

From the aforementioned studies, it appears that a certain intermediate level of simplification between the fully physically-based and the mentioned conceptual models is necessary to properly assess green roof hydrological impact. Conceptual reservoir-based models seem to

match this requirement. By treating a green roof substrate, or other porous medium, as a reservoir of certain capacity from which water leaks following either linear, or non-linear (power) law, it is possible to numerically/analytically express the drained outflow. The concept of a linear reservoir is simpler but less reliable, due to the fact that the water flow through a porous medium follows a linear law only at saturation (Darcy's law). Nevertheless, this concept has been widely used for presenting a green roof either with an individual reservoir (Versini et al., 2016), or with several linear reservoirs describing different layers on the roof (Versini et al., 2015), or by using a cascade of linear reservoirs, which can be analytically described (Zimmer & Geiger, 1997). On the contrary, non-linear reservoir (NLR) is more physically-based concept that can be also described either numerically (Todini, 1996) or analytically with some simplifications (Liu & Todini, 2002). It has been shown that this concept can provide a reliable interpretation of the outflows measured on green roofs (Kasmin et al., 2010; Locatelli et al., 2014) and river catchments (Todorović et al., 2019).

In this work the emphasis was put on two goals. First one is to point out the physical basis of the NLR concept through the link with Richards law, similarly as done by Hooshyar & Wang (2016) in case of the SCS hydrological method. Therefore, the existing analytical expression for the leakage from a NLR (Liu & Todini, 2002) has been derived through an analytical solution of simplified Richards equation, which is used to point out the limitations of the NLR concept.

This leads to the second goal of this study, to develop more generalized concept that secures more reliable interpretation of Richards law - a cascade of NLRs (CNLR). Under the free drainage condition, the CNLR model represents an analytical alternative to the standard numerical models based on Richards law, and as such it is rather efficient and convenient for implementation in fully distributed hydrological models (e.g. MULTIHIDRO - Ichiba et al., 2018). The CNLR contains multiple reservoirs, where the outflow from one reservoir is the inflow to another located below. In order to develop more physically-based model, the outflow from each reservoir is described by means of the hydraulic conductivity function derived in Chapter 3.2. Besides the parameters related to the soil hydraulic properties, the leakage from a CNLR strongly depends on the number of reservoirs in a cascade. Less reservoirs corresponds to an almost uniformly distributed water contents along the thickness of a soil layer, while more reservoirs simulate a pronounced wetting front, usually related to less permeable materials. The CNLR model has been firstly validated through the comparison with the standard implicit numerical scheme for solving Richards equation (van Dam & Feddes, 2000), which also uses the water retention and the hydraulic conductivity functions presented in Chapter 3.2. Furthermore, the model has been tested on the rainfall-runoff measurements captured on Green Wave (Versini et al., 2018; Stanić et al., 2019). Impacts of vegetation and evapotranspiration on green roofs have not been considered in this work.

5.1.2. Methodology

Functions describing the soil hydraulic properties

In Chapter 3.2 is proposed a new physically-based hydraulic properties model for the entire range of matric suctions. The work presented has shown that in case of green roof substrates

and similar coarse materials, adsorption mechanism can be ignored at lower capillary-dominated suctions that are of particular interest from the aspect of hydrological modeling. Thus, solely the capillary-based water retention ($S_e = S_e^{cap}$) and the relative hydraulic conductivity functions ($K_r = K_r^{cap}$) are considered in this work (see Chapter 3.2 for more details). The water retention function is expressed as follows:

$$S_e(h_k) = \frac{\theta(h_k) - \theta_r}{\theta_s - \theta_r} = \begin{cases} 1, & h_k < h_{k,a} \\ 1 - \frac{1 - \left(\frac{h_k}{h_{k,a}}\right)^{D_f - 3}}{\theta_s - \theta_r}, & h_{k,a} < h_k < h_{k,r} \end{cases} \quad (5.1-1)$$

where S_e is degree of saturation [0 – 1], h_k is the suction expressed in water level height [L], $h_{k,a}$ is the air entry value [L], while θ , θ_s and θ_r are the actual, saturated and residual water contents [-], respectively. Parameter D_f is a fractal dimension of grains [2 - 3] that rates gradation of material (the higher the value of D_f , the wider the spectrum of grain and pore sizes). Equation (5.1-1) is valid for suctions smaller than $h_{k,r} = h_{k,a} [1 - (\theta_s - \theta_r)]^{\frac{1}{D_f - 3}}$, a value of suction at which capillary water is considered to be totally drained ($S_e(h_{k,r}) = 0$). By introducing Equation (5.1-1) into Mualem (1976)'s analytical model, the analytical hydraulic conductivity function presented in Chapter 3.2 is derived. The obtained function can be simplified (see Appendix A4) and expressed in a form similar to the one proposed by Brooks & Corey (1964):

$$K(S_e) = K_s S_e^{l+2m} \quad (5.1-2)$$

where K_s is the saturated hydraulic conductivity [L/T], l is Mualem (1976)'s parameter [-] that accounts for the pore connectivity and tortuosity (can be both positive and negative), and m is a physically-based exponent [-] that depends on $(\theta_s - \theta_r)$ and D_f :

$$m = \frac{1}{\ln(S_{e,x})} \ln \left[\left(\left(1 + S_{e,x} \frac{\theta_s - \theta_r}{1 - (\theta_s - \theta_r)} \right)^{\frac{D_f - 4}{D_f - 3}} - 1 \right) / \left(\left(\frac{1}{1 - (\theta_s - \theta_r)} \right)^{\frac{D_f - 4}{D_f - 3}} - 1 \right) \right] \quad (5.1-3)$$

where $S_{e,x}$ is the fixed value of saturation degree that secures the best overall agreement between the original and simplified (Equation 5.1-2) expression. The value of $S_{e,x}$ depends on $(\theta_s - \theta_r)$ and D_f , and its determination is described in details in Appendix A4. Note that both water retention (Equation 5.1-1) and hydraulic conductivity (Equation 5.1-2) functions depend on physically-based parameters.

Physical basis of Non-Linear Reservoir (NLR) concept

In case of green roofs and similar coarse materials of relatively small thickness H [L], water flow is dominantly vertical, with insignificant lateral movement even at slope (see Bengtsson, 2005). Similar conclusion was made based on the analysis of in situ measurements presented in Chapter 4. Thus, water flow can be described by using a general form of Richards equation:

$$\frac{\partial \theta(z,t)}{\partial t} = - \frac{\partial q}{\partial z} \quad (5.1-4)$$

where t is time [T], q is the water flux [L/T] and z is a vertical axis oriented downwards ($z = 0$ – top surface; $z = H$ – bottom surface). If the water coming from the external inflow at $z = 0$ is rapidly distributed along H , meaning that the wetting front is not pronounced (assumed to be the case for green roofs), Equation (5.1-4) can be integrated with respect to z . Thus, only the overall change along H is considered:

$$\int_0^H \frac{\partial \theta(z,t)}{\partial t} dz = - \int_{q_{in}}^{q_d} dq \quad (5.1-5)$$

$$\frac{d\theta(t)}{dt} H = q_{in} - q_d \quad (5.1-6)$$

where q_{in} is the flux [L/T] at $z = 0$, while q_d is the flux drained from the bottom at $z = H$, and $\theta(t)$ is soil water content averaged over H . Equation (5.1-6), which describes the water balance, can be transformed into the drainage equation by getting rid of q_{in} . This can be done by adding its contribution to the water content at the initial time (acceptable for short time intervals Δt). In this case, θ immediately increases from θ_0 ($\theta = \theta_0 + \frac{q_{in}\Delta t}{H}$), the volumetric water content value reached at the end of the previous interval Δt . Thus, solely drainage process is considered afterwards:

$$\frac{d\theta}{dt} H = -q_d \quad (5.1-7)$$

If the free drainage condition ($\frac{\partial h_k}{\partial z} = 0$) is secured at $z = H$, q_d can be expressed through the modification of Darcy's law used for unsaturated conditions:

$$q_d = -K(\theta) \left(\frac{\partial h_k}{\partial z} - 1 \right) = K(\theta) \quad (5.1-8)$$

By introducing Equation (5.1-8) into (5.1-7) and by using notation $S_e = \frac{\theta - \theta_r}{\theta_s - \theta_r}$, the following is obtained:

$$\frac{dS_e}{dt} H(\theta_s - \theta_r) = -K(S_e) \quad (5.1-9)$$

If $K(S_e)$ is described by means of (Equation 5.1-2), the variables can be separated and the change of the effective saturation degree ΔS_e during Δt can be analytically expressed:

$$\int_{S_{e,0}}^{S_{e,0} + \Delta S_e} \frac{dS_e}{S_e^{l+2m}} = - \frac{1}{H(\theta_s - \theta_r)} \int_0^{\Delta t} dt \quad (5.1-10)$$

$$\Delta S_e = S_{e,0} - \left(S_{e,0}^{1-l-2m} - \frac{\Delta t}{H} \frac{K_s}{(\theta_s - \theta_r)} (1-l-2m) \right)^{\frac{1}{1-l-2m}} \quad (5.1-11)$$

Finally, q_d over the time interval Δt is obtained:

$$q_d = \Delta S_e (\theta_s - \theta_r) \frac{H}{\Delta t} \quad (5.1-12)$$

The way Equation (5.1-12) has been derived clearly shows that the NLR concept is reliable only for relatively small values of H and for materials that are able to rapidly distribute the water along H (q_d is triggered right after q_{in}). For those materials, the retention properties can be reduced to the basic retention capacity level ($\theta_s - \theta_r$), without considering the dynamics of water release.

Cascade of Non-Linear Reservoirs (CNLR) - generalization of NLR concept

In less permeable porous media water is not rapidly distributed along H , which creates strongly pronounced wetting front (non-uniform distribution of water contents along H). Therefore, Equation (5.1-12) becomes inappropriate due to the over-simplified retention properties (retention capacity is not sufficient). To cope with this, a cascade of NLR (CNLR) is created, where the number of reservoirs in a cascade dictates the dynamics of water release. In the CNLR model, the outflow from one reservoir is the inflow to the next one placed below, which is illustrated in *Figure 5.1-1*.

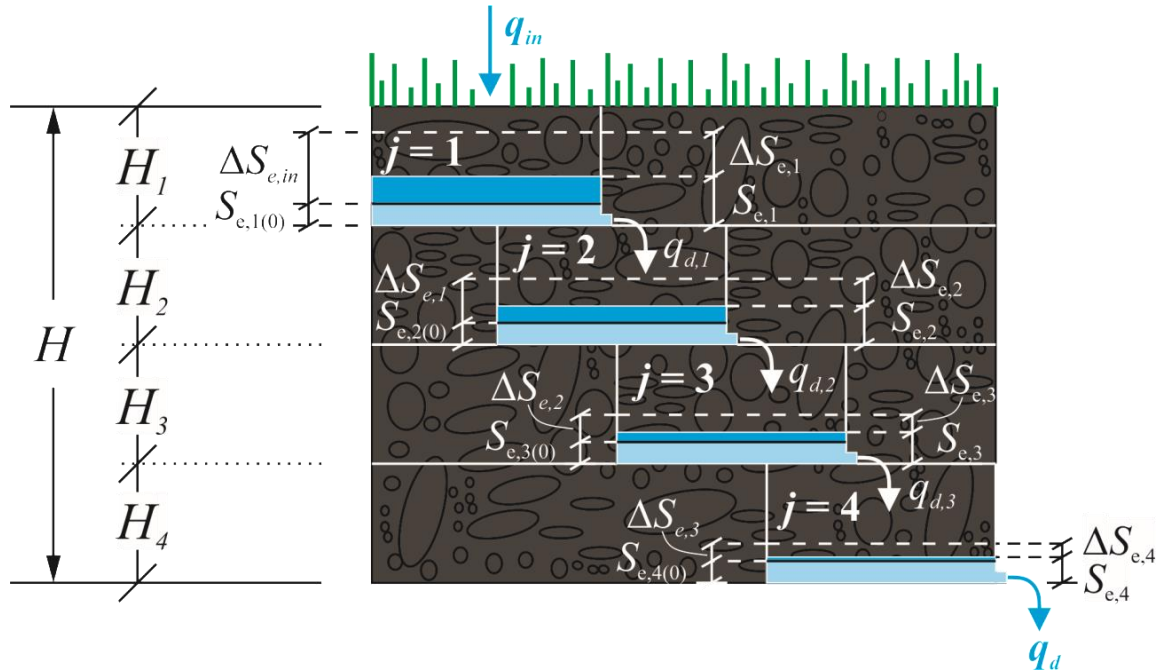


Figure 5.1-1. Illustration of the CNLR concept – procedure for applying for a single time interval Δt (example with $n_{res} = 4$)

The initial saturation degree for each NLR ($j = 1$ to n_{res}) at the beginning of Δt is calculated as $S_{e,j(0^*)} = S_{e,j(0)} + \Delta S_{e,(j-1)}$, where $S_{e,j(0)}$ is the value of saturation degree in reservoir j at the end of previous Δt , while $\Delta S_{e,(j-1)}$, which is related to the current Δt and reservoir placed above ($j - 1$), is computed using Equation (5.1-11). For $j = 1$ (top reservoir), $S_{e,1(0^*)} = S_{e,1(0)} + \Delta S_{e,in}$, where $\Delta S_{e,in} = \frac{q_{in}\Delta t}{H(\theta_s - \theta_r)}$, while for $j = n_{res}$ (bottom reservoir) q_d is calculated by introducing $\Delta S_{e,n_{res}}$ into Equation (5.1-12). Note that the standard NLR model is a special case of the CNLR model for $n_{res} = 1$.

Figure 5.1-2 illustrates the impact of n_{res} on q_d . Clearly, larger n_{res} secures more significant peak of q_d with stronger delay with respect q_{in} , while $n_{res} = 1$ (NLR model) provides mitigated peak, but q_d is triggered immediately after q_{in} . This is because for $n_{res} > 1$ water needs more time to descend from the upper to the bottom reservoir, while for $n_{res} = 1$ q_{in} immediately initiates q_d . In all three cases presented in Figure 5.1-2, the total quantity of water drained over a longer time period is the same, confirming that n_{res} mainly affects the dynamics of its release.

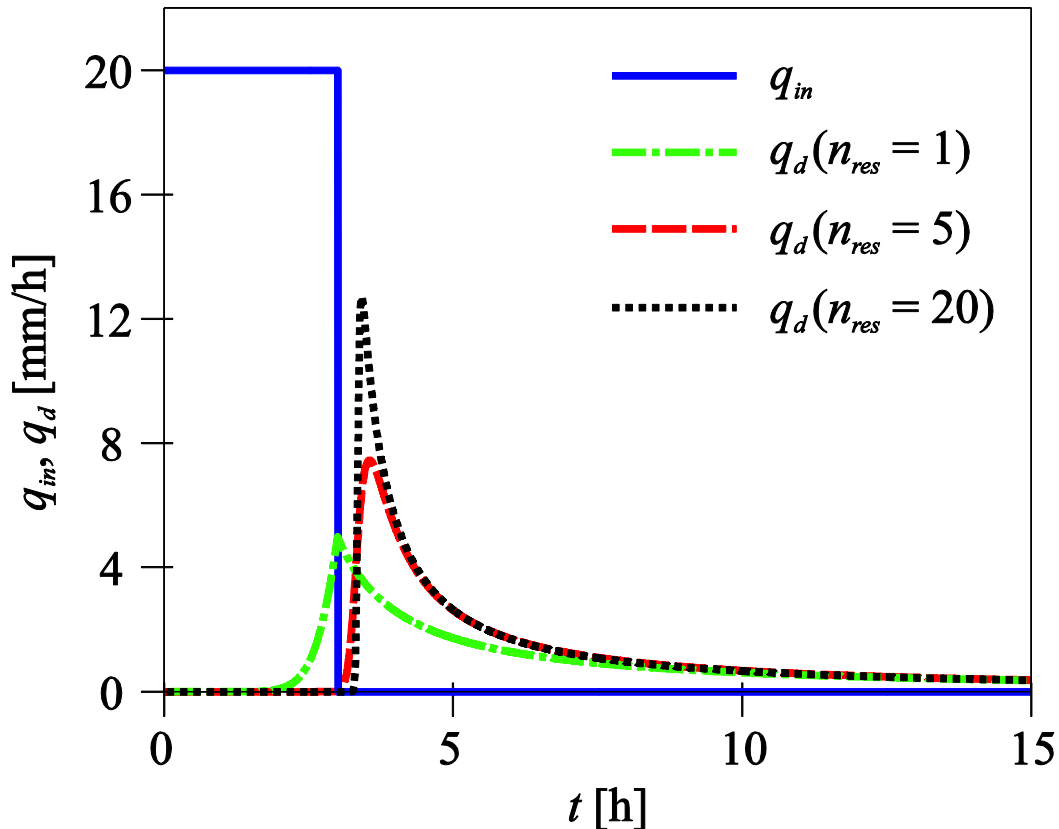


Figure 5.1-2. Influence of n_{res} on q_d computed using the CNLR model with parameter values from Chapter 3.2 ($H = 20$ cm, $\theta_s = 0.395$, $\theta_r = 0.045$, $D_f = 2.95$, $h_{k,a} = 0.9$ cm, $K_s = 8.11 \times 10^{-6}$ m/s, $l = -1.35$)

In other words, the NLR model assumes suction gradient $\frac{dh_k}{dz}$ to be zero (no wetting front), while the CNLR model enables to simulate stronger gradient (pronounced wetting front) by adding more NLRs in a cascade.

Limitation of the CNLR model is that it requires water to be freely drained from the top to the bottom, meaning the impact exclusively propagates downstream. Therefore, every NLR in a cascade needs to be equally or more permeable than the one placed above, in order to avoid the impedance effect which would cause the propagation in the upstream direction.

5.1.3. Results

In order to validate the analytical CNLR approach, it has been first compared with the numerical model for solving Richards equation (see Appendix A5), where both models use the parameter values describing the experimentally determined hydraulic properties of the Green Wave substrate (see Chapter 3.2). The second part is related to the application of the CNLR model on real rainfall – runoff measurements captured on Green Wave (Chapter 4.1).

Comparison between the CNLR model and the Numerical model

To apply the CNLR model on the Green Wave substrate (parameters taken from Chapter 3.2), n_{res} is adjusted to secure the best agreement between the outflows computed by means of the CNLR model and the numerical model (both models are implemented in Matlab). This is done for a 3 h long constant inflow $q_{in} = 20$ mm/h, as illustrated in *Figure 5.1-3*. To cope with q_d simulated using the numerical model (dashed line), the CNLR model requires $n_{res} = 13$ (black solid line) for the same values of model parameters taken from Chapter 3.2. Results obtained using the CNLR model and the numerical model match almost perfectly, while those related to the NLR (dash-dotted line) are significantly different.

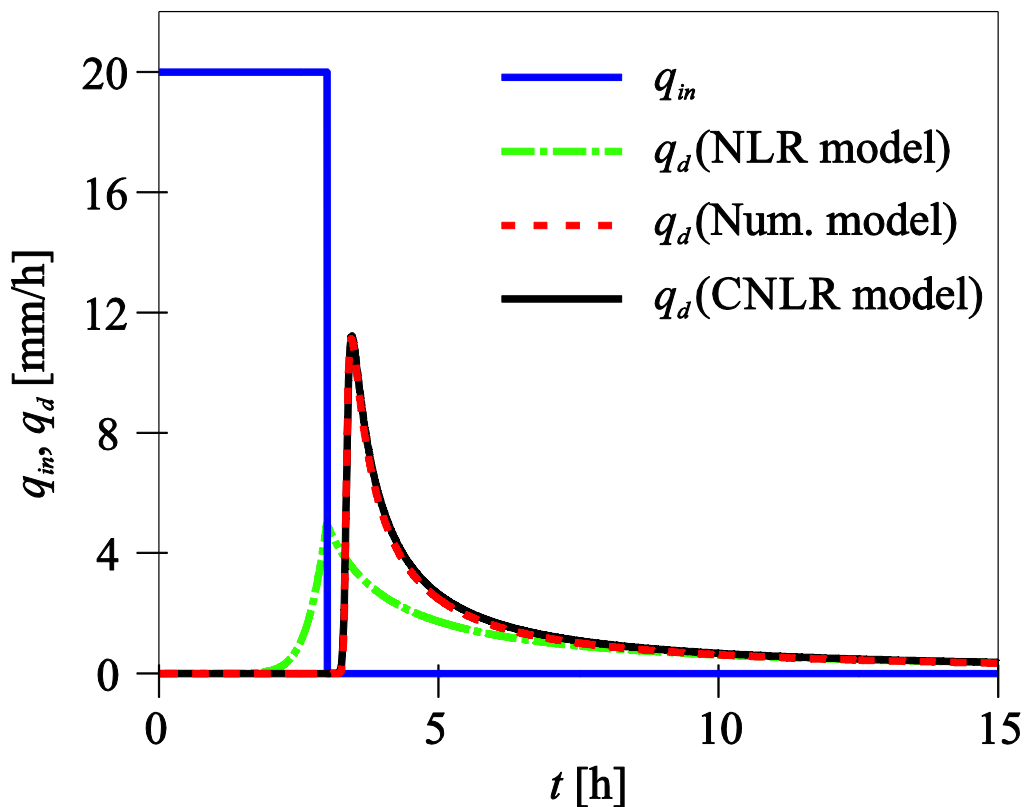


Figure 5.1-3. Comparison between q_d values calculated using the NLR model (dash-dotted line), the numerical model (dashed line), and the CNLR model with $n_{res} = 13$ (solid line), for the constant 3 h long inflow $q_{in} = 20$ mm/h. All models use parameter values taken from Chapter 3.2 (listed in the caption of Figure 5.1-2)

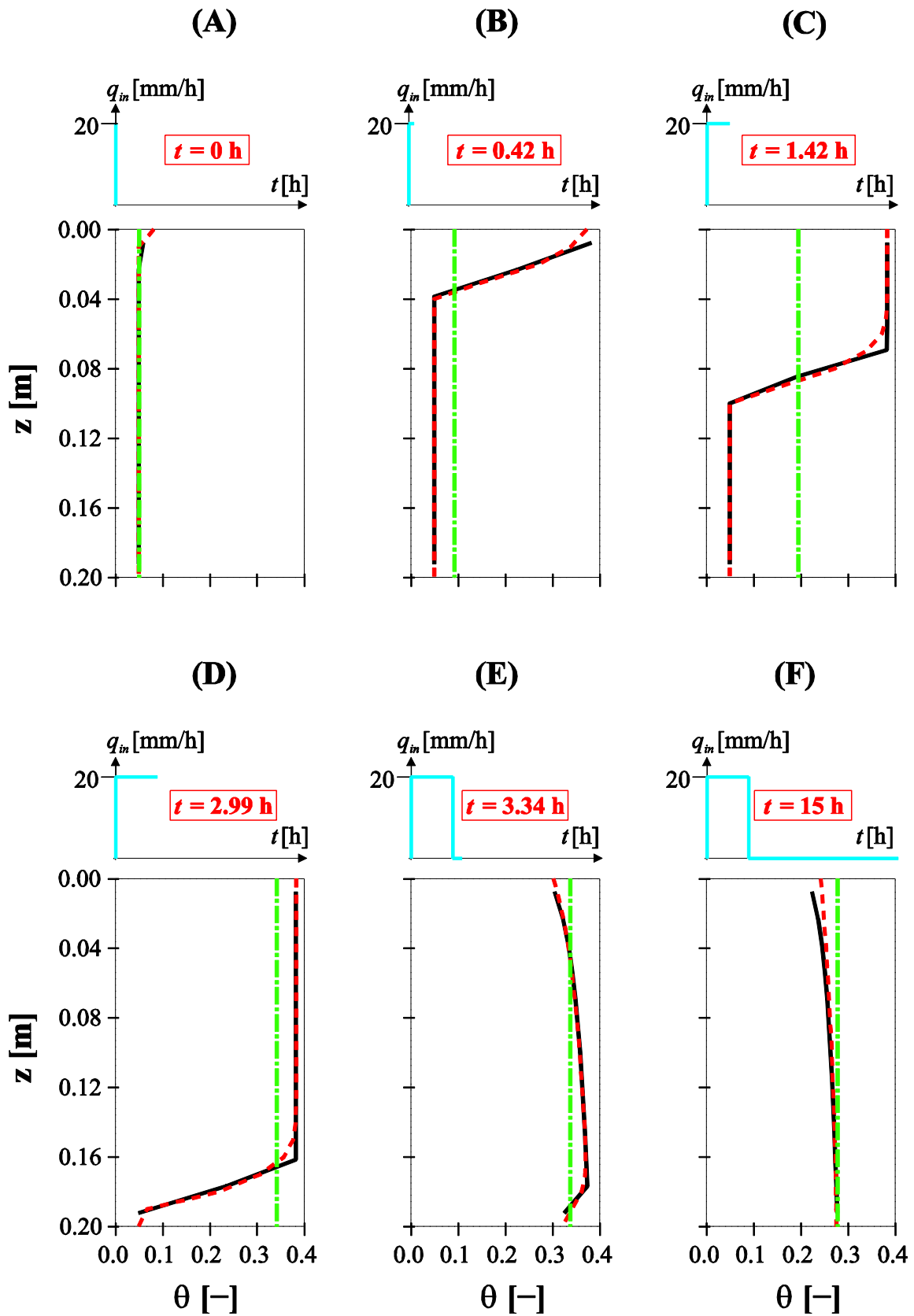


Figure 5.1-4. Comparison between the wetting fronts obtained by using the NLR model (dash-dotted line), the numerical model (dashed line), and the CNLR model with $n_{res} = 13$ (solid line)

For the same values of inflow and model parameters, in *Figure 5.1-4* are presented distributions of water contents along H (wetting front) at different time steps, obtained using the three mentioned models. The NLR assumes uniform distribution of θ along H (dash-dotted line), which deviates significantly from the distributions computed using the CNLR model (solid line) and the numerical model (dashed line). Note that in case of the CNLR model, $\theta(z)$ is computed for each of 13 reservoirs, based on the calculated S_e . Clearly, the hydrological behavior of the Green Wave substrate in its initial state (model parameters taken from Chapter 3.2) cannot be properly described with a single nonlinear reservoir (the NLR model). On the contrary, the CNLR model interprets results of the numerical model quite well. For $t < 3$ h (*Figure 5.1-4a, b, c, d*) water is firstly accumulated in the upper layer ($\theta(z=0)$ increases), after which it starts to descend progressively towards the bottom ($z=H$). At $t = 3$ h (*Figure 5.1-4d*), q_{in} becomes zero and the substrate starts to drain. At $t = 3.34$ h (*Figure 5.1-4e*), $\theta(z=H)$ is close to its maximal value, which corresponds to time when q_d peak is reached in *Figure 5.1-4*. After that, the overall decrease in both $\theta(z)$ (*Figure 5.1-4f*) and q_d (*Figure 5.1-4*) can be observed.

Application of the CNLR model on the real rainfall-runoff data

The concept of CNLR has been also tested on the rainfall-runoff data monitored on a large part (3511 m²) of Green Wave. In *Figure 5.1-5*, rainfall intensities (30 s time discretization) measured by PWS100 disdrometer (Gires et al., 2018) installed next to Green Wave, have been used as q_{in} (blue solid line). As described in Chapter 4.1, q_d is measured based on the water level change in the storage unit (15 s time discretization), and it is presented with grey filled dots in *Figure 5.1-5*. The measurements presented cover the period between 15th and 26th of January, 2018, with the total amount of rainfall of 60 mm. As the presented event occurred in winter, the evapotranspiration is ignored.

Black solid line presented in *Figure 5.1-5* illustrates q_d computed using the CNLR model with $n_{res} = 13$ and parameter values presented in *Figure 5.1-4* (or Chapter 3.2). As previously explained, these results describe the hydrological behavior of Green Wave in its initial state. On the contrary, red solid line is the result of the CNLR model after adjusting values of parameters ($n_{res} = 6$, $D_f = 2.63$, $\theta_r = 0.01$, $K_s = 1.5 \times 10^{-4}$ m/s, while the rest are the same as in Chapter 3.2) to secure the best agreement between the computed and measured q_d . Thus, it is assumed that these results correspond to the current state of the Green Wave substrate. As illustrated in the Figure, red solid line fits quite well to measurements (Nash-Sutcliffe coefficient is equal to 0.82), while black solid line shows rather poor agreement.

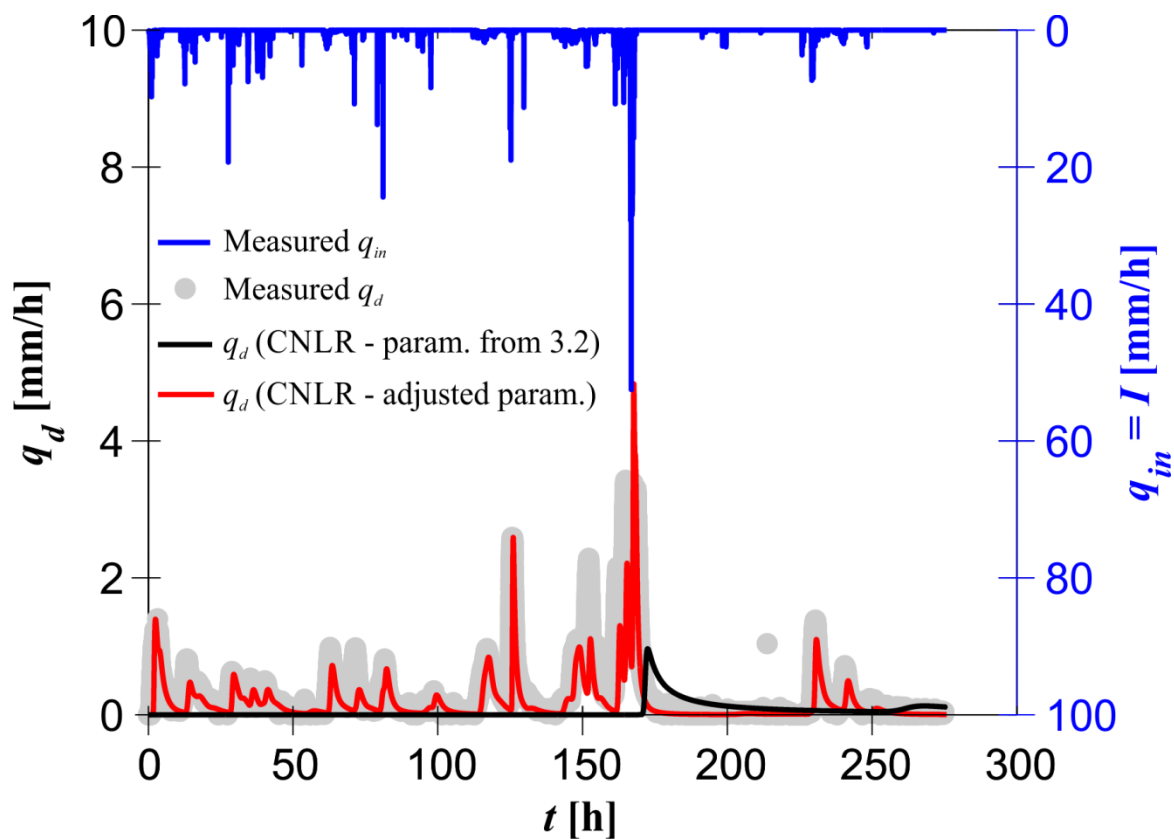


Figure 5.1-5. Comparison between the measured q_d (dots), the CNLR model that uses parameter values from Chapter 3.2 (black solid line) and the CNLR model whose parameter values are manually adjusted (red solid line) to provide the best agreement with measured q_d . Input for the CNLR model is the measured rainfall intensity q_{in} (blue solid line)

Significant difference between two results (two sets of parameters) can be related to the flushing of fine substrate particles that are accumulated in the drainage conduits. This is a general problem with green roofs, as reported by Berndtsson (2010) and Li & Babcock Jr (2014). Since fines are no more filling the voids between coarse grains, pore sizes have increased and their distribution became more uniform, which implies reduction of D_f (from 2.95 to 2.63) and increase of K_s (from 8.11×10^{-6} m/s to 1.5×10^{-4} m/s). Also, θ_r is strongly related to the quantity of fine particles. Thus, it is assumed to be also reduced (from 0.045 to 0.01). The aforementioned modified soil properties describe substrate with less pronounced wetting front compared to the Green Wave substrate in its initial state, leading to a reduced number of reservoirs in the CNLR model (from $n_{res} = 13$ to $n_{res} = 6$).

The main advantage of the CNLR analytical model is its computational efficiency. Computational time required for a continuous simulation such as the one presented in Figure 5.1-5, is two orders of magnitude lower than in case of the numerical model. That, in combination with the proved physical background, establishes the CNLR model as a good basis for hydrological simulations on urban catchment scales. Also, if implemented in fully distributed hydrological models, the CNLR model gives the possibility to efficiently treat the spatial heterogeneity at such scales.

5.1.4. Conclusion & Perspectives

The main goal of this work is to point out the physical basis of the proposed CNLR (Cascade of Non-Linear Reservoirs) model which extends the application of the standard NLR (Non-Linear Reservoir) model, and helps to replace, in some cases, time-demanding numerical models based on Richards law. This work shows that the link between the NLR concept and Richards law clearly exists in case of highly permeable and thin substrate layers, where water is freely drained from the bottom. For such materials water retention properties are reduced to the basic retention capacity level, and the analytical solution describing the leakage from the NLR is derived. However, the NLR model is not suitable for substrates where water is not rapidly distributed along the substrate thickness, but progressively descends towards the bottom. In such case, the CNLR model with an optimal number of reservoirs compensates for the over-simplified retention properties of a single NLR, simulating properly the dynamic of water release, and hence the outflow from a substrate's bottom.

According to results, the proposed CNLR model with an optimal number of reservoirs is able to accurately and significantly faster interpret numerically computed outflows from a substrate, if free drainage is secured at substrate's bottom. Comparison between the CNLR, the NLR, and the numerical model is done for a constant inflow, where all three models use the same parameter values (taken from Chapter 3.2) describing the Green Wave substrate in its initial state. For such material, the best agreement between the CNLR and the numerical model is obtained if using a cascade of 13 reservoirs, while the standard NLR model shows significantly different results.

The CNLR model has been also compared with monitored rainfall-runoff data captured on Green Wave. The agreement between the simulated and measured data is rather good, but the best fitting parameter values deviate from those presented in Chapter 3.2. The main reason for this is assumed to be the flushing of a significant amount of fine substrate particles during the past years, which causes more uniform distribution of pore sizes, increased saturated hydraulic conductivity, and lower residual water content. All this leads to a reduced number of reservoirs in the CNLR model, as well. The main contribution of the presented CNLR model is its computational efficiency which is proved to be more than two orders of magnitude higher than in case of the standard numerical models based on Richards law.

In future work, the CNLR model and its application should be improved in several aspects. Firstly, the link between the optimal number of reservoirs in a cascade and the parameters describing the soil hydraulic properties needs to be defined. Secondly, different layers of green roof should be included into consideration (vegetation layer, substrate layer, drainage layer), creating thus the conditions that correspond better to properly maintained green roof. Finally, under the free drainage condition at green roofs bottom, this model can be implemented into a fully distributed hydrological model to efficiently treat the spatial heterogeneity of green roofs at larger (catchment) scales. This can improve the assessment of hydrological impacts of this type of Natural Based Solutions.

5.1.5. References:

- Alfredo, K., F. Montalto, M. Asce, and A. Goldstein. 2010. "Observed and Modeled Performances of Prototype Green Roof Test Plots Subjected to Simulated Low- and High-Intensity Precipitations in a Laboratory Experiment." *Journal of Hydrologic Engineering* 15 (6): 444–57. [https://doi.org/10.1061/\(ASCE\)HE.1943-5584.0000135](https://doi.org/10.1061/(ASCE)HE.1943-5584.0000135).
- Bengtsson, L. 2005. "Peak Flows from Thin Sedum-Moss Roof." *Nordic Hydrology* 36 (3): 269–80.
- Berndtsson, J. C. 2010. "Green Roof Performance towards Management of Runoff Water Quantity and Quality : A Review." *Ecological Engineering* 36 (4): 351–60. <https://doi.org/10.1016/j.ecoleng.2009.12.014>.
- Brooks, R. H., and A. T. Corey. 1964. "Hydraulic Properties of Porous Media." *Hydrology Papers*, no. 3: 1–27.
- Burszta-Adamiak, E., and M. Mrowiec. 2015. "Modelling of Green Roofs ' Hydrologic Performance Using EPA ' s SWMM." *Water Science & Technology* 68 (1): 36–42. <https://doi.org/10.2166/wst.2013.219>.
- Carter, T., and C. R. Jackson. 2007. "Vegetated Roofs for Stormwater Management at Multiple Spatial Scales." *Landscape and Urban Planning* 80: 84–94. <https://doi.org/10.1016/j.landurbplan.2006.06.005>.
- Dam, J. C. van, and R. A. Feddes. 2000. "Numerical Simulation of Infiltration, Evaporation and Shallow Groundwater Levels with the Richards Equation." *Journal of Hydrology* 233: 72–85.
- Fassman-Beck, E., E. Voyde, R. Simcock, and Y. Sing. 2013. "4 Living Roofs in 3 Locations : Does Configuration Affect Runoff Mitigation ?" *Journal of Hydrology* 490: 11–20. <https://doi.org/10.1016/j.jhydrol.2013.03.004>.
- Genuchten, M. Th. van. 1980. "A Closed-Form Equation for Predicting the Hydraulic Conductivity of Unsaturated Soils." *Soil Science Society of America Journal* 44 (5): 892–98. <https://doi.org/10.2136/sssaj1980.%0A03615995004400050002x>.
- Getter, K. L., D. B. Rowe, and J. A. Andresen. 2007. "Quantifying the Effect of Slope on Extensive Green Roof Stormwater Retention." *Ecological Engineering* 3 (1): 225–31. <https://doi.org/10.1016/j.ecoleng.2007.06.004>.
- Gires, A., I. Tchiguirinskaia, and D. Schertzer. 2018. "Two Months of Disdrometer Data in the Paris Area." *Earth System Science Data* 10: 941–50. <https://doi.org/10.5194/essd-10-941-2018>.
- Hakimdavar, R., P. J. Culligan, M. Finazzi, S. Barontini, and R. Ranzi. 2014. "Scale Dynamics of Extensive Green Roofs : Quantifying the Effect of Drainage Area and Rainfall Characteristics on Observed and Modeled Green Roof Hydrologic Performance." *Ecological Engineering* 73: 494–508. <https://doi.org/10.1016/j.ecoleng.2014.09.080>.
- Hilten, R. N., T. M. Lawrence, and E. W. Tollner. 2008. "Modeling Stormwater Runoff from Green Roofs with HYDRUS-1D." *Journal of Hydrology (2008)* 358: 288–93. <https://doi.org/10.1016/j.jhydrol.2008.06.010>.
- Hooshyar, M., and D. Wang. 2016. "An Analytical Solution of Richards' Equation Providing the Physical Basis of SCS Curve Number Method and Its Proportionality Relationship."

-
- Water Resources Research* 52: 1–10. <https://doi.org/10.1002/2016WR018885>. Received.
- Ichiba, A., A. Gires, I. Tchiguirinskaia, D. Schertzer, P. Bompard, and M. -C. T. Veldhuis. 2018. “Scale Effect Challenges in Urban Hydrology Highlighted with a Distributed Hydrological Model.” *Hydrology and Earth System Sciences* 22: 331–50. <https://doi.org/10.5194/hess-22-331-2018>.
- Kasmin, H., V. R. Stovin, and E. A. Hathway. 2010. “Towards a Generic Rainfall-Runoff Model for Green Roofs.” *Water Science & Technology* 62 (4): 898–905. <https://doi.org/10.2166/wst.2010.352>.
- Li, Y., and R. W. Jr. Babcock. 2014. “Green Roof Hydrologic Performance and Modeling: A Review.” *Water Science & Technology* 69 (4): 727–38. <https://doi.org/10.2166/wst.2013.770>.
- Liu, Z., and E. Todini. 2002. “Towards a Comprehensive Physically-Based Rainfall-Runoff Model.” *Hydrology and Earth System Sciences* 6 (5): 859–81.
- Locatelli, L., O. Mark, P. Steen, K. Arnbjerg-Nielsen, M. Bergen, and P. John. 2014. “Modelling of Green Roof Hydrological Performance for Urban Drainage Applications.” *JOURNAL OF HYDROLOGY*. <https://doi.org/10.1016/j.jhydrol.2014.10.030>.
- Mualem, Y. 1976. “A New Model for Predicting the Hydraulic Conductivity of Unsaturated Porous Media.” *Water Resources Research* 12 (3): 513–22. <https://doi.org/10.1029/WR012i003p00513>.
- Palla, A., I. Gnecco, and L. G. Lanza. 2009. “Unsaturated 2D Modelling of Subsurface Water Flow in the Coarse-Grained Porous Matrix of a Green Roof.” *Journal of Hydrology* 379 (1–2): 193–204. <https://doi.org/10.1016/j.jhydrol.2009.10.008>.
- Palla, A., J. J. Sansalone, I. Gnecco, and L. G. Lanza. 2011. “Storm Water Infiltration in a Monitored Green Roof for Hydrologic Restoration.” *Water Science & Technology* 64 (3): 766–74. <https://doi.org/10.2166/wst.2011.171>.
- Richards, L. A. 1931. “Capillary Conduction of Liquids through Porous Media.” *Physics* 1: 318–33.
- She, N., and J. Pang. 2010. “Physically Based Green Roof Model.” *Journal of Hydrologic Engineering* 15 (6): 458–64. [https://doi.org/10.1061/ASCE1084-0699\(2010\)15:6\(458\)1.0.CO;2](https://doi.org/10.1061/ASCE1084-0699(2010)15:6(458)1.0.CO;2).
- Šimůnek, J., M. Th. van Genuchten, and M. Šejna. 2008. “Released Online.” *Vadose Zone Journal* 7 (2): 587–600. <https://doi.org/10.2136/vzj2007.0077>.
- Stanić, F., Y.-J. Cui, P. Delage, E. De Laure, P.-A. Versini, D. Schertzer, and I. Tchiguirinskaia. 2019. “A Device for the Simultaneous Determination of the Water Retention Properties and the Hydraulic Conductivity Function of an Unsaturated Coarse Material ; Application to a Green- Roof Volcanic Substrate.” *Geotechnical Testing Journal*. <https://doi.org/10.1520/GTJ20170443>.
- Stovin, V., S. Poë, S. De-ville, and C. Berretta. 2015. “The Influence of Substrate and Vegetation Configuration on Green Roof Hydrological Performance.” *Ecological Engineering* 85: 159–72. <https://doi.org/10.1016/j.ecoleng.2015.09.076>.
- Stovin, V., G. Vesuviano, and H. Kasmin. 2012. “The Hydrological Performance of a Green Roof Test Bed under UK Climatic Conditions.” *Journal of Hydrology* 414–415: 148–61. <https://doi.org/10.1016/j.jhydrol.2011.10.022>.
- Todini, E. 1996. “The ARNO Rainfall-Runoff.” *Journal of Hydrology* 175: 339–82.
-

-
- Todorović, A., M. Stanić, Ž. Vasilčić, and J. Plavšić. 2019. “The 3DNet-Catch Hydrologic Model : Development and Evaluation.” *Journal of Hydrology* 568 (June 2018): 26–45. <https://doi.org/10.1016/j.jhydrol.2018.10.040>.
- Versini, P. -A., A. Gires, I. Tchiguirinskaia, and D. Schertzer. 2018. “Toward an Assessment of the Hydrological Components Variability in Green Infrastructures: Pilot Site of the Green Wave (Champs-Sur-Marne).” *La Houille Blanche*, no. 4: 34–42. <https://doi.org/10.1051/lhb/2018040>.
- Versini, P. -A., A. Gires, I. Tchinguirinskaia, and D. Schertzer. 2016. “Toward an Operational Tool to Simulate Green Roof Hydrological Impact at the Basin Scale: A New Version of the Distributed Rainfall–Runoff Model Multi-Hydro.” *Water Science & Technology* 74 (8): 1845–54. <https://doi.org/10.2166/wst.2016.310>.
- Versini, P. -A., D. Ramier, E. Berthier, and B. de Gouvello. 2015. “Assessment of the Hydrological Impacts of Green Roof : From Building Scale to Basin Scale.” *Journal of Hydrology* 524: 562–75. <https://doi.org/10.1016/j.jhydrol.2015.03.020>.
- Zimmer, U., and W. F. Geiger. 1997. “MULTILAYERED INFILTRATION SYSTEMS.” *Water Science & Technology* 36 (8–9): 301–6. [https://doi.org/10.1016/S0273-1223\(97\)00582-9](https://doi.org/10.1016/S0273-1223(97)00582-9).

6. Conclusions & Future work

6.1. Conclusions

In order to better understand and predict hydrological performances of green roofs, in terms of their abilities to retain and mitigate urban runoffs, it was necessary to investigate different properties of green roof substrate at different scales. Detailed investigation was carried out from the scale of the specimen used in laboratory conditions, up to the scale of a single green roof (Green Wave in this case), while the physically-based link between scales was obtained by means of the UM theoretical framework. The work presented here provides several new contributions:

1. A new experimental device and new inverse analytical methods for measuring the hydraulic conductivity of unsaturated medium through a multistep suction test. By means of a high precision pressure transducer and a specially designed overflow system, the apparatus provides accurate measurements of the transient outflows initiated by imposing a suction step, allowing for an accurate determination of the water retention curve. In addition, two inverse methods to account for the specific boundary conditions of the apparatus enabled a reliable and convenient determination of the hydraulic conductivity function, based on the analysis of the outflows time series.

The determination of the retention and transfer properties of the Green Wave coarse volcanic material using these apparatus and methods appeared to be relatively efficient (about 10 days for both properties), simple and robust, with no specific and financially demanding equipment required. Thanks to that, accurate and convenient experimental investigations at small scales (REV) are provided to hydrological scientists.

2. New analytical soil properties functions accounting for the heterogeneity of a porous medium. These models are derived by analyzing the scaling behavior of the soil density indicator field, obtained using X-ray CT, by means of the UM framework which enables to relate the grain size distribution and the hydraulic properties of the material investigated. This is an useful tool for predicting the water retention and hydraulic conductivity curves of the material based on its grain size distribution and other basic physical characteristics (bulk density, grain density, porosity) that can be easily measured. The proposed approach has been validated through the experimentally determined physical and hydraulic properties of the Green Wave substrate, as well as some published experimental data of other soil types.
3. A detailed monitoring system of the different water balance components (rainfall rate, change of water content and drained discharge) at the roof scale, and a novel application of the Universal Multifractal framework on the obtained measurements for assessing behavior of green roofs. Besides the standard rainfall-runoff ratio, the temporal variabilities of the provided data are characterized by means of Universal Multifractals, giving further insight into the in situ behavior of green roofs in terms of: *i*) its ability to mitigate strong fluctuations coming from rainfall, and *ii*) the impact of roof inclination on the lateral water movement.

-
4. A new analytical hydrological model based on the concept of a cascade of non-linear reservoirs, with the hydraulic properties previously described within the UM framework. The validity of the model was confirmed through the comparison with the traditional numerical solving of Richards equation, and with the drained outflows monitored on Green Wave. The model proved to be reliable and significantly faster than usual numerical models, making it quite convenient for designing green roofs, and also for simulating hydrological responses at larger scales through the discretization of the green roofs areas.

Finally, it can be concluded that using the material basic physical properties, such as the grain size distribution, bulk density, grain density and porosity, it is possible to estimate with some uncertainties the hydraulic properties of materials used for covering green roofs, and thus to predict their hydrological impact using the new proposed hydrological model. This can help designers to narrow the range of materials considered as adequate for covering green roofs, but also to more accurately estimate the hydrological impacts of green roofs on the scale of a catchment, by rasterizing its area. This way the abilities of green roofs to meet the regulations given by the local authorities in charge of the storm water management can be assessed with better accuracy. Note that, for the final selection of the material used as a green roof substrate, it is recommended to carry out the experimental investigation of the soil hydraulic properties, which can be done efficiently using the methodology developed in this work.

6.2. Future work

In order to upgrade the work presented and to make it more useful for engineering practice, the following remains to be done:

1. To account for the effects of vegetation, firstly at small scales. In this work, vegetation was not considered, even though it may have an important influence on the hydrological performances of green roofs. In the case of Green Wave, a few centimeters thick vegetation “carpet”, provided by SOPREMA (<https://www.soprema.fr/fr/sopranature>), was placed on a 20 cm thick substrate layer. Like for the substrate, the hydraulic properties of the carpet were experimentally determined during this project, through the multistep suction experiment. However, the water retention and hydraulic conductivity curves determined are associated with the mixture of roots, leaves and sandy particles contained in the carpet, making it difficult to determine some basic soil properties such as the GSD and porosity. Also, the micro-structure of the carpet does not include only pores and grains, but also the roots, which prevents to fully follow the presented approach founded on the analysis of density fields, and thus requires some modifications. This is a work remaining to be done in the near future, which will also enable to model a green roof medium as a two-layered material consisting of a substrate and a vegetation layer. Finally, this can be helpful to get more realistic predictions of green roof hydrological responses at different scales.
2. To further analyze the monitored in situ (roof scale) spatial heterogeneity of water content, so as to enable a more realistic simulation of in situ conditions using the fully

distributed models. In this work, emphasis was put on the temporal variabilities of water balance components at the roof scale, while the spatial distribution of water content was considered solely in the context of a roof inclination effect. For performing UM two-dimensional analysis at roof scale, more than 16 water content sensors are required, which can be rather costly.

3. To investigate the link between the physically-based parameters in the proposed CNLR model (especially the fractal dimension of grains) and the adequate number of reservoirs used in a cascade. This can be also rather helpful when accounting for the spatial heterogeneity, since the number of reservoirs securing reliable simulation of water flow can be determined directly based on the soil properties defined at a specific domain.
4. To account for the evapotranspiration effect. Evapotranspiration can be also simulated using the model developed here. Instead of providing positive inflow data (precipitation rate) as a boundary condition on the top soil surface, negative values indicating water loss due to the evapotranspiration need to be defined. Evapotranspiration can be introduced in relation with vegetation, but also with water content assessment during dry periods. However, these values cannot be measured directly (as in the case of precipitation), but indirectly through the measurement / calculation of different energy balance components. This is the topic of another ongoing thesis (Castellanos Díaz et al., 2019), the results of which can be combined with those obtained in this work.
5. To introduce the proposed hydrological model into the fully distributed rainfall-runoff model called MULTIHYDRO (Ichiba et al., 2018). In this way, the spatial heterogeneity beyond the largest scale investigated here (roof scale) can be efficiently simulated by rasterizing the domain investigated, where each cell of the raster has slightly different characteristics (described with model parameters) that correspond to those observed in situ. This certainly affects the final outflow obtained by superposing individual hydrograms from each cell that are computed using the analytical CNLR model proposed in this work.

Acknowledgment

This inter-laboratory thesis is founded on the collaboration between HM&Co (Hydrology Meteorology & Complexity) laboratory and Geotechnical group CERMES / NAVIER. The candidate greatly acknowledges for the Inter-laboratory PhD Merit Scholarship, provided by Research Direction of Ecole des Ponts ParisTech, which made this collaborative work possible.

The monitoring campaign dedicated to Green Wave was initiated during the Climate-KIC funded Blue Green Dream project (<http://bgd.org.uk/>). It has also been supported by the Academic Chair “Hydrology for Resilient City”, a partnership between Ecole des Ponts ParisTech and the Veolia group, and the ANR EVNATURB project dealing with the evaluation of ecosystem performances for re-naturing urban environment.

References (Chapters 1 & 6):

- Berndtsson, J. C. 2010. "Green Roof Performance towards Management of Runoff Water Quantity and Quality : A Review." *Ecological Engineering* 36 (4): 351–60. <https://doi.org/10.1016/j.ecoleng.2009.12.014>.
- Brooks, R. H., and A. T. Corey. 1964. "Hydraulic Properties of Porous Media." *Hydrology Papers*, no. 3: 1–27.
- Carter, T., and C. R. Jackson. 2007. "Vegetated Roofs for Stormwater Management at Multiple Spatial Scales." *Landscape and Urban Planning* 80: 84–94. <https://doi.org/10.1016/j.landurbplan.2006.06.005>.
- Castellanos Díaz, L. A., P. -A. Versini, D. Ramier, I. Tchiguirinskaia, and O. Bonin. 2019. "Characterization of the Evapotranspiration Flux on a Blue Green Solution (Blue Green Wave)." In *EGU General Assembly*, 15852. Vienna.
- Fassman-Beck, E., E. Voyde, R. Simcock, and Y. Sing. 2013. "4 Living Roofs in 3 Locations : Does Configuration Affect Runoff Mitigation ?" *Journal of Hydrology* 490: 11–20. <https://doi.org/10.1016/j.jhydrol.2013.03.004>.
- Francis, L. F. M., and M. B. Jensen. 2017. "Benefits of Green Roofs : A Systematic Review of the Evidence for Three Ecosystem Services." *Urban Forestry & Urban Greening*. <https://doi.org/10.1016/j.ufug.2017.10.015>.
- Genuchten, M. Th. van. 1980. "A Closed-Form Equation for Predicting the Hydraulic Conductivity of Unsaturated Soils." *Soil Science Society of America Journal* 44 (5): 892–98. <https://doi.org/10.2136/sssaj1980.%0A03615995004400050002x>.
- Hakimdavar, R., P. J. Culligan, M. Finazzi, S. Barontini, and R. Ranzi. 2014. "Scale Dynamics of Extensive Green Roofs : Quantifying the Effect of Drainage Area and Rainfall Characteristics on Observed and Modeled Green Roof Hydrologic Performance." *Ecological Engineering* 73: 494–508. <https://doi.org/10.1016/j.ecoleng.2014.09.080>.
- Hilten, R. N., T. M. Lawrence, and E. W. Tollner. 2008. "Modeling Stormwater Runoff from Green Roofs with HYDRUS-1D." *Journal of Hydrology (2008)* 358: 288–93. <https://doi.org/10.1016/j.jhydrol.2008.06.010>.
- Ichiba, A., A. Gires, I. Tchiguirinskaia, D. Schertzer, P. Bompard, and M. -C. T. Veldhuis. 2018. "Scale Effect Challenges in Urban Hydrology Highlighted with a Distributed Hydrological Model." *Hydrology and Earth System Sciences* 22: 331–50. <https://doi.org/10.5194/hess-22-331-2018>.
- Johannessen, B. G., T. M. Muthanna, and B. C. Braskerud. 2018. "Detention and Retention Behavior of Four Extensive Green Roofs in Three Nordic Climate Zones." *Water* 10. <https://doi.org/10.3390/w10060671>.
- Kabisch, N., N. Frantzeskaki, S. Pauleit, S. Naumann, M. Davis, M. Artmann, D. Haase, et al. 2016. "Nature-Based Solutions to Climate Change Mitigation and Adaptation in Urban Areas : Perspectives on Indicators , Knowledge Gaps , Barriers , and Opportunities for Action." *Ecology and Society* 21 (2). <https://doi.org/http://dx.doi.org/10.5751/ES-08373-210239>.
- Li, Y., and R. W. Jr. Babcock. 2014. "Green Roof Hydrologic Performance and Modeling: A Review." *Water Science & Technology* 69 (4): 727–38.

<https://doi.org/10.2166/wst.2013.770>.

- Liu, X., 2017. "Hydrological and energy performance of multifunctional green roofs." Imperial College London
- Maksimović, Č., S. Stanković, X. Liu, and M. Lalić. 2013. "Blue Green Dream Project's Solution for Urban Areas in the Future." In . *Recici* (Montenegro).
- Oberndorfer, E., J. Lundholm, B. Bass, R. R. Coffman, H. Doshi, N. Dunnett, S. Gaffin, M. Köhler, and K. K. Y. Liu. 2007. "Green Roofs as Urban Ecosystems : Ecological Structures , Functions , and Services." *Bio Science* 57 (10).
- Palla, A., I. Gnecco, and L. G. Lanza. 2009. "Unsaturated 2D Modelling of Subsurface Water Flow in the Coarse-Grained Porous Matrix of a Green Roof." *Journal of Hydrology* 379 (1–2): 193–204. <https://doi.org/10.1016/j.jhydrol.2009.10.008>.
- Petrucci, G., E. Rioust, J. -F. Deroubaix, and B. Tassin. 2013. "Do Stormwater Source Control Policies Deliver the Right Hydrologic Outcomes ?" *Journal of Hydrology* 485: 188–200. <https://doi.org/10.1016/j.jhydrol.2012.06.018>.
- Pinder, G. F., and M. A. Celia. 2006. *SUBSURFACE HYDROLOGY*. New Jersey: WILEY-INTERSCIENCE.
- Pokrajac, D., and K. Howard. 2010. *Advanced Simulation and Modelling for Urban Groundwater Management – UGROW*. Edited by Čedo Maksimović, Alberto Tejada-Guibert, and Sarantuyaa Zandaryaa. UNESCO and Taylor & Francis.
- Schertzer, D., and S. Lovejoy. 1987. "Physical Modeling and Analysis of Rain and Clouds by Anisotropic Scaling Multiplicative Processes." *Journal of Geophysical Research* 92: 9693–9714.
- Stanić, F., Y.-J. Cui, P. Delage, E. De Laure, P.-A. Versini, D. Schertzer, and I. Tchiguirinskaia. 2019. "A Device for the Simultaneous Determination of the Water Retention Properties and the Hydraulic Conductivity Function of an Unsaturated Coarse Material ; Application to a Green- Roof Volcanic Substrate." *Geotechnical Testing Journal*. <https://doi.org/10.1520/GTJ20170443>.
- Stovin, V., S. Poë, S. De-ville, and C. Berretta. 2015. "The Influence of Substrate and Vegetation Configuration on Green Roof Hydrological Performance." *Ecological Engineering* 85: 159–72. <https://doi.org/10.1016/j.ecoleng.2015.09.076>.
- Stovin, V., G. Vesuviano, and H. Kasmin. 2012. "The Hydrological Performance of a Green Roof Test Bed under UK Climatic Conditions." *Journal of Hydrology* 414–415: 148–61. <https://doi.org/10.1016/j.jhydrol.2011.10.022>.
- Versini, P. -A., A. Gires, I. Tchiguirinskaia, and D. Schertzer. 2018. "Toward an Assessment of the Hydrological Components Variability in Green Infrastructures: Pilot Site of the Green Wave (Champs-Sur-Marne)." *La Houille Blanche*, no. 4: 34–42. <https://doi.org/10.1051/lhb/2018040>.
- Versini, P. -A., A. Gires, I. Tchiguirinskaia, and D. Schertzer. 2016. "Toward an Operational Tool to Simulate Green Roof Hydrological Impact at the Basin Scale: A New Version of the Distributed Rainfall–Runoff Model Multi-Hydro." *Water Science & Technology* 74 (8): 1845–54. <https://doi.org/10.2166/wst.2016.310>.
- Versini, P. -A., D. Ramier, E. Berthier, and B. de Gouvello. 2015. "Assessment of the Hydrological Impacts of Green Roof : From Building Scale to Basin Scale." *Journal of Hydrology* 524: 562–75. <https://doi.org/10.1016/j.jhydrol.2015.03.020>.

Appendix

A1: Derivation of Gardner's method

Gardner's method is based on both Richards equation (A1-1) and the Terzaghi-Fröhlich consolidation equation (Equation 2.2-1). In 1D condition with vertical water flux, as in the case of Stanić et al. (2019)'s experimental device, Richards equation writes as follows:

$$\frac{\partial \theta(z,t)}{\partial t} = -\frac{\partial}{\partial z} \left(K(h_k) \left(\frac{\partial h_k(z,t)}{\partial z} + 1 \right) \right) \quad (\text{A1-1})$$

where z is defined by a vertical axis oriented upwards ($z = H$ – top surface; $z = 0$ – bottom surface), t is time [T], θ is the volumetric water content [-], and $K(h_k)$ the hydraulic conductivity [L/T]. The effects of gravity are accounted by the term $+ 1$ in the right side, that accounts for the changes in hydraulic conductivity with respect to z .

Integration of Richards equation according to z , and multiplication with specimen cross-sectional area A [L²] gives a simple water balance equation: $dV(t)/dt = Q(t)$, where $Q(t)$ is expressed as the multiplicative of A and the flux at the specimen bottom ($z = 0$):

$$Q(t) = -AK(h_k) \left(\frac{\partial h_k(z,t)}{\partial z} \Big|_{z=0} + 1 \right) \quad (\text{A1-2})$$

Since the change in volume $V(t)$ is measured during the suction step outflow test, Equation (A1-2) should be integrated with respect to time (from 0 to t):

$$V(t) = -A \int_0^t K(h_k) \left(\frac{\partial h_k(z,t)}{\partial z} \Big|_{z=0} + 1 \right) dt \quad (\text{A1-3})$$

Based on the representation of $h_k(z, t)$ elaborated in the main text, the gradient $\frac{\partial h_k(z,t)}{\partial z} \Big|_{z=0}$ can be presented as:

$$\frac{\partial h_k(z,t)}{\partial z} \Big|_{z=0} = \frac{\partial h_k(z,t=0)}{\partial z} + \frac{\partial \Delta h_k(z,t)}{\partial z} \Big|_{z=0} = -1 + \frac{\partial \Delta h_k(z,t)}{\partial z} \Big|_{z=0} \quad (\text{A1-4})$$

where $\frac{\partial h_k(z,t=0)}{\partial z} = -1$ corresponds to hydrostatic conditions (equilibrium state) established at $t = 0$. By using Equation (2.2-1) to describe $\Delta h_k(z, t)$, the derivative presented in Equation (A1-4) at $z = 0$ can be expressed as:

$$\frac{\partial h_k(z,t)}{\partial z} \Big|_{z=0} = -1 - \frac{2\Delta h_i}{H_s} \sum_{n=1,3,5,\dots}^{\infty} e^{-\frac{(n/2)^2 \pi^2 t D(h_k)}{H_s^2}} \quad (\text{A1-5})$$

As explained in the text, Gardner's method assumes $D(h_k) = \text{const.}$ and $C(h_k) = \text{const.}$ along the imposed suction step (Δh_i), leading to $K(h_k) = D(h_k)C(h_k) = \text{const.}$ over the same Δh_i .

Based on this and by using Equation (A1-6) to describe the suction gradient at specimen bottom, Equation (A1-3) can be presented in the following form:

$$V(t) = D(h_k)C(h_k)A \frac{2\Delta h_i}{H_s} \sum_{n=1,3,5,\dots}^{\infty} \int_0^t e^{-\frac{(n/2)^2 \pi^2 t D(h_k)}{H_s^2}} dt \quad (\text{A1-6})$$

giving, after solving the time integral in equation (A1-6):

$$V(t) = -H_s \Delta h_i C(h_k) A \frac{8}{\pi^2} \sum_{n=1,3,5,\dots}^{\infty} \frac{1}{n^2} \left(e^{-\frac{(n/2)^2 \pi^2 t D(h_k)}{H_s^2}} - 1 \right) \quad (\text{A1-7})$$

Since the total water volume drained is $V_{\infty} = H_s \Delta h_i C(h_k) A = H_s \Delta \theta A$ and $\frac{8}{\pi^2} \sum_{n=1,3,5,\dots}^{\infty} \frac{1}{n^2} = 1$, Equation (A1-7) can be transformed into the final form of Gardner's method described with Equation (2.2-2) in the main text.

A2: Kunze & Kirkham's graphical method

Kunze & Kirkham's solution is graphically presented through various curves showing the changes in $V(t)/V_\infty$ with respect to the variable $A_1^2 D(h_k)t/H_s^2$, in which parameter A_1 is the first solution of the equation $aA_n = \cot(A_n)$ (a is the ratio between the impedance of the ceramic disk and that of the specimen). The various curves correspond to various values of parameter a (see *Figure A2-1*). By shifting theoretical curves along the time axis (top x-axis in *Figure A2-1*), the curve that shows the best agreement with experimental data (presented in the form $V(t)/V_\infty$ versus t) is chosen to define the value of a . A reference time t_{RP} is also graphically determined for $A_1^2 Dt/H_{soil}^2 = 1$ (arrow in *Figure A2-1*). Kunze & Kirkham (1962) remarked that only a portion of the experimental data corresponded to the theoretical curves, so they recommended to rather fit the curves at small times. Based on the chosen value of a , the corresponding value of A_1^2 is adopted from the table presented in Kunze & Kirkham (1962), and used to calculate diffusion coefficient as $D(h_k) = H_s^2 / A_1^2 t_{RP}$ and the hydraulic conductivity as $K(h_k) = D(h_k) \Delta\theta/\Delta h_i$.

In *Figure A2-1* is presented an example that illustrates some level of subjectivity of this graphical method. If one follows the recommendation to fit only a portion of measurements (circles) at small times with theoretical curves (*Figure A2-1a*), curve $a = 0.2$ (solid line) seems to best match, as seen in log-log scale (left graph of *Figure A2-1a*). On the contrary, a time logarithmic scale (*Figure A2-1a* - right) gives better insight on the overall agreement, showing a significant deviation between the curve $a = 0.2$ and measurements for $t > 1000$ s. By shifting the family of curves to the left (reducing t_{rp}), the best agreement over the entire range of t is obtained for $a = 10$ (solid line in *Figure A2-1b* - right), which is however not observable in log-log scale (left graph in *Figure A2-1b*). In addition, the deviation between different theoretical curves becomes less observable for higher a values (stronger impedance), which makes choosing the adequate curve even more difficult (e.g. $a = 10$ and $a = 1000$ are almost overlapping – *Figure A2-1b*).

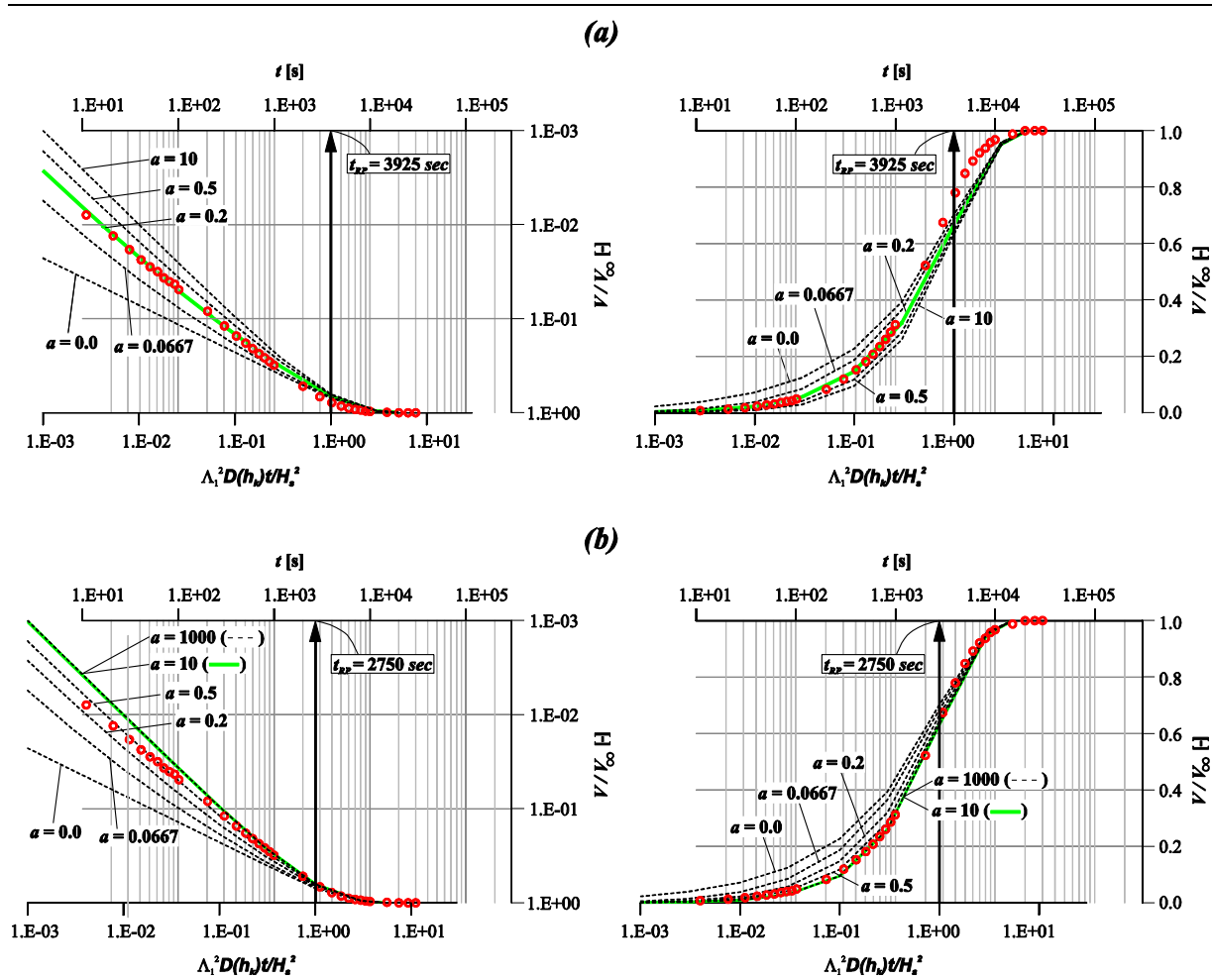


Figure A2-1. Correspondence between measured data (circles) and theoretical curves presented in log-log scale (left graphs) and time logarithmic scale (right graphs); (a) theoretical curves (and axis $\Lambda_1^2 D(h_k)t/H_s^2$) are shifted from $t_{rp} = 1E+4$ s (initial position) to $t_{rp} = 3925$ s to obtain the best agreement with data at small times ($a = 0.2$ – solid line); (b) best overall fit between data and curves is obtained for $t_{rp} = 2750$ ($a = 10$ – solid line)

A3: Analogy with the dry sieving method

The analogy between Equation (3.1-8) (the up-scaling approach) and the dry sieving method can be derived under the following assumptions:

1. Three-dimensional space is considered ($E = 3$) since the dry sieving method is based on the grain masses.
2. All grains have the same shape and density ρ_s .
3. A discrete number of sieves is used, and hence the size of voids on each sieve follows the size of voxels $L_1(\lambda_{n-i})$ at different λ_{n-i} , where $i = [0 \div n]$.

The total mass of the specimen (M_{total}) is placed on the cascade of sieves arranged in a descending order (the largest void size is on the top, while the smallest one is on the bottom). If all grains are distributed on the corresponding sieves $i = [0 \div n]$, it can be assumed that those staying on a certain sieve have diameter equal to the size of sieve voids. Therefore, the following can be written for $i = 0$:

$$M(d \geq L_1(\lambda_n)) = M_{total} = C_V \rho_s \sum_{j=0}^n N_g(\lambda_{n-j}) L_1(\lambda_{n-j})^3 \quad (\text{A3-1})$$

where C_V is the volume shape coefficient [-] (for cube $C_V = 1$, for sphere $C_V = \pi / 6$), $N_g(\lambda_{n-j})$ is the number of grains [-] that stay on the sieve of void size $L_1(\lambda_{n-j})$ [L] ($j = 0 \div n$). Since grains that stay on the sieve $l(\lambda_n)$ are assumed to have identical diameters, $L_1(\lambda_n)^3$ can be pulled outside the sum, and the following is obtained:

$$M(d \geq L_1(\lambda_n)) = C_V \rho_s L_1(\lambda_n)^3 \sum_{j=0}^n N_g(\lambda_{n-j}) \left(\frac{L_1(\lambda_{n-j})}{L_1(\lambda_n)} \right)^3 \quad (\text{A3-2})$$

$$N_g^{cum}(\lambda_n) \approx C_V \sum_{j=0}^n N_g(\lambda_{n-j}) \left(\frac{L_1(\lambda_{n-j})}{L_1(\lambda_n)} \right)^3 \quad (\text{A3-3})$$

where $N_g^{cum}(\lambda_n)$ is the cumulative number of grains equal to or larger than $d_{g,min} = L_1(\lambda_n)$. Following Equation (A3-2), the cumulative mass of all grains equal to or larger than $L_1(\lambda_{n-i})$ can be expressed as the following:

$$M(d \geq L_1(\lambda_{n-i})) = C_V \rho_s L_1(\lambda_{n-i})^3 \sum_{j=i}^n N_g(\lambda_{n-j}) \left(\frac{L_1(\lambda_{n-j})}{L_1(\lambda_{n-i})} \right)^3 \quad (\text{A3-4})$$

$$N_g^{cum}(\lambda_{n-i}) \approx C_V \sum_{j=i}^n N_g(\lambda_{n-j}) \left(\frac{L_1(\lambda_{n-j})}{L_1(\lambda_{n-i})} \right)^3 \quad (\text{A3-5})$$

By introducing Equation (A3-3) into (A3-2) and Equation (A3-5) into (A3-4), the GSD can be expressed as:

$$P(d < L_1(\lambda_{n-i})) = 1 - \frac{M(d \geq L_1(\lambda_{n-i}))}{M(d \geq L_1(\lambda_n))} \quad (\text{A3-6})$$

$$P(d < L_1(\lambda_{n-i})) = 1 - \frac{N_g^{cum}(\lambda_{n-i})}{N_g^{cum}(\lambda_n)} \left(\frac{L_1(\lambda_{n-i})}{L_1(\lambda_n)} \right)^3 \quad (\text{A3-7})$$

Note that $N_g^{cum}(\lambda_{n-i})$ and $N_g^{cum}(\lambda_n)$ correspond to $N(\rho^{ind}(\lambda) \geq \rho_{s,min}^{ind})$ and $N(\rho^{ind}(\lambda_n) \geq \rho_{s,min}^{ind})$ in Equation (3.1-8), respectively, while $\frac{L_1(\lambda_{n-i})}{L_1(\lambda_n)} = \frac{\lambda_n}{\lambda_{n-i}}$. Therefore, Equation (A3-7) is identical to Equation (3.1-8) for $E = 3$, just in a discrete form.

A4: Simplification of hydraulic conductivity function

Having on mind that capillarity dominantly affects water retention and water transfer properties of green roof substrates, K can be reduced to K^{cap} (Equation 3.2-10) and S_e to S_e^{cap} . In order to simplify Equation (3.2-10), it was decided to express $F = \left((h_k/h_{k,a})^{D_f-4} - (h_{k,r}/h_{k,a})^{D_f-4} \right) / \left(1 - (h_{k,r}/h_{k,a})^{D_f-4} \right)$ as S_e^m (both F and S_e take values between 0 and 1), where exponent m needs to be a function of physically-based parameters used in Equation (3.2-10). By using Equation (5.1-1), F can be regrouped and presented as a function of S_e :

$$F(S_e) = \left(\left(1 + S_e \frac{\theta_s - \theta_r}{1 - (\theta_s - \theta_r)} \right)^{\frac{D_f-4}{D_f-3}} - 1 \right) / \left(\left(\frac{1}{1 - (\theta_s - \theta_r)} \right)^{\frac{D_f-4}{D_f-3}} - 1 \right) \quad (A4-1)$$

The best agreement between $F(S_e)$ and S_e^m can be obtained by using the minimal quadratic difference as the criterion function f :

$$f = (F(S_e) - S_e^m)^2 \quad (A4-2)$$

If the first derivative of Equation (A4-2) with respect to m is equal to zero, the following is obtained:

$$\frac{\partial f}{\partial m} = 2[F(S_e) - S_e^m] \left[\frac{\partial F(S_e)}{\partial m} - S_e^m \ln(S_e) \right] = 0 \quad (A4-3)$$

Note that $\frac{\partial F}{\partial m} = 0$ because $F(S_e)$ does not depend on m , and thus Equation (A4-3) can be expressed as the following:

$$-2S_e^m [F(S_e) - S_e^m] \ln(S_e) = 0 \quad (A4-4)$$

Equation (A4-4) is equal to zero for: *i*) $S_e = 0$ and $S_e = 1$, which is independent of m ; *ii*) $[F(S_e) - S_e^m] = 0$, which is of interest here. Based on *ii*), the following expression is obtained:

$$m = \frac{\ln(F(S_e))}{\ln(S_e)} \quad (A4-5)$$

After introducing Equation (A4-1) into Equation (A4-5), Equation (5.1-3) is obtained. Since both $F(S_e)$ (Equation A4-1) and S_e^m are equal to zero for $S_e = 0$, and to 1 for $S_e = 1$, they need to cross each other at some point where $F(S_e) = S_e^m$ ($f = 0$ - see *Figure A4-1*).

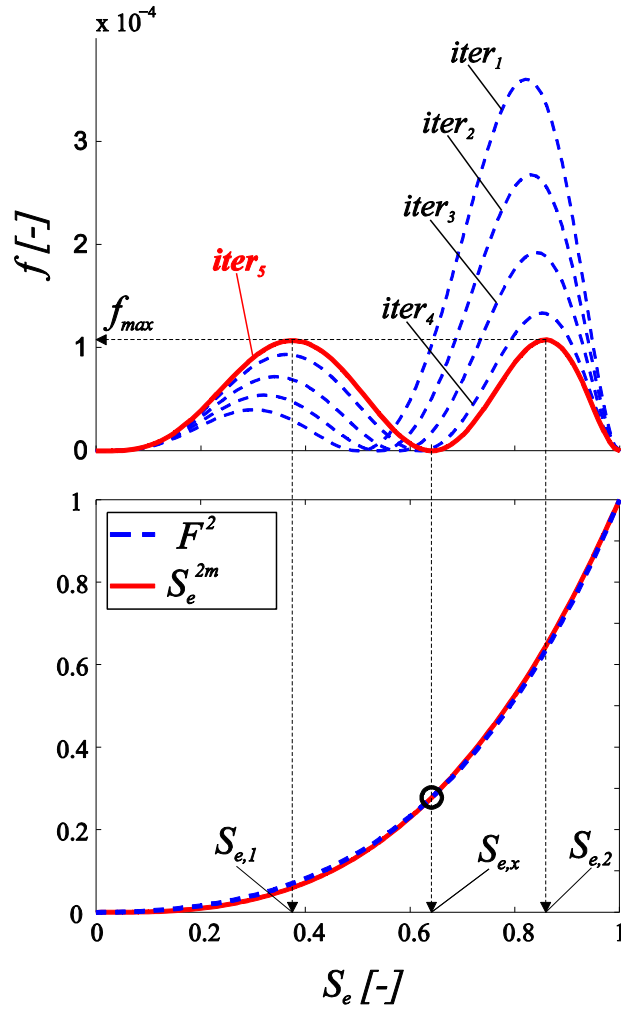


Figure A4-1. Iterative process for determination of the optimal $S_{e,x}$ value

For obtaining the best overall agreement between two functions, it is necessary to find the optimal crossing point $S_{e,x}$ (see Equation 5.1-3) that secures identical maximal f values for $S_e < S_{e,x}$ and for $S_e > S_{e,x}$ (see Figure A4-1 - top). If these values are met at $S_{e,1}$ and $S_{e,2}$, the following can be written:

$$|f(S_{e,1}) - f(S_{e,2})| \leq err \quad (\text{A4-6})$$

where err is the absolute difference [-] that is close to zero ($err = 1 \times 10^{-6}$ adopted in this work). Since f reaches maximal value for both $S_{e,1}$ and $S_{e,2}$, the following can be written:

$$\left. \frac{\partial f}{\partial S_e} \right|_{S_e=S_{e,1}} = 0 \quad (\text{A4-7})$$

$$\left. \frac{\partial f}{\partial S_e} \right|_{S_e=S_{e,2}} = 0 \quad (\text{A4-8})$$

By using Equations (A4-6) – (A4-8), $S_{e,x}$ can be determined iteratively, in the following way. After assuming the initial value of $S_{e,x}$, $m(S_{e,x})$ is calculated by using Equation (5.1-3), and

function f (Equation A4-1) is determined. Values of $S_{e,1}$ and $S_{e,2}$ are then implicitly calculated from Equations (A4-7) and (A4-8), and the validity of Equation (A4-6) is checked. If the condition is satisfied, the calculation is stopped and the temporary $S_{e,x}$ value is adopted, while in the opposite case $S_{e,x}$ is slightly changed and the procedure is repeated. Since the optimal $S_{e,x} > 0.5$ for all relevant values of $(\theta_s - \theta_r)$ and D_f , it is recommended to adopt $S_{e,x} = 0.5$ as the initial value, and to increase it slightly in every iteration until the optimal value is reached. The value of increment should decrease as Equation (A4-6) approaches to err in order not to overestimate the optimal $S_{e,x}$.

A5: Numerical scheme for solving Richards equation – Finite Differences Method

Standard numerical scheme for solving Richards equation by using finite differences method (van Dam & Feddes, 2000) can be presented as following:

$$\frac{\theta_j^{i+1,p-1} - \theta_j^i}{\Delta t} + \frac{C_j^{i+1}}{\Delta t} (h_{k,j}^{i+1,p} - h_{k,j}^{i+1,p-1}) = \frac{1}{\Delta z} (q_{j+1/2}^{i+1-e} - q_{j-1/2}^{i+1-e}) \quad (\text{A5-1})$$

Where fluxes $q_{j+1/2}^{i+1-e}$ and $q_{j-1/2}^{i+1-e}$ can be presented as:

$$q_{j+1/2} = -K_{j+1/2}^{i+1-e} \left(\frac{((1-e)h_{k,j}^{i+1,p} + eh_{k,j}^i - (1-e)h_{k,j+1}^{i+1,p} - eh_{k,j+1}^i)}{\Delta z} + 1 \right) \quad (\text{A5-2})$$

$$q_{j-1/2} = -K_{j-1/2}^{i+1-e} \left(\frac{((1-e)h_{k,j-1}^{i+1,p} + eh_{k,j-1}^i - (1-e)h_{k,j}^{i+1,p} - eh_{k,j}^i)}{\Delta z} + 1 \right) \quad (\text{A5-3})$$

$$K_{j+1/2}^{i+1-e} = \frac{(1-e)K_j^{i+1,p-1} + eK_j^i + (1-e)K_{j+1}^{i+1,p-1} + eK_{j+1}^i}{2} \quad (\text{A5-4})$$

$$K_{j-1/2}^{i+1-e} = \frac{(1-e)K_{j-1}^{i+1,p-1} + eK_{j-1}^i + (1-e)K_j^{i+1,p-1} + eK_j^i}{2} \quad (\text{A5-5})$$

In Equation (A5-1) element $(h_{k,j}^{i+1,p} - h_{k,j}^{i+1,p-1})$ is introduced as the mass conservation parameter which becomes insignificant as the convergence progresses. Index j is related to the space discretization [1 to N], i to the time discretization and p to the iteration level. Also, by introducing factor e [0 to 1] which is related to the time interpolation, it is possible to use fully implicit ($e = 0$), explicit ($e = 1$), or semi-implicit scheme ($0 < e < 1$). In this work $e = 0$ is used, while for $e = 0.5$ the Crank-Nicolson scheme is obtained. Soil hydraulic properties can be described using Equations (5.1-1) and (5.1-2), and hence $K_j^i = K(S_{e,j}^i)$ and $C_j^i = \frac{D_f - 3}{h_{k,a}} \left(\frac{h_{k,j}^i}{h_{k,a}} \right)^{D_f - 4}$.

In case of green roofs, two boundary conditions are mostly interesting: defined flux on the soil top surface and free drainage condition at the bottom. For $j = 1$ we have $q_{j-1/2}^{i+1-e} = -q_{in}$ (sign minus indicates the negative value of flux), and thus Equation (A5-1) can be presented as:

$$\frac{\theta_1^{i+1,p-1} - \theta_1^i}{\Delta t} + \frac{C_1^{i+1}}{\Delta t} (h_{k,1}^{i+1,p} - h_{k,1}^{i+1,p-1}) = \frac{1}{\Delta z/2} (q_{3/2}^{i+1-e} + q_{in}^{i+1}) \quad (\text{A5-6})$$

On the contrary, $q_{j+1/2}^{i+1-e} = -K_N^{i+1-e} = (1-e)K_N^{i+1,p-1} + eK_N^i$ for $j = N$, and Equation (A5-1) becomes:

$$\frac{\theta_N^{i+1,p-1} - \theta_N^i}{\Delta t} + \frac{C_N^{i+1}}{\Delta t} (h_{k,N}^{i+1,p} - h_{k,N}^{i+1,p-1}) = \frac{1}{\Delta z/2} (-K_N^{i+1-e} - q_{N-1/2}^{i+1-e}) \quad (\text{A5-7})$$

Note that $\Delta z / 2$ is used for both boundary conditions (Equations A5-6 and A5-7), because uniform space discretization is applied. The proposed numerical scheme can be presented in a vector form, similar as presented in van Dam & Feddes (2000).

List of Figures:

Figure 1.2-1. Illustration of different scales

Figure 1.3-1. The “Green Wave” of the Bienvenue building located close to Ecole des Ponts ParisTech, Marne la Vallée

Figure 2.1-1. Photo of the volcanic substrate used for the “Green Wave”

Figure 2.1-2. Grain size distribution curve of the volcanic substrate

Figure 2.1-3. General lay-out of the hanging column system

Figure 2.1-4. Description of the two procedures used: a) change in water level observed the in outer tube (ΔH_1) with valve V4 closed and valve 5 opened; b) change in water level observed in the inner tube (ΔH_2) with valve 4 opened and valve 5 closed.

Figure 2.1-5. Continuous monitoring of the imposed suctions during the 13 steps, provided by the differential pressure transducer.

Figure 2.1-6. Zoom of the suction changes (solid line with rectangles – imposed suction; dashed line with triangles – calculated suction at the top of the ceramic disk): a) steps 1 and 2; b) steps 11 and 12

Figure 2.1-7. Water retention curve obtained using both techniques of controlling suction (hanging column and axis translation)

Figure 2.1-8. Data of the constant water head hydraulic conductivity measurement of the saturated material.

Figure 2.1-9. Kunze and Kirkham's method applied to steps 1 and 2 (arrow indicates t_{RP})

Figure 2.1-10. Data from Gardner's method, suction steps 2' and 5 – 13

Figure 2.1-11. Hydraulic conductivity function (HCF)

Figure 2.2-1. Simplified scheme of the hanging column apparatus of Stanić et al. (2019), where the water drained from the specimen overflows from the inner to the outer tube (initial suction equal to zero)

Figure 2.2-2. Simplified scheme of Stanić et al. (2019)'s device, in the case when the water extracted from the specimen is collected in the inner tube (no overflow), resulting in a non-constant suction step

Figure 2.2-3. WRCs of (a) the coarse substrate determined by Stanić et al. (2019); (b) of the remolded poorly graded sand (RPGS) and undisturbed silty clay (USC) determined by Wayllace & Lu (2011). Saturated water content (θ_s) is indicated in each graph

Figure 2.2-4. Green Wave substrate; top graphs - suction change at specimen bottom, at contact with ceramic disk; bottom graphs - measured outflow (circles) compared with calculated values from different methods (indicated on the Figure); (a) suction step 1 - impedance effect; (b) suction step 4 – non-constant suction increment; (c) suction step 11 – same as in (b)

Figure 2.2-5. Change of hydraulic conductivity of the coarse substrate with respect to increased suction obtained using 3 different methods: Kunze & Kirkham's method (squares), Gardner's method (triangles) and methods developed in this work (circles). Hydraulic conductivity values obtained by analyzing volume change measurements at larger times (Equation 2.2-3) are presented with blue symbols

Figure 2.2-6. (a) Poorly graded sand (data from Wayllace & Lu, 2011); top - Suction change at specimen bottom, at contact with ceramic disk, bottom – measured outflow (circles) compared with calculated values from different methods (indicated on the Figure); (b) Undisturbed silty clay (data from Wayllace & Lu, 2011): same as in (a)

Figure 3.1-1. Eight horizontal $\rho^{ind}(\lambda_n = 1024)$ fields analyzed in this work (vertical distance between two consecutive planes is ≈ 1.6 cm)

Figure 3.1-2. Change of the two-dimensional $\rho^{ind}(\lambda)$ field (Horiz. plane 4 in Figure 3.1-1) with λ at: (A) $\lambda = 128$; (B) $\lambda = 64$; (C) $\lambda = 32$; (D) $\lambda = 16$; (E) $\lambda = 8$; (F) $\lambda = 4$.

Figure 3.1-3. Comparison between the probability of exceeding i) a resolution dependent threshold λ^γ (Equation (3.1-1) – different dashed lines for different γ values) and ii) a fixed threshold value $\rho_{s,min}^{ind} = 1.55$ (Equation (3.1-11)- solid line). UM parameter values are related to the Horizontal plane 4 (see Table 3.1-1 later in the text): $C_1 = 2.23 \times 10^{-2}$, $\alpha = 1.67$

Figure 3.1-4. Scaling of statistical moments for eight $\rho^{ind}(\lambda)$ fields presented in Figure 3.1-1

Figure 3.1-5. Moment scaling functions $K(p)$ obtained by applying TM technique on eight horizontal $\rho^{ind}(\lambda)$ fields presented in Figure 3.1-1 (different solid lines) and eight vertically oriented $\rho^{ind}(\lambda)$ fields (dashed lines)

Figure 3.1-6. Behavior of the proposed GSD model when changing values of: a) C_1 ; b) α ; c) $\rho_{s,min}^{ind}$; d) $d_{g,min}$. Initial parameter values (solid line in each graph) are $C_1 = 1.85 \times 10^{-2}$, $\alpha = 1.3$, $\rho_{s,min}^{ind} = 1.55$ and $d_{g,min} = 1 \times 10^{-3}$ mm

Figure 3.1-7. Comparison between: A) Equation (3.1-12) applied on the Horizontal plane 4 ($L = 60$ mm, $\rho_{s,min}^{ind} = 1.55$, $\lambda_n = 1024$, $C_1 = 2.23 \times 10^{-2}$, $\alpha = 1.67$), Equation (3.1-8) applied on the same field ($\rho_{s,min}^{ind} = 1.55$, $\lambda_n = 1024$), and truncated experimental GSD data ($d_g \geq 50$ μ m); B) Equation (3.1-12) applied on eight $\rho^{ind}(\lambda)$ fields presented in Figure 3.1-1 ($L = 60$ mm, $\rho_{s,min}^{ind} = 1.55$, $\lambda_n = 1024$, while α and C_1 are presented in Table 3.1-1), and truncated experimental GSD data ($d_g \geq 50$ μ m); C) Equation (3.1-12) (same as in B) just for $d_{g,min} = 1$ μ m) and the full-range experimental GSD data ($d_g \geq 1$ μ m)

Figure 3.1-8. Comparison between the experimental GSD data (GW substrate – squares; ASCL – circles; YCL - diamonds) and Equation (3.1-13) (solid lines) and Equation (3.1-14) (dashed lines). The adjusted values of C_1 and α (Equation 3.1-13) and $D_{f,PSF}$ (Equation 3.1-14) are presented in Table 3.1-2

Figure 3.2-1. Procedure for determination of the fractal dimension of white pixels ($\rho^{ind} = \text{const.} > 0$). Resolution λ of the binary image decreases starting from (A) to (F) by factor 2. Axis of each image indicates the number of pixels in two orthogonal directions that correspond to λ

Figure 3.2-2. Empty and filled dots illustrate the representations of white and black pixels that are counted at different λ of Figure 3.2-1; Solid and dashed lines illustrate the change of white and black pixels, respectively, according to the fractal-based approach presented

Figure 3.2-3. Comparison between the proposed model and the water retention (top graph) and hydraulic conductivity (bottom graph) experimental data taken from Stanić et al. (2019b)

Figure 3.2-4. Comparison between the proposed model and 6 data sets from the literature. Top graphs present water retention data, bottom graphs hydraulic conductivity functions, all with respect to suction changes

Figure 3.2-5. Comparison between the proposed model and 3 additional data sets from the literature. Left-side graphs deal with water retention data, whereas right-side graphs deal with hydraulic conductivity functions with respect to changes in water content

Figure 4.1-1. The Blue Green Wave monitoring site of ENPC: (a) pictures, (b) vertical representation and flow path lengths, (c) aerial representation showing the monitored area, and (d) profile of the section where the water content sensors were implemented indicating the slopes

Figure 4.1-2. Vertical profile of the Green Wave structure

Figure 4.1-3. Comparison between Topp Equation (black solid line) and experimentally determined correlations between k_a and θ , for the Green Wave substrate, for different levels of compaction obtained in laboratory conditions

Figure 4.1-4. Validation of the application of Manning-Strickler equation for estimating drained discharge based on the measurements of water level inside the drainage pipe

Figure 4.1-5. Location of the water level sensors in the stormwater network

Figure 4.1-6. Relationship adjusted between the water level H_1 and the downstream discharge Q_2

Figure 4.1-7. Rainfall and computed discharges for the whole time period

Figure 4.1-8. Rainfall and Dielectric Constant for 16 TDR sensors

Figure 4.2-1. Example of an one-dimensional multifractal field (time series)

Figure 4.2-2. Dependence of $c(\gamma)$ (top row) and $K(p)$ (bottom row) on UM parameters α and C_1 . Dashed line is related to $\alpha = 2$, solid line to $0 < \alpha < 2$ and dash-dotted line to $\alpha = 0$. Concerning parameter C_1 , three cases are presented: a) C_1 is approximately zero; b) C_1 takes value between 0 and E; c) C_1 takes maximal value E. Values of the maximal observable singularity γ_s and the corresponding p_s are marked in the graphs

Figure 4.2-3. Legendre transform

Figure 4.2-4. Trace Moment (TM) technique (dashed line represents the mean value)

Figure 4.2-5. Double Trace Moment (DTM) technique (dashed line represents the mean value)

Figure 4.2-6. Configuration of TDR sensors in case of: a) events 1 and 2; b) event 3

Figure 4.2-7. Data of the rainfall intensity I (top subplot), dielectric constant k_a (15 subplots in the center corresponding to 15 TDR sensors) and drained discharge Q_d (bottom subplot) captured during event 1 (07.03.2018)

Figure 4.2-8. Scaling of the average statistical moments of order p ($\langle \varepsilon_\lambda^p \rangle$) applied on data of event 1. Subplots are distributed the same way as in Figure 4.2-7, with the following symbols representing values of $\langle \varepsilon_\lambda^p \rangle$ for: \blacktriangledown ($p = 3.0$), \blacktriangle ($p = 2.5$), \blacksquare ($p = 1.5$), \blacklozenge ($p = 1.01$), $+$ ($p = 0.1$)

Figure 4.2-9. Empirical $K(p)$ functions obtained for rainfall intensity, dielectric constant increments and discharge increments data (event 1)

Figure 4.2-10. Results of DTM technique applied on data of event 1 – $\log(\langle \varepsilon_\lambda^{(\eta)p} \rangle)$ versus $\log(\lambda)$. Subplots are distributed the same was as in Figure 4.2-7, with the following symbols representing values of $\langle \varepsilon_\lambda^{(\eta)p} \rangle$ for $p = 1.5$ and: \blacklozenge ($\eta = 2.84$), \bullet ($\eta = 1.87$), x ($\eta = 1.23$), $+$ ($\eta = 0.81$)

Figure 4.2-11. Results of DTM technique applied on data of event 1 - $\log(K(p, \eta))$ versus $\log(\eta)$ obtained from results presented in Figure 4.2-10. Subplots are distributed the same was as in Figure 4.2-7, where solid line in each subplot indicates linear part of the graph from which characteristics UM parameters are determined

Figure 4.2-12. Comparison between the empirical $K(p)$ curves (solid lines) taken from Figure 4.2-9, and Equation (4) computed by means of α_{TM} , $C_{1, TM}$ (dashed line) and α_{DTM} , $C_{1, DTM}$ (dash-dotted line). Subplots are distributed the same was as in Figure 4.2-7

Figure 4.2-13. Data of the rainfall intensity (top subplot), dielectric constant (8 subplots in the center corresponding to 8 TDR sensors) and drained discharge (bottom subplot) captured during event 2 (11.11.2017)

Figure 4.2-14. Empirical $K(p)$ functions obtained for rainfall intensity, dielectric constant increments and discharge increments data (event 2)

Figure 4.2-15. Comparison between the empirical $K(p)$ curves (solid lines) taken from Figure 4.2-14, and Equation (4) computed by means of α_{TM} , $C_{1, TM}$ (dashed line) and α_{DTM} , $C_{1, DTM}$ (dash-dotted line). Subplots are distributed the same was as in Figure 4.2-13

Figure 4.2-16. Data of the rainfall intensity (top subplot), dielectric constant (9 subplots in the center corresponding to 9 TDR sensors) and drained discharge (bottom subplot) captured during event 3 (25.08.2017)

Figure 4.2-17. Empirical $K(p)$ functions obtained for rainfall intensity, dielectric constant increments and discharge increments data (event 3)

Figure 4.2-18. Comparison between the empirical $K(p)$ curves (solid lines) taken from Figure 4.2-17, and Equation (4) computed by means of α_{TM} , $C_{1, TM}$ (dashed line) and α_{DTM} , $C_{1, DTM}$ (dash-dotted line). Subplots are distributed the same was as in Figure 4.2-16

Figure 5.1-1. Illustration of the CNLR concept – procedure for applying for a single time interval Δt (example with $n_{res} = 4$)

Figure 5.1-2. Influence of n_{res} on q_d computed using the CNLR model with parameter values from Chapter 3.2 ($H = 20$ cm, $\theta_s = 0.395$, $\theta_r = 0.045$, $D_f = 2.95$, $h_{k,a} = 0.9$ cm, $K_s = 8.11 \times 10^{-6}$ m/s, $l = -1.35$)

Figure 5.1-3. Comparison between q_d values calculated using the NLR model (dash-dotted line), the numerical model (dashed line), and the CNLR model with $n_{res} = 13$ (solid line), for the constant 3 h long inflow $q_{in} = 20$ mm/h. All models use parameter values taken from Chapter 3.2 (listed in the caption of Figure 5.1-2)

Figure 5.1-4. Comparison between the wetting fronts obtained by using the NLR model (dash-dotted line), the numerical model (dashed line), and the CNLR model with $n_{res} = 13$ (solid line)

Figure 5.1-5. Comparison between the measured q_d (dots), the CNLR model that uses parameter values from Chapter 3.2 (black solid line) and the CNLR model whose parameter values are manually adjusted (red solid line) to provide the best agreement with measured q_d . Input for the CNLR model is the measured rainfall intensity q_{in} (blue solid line)

Figure A2-1. Correspondence between measured data (circles) and theoretical curves presented in log-log scale (left graphs) and time logarithmic scale (right graphs); (a) theoretical curves (and axis $\Lambda_1^2 D(h_k)t/H_s^2$) are shifted from $t_{rp} = 1E+4$ s (initial position) to $t_{rp} = 3925$ s to obtain the best agreement with data at small times ($a = 0.2$ – solid line); (b) best overall fit between data and curves is obtained for $t_{rp} = 2750$ ($a = 10$ – solid line)

Figure A4-1. Iterative process for determination of the optimal $S_{e,x}$ value

List of Tables

Table 2.1-1. Basic characteristics of “Green Wave” substrate

Table 2.2-1. Parameters used and hydraulic conductivity values obtained for Gardner’s method, our method and Kunze & Kirkham’s method for the poorly graded sand and the undisturbed silt clay investigated in Wayllace & Lu (2011)

Table 3.1-1. Determined UM parameters for eight analyzed ρ^{ind} fields

Table 3.1-2. Basic physical parameters related to the GW substrate, ASCL and YCL, together with the manually adjusted values of UM parameters (THIS WORK) and fractal coefficient (PSF MODEL)

Table 3.2-1. Measured (θ_s , K_s^{cap}) and determined / adjusted values (highlighted in grey) of the model parameters

Table 4.2-1. Event 1 - values of UM parameters obtained by both TM (α_{TM} and $C_{1, TM}$) and DTM (α_{DTM} and $C_{1, DTM}$) techniques, values of p_D and p_s calculated based on α_{DTM} and $C_{1, DTM}$, and the maximal and the minimal values of R^2 parameter related to the scaling of $\langle \varepsilon_\lambda^p \rangle$

Table 4.2-2. The same as in Table 4.2-1, just for event 2

Table 4.2-3. The same as in Table 4.2-1 and Table 4.2-2, just for event 3